# Metamaterials and Plasmonics: Fundamentals, Modelling, Applications

# NATO Science for Peace and Security Series

This Series presents the results of scientific meetings supported under the NATO Programme: Science for Peace and Security (SPS).

The NATO SPS Programme supports meetings in the following Key Priority areas: (1) Defence Against Terrorism; (2) Countering other Threats to Security and (3) NATO, Partner and Mediterranean Dialogue Country Priorities. The types of meeting supported are generally "Advanced Study Institutes" and "Advanced Research Workshops". The NATO SPS Series collects together the results of these meetings. The meetings are co-organized by scientists from NATO countries and scientists from NATO's "Partner" or "Mediterranean Dialogue" countries. The observations and recommendations made at the meetings, as well as the contents of the volumes in the Series, reflect those of participants and contributors only; they should not necessarily be regarded as reflecting NATO views or policy.

**Advanced Study Institutes (ASI)** are high-level tutorial courses intended to convey the latest developments in a subject to an advanced-level audience

**Advanced Research Workshops (ARW)** are expert meetings where an intense but informal exchange of views at the frontiers of a subject aims at identifying directions for future action

Following a transformation of the programme in 2006 the Series has been re-named and re-organised. Recent volumes on topics not related to security, which result from meetings supported under the programme earlier, may be found in the NATO Science Series.

The Series is published by IOS Press, Amsterdam, and Springer, Dordrecht, in conjunction with the NATO Public Diplomacy Division.

**Sub-Series**

| | | |
|---|---|---|
| A. | Chemistry and Biology | Springer |
| B. | Physics and Biophysics | Springer |
| C. | Environmental Security | Springer |
| D. | Information and Communication Security | IOS Press |
| E. | Human and Societal Dynamics | IOS Press |

http://www.nato.int/science
http://www.springer.com
http://www.iospress.nl

**Series B: Physics and Biophysics**

# Metamaterials and Plasmonics: Fundamentals, Modelling, Applications


Edited by

Saïd Zouhdi
University Paris Sud
Orsay, France

Ari Sihvola
Helsinki University of Technology
Espoo, Finland

and

Alexey P. Vinogradov
Russian Academy of Sciences
Moscow, Russia



Springer

Published in cooperation with NATO Public Diplomacy Division

Proceedings of the NATO Advanced Research Workshop on
Metamaterials for Secure Information and Communication Technologies
Marrakech, Morocco
7–10 May 2008

Library of Congress Control Number: 2008940143

ISBN 978-1-4020-9406-4 (PB)
ISBN 978-1-4020-9405-7 (HB)
ISBN 978-1-4020-9407-1 (e-book)

---

Published by Springer,
P.O. Box 17, 3300 AA Dordrecht, The Netherlands.

*www.springer.com*

*Printed on acid-free paper*

---

# Contents

# Preface

**Saïd Zouhdi[1], Ari Sihvola[2], and Alexey Vinogradov[3]**

[1]LGEP–Supélec, Plateau de Moulon, 91192 Gif-sur-Yvette, France
said.zouhdi@supelec.fr
[2]Helsinki University of Technology, Department of Radio Science and Engineering
Box 3000, FI–02015 TKK, Finland
ari.sihvola@tkk.fi
[3]Institute for Theoretical and Applied Electrodynamics, Russian Academy of Sciences
Ul. Izhorskaya, Moscow, 125412, Russia
a-vinogr@yandex.ru

The cross-disciplinary field of metamaterials is emerging into the mainstream of electromagnetics and materials science research. The spark ignited by the theoretical speculations of double-negative media in the famous article by Victor Veselago stayed unnoticed for over 30 years before it expanded into flames of active research during the present century. Metamaterials are presently the topic of scientific discussions, seminars, sessions, conferences, at least one dedicated journal, research programs, networks, and increasingly growing amount of proposals for research funding.

Networking is one of the characteristic features in the new wave of metamaterials research. Due to its interdisciplinary character, it transcends boundaries between research fields. Investigators come from different traditions. They approach metamaterials problems, succeed in solving some, fail with others, create new, and change the way we see the field. The backgrounds are in electrical engineering, electromagnetics, solid state physics, microwave and antenna engineering, optoelectronics, classical optics, materials science, semiconductor engineering, and nanotechnology. The research orientations vary from theoretical analysis, computational and analytical modeling, and experimentalist approach to application-interested engineering.

META'08, the NATO Advanced Research Workshop with the subtitle *Metamaterials for Secure Information and Communication Technologies*, was organized in the city of Marrakech in Morocco in early May, 2008. Over 200 participants from 34 countries had the possibility to hear about the latest advances in the theory and applications of metamaterials from 13 plenary talks, and in 26 oral sessions and two poster sessions. META'08 was part of "The Science for Peace and Security Program" which is open to scientists from NATO, Partner, and Mediterranean Dialogue countries. In particular, the meeting enjoyed the high patronage of His Majesty Mohammed VI, King of Morocco.

This book attempts to chart the state-of-the-art of metamaterials research. The chapters to follow have been invited from selected speakers in META'08. The contributions are extended articles based on the presentations in the meeting.

The chairman of META'08 was Professor Saïd Zouhdi from the University Paris Sud, France. The local organizing committee was chaired by Professor Rachid Dkiouak from the University Abdelmalek Essaadi. Dr. Alexei Vinogradov (Institute of Theoretical and Applied Electromagnetism in Moscow, Russia) served as co-director of the NATO ARW. The meeting was also sponsored by the METAMORPHOSE Network of Excellence (EU), the Office of Naval Research Global (UK), GDR Ondes (France), US Army International Technology Center (UK), SUPELEC (France), CNRS (France), DGA (France), CST (Germany), IEEE-APS (USA), URSI (Belgium), University Abdelmalek Essaadi (Morocco), and Laboratoire de Génie Electrique de Paris (France).

A meeting devoted to metamaterials has also its history. META'08 can be connected to the series of chiral and bi-anisotropics workshops and conferences that took place in 1990s, and focused on emergent electromagnetic properties in complex materials and their applications. Two times before, such conferences have been arranged in the format of NATO Advanced Research Workshop: in 1996 (in Russia [1]) and in 2002 (also in Marrakech [2]).

## References


1. Priou, A., Sihvola, A., Tretyakov, S., Vinogradov, A. (eds.): Advances in Complex Electromagnetic Materials. NATO ASI Series: 3: High Technology, **28**, Kluwer, Dordrecht (1997)
2. Zouhdi, S., Sihvola, A., Arsalane, M. (eds.): Advances in Electromagnetics of Complex Media and Metamaterials. NATO Science Series: II: Mathematics, Physics, and Chemistry, **89**, Kluwer, Dordrecht (2003)


**Photo on the facing page**: the plenary speakers of the Advanced Research Workshop META'08 standing in the courtyard of the Hotel Atlas Asni in Marrakech.

# Handedness in Plasmonics: Electrical Engineer's Perspective

**Ari Sihvola**[1] **and Saïd Zouhdi**[2]

[1]Helsinki University of Technology, Department of Radio Science and Engineering
Box 3000, FI–02015 TKK, Finland
ari.sihvola@tkk.fi
[2]LGEP – Supélec, Plateau de Moulon, 91192 Gif-sur-Yvette, France
said.zouhdi@supelec.fr

**Abstract** In this article, the concepts of handedness and negative material parameters are analyzed at a general and qualitative level. Three different usages of handedness in metamaterials and electromagnetics are distinguished: left-handedness as characterization of double-negative materials, handedness of the polarization of a plane wave, and chirality in the structure of matter. The symmetry of the treatment between left and right is discussed from the point of view of the three uses of the handedness. It is essential to distinguish the helicity of the spatial shape of the field vector as opposed to the temporal behavior of the field at a given position in space. Negative refraction and backward-wave characteristics are discussed in the case when structural chirality of the medium splits the wave numbers of the eigenwaves. Finally, negative refraction is connected with anisotropic and bi-anisotropic materials.

## 1 Introduction

Metamaterials form such a wide and uncharted range of materials that a coherent presentation of the possible examples of media that fall in this class is beyond reach [1]. With powerful new technologies that allow processing of materials at nanoscales, many types of artificial materials can be fabricated which are endowed with engineered properties that could only be dreamed of in the past [2]. In addition to man-made materials, also many naturally existing media display strange and emergent properties [3]. This fact contributes further to the fact that it is difficult to draw lines that would separate metamaterials from other, evenly interesting substances.

Typical to an emergent research field like metamaterials is also its interdisciplinary character that transcends previously respected boundaries between research fields. We see people from different traditions and backgrounds approaching and attacking

S. Zouhdi et al. (eds.), *Metamaterials and Plasmonics: Fundamentals, Modelling, Applications*,

metamaterials problems, solving those, and creating new ideas. These researchers come from electrical engineering, electromagnetics, solid state physics, microwave and antenna engineering, optoelectronics, classical optics, materials science, semiconductor engineering, nanoscience, etc.

The diversity of backgrounds and paradigms is a source of fruitful cross-fertilization of ideas, and potential for joint research networks where different strengths and capacities can be successfully combined. But the challenge is to find the internal cohesion for such joint efforts. Within different domains of science and engineering, the traditions of doing research and analyzing problems may differ. Even the formalism and terminology of quantities of the same physical phenomenon may vary when researchers from different backgrounds approach the problem. For example in discussions about magnetism and reciprocity, or plasmonics and surface waves, concepts may cause initial difficulties in understanding the language of a colleague.

The present article attempts to cast some light into one area of metamaterials studies where misunderstandings and ambiguous concepts are being used. What does it mean to say that something is "left-handed" or "right-handed"? How does the important phenomenon of negative refraction or backward wave propagation connect with handedness? How symmetric is the distinction between left and right? Various ways of looking at handedness, helicity, chirality, order, and symmetry are discussed. The metamaterials under study are also analyzed from the point of view of bi-anisotropic classification where the number of degrees of freedom in characterizing the medium becomes many times larger.

## 2 Close-Reading of the Term "Handedness"

Handedness is a term that is very much used in the metamaterials literature. Let us start by discussing the various meanings of handedness within the electromagnetics discipline. It is essential to define and analyze these meanings because very often in even scientific discussions they are used parallel and grave misunderstandings may result from a wrong association of this term.

### *2.1 The three meanings of handedness in electromagnetics*

Let us separate three different meanings of handedness in electromagnetics and materials [4]:

1. Metamaterials as "left-handed" media
2. Handedness of the circularly (or elliptically) polarized wave
3. Chirality as geometrical structure of matter

### 2.1.1 Metamaterials as left-handed media

The use of the label "left-handed" materials for a certain class of metamaterials has its rationale from the handedness of the vector triplet (**E**, **H**, **k**) of a linearly polarized wave propagating in such media; these vectors here refer to the electric field, magnetic field, and wave vector. Such left-handedness is the situation if both the dielectric permittivity and magnetic permeability are both negative.

With time-harmonic convention exp(jωt), Maxwell curl equations read for plane-wave functional dependence $\exp(-j\mathbf{k}\cdot\mathbf{r})$ as

$$\mathbf{k}\times\mathbf{E} = \omega\,\mathbf{B} = \omega\mu\mathbf{H}, \qquad \mathbf{H}\times\mathbf{k} = \omega\,\mathbf{D} = \omega\varepsilon\mathbf{E} \tag{1}$$

in homogeneous, isotropic, source-free background with permittivity ε and permeability μ. For ordinary media (which have positive permittivity and positive permeability), the (**E**, **H**, **k**) triplet is right-handed; however in case of both $\varepsilon < 0$ and $\mu < 0$, Eq. (1) makes it left-handed.[1] Likewise, the time-dependent Poynting vector $\mathbf{S} = \mathbf{E}\times\mathbf{H}$ is parallel to **k** in the first case and antiparallel in the latter one, as shown in Fig. 1.[2]

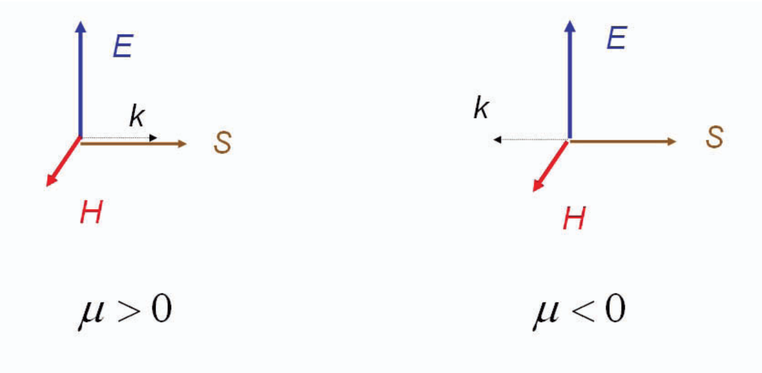


**Fig. 1** For "ordinary" isotropic media (*left*), the triplet (**E**, **H**, **k**) is right-handed and the wavevector **k** points parallel to the Poynting vector **S**, whereas for negative parameters (*right*), the wavevector changes direction and the triplet becomes left-handed (and **k** and **S** become antiparallel).

---

[1] Note, however, that even if the handedness of (**E**, **H**, **k**) depends on the sign of ε and μ, the triplets (**E**, **B**, **k**) and (**D**, **H**, **k**) are both right-handed, irrespective of the signs of the material parameters.

[2] Faraday's law $\mathbf{k}\times\mathbf{E} = \omega\,\mathbf{B} = \omega\mu\mathbf{H}$ seems to lead to the conclusion that it is only the sign of μ that determines the right/left-handedness of the triplet (**E**, **H**, **k**). However, it is important to keep in mind that in order for the waves to propagate, a negative μ has to be complemented with a negative ε, due to the wave number dependence on the material parameters $k = \omega(\mu\varepsilon)^{1/2}$.

Such type of metamaterials obey many other names in addition to “left-handed media” [5]: double-negative materials, negative-index materials, negative-phase-velocity materials, backward-wave media, and – due to the theoretical prediction of their existence in the 1960s [6] – Veselago media.

### 2.1.2 Handedness of a circularly polarized wave

In the language of electrical engineers, especially antenna engineers, the term handedness appears in connection with polarization of the electromagnetic wave or a radio wave. Polarization then refers to the direction and behavior of the electric field vector which for a circular or elliptical polarization has a character of helicity, or handedness. The wave is propagating in a certain direction and (in isotropic media) the electric field is transversal ($\mathbf{k} \cdot \mathbf{E} = 0$). In the transversal plane, the temporal oscillations of the field vector follow an ellipse or circle (in the case of linear polarization, the ellipse shrinks to a line).

When looking along the wave propagation direction, the wave may rotate in two directions. According to the Federal Standard 1037C, the polarization is defined right-handed if the temporal rotation is clockwise when looking from the transmitter (in the propagation direction), and left-handed if the rotation is counterclockwise. Hence, the wave depicted in Fig. 2 would be right-handed circularly polarized.

It is important to bear in mind that this handedness definition is not universal. For example, astronomers [7] are always looking towards the source (transmitter), and hence into the opposite direction of the wave propagation. Then also clockwise and counterclockwise senses swap as compared to the engineering point of view, and likewise the definition of right- and left-handedness is just the opposite. Figure 2, however, shows also that if we focus on the *spatial* behavior of the electric field instead of the time dependence, the field vector in space at a certain moment draws a left-handed spiral. The handedness of a fixed object remains the same even if it is turned or rotated. Both the antenna engineer behind the transmitter and the astronomer observing the emitted signal in front of the source agree that the spatial spiral is left-handed. (This fact would favor the astronomy definition of handedness by removing some arbitrariness in the handedness of the polarization.)[3]

---

[3] The talk about handedness is very human-centered. One may ask whether there might be more “objective” ways to define this difficult concept; for example, by defining in cold mathematical terms a positive or negative attribute to a structure with a given helicity. It has been pointed out that the emphasis on right-hand rules and memorizations in engineering education (which is very common) does not take into account the natural capabilities of all students, especially handicapped: how does an invalid who has lost both hands benefit from such rules of thumb?

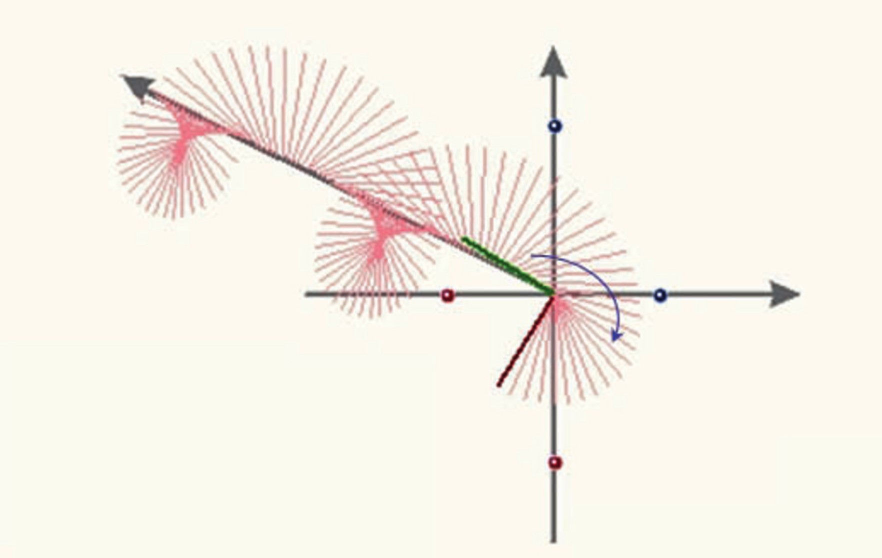

**Fig. 2** A circularly polarized wave has a sense of rotation and hence can be identified with a definition of handedness. In this figure the curved arrow shows the temporal rotation of the field vector in the plane of the two axes and the phase propagation direction is into the paper, shown with slightly oblique perspective. According to the Federal Standard [8] definition, this wave is right-handed circularly polarized. Note, however, that the curved spatial structure is a left-handed spiral. For an interactive applet showing the real temporal behavior of this polarization, see [9].

### 2.1.3 Chirality as geometrical structure of matter

Handedness is also an everyday concept affiliated with material objects, like corkscrews, ice hockey clubs, scissors, and construction tools. The mirror image of a right-handed object is otherwise the same as the original but it is left-handed. A non-handed object remains the same within this mirror-image operation, because such an object, after imaging, can be brought into congruence with the original by simple translations and rotations.

A handed object is called "chiral",[4] and if molecules or other small elements with a particular handedness form a macroscopically homogeneous medium with net handedness, such a composite can be called chiral medium. Chiral media possess so-called *optical activity*, meaning that the polarization is affected. The effect of the handed microstructure is that the polarization plane of a linearly polarized electromagnetic wave is rotated along the propagation path. The connection of chiral microstructure to macroscopic optical rotatory power was discovered by Louis Pasteur in 1840s. Although analogous to the Faraday rotation

[4] From the word in Greek language for "hand."

in magnetoplasma, the chirality-induced optical activity is a reciprocal effect, whereas the classical Faraday effect is non-reciprocal and anisotropic due to the biasing magnetic field [10].

The mirror image operation is also called parity transformation (all spatial axes are reversed when parity is changed), and it is a fundamental property of physics that parity symmetry is broken in subatomic interactions [11]. And also on several different scales and levels of nature, parity is not balanced. From amino acids through bacteria, winding plants, right-handed human beings to spiral galaxies, one of the handednesses dominates over the other [12].

Obviously chirality in structural objects and continuous media is a very basic manifestation of handedness. Since it also causes observable and particular electromagnetic effects (optical activity), one has to pay particular attention in analyzing phenomena where other meanings of handedness are relevant.

## *2.2 Equal or discriminative treatment between left and right*

Symmetry is an essential concept in analyzing handedness. Symmetry would also call for equality between the corresponding right- and left-handed objects; at least it is very compatible with the idea of equal status of two entities that are the same in all other respects except that they are each other's mirror images.

How do the three ways of looking at handedness, introduced in the previous section, differ as far as this aspect of left–right classification is concerned?

We can immediately note that very obviously the circular-polarization-based handedness property is fully symmetric. In other words, both senses of polarization are as easy to generate, and certainly one is as useful as the other. Even if the conventions differ and definitions regarding which wave is right-handed were not the same over scientific disciplines, at least it is only a question of phase shift in dipole antennas with which handedness the radiated wave is polarized.

On the other hand, the use of handedness with the reference to Veselago-type metamaterials is the totally opposite in this respect. There the "natural" state of affairs is the ordinary world of "right-handed" materials, as in Fig. 1: permittivity and permeability are positive as in ordinary materials. Only metamaterials, which by certain definitions are such media that do not exist naturally [3, 5], can display material parameters which both are simultaneously negative. As "left-handed" materials they belong certainly to another class of media which cannot by any means be treated as parallel status as "right-handed" ones.

What can we say about the third possibility of looking at handedness: the structural chirality? Very tempting would be to observe that the parity operation (mirror-imaging the object) does not change chemical or physical properties, capacity to be of use for something, or value of the original. The whole world and universe would probably not notice any difference if it were suddenly mirror-imaged at all levels.

On the other hand, it is clear that when parity is broken at a certain scale and entities of a given handedness dominate, such balance is self-preserving and positive feedback mechanisms perpetuate such a state. When all DNA molecules twist with the right-handed sense,[5] there is no chance of the opposite handedness to survive. However, the parity balance is turned around on the level of amino acids: only left-handed ones exist in natural proteins [12].

So, even if by coincidence of evolution and chance parity is broken on various scales in the natural world, it is nevertheless broken to both directions, left and right, and one might expect equal treatment with respect to this left–right variation on the global level. However, the human preference of right over left can be seen in the taxonomy of animal species. As Fig. 3 illustrates, the sea snail of genus *Busycon*, displaying left-handed chirality in its structure, has been given as its species identification the label *perversum*. The origin of such a derogatory name is most probably due the abnormality of left-handedness: such whelk molluscs are predominantly dextral, right-handed.

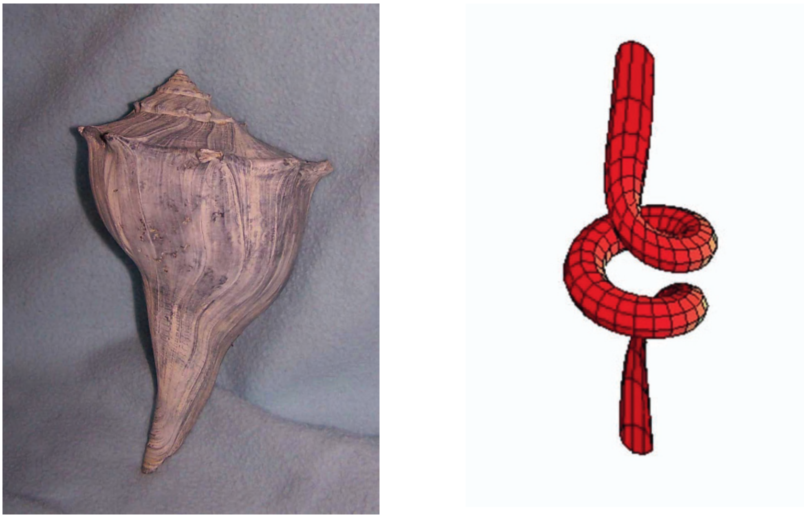

**Fig. 3** The marine mollusk *Busycon perversum* (lightning whelk) is left-handed in the sense of a three-dimensional screw (on the *right-hand side* of the figure). The strangeness of the handedness (most seashells show rotation along the right-handed sense) is most probably the reason behind the discriminative label (perverse!) for this species. (Image of the whelk taken from Wikipedia Commons.)

[5] The left-handed version of such nucleotides can be prepared in the laboratory; but in nature, only right-handed isomers exist.

# 3 Chirality and Negative Material Parameters

Isotropic Veselago materials with simultaneously negative permittivity and permeability cause waves to behave in interesting ways. However, if structural handedness is added to such materials, the parameters that account for the chirality also affect the wave propagation problem. Chirality brings in magnetoelectric coupling and birefringence. But it also leads to the imperative that the phenomenon of negative refraction needs to be generalized.

## *3.1 Bi-isotropy and eigenwaves*

As is well known [10], net chirality in the continuum matter brings forth magnetoelectric coupling. In other words, electric field excitation causes magnetic polarization in the medium and vice versa. Hence the material response relations have to be rewritten from their dielectric–magnetic form.

### 3.1.1 Bi-isotropic constitutive relations

On the level on constitutive relations, the magnetoelectric cross-coupling means that in addition to the permittivity $\varepsilon$ and permeability $\mu$, a parameter measuring the strength of chirality $\kappa$ has to appear:

$$\mathbf{D} = \varepsilon\mathbf{E} + (\chi - \mathrm{j}\kappa)\mathbf{H}, \quad \mathbf{B} = (\chi + \mathrm{j}\kappa)\mathbf{E} + \mu\mathbf{H} \tag{2}$$

with the electric (**E**) and magnetic (**H**) field strengths, and electric (**D**) and magnetic (**B**) flux densities.

In isotropic media, the material parameters are equivalent to scalars. Here now, to emphasize the magnetoelectric coupling, the relations are termed *bi-isotropic*, and due to the fact that there are two exciting fields and two response flux densities, in the most general case four material parameters are needed.

The missing fourth parameter is already included in Eq. (2): it is the so-called Tellegen parameter $\chi$, which is a measure of non-reciprocal magnetoelectric coupling. This mechanism is another type of coupling that can be achieved by artificial (or natural) coupling of permanent electric and magnetic moments [13, 14]. Note the appearance of the imaginary unit j in the relations (2). It shows the 90° phase shift of the response due to chirality effect (charge separation in a spiral creates a circulating current which is proportional to the time derivative of charge density), as compared to the in-phase response of the non-reciprocal magneto-electric (Tellegen) effect.

Media with nonzero non-reciprocity parameter $\chi$ are sometimes called Tellegen media, whereas in case of chiral materials (nonzero $\kappa$) one often speaks about Pasteur media.

### 3.1.2 Effect of magnetoelectric coupling on wave propagation

Unlike to the ordinary isotropic materials and double-negative Veselago media, bi-isotropic materials are birefringent: the two eigenwaves propagating in bi-isotropic media have different propagation factors:

$$k_{\pm} = \omega \left( \sqrt{\mu\varepsilon - \chi^2} \pm \kappa \right) \tag{3}$$

Both magnetoelectric parameters $\chi$ and $\kappa$ affect the phase of the wave.[6]

The effect of the chirality parameter is to split the refractive index. This leads to a need to take a closer look at the backward-wave properties of media with negative permittivity and permeability. Figure 4 shows on the left panel the division of isotropic media into four classes depending on whether $\varepsilon$ and/or $\mu$ are positive or negative [16], and a propagating wave requires the parameters be of the same sign. Double-negative media support backward waves.

However, when the chirality parameter is allowed to be nonzero, the situation is characterized by the right panel in Fig. 4 (there, for simplicity, the Tellegen parameter $\chi$ is assumed to be zero). The permittivity and permeability are assumed to be of the same sign, and the square root of their product is assumed to have the same sign as $\varepsilon$ and $\mu$. Depending on the magnitude of the chirality parameter, both eigenwaves can be forward (the wave vector amplitudes both positive), both backward (both wave vector amplitude negative), or one of the waves forward, one backward. A corollary is that in order to create negative-index materials (backward-wave media), it is not a necessary condition to have double-negative material. It suffices that the chirality parameter exceeds the magnitude of square root of $\mu\varepsilon$.

---

[6] It turns out that the losslessness condition [15] leads to the requirement that all the four material parameters in Eq. (2) be real-valued. (Of course, when dispersion is taken into consideration, losses and the imaginary parts for these parameters need be accounted for, and we need to deal with four complex medium parameters.) It is therefore wrong to interpret in the constitutive relations (2) the magnetoelectric coefficients $\chi + j\kappa$ and $\chi - j\kappa$ as complex conjugates of each other in the sense that $\kappa$ would be the imaginary part of the whole coefficient. (The complex conjugate of $\chi + j\kappa$ is $\chi^* - j\kappa^*$.)

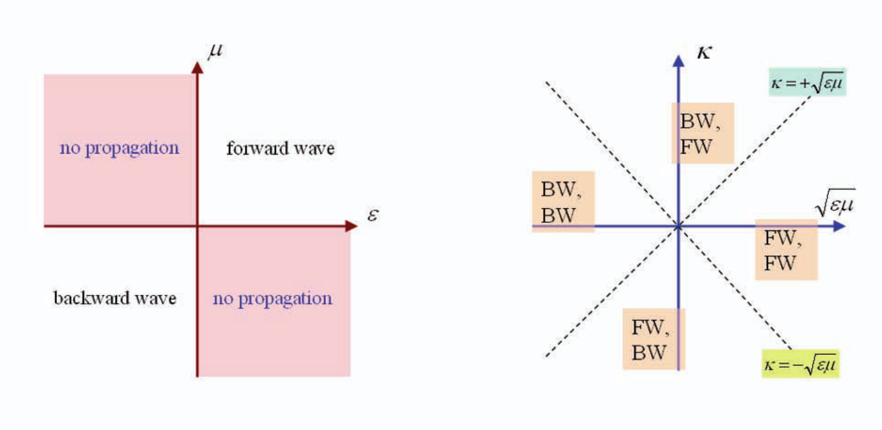


**Fig. 4** The effect of chirality on the backward-wave characteristics of bi-isotropic media. *Left side*: in isotropic media, waves propagate only if the permittivity and permeability are of the same sign, and positive parameters lead to forward waves, negative to backward ones. *Right side*: when ε and μ have the same sign, a sufficiently large chirality parameter κ creates a situation where one of the eigenwaves is backward, while the other is forward. (The sign of the square root of εμ is assumed the same as that of ε and μ in this figure).

Hence sufficiently small (absolute) values of ε and μ lead to interesting possibilities in connection with chiral properties. The extreme case in this respect is the so-called *chiral nihility* [17] where $\mu\varepsilon = 0$ but the medium still possesses a nonzero chirality parameter. The nonzero value of κ splits the eigenwaves such that they have equal but opposite wave numbers.

Also even without the chirality effect, in the plain isotropic domain, the regime of very small values for the permittivity and permeability are of interest in metamaterials research. Such media, also called as zero-index media (ZIM),[7] would be extremely useful in very-high frequency applications of novel materials, such as for example optical circuits. To transfer the machinery electronics into optical wavelengths and to make use of the theories and powerful results of circuit theory in the nanoworld would create a new paradigm, *metactronics*, as has been visioned by Nader Engheta [19].

[7] It is worth noting that although media with "very small" permittivity *and* permeability lead to a material with very small index of refraction and eventually ZIM, the reverse is not necessarily true. Even using non-magnetic materials (for which the permeability is the same as that in free space), one can approximate ZIM if only the permittivity is sufficiently small. Such media have been called epsilon-near-zero materials (ENZ). Such materials are being studied due to their potential applications, for example, in directive emission [18] and squeezing light in optical nanocircuits.

### 3.1.3 Non-reciprocity and wave propagation

The effect of the Tellegen parameter $\chi$ on the forward–backward characteristics is different from that of the chirality parameter $\kappa$. When the magnitude of $\chi$ exceeds that of the square root of $\varepsilon\mu$, the waves change character: they attain an imaginary part and become attenuating. (However, in such case there may still be phase variation: the real part of the wave vector is given by $\kappa$, as Eq. (3) shows). Nevertheless, also in the case when the Tellegen parameter of the medium is nonzero, backward waves are possible.

The interrelation of the domains of backward-wave media and the four subclasses of bi-isotropic materials is illustrated in Fig. 5.

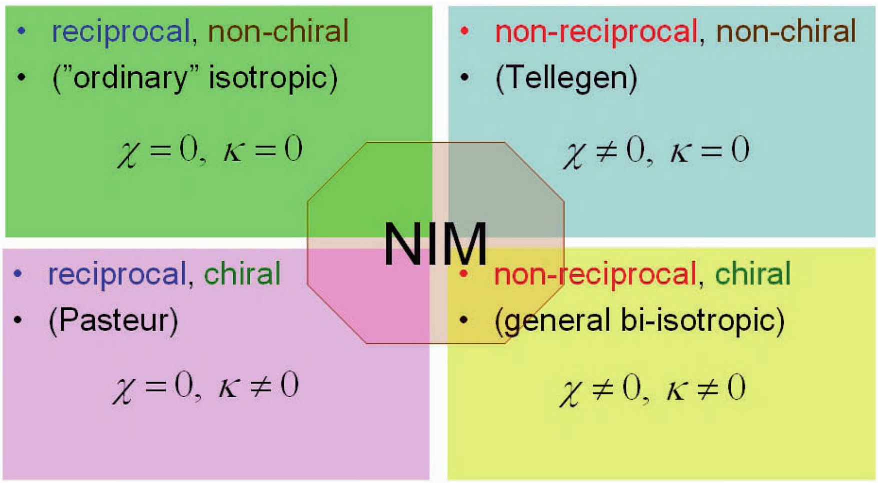


**Fig. 5** Negative-index media (NIM, here referring to media in which a plane eigenwave is allowed to display backward propagation, in other words negative phase velocity) are allowed in all subfields of bi-isotropic materials: chiral (handed) and non-chiral, reciprocal and non-reciprocal.

## *3.2 Optical activity and polarization rotation*

Pasteur's discovery (connection of microstructural chirality with macroscopically observable polarization rotation) was qualitative. To present a formula for calculating the angle of rotation as function of the chiral activity requires solution of Maxwell's equations with the constitutive relations (2). In light of the theme of the present article, handedness, it is especially interesting to find out which is the sense of helicity (right- or left-handed) for a given chirality parameter (positive or negative).

The eigenwaves in homogeneous chiral media are the two circularly polarized (right- and left-handed) waves [10]. Let us assume that the waves are propagating into the direction of the positive $z$ axis. Then their dependence upon the propagation distance is $\exp(-jk_{\pm}z)$, with $k_{\pm}$ being the propagation constant of the right-handed (+) and left-handed (−) eigenwave.

The electric field vectors rotate in the $xy$ plane (unit vectors $\mathbf{u}_x$ and $\mathbf{u}_y$), and as complex vectors they can be written as

$$\begin{cases} \mathrm{RCP}: & \mathbf{u}_\mathrm{x} - \mathrm{j}\mathbf{u}_\mathrm{y}; \quad \exp(-\mathrm{j}k_+ z), \quad k_+ = \omega(\sqrt{\mu\varepsilon} + \kappa) \\ \mathrm{LCP}: & \mathbf{u}_\mathrm{x} + \mathrm{j}\mathbf{u}_\mathrm{y}; \quad \exp(-\mathrm{j}k_- z), \quad k_- = \omega(\sqrt{\mu\varepsilon} - \kappa) \end{cases} \tag{4}$$

If the wave is linearly $x$ polarized at $z = 0$, it is the sum of RCP and LCP, both of equal amplitudes. For positive $\kappa$, the wave number of RCP is larger than that of LCP. Hence its phase changes faster. The result is that at a distance into positive $z$, the vector direction of the electric field is

$$\begin{aligned} &(\mathbf{u}_\mathrm{x} - \mathrm{j}\mathbf{u}_\mathrm{y})\exp(-\mathrm{j}k_+ z) + (\mathbf{u}_\mathrm{x} - \mathrm{j}\mathbf{u}_\mathrm{y})\exp(-\mathrm{j}k_- z) \\ &= 2\left[\mathbf{u}_\mathrm{x}\cos(\omega\kappa z) - \mathbf{u}_\mathrm{y}\sin(\omega\kappa z)\right]\exp(-\mathrm{j}\omega\sqrt{\mu\varepsilon}\, z) \end{aligned} \tag{5}$$

from which it can be seen that at position $z = 0$, the field vector is $x$-polarized as assumed.

In particular, Eq. (5) shows that at any fixed position $z$, the electric field is linearly polarized (the vector multiplying the phase exponential is real). The plane of polarization of the wave in the transversal $xy$-plane, however, depends on the position $z$. As the field penetrates into the chiral medium and $z$ increases, the field polarization starts to attain a negative $y$ component. This means that the polarization rotation is counterclockwise (for positive $\kappa$) when one is looking along the propagation direction.

This analysis can be illustrated by the situation in Fig. 6. There the sign of $\kappa$ is assumed positive in the chiral material, and the plane of polarization of the propagating wave rotates counterclockwise.[8]

[8] One has to bear in mind that over a larger spectral range, the chirality parameter is dispersive: its magnitude varies as function of frequency. For resonating particles, the rotatory dispersion can be so strong that it even changes sign [20]. This leads to a paradoxical situation: a sample of material which is, say, dextral (i.e., it has right-handed microstructure), can have the power of rotating the wave polarization in either right- or left-handed sense, depending on the frequency of the radiation.

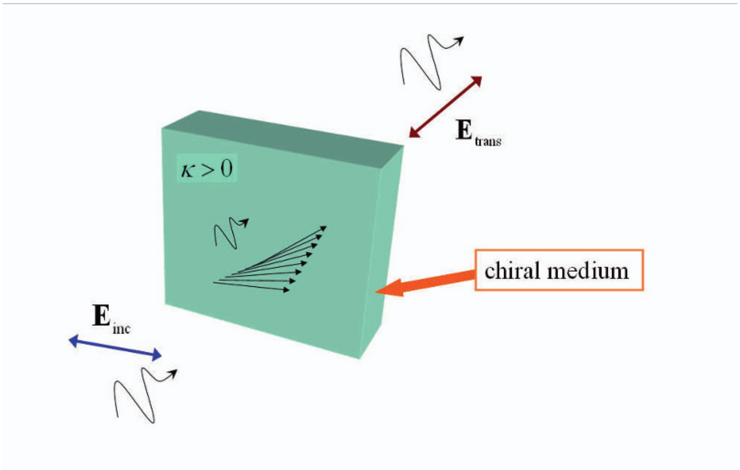


**Fig. 6** The rotation of the polarization plane of a linearly polarized wave as it enters a chiral medium and propagates through it. Here the chirality parameter κ is assumed to be *positive* (for negative κ, the rotation would run in the opposite sense). The important conclusion of the figure is that the rotation is *counterclockwise* as one looks into the propagation direction. (Of course there also is a reflection, caused by the possible impedance mismatch at the boundary; it is omitted here because the chirality parameter does not affect the reflection coefficient for normal incidence.) Note that here the constitutive relations defined in (2) are used (the non-reciprocity parameter χ does not affect the rotation). Also, the time-harmonic convention is exp(jωt); evidently the convention exp(−iωt) would chance the sense of rotation.[9]

There are two "wavelengths" that can be distinguished in wave propagation in chiral medium, evident from the field dependence in Eq. (5). As Fig. 6 shows, the polarization rotates, and after a certain distance $\lambda_{pol}$, the field polarization aligns with its original direction. This could be termed the "polarization wavelength." According to Eq. (5) this happens when $\omega\kappa\lambda_{pol} = 2\pi$.

The other wavelength is the ordinary wavelength $\lambda_{ph}$ separating spatial places where the phase of the wave has increased by 2π. Equation (5) gives the condition for this: $\omega(\mu\varepsilon)^{1/2}\,\lambda_{ph} = 2\pi$.

The ratio between these two wavelengths is

[9] A comparison of the field rotations of Figs. 6 and 2 needs a word of caution because a fixed-in-time image may lead to wrong associations. Here (Fig. 6) the fields shown are linearly polarized; hence, in time they always keep the same vector direction shown in the picture but oscillate sinusoidally. The situation of the circularly polarized wave of Fig. 2 the situation is different: there the picture shows a snapshot (at a certain time instant) of the field vector direction simultaneously at different places. With time, the helical spiral representing the field moves forward so that at any fixed point in space, the field vector draws a clockwise circle like RCP.

$$\frac{\lambda_{\text{ph}}}{\lambda_{\text{pol}}} = \frac{\kappa}{\sqrt{\mu\varepsilon}} \tag{6}$$

which relation reveals an interesting connection to the backward-wave characteristics in chiral media. As shown in Fig. 4, if the chirality parameter $\kappa$ exceeds the value of the square root of the product $\varepsilon\mu$, one of the eigenwaves is backward. According to Eq. (6), this very same limiting condition corresponds to the case of the two wavelengths (polarization, $\lambda_{\text{pol}}$, and phase, $\lambda_{\text{ph}}$) being equal.

### *3.3 Rotation of reflection from Tellegen medium*

The other magnetoelectric effect, the non-reciprocal Tellegen coupling, has a complementary effect on wave propagation. Instead of affecting, in a rotatory manner, the plane of the transmitted wave, it has an effect on the reflection. As is known, reflection coefficient is determined by the wave impedance. A Tellegen medium is bi-impedant whereas the chiral medium is bi-refringent.

For an ordinary isotropic dielectric–magnetic medium, there are two Fresnel reflection coefficients, one for the parallel and one for the perpendicular polarization. Since a magnetoelectric medium is more complex than an isotropic medium, the eigenpolarizations are no longer these simple linear solutions. The reflection problem needs to be described by a reflection matrix.

Let us study the reflection problem from a half space of Tellegen material with material parameters $\varepsilon$, $\mu$, and non-reciprocity parameter $\chi$. For simplicity, let the incident wave fall from free space (wave impedance $\eta_0$) with normal incidence on the planar boundary, according to Fig. 7. Then [10] the co-polarized and cross-polarized reflection coefficients can be written as functions of the parameters of the Tellegen half space:

$$R_{\text{co}} = \frac{\eta^2 - \eta_0^2}{\eta^2 + \eta_0^2 + 2\eta\eta_0\cos\theta}, \quad R_{\text{cross}} = \frac{-2\eta\eta_0\sin\theta}{\eta^2 + \eta_0^2 + 2\eta\eta_0\cos\theta}$$
$$\text{with} \quad \sin\theta = \frac{\chi}{\sqrt{\mu\varepsilon}}, \quad \cos\theta = \sqrt{1 - \frac{\chi^2}{\mu\varepsilon}}, \quad \eta = \sqrt{\frac{\mu}{\varepsilon}} \tag{7}$$

Here the Tellegen character of the medium is measured by a slightly more convenient parameter $\theta$ which has a straightforward connection with $\chi$. The special case of reflection problem from an isotropic, reciprocal half space (for which the Tellegen parameter $\chi$ vanishes: $\sin\theta = 0$, $\cos\theta = 1$) is easily seen to follow from Eq. (7): no cross-polarized reflection, and the co-polarized reflection coefficient becomes the well known relation $(\eta - \eta_0)/(\eta + \eta_0)$.

Very interesting in the result (7) is the direction of the cross-polarization. When a linearly polarized wave is reflected from Tellegen medium, the reflected field is also linearly polarized but it is pointing to a different direction. The rotation angle is affected by both the impedance contrast of the medium and vacuum, and particularly the Tellegen parameter. For a "high-impedance" surface ($\eta > \eta_0$), the reflected wave is rotated counterclockwise for positive values of $\chi$, and clockwise for negative values.[10] Due to the fact that the co-polarized reflection coefficient keeps the sign of $\eta - \eta_0$, the rotation is inverted for "low-impedance" surfaces ($\eta < \eta_0$). In that case there is also a 180° phase shift in the co-polarized reflection but nevertheless the polarization plane of the reflected field is rotated clockwise (for positive $\chi$).

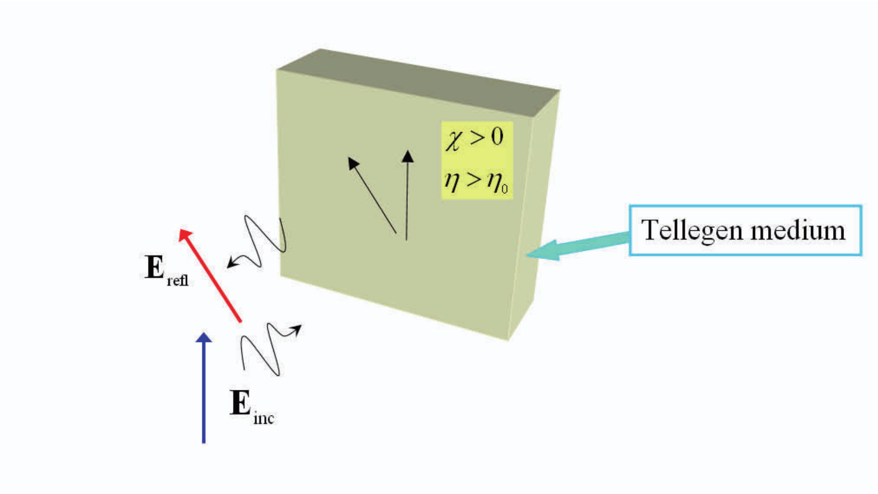


**Fig. 7** The rotation of the polarization plane of the reflected field when a linearly polarized wave hits a planar boundary between free space and Tellegen medium. The Tellegen parameter $\chi$ is assumed positive and its impedance $\eta$ is assumed higher than that of free space. In this case the reflection is counterclockwise as shown. Changing either of the conditions causes the rotation be clockwise. (In the general case, there also exists a transmitted wave that penetrates the Tellegen medium; it is, however, omitted here because the most interesting effect of $\chi$ is on reflection).

[10] From the rotatory power in reflection it can be inferred that Tellegen medium is non-reciprocal: one cannot change the incident and reflected fields in Fig. 7 because a field approaching the surface with the orientation of the reflected field would suffer a further rotation into the *same* direction as the rotation in the figure, and the rotation would not be unwound.

### *3.4 Generalization to bi-anisotropy*

When the assumption of isotropy (or bi-isotropy) is relaxed, very many more dimensions are needed to characterize media. Anisotropy means that the direction of the field force of excitation affects the amplitude of the response and such a situation may appear when the microstructure of the medium does not possess a spherical or cubic symmetry, it is, for instance, composed of oriented needle-like elements. For anisotropic media, in the constitutive relations, permittivity and permeability have to be described by dyadics or second-rank tensors, instead of scalars like in Eq. (2). In three-dimensional space, a dyadic can be expanded as a 3 × 3 matrix, and hence the most general anisotropic permittivity has 9 degrees of freedom, likewise the anisotropic permeability.

When anisotropy and magnetoelectric coupling are both allowed, all four parameters ε, μ, χ, and κ become dyadics (in the following denoted by a bar under the symbol), and one can say that to span the full material space requires 36 dimensions [21], cf. Fig. 8.

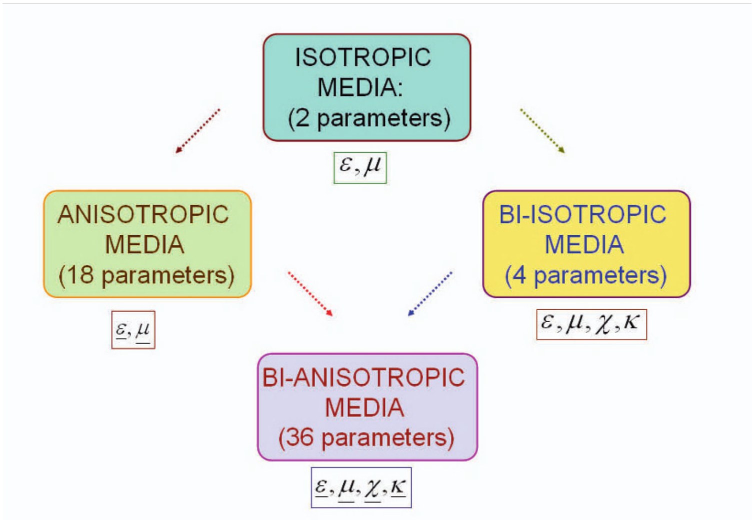


**Fig. 8** Bi-anisotropic media are very general linear media, and the four material dyadics comprise together 36 parameters responsible for the magnetoelectric behavior. Anisotropic, bi-isotropic, and isotropic media can be considered as subclasses of bi-anisotropic materials with 18, 4, and 2 degrees of freedom, respectively.

On the level of equations, the constitutive relations can be collected into a six-vector presentation where electric and magnetic vector quantities (field strengths **E** and **H** on one hand, and the flux densities **D** and **B** on the other) are joined together in the following manner:

$$\begin{pmatrix} \mathbf{D} \\ \mathbf{B} \end{pmatrix} = \begin{pmatrix} \underline{\varepsilon} & \underline{\chi}^{\mathrm{T}} - \mathrm{j}\underline{\kappa}^{\mathrm{T}} \\ \underline{\chi} + \mathrm{j}\underline{\kappa} & \underline{\mu} \end{pmatrix} \cdot \begin{pmatrix} \mathbf{E} \\ \mathbf{H} \end{pmatrix} = C \cdot \begin{pmatrix} \mathbf{E} \\ \mathbf{H} \end{pmatrix} \tag{8}$$

and here the four dyadics are generalizations of the scalar bi-isotropic material parameters. The equation also defines the material matrix C. Note the transpose operation of the magnetoelectric dyadics in the upper right position of the material matrix. It is with this definition that the reciprocal ($\kappa$) and non-reciprocal ($\chi$) parts of the magnetoelectric effects are kept separate.

How, then, does the discussion in the previous subsection concerning the backward-wave characteristics of media apply to the bi-anisotropic environment? An effective tool for answering this question turns out [22] to be the material matrix C in Eq. (4). For lossless media, the matrix C is Hermitian (it is equal to its conjugate transpose) [15]. For ordinary double-positive isotropic medium, the eigenvalues of the C matrix are all positive, for double-negative media they are all negative. Indeed, for general bi-anisotropic materials, the character of definiteness of matrix C determines the forward–backward character of its eigenwaves. If C is positive definite (all of its six eigenvalues are positive; note that the eigenvalues of a Hermitian matrix are real), all waves that propagate in it are forward waves. In the case of negative definite matrix C, the waves are all backward. However, if the matrix is non-definite, there are several possibilities: some of the waves may be forward, some backward, or it may even happen that some or all waves are evanescent, they do not propagate.

# 4 Conclusion

Within a multidisciplinary research field such as metamaterials, the terminology and labeling of phenomena and quantities under discussion need be carefully analyzed. Many aspects on parity, symmetry, and handedness were discussed in the present article. The division of semantics of handedness – with respect to electromagnetics – into three categories (negative-index and plasmonic media as left-handed materials, polarization of circularly/elliptically polarized wave, and geometrical parity-breaking structure of matter) helps in understanding and categorizing complex effects involving metamaterials. Especially the question of treatment between left and right (whether on equal basis or as the left-handed phenomenon as anomaly) was shown to be essential. In a general frame of electromagnetics of bi-anisotropic media, the three aspects of handedness can be clearly seen to occupy distinct places in the characterization of macroscopic effects of metamaterials.

**Acknowledgments** The Academy of Finland has supported this research.

## References


1. Lapine, M.: The age of metamaterials (Editorial). Metamaterials **1**, 1 (2007) doi: 10.1016/j.metamat.2007.02.006
2. Boltasseva, A., Shalaev, V.M.: Fabrication of optical negative-index metamaterials: Recent advances and outlook. Metamaterials **2**, 1–17 (2008) doi: 10.1016/j.metamat.2008.03.004
3. Sihvola, A.: Electromagnetic emergence in metamaterials. Deconstruction of terminology of complex media. In: Zouhdi, S., Sihvola, A., Arsalane, M. (eds.) Advances in Electromagnetics of Complex Media and Metamaterials, pp. 1–17. NATO Science Series: II: Mathematics, Physics, and Chemistry, **89**, Kluwer, Dordrecht (2003)
4. Sihvola, A., Lindell, I.: On the three different denotations of handedness in wave-material interaction. Proceedings of the International Symposium on Electromagnetic Theory (URSI), pp. 84–86, May 23–27, 2004, Pisa, Italy
5. Sihvola, A.: Metamaterials in electromagnetics. Metamaterials **1**, 2–17 (2007) doi: 10.1016/j.metamat.2007.02.003
6. Veselago, V.G.: The electrodynamics of substances with simultaneously negative values of $\varepsilon$ and $\mu$. Soviet Physics Uspekhi **10**(4), 509–514 (1968). (Translation form the original Russian article, Uspekhi Fizicheskii Nauk **92**, 517–526 (1967))
7. Bohren, C.F., Huffman, D.R.: Absorption and Scattering of Light by Small Particles. Wiley, New York (1983)
8. Federal Standard 1037C, Telecommunications. Glossary of Telecommunication Terms, August 7, 1996
9. http://www.tkk.fi/Yksikot/Sahkomagnetiikka/kurssit/animaatiot/ymppolar.html
10. Lindell, I.V., Sihvola, A.H., Tretyakov, S.A., Viitanen, A.J.: Electromagnetic Waves in Chiral and Bi-isotropic Media, Artech House, Norwood, MA (1994)
11. Lee, T.D., Yang, C.N.: Question of parity conservation in weak interactions. Physical Review **104**(1), 254–258 (1956)
12. Hegstrom, R.A., Kondepundi, D.K.: The handedness of the universe. Scientific American **262**, 108–115 (January 1990)
13. Tretyakov, S.A., Maslovski, S.I., Nefedov, I.S., Viitanen, A.J., Belov, P.A., Sanmartin, A.: Artificial Tellegen particle. Electromagnetics **23**(8), 665–680 (2003)
14. Ghosh, A., Sheridon, N.K., Fischer, P.: Janus particles with coupled electric and magnetic moments make a disordered magneto-electric medium. arXiv.org > cond-mat > arXiv: 0708.1126v1
15. Lindell, I.V.: Methods for Electromagnetic Field Analysis. Oxford University Press/IEEE Press, Oxford (1992, 1995)
16. Engheta, N., Ziolkowski, R.W.: Metamaterials. Physics and Engineering Explorations. IEEE Press/Wiley, New York (2006)
17. Tretyakov, S., Nefedov, I., Sihvola, A., Maslovski, S., Simovski, C.: Waves and energy in chiral nihility. Journal of Electromagnetic Waves and Applications **17**(5), 695–706 (2003)
18. Enoch, S., Tayeb, G., Sabouroux, P., Guérin, N., Vincent, P.: A metamaterial for directive emission. Physical Review Letters **89**, 213902 (2002)
19. Engheta, N.: Metactronics: Optical circuits and information processing in nanoworlds. Proc. META’08, NATO Advanced Research Workshop, 7–10 May 2008, p. 533, Marrakech, Morocco
20. Klyne, W.: Carboxyl and aromatic chromophores: optical rotatory dispersion and circular dichroism studies. Proceedings of the Royal Society (London), Series A, **297**, 66–78 (1967)
21. Serdyukov, A., Semchenko, I., Tretyakov, S., Sihvola, A.: Electromagnetics of Bi-anisotropic Materials: Theory and Applications. Gordon and Breach, Amsterdam (2001)
22. Lindell, I.V., Sihvola, A.H.: Negative-definite media, a class of bi-anisotropic metamaterials. Microwave and Optical Technology Letters **48**(3), 602–606 (2006)

# Bounds on Metamaterials – Theoretical and Experimental Results

**Gerhard Kristensson, Christer Larsson, Christian Sohl, and Mats Gustafsson**

Department of Electrical and Information Technology, Lund University, P.O. Box 118, SE-221 00 Lund, Sweden
{Gerhard.Kristensson,Christer.Larsson,Christian.Sohl,Mats.Gustafsson}@eit.lth.se

**Abstract** A dispersion relation for the combined effect of scattering and absorption of electromagnetic waves is employed. By invoking the optical theorem, the result states that the extinction cross section integrated over all frequencies is related to the static polarizability dyadics. In particular, it is established that the integrated extinction is the same for all materials having identical static properties, irrespectively whether the permittivity or the permeability have negative real parts at non-zero frequencies or not. The theory is illustrated numerically, and, moreover, it is verified experimentally on a sample consisting of a single-layer planar array of capacitive resonators claimed to form a negative permittivity metamaterial. It is concluded that the theory is in good agreement with measurements in the microwave region.

## 1 Background

In a series of papers [15–17], the holomorphic properties of the forward scattering amplitude have been exploited and experimentally verified. As a result, a sum rule for the extinction cross section is established. This outcome hinges on the physical principles of causality and energy conservation – both well established and tested – and relates the (weighted) integrated extinction to the static material properties of the obstacle. A rather intriguing consequence of this sum rule is that the static properties – quantified by the polarizability dyadics – measure the broadband scattering and absorption strengths of the obstacle. Fortunately, a large literature exists on how to compute the polarizability dyadics, and for several canonical geometries analytic expressions exist, see e.g., [3, 18, 19]. The sum rule has also been exploited in antenna applications to give new bounds on the product of gain and bandwidth of antennas of arbitrary shape [2, 14].

S. Zouhdi et al. (eds.), *Metamaterials and Plasmonics: Fundamentals, Modelling, Applications*,

The direct measurement of the forward radar cross section (RCS) in free space is experimentally difficult since the largest part of the detected field at the receiving antenna consists of a direct illumination by the transmitting antenna. The direct illumination contributes with a dominating background that has to be removed from the detected field, either using coherent background subtraction or other signal processing methods. Monostatic RCS measurements are therefore to be preferred, compared to forward RCS measurements, if they can be used for the purpose at hand. This paper describes a method to determine the extinction cross section for a thin and non-magnetic planar object over a large bandwidth in the microwave region. The method is based on a conventional measurement of the monostatic RCS and the fact that the RCS amplitude in the forward and backward directions are equal if the illuminated object is planar and non-magnetic [12, 17]. The monostatic method is compared to and validated with a more general measurement technique based on the RCS in the forward direction.

## 2 A Sum Rule for the Extinction Cross Section

This section sets the notation of the problem and states the main theoretical results used in this paper, but no proofs are given. For proofs we refer to the pertinent published papers [15, 16].

Consider the scattering problem of a plane electromagnetic wave $\mathbf{E}\exp\{\mathrm{i}k\hat{\mathbf{k}}\cdot\mathbf{x}\}$ (time dependence $\exp\{-\mathrm{i}\omega t\}$) impinging in the $\hat{\mathbf{k}}$-direction on a target embedded in free space. The wave number in free space is denoted by $k=\omega/\mathrm{c}_0$. The target can be a single scatterer or it may consist of several non-connected parts. The material of the scatterer is modeled by a set of linear and passive constitutive relations which are assumed to be invariant under time translations (i.e., stationary constitutive relations). The scattering dyadic $\mathbf{S}$ is independent of $\mathbf{E}$, and it is defined in terms of the scattered electric field $\mathbf{E}_\mathrm{s}$ as [1, 7]

$$\mathbf{S}(k;\hat{\mathbf{k}}\curvearrowright\hat{\mathbf{x}})\cdot\mathbf{E}=\lim_{x\to\infty} x\mathrm{e}^{-\mathrm{i}kx}\mathbf{E}_\mathrm{s}(k;\mathbf{x})$$

where $x=|\mathbf{x}|$ denotes the magnitude of the position vector, and $\hat{\mathbf{x}}=\mathbf{x}/x$. A target's overall scattering properties are commonly quantified by the scattering cross section $\sigma_\mathrm{s}$, defined as the total power scattered in all directions divided by the incident power flux. The extinction cross section $\sigma_\mathrm{ext}=\sigma_\mathrm{s}+\sigma_\mathrm{a}$ is defined as the sum of the scattering and absorption cross sections, where the latter is a measure of the absorbed power in the target [1]. The extinction cross section is also determined from the knowledge of the scattering dyadic in the forward direction, $\hat{\mathbf{x}}=\hat{\mathbf{k}}$, *viz.*,

$$\sigma_\mathrm{ext}(k;\hat{\mathbf{k}},\hat{\mathbf{e}})=\frac{4\pi}{k}\operatorname{Im}\left\{\hat{\mathbf{e}}^*\cdot\mathbf{S}(k;\hat{\mathbf{k}}\curvearrowright\hat{\mathbf{k}})\cdot\hat{\mathbf{e}}\right\} \tag{1}$$

An asterisk denotes the complex conjugate, and the electric polarization $\hat{\mathbf{e}} = \mathbf{E}/|\mathbf{E}|$. Relation (1) is known as the optical theorem or forward scattering theorem [1, 7].

A dispersion relation for the combined effect of scattering and absorption of electromagnetic waves is derived in [15] from the holomorphic properties of the forward scattering dyadic. One of the underlying assumptions of the result is that the forward scattering is causal, i.e., the scattered field must not precede the incident field in the forward direction. The result is a sum rule for the extinction cross section valid for a large class of linear and passive targets:[1]

$$\int_0^\infty \frac{\sigma_{\mathrm{ext}}(k;\hat{\mathbf{k}},\hat{\mathbf{e}})}{k^2}\,\mathrm{d}k = \frac{\pi}{2}\left(\hat{\mathbf{e}}^*\cdot\gamma_{\mathrm{e}}\cdot\hat{\mathbf{e}} + (\hat{\mathbf{k}}\times\hat{\mathbf{e}}^*)\cdot\gamma_{\mathrm{m}}\cdot(\hat{\mathbf{k}}\times\hat{\mathbf{e}})\right) \tag{2}$$

where $\gamma_{\mathrm{e}}$ and $\gamma_{\mathrm{m}}$ denote the electric and magnetic polarizability dyadics, respectively [3, 18]. This identity holds for all scatterers satisfying the assumption above, and it constitutes the main theoretical result used in this paper. This rather intriguing result has far-reaching consequences on how much an obstacle scatters and absorbs, and it also quantifies the interaction between parts with different materials.

The electric (or magnetic) polarizability dyadic is accessible as an analytic expression for a limited set of canonical bodies, e.g., a homogenous, isotropic dielectric sphere of radius $a$ with static permittivity $\varepsilon(0)$ has the polarizability dyadic $\gamma_{\mathrm{e}}$ [3, 18]

$$\gamma_{\mathrm{e}} = 3\frac{\varepsilon(0)-1}{\varepsilon(0)+2}\frac{4\pi a^3}{3}\mathbf{I}$$

where $\mathbf{I}$ denotes the unit dyadic. Fortunately, for other more complex geometries, the polarizability dyadic is easy to compute using e.g., a finite element (FEM) solver.

The integrand on the left-hand side of (2) is non-negative. Therefore, for any finite frequency interval $K = k_0[1-B/2, 1+B/2]$ with center frequency $k_0$ and relative bandwidth $B$, the identity implies for some $\kappa \in K$

$$\frac{B\sigma(\kappa)}{k_0(1-B^2/4)} = \int_K \frac{\sigma(k)}{k^2}\,\mathrm{d}k \leq \frac{\pi}{2}\left(\hat{\mathbf{e}}^*\cdot\gamma_{\mathrm{e}}\cdot\hat{\mathbf{e}} + (\hat{\mathbf{k}}\times\hat{\mathbf{e}}^*)\cdot\gamma_{\mathrm{m}}\cdot(\hat{\mathbf{k}}\times\hat{\mathbf{e}})\right) \tag{3}$$

where $\sigma$ denotes any of the cross sections $\sigma_{\mathrm{ext}}, \sigma_{\mathrm{s}}$, and $\sigma_{\mathrm{a}}$. For all scatterers with the same static polarizability dyadics, this inequality shows that large scattering in a frequency interval is traded for smaller bandwidth, since the left-hand side of the inequality is bounded from above by the right-hand side.

The extinction cross section $\sigma_{\mathrm{ext}}$ measures the total interaction of the incident plane wave with the obstacle, and the integral on the left-hand side of (2) provides a measure of the overall scattering and the absorption properties of the obstacle. As a consequence of (2), large scattering or absorption effects, i.e., a large left-hand side of (2), call for large electric and/or magnetic polarizability dyadics. In

[1] A similar, but less developed, sum rule has been reported in the literature, see e.g., [9, p. 423]. The first employment of the sum rule in electromagnetics seems to go back to Purcell, who presented the sum rule for dielectric spheroidal scatterers [11].

other applications, like cloaking, the extinction effects must be small (at least in a finite frequency interval) and the electric and magnetic polarizability dyadics have to be as small as possible for a given volume. In both cases, the static properties act as a measure of the dynamic effects. We also immediately conclude that all scatterers having the same right-hand side, i.e., polarizability properties, have the same integrated extinction.

The effects of (2) are exploited in this paper, and in a few numerical examples, see Section 4, we illustrate that two materials with the same static properties have identical integrated extinctions. Several of these examples show metamaterial characteristics, i.e., the material has temporally dispersive material parameters where both the real parts of the permittivity and the permeability are negative in the same frequency interval. In all cases it is the static properties of the obstacle that determine the integrated scattering properties. The experimental verification of the sum rule is presented in Section 5.

## 3 Material Modeling

At a single frequency, when causality has no meaning, the material modeling of the scatterer is less critical. However, dealing with the broadband properties of a scatterer, it becomes important to use physically suitable dispersion models. In particular, the models have to be consistent with the passivity and causality assumptions made above. As a consequence, the material models have to satisfy the Kramers-Kronig relations [1,5]. This is a consequence of the fact that $f(\omega) = \omega\varepsilon(\omega)$ is a Herglotz function [8] in the variable $\omega$. Basically, a Herglotz function is analytic in the upper half complex plane, and it maps the upper complex plane into itself.

In this paper we use the Lorentz model, which models the resonance behavior of many solid materials. The relative permittivity of the Lorentz model is:

$$\varepsilon(\omega) = \varepsilon_\infty - \frac{\omega_\mathrm{p}^2}{\omega^2 - \omega_0^2 + \mathrm{i}\omega\nu} = \varepsilon_\infty - \frac{(\omega_\mathrm{p} a/\mathrm{c}_0)^2}{(ka)^2 - (\omega_0 a/\mathrm{c}_0)^2 + \mathrm{i}ka(\nu a/\mathrm{c}_0)} \tag{4}$$

The positive constant $\varepsilon_\infty$ is the optical response of the permittivity, and the constant $\omega_\mathrm{p}$ is the plasma frequency that models the strength of the dispersion. The resonance frequency of the model is determined by the angular frequency, $\omega_0$, and the collision frequency $\nu > 0$. With appropriate choice of the material parameters, the real part of the permittivity becomes negative. The explicit value of the permittivity in the static limit ($\omega = 0$) is $\varepsilon(0) = \varepsilon_\infty + \omega_\mathrm{p}^2/\omega_0^2$. A similar model is also used for the relative permeability $\mu$. The Lorentz model employed in this paper has the parameters $\varepsilon_\infty = 1$, $\omega_\mathrm{p} a/\mathrm{c}_0 = 3$, $\omega_0 a/\mathrm{c}_0 = 2$, and $\nu a/\mathrm{c}_0 = 0.6$.

The Drude model is a special case of the Lorentz model for which $\omega_0 = 0$, i.e.,

$$\varepsilon(\omega) = \frac{((ka)^2 + (\nu a/\mathrm{c}_0)^2)\varepsilon_\infty - (\omega_\mathrm{p} a/\mathrm{c}_0)^2}{(ka)^2 + (\nu a/\mathrm{c}_0)^2} + \mathrm{i}\frac{(\omega_\mathrm{p} a/\mathrm{c}_0)^2(\nu a/\mathrm{c}_0)}{ka((ka)^2 + (\nu a/\mathrm{c}_0)^2)}$$

This choice implies that the real part of the permittivity is negative over a large frequency interval, i.e., $\omega^2 \leq \omega_p^2/\varepsilon_\infty - \nu^2$. This model is used to describe the dispersive behavior of metamaterials, and at low frequencies it shows strong affinity with the conductivity model $\varepsilon(\omega) = \varepsilon_\infty + i\varsigma/(\varepsilon_0\omega)$. In fact, the conductivity $\varsigma = \varepsilon_0\omega_p^2/\nu$ can be identified from Drude's model.

# 4 Numerical Illustrations – Spheres-Doublets

In this section, we illustrate the theoretical results presented in Section 2 in two numerical examples using the material models described in Section 3. The scattering geometry consists of two spheres, radii $a$ and $b$, respectively, as illustrated in Fig. 1. In all examples, the plane wave impinges along the symmetry axis of the scatterer with an electric polarization $\hat{\mathbf{e}}$ in the $xy$-plane, which can be either a real- or a complex-valued unit vector. All frequencies are measured in the dimensionless parameter $\kappa = ka$, and all cross sections are scaled with $2\pi a^2$. The identity in (2), then reads

$$\int_0^\infty \frac{\sigma_{\text{ext}}(\kappa;\hat{\mathbf{k}},\hat{\mathbf{e}})}{\kappa^2}\,\mathrm{d}\kappa = \frac{\pi}{3}\frac{1}{4\pi a^3/3}\left(\hat{\mathbf{e}}^*\cdot\gamma_\mathrm{e}\cdot\hat{\mathbf{e}} + (\hat{\mathbf{k}}\times\hat{\mathbf{e}}^*)\cdot\gamma_\mathrm{m}\cdot(\hat{\mathbf{k}}\times\hat{\mathbf{e}})\right) \tag{5}$$

The numerical computations in this paper utilize the null-field approach, which is an efficient method to evaluate scattering by non-connected objects [10].

In the first example the extinction cross section of two identical touching Drude spheres (radii $a = b$ and $d = 2a$) is computed for two material settings. In the first setting $\varepsilon = \mu$ at all frequencies, i.e., a material that shows metamaterial characteristics at low frequencies, and in the second setting both spheres are non-magnetic, $\mu = 1$. The result is shown to the left in Fig. 2. Explicit values of the permittivities are given in Section 3.

The contribution to both the electric and the magnetic polarizability dyadics in the case $\varepsilon = \mu$ is [19]

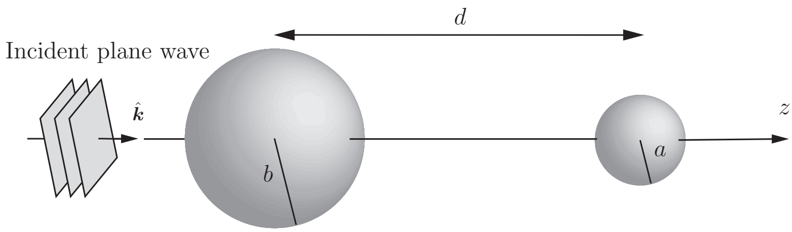


**Fig. 1** The geometry of the two spheres. The sphere with radius $a$ is located at $d\hat{\mathbf{z}}/2$ and the sphere with radius $b$ is located at $-d\hat{\mathbf{z}}/2$. The direction of the incident wave in all examples is $\hat{\mathbf{k}} = \hat{\mathbf{z}}$.

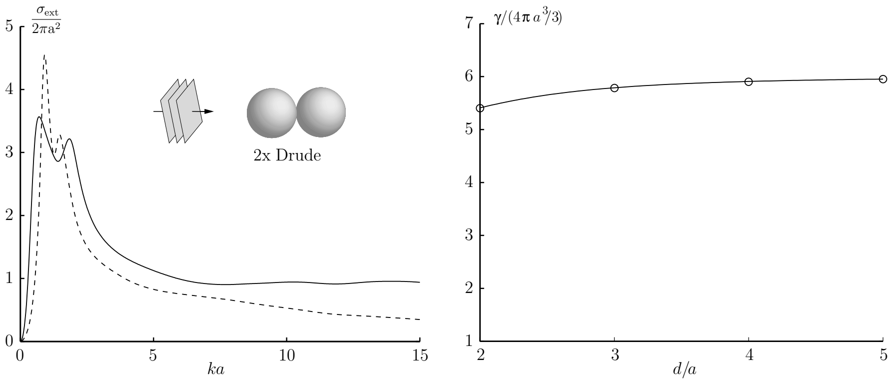


**Fig. 2** (*Left figure*) The extinction cross section of two equal, touching ($d = 2a$) Drude spheres (radii $a = b$) as a function of $ka$. The solid curve shows the extinction cross section for $\varepsilon = \mu$, and the broken curve when both spheres are non-magnetic, $\mu = 1$. All cross sections are normalized with $2\pi a^2$. (*Right figure*) The electric (or magnetic) polarizability, normalized with $4\pi a^3/3$, for the same geometry as a function of the separation distance $d$. The circles illustrate the numerical values.

$$\hat{\mathbf{e}}^* \cdot \gamma_{\rm e} \cdot \hat{\mathbf{e}} = (\hat{\mathbf{k}} \times \hat{\mathbf{e}}^*) \cdot \gamma_{\rm m} \cdot (\hat{\mathbf{k}} \times \hat{\mathbf{e}}) = \frac{9}{2}\zeta(3)\frac{4\pi a^3}{3}$$

where $\zeta(z)$ is the Riemann zeta-function. The non-magnetic spheres have no magnetic contribution, but only an electric contribution. The right-hand side of (5) for the two curves in Fig. 2 therefore assumes the values $3\pi\zeta(3) = 11.33$ and $3\pi\zeta(3)/2 = 5.66$, respectively. These figures are retrieved using numerical integration over the frequency interval in Fig. 2 with three digits (11.3 and 5.66, respectively). It is intriguing to conclude that these numbers are independent of all the material parameters of the Drude spheres, i.e., independent of $\varepsilon_\infty$, $\omega_{\rm p}$, and $\nu$.

A further verification of the integrated extinction in (5) is presented to the right in Fig. 2. This figure shows the analytically computed polarizability, $\gamma$, of two identical Drude spheres [19] as a function of the separating distance $d$. The values obtained by numerical integration according to (5) are shown with circles.

The second example illustrates the computation of the extinction cross sections for two different sets of material parameters with identical static values. Two touching, $d = 3a$, non-magnetic Lorentz spheres, radii $a$ and $b = 2a$, respectively, are used. The result is displayed in Fig. 3. The solid curve shows the extinction cross section when the two spheres have materials as given in Section 3. The broken curve shows the extinction cross section for two Lorentz spheres both having parameters $\varepsilon_\infty = 1$, $\omega_{\rm p} a/{\rm c}_0 = 4.5$, $\omega_0 a/{\rm c}_0 = 3$, and $\nu a/{\rm c}_0 = 0.6$. These two sets of materials have a static permittivity $\varepsilon(0) = 13/4$, and therefore the same right-hand side of (5). The boxes shown in Fig. 3 also have the same integrated extinction, and they indicate the bandwidth of the scattering at the first resonance frequency.

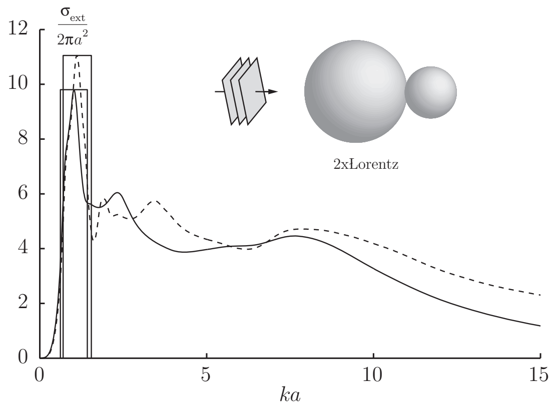


**Fig. 3** The extinction cross section of two touching Lorentz spheres as a function of $ka$. Both spheres have identical material parameters and they are non-magnetic, $\mu = 1$, with radii $a$ and $b = 2a$. The data of the scatterers are given in the text. The boxes have the same integrated extinction as both curves. All cross sections are normalized with $2\pi a^2$.

The polarizability dyadic contributions from the two Lorentz spheres are the same, i.e.,

$$\hat{\mathbf{e}}^* \cdot \gamma_e \cdot \hat{\mathbf{e}} = 11.29 \frac{4\pi a^3}{3}$$

The right-hand side of (5) then becomes 11.82 in both cases. The integrated extinction is computed using numerical integration over the frequency interval in Fig. 3. The results are 11.8 and 11.7, respectively, for the two curves.

## 5 Experimental Verification

The bistatic RCS, $\sigma_{RCS}$, is defined as

$$\sigma_{RCS}(k; \hat{\mathbf{x}}, \hat{\mathbf{e}}_s) = |A(k; \hat{\mathbf{x}}, \hat{\mathbf{e}}_s)|^2 \tag{6}$$

where $A(k; \hat{\mathbf{x}}, \hat{\mathbf{e}}_s) = 2\sqrt{\pi}\hat{\mathbf{e}}_s^* \cdot \mathbf{S}(k; \hat{\mathbf{k}} \curvearrowright \hat{\mathbf{x}}) \cdot \hat{\mathbf{e}}$, and where $\hat{\mathbf{e}}_s$ denotes the polarization of the scattered field in the $\hat{\mathbf{x}}$ direction. Evaluated in the backward direction, $\hat{\mathbf{x}} = -\hat{\mathbf{k}}$, produces the familiar expression for the monostatic RCS [4, 12]. Using this notation, the sum rule for the extinction cross section in (2) then reads

$$\frac{1}{\pi^{3/2}} \int_0^\infty \frac{\sigma_{ext}(k; \hat{\mathbf{k}}, \hat{\mathbf{e}})}{k^2} \, dk = \lim_{k \to 0} \frac{A(k; \hat{\mathbf{k}}, \hat{\mathbf{e}})}{k^2} \tag{7}$$

From the integral representations of the scattered field or the discussion in [12], it follows that for a planar and infinitely thin scatterer subject to a wave impinging

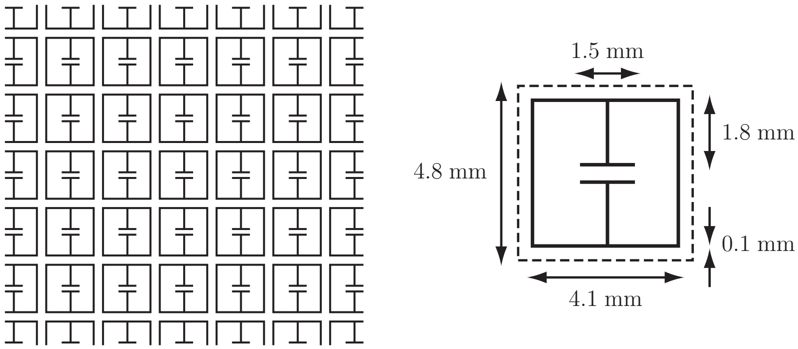


**Fig. 4** A section of the array of capacitive resonators (*left figure*) and one unit cell of the array (*right figure*).

at normal incidence, the RCS amplitudes in the forward and backward directions, $\hat{\mathbf{x}} = \hat{\mathbf{k}}$ and $\hat{\mathbf{x}} = -\hat{\mathbf{k}}$, respectively, are identical, i.e.,

$$A(k;\hat{\mathbf{k}},\hat{\mathbf{e}}) = A(k;-\hat{\mathbf{k}},\hat{\mathbf{e}})$$

Combining this relation with the optical theorem makes it possible to determine $\sigma_{\text{ext}}$ and verify (7) from a conventional measurement of the monostatic RCS amplitude.

The sample design shown in Fig. 4 was used for the experiments. The fabricated single-layer planar array of capacitive resonators is referred to in the literature as a negative permittivity metamaterial [13]. The sample was tuned to be resonant at 8.5 GHz. It consists of $29 \times 29$ unit cells supported by a 0.3 mm thick $140 \times 140\,\text{mm}^2$ FR4 substrate, see Fig. 4. The relative dielectric constant of the substrate varies between 4.4 and 4.2 in the frequency range $[2,20]$ GHz with an overall loss tangent less than $5 \cdot 10^{-3}$.

## 5.1 Quasi-monostatic and forward RCS measurements

Monostatic RCS measurements were performed in an anechoic chamber with two dual-polarized ridged circular waveguide horns positioned at a distance of 3.5 m from the sample, see the left hand side of Fig. 5. The polarizations of the transmitted and received waves were vertical with respect to the pattern in Fig. 4 – only the co-polarized contribution enters in the optical theorem. The frequency interval $[3.2,19.5]$ GHz was sampled with 7,246 equidistant points corresponding to an unambiguous range of 66.7 m (445 ns). This was sufficient to avoid influence of room reverberations.

Calibration including both amplitude and phase was performed using a metal plate with the same outer dimensions as the sample. The measured data were

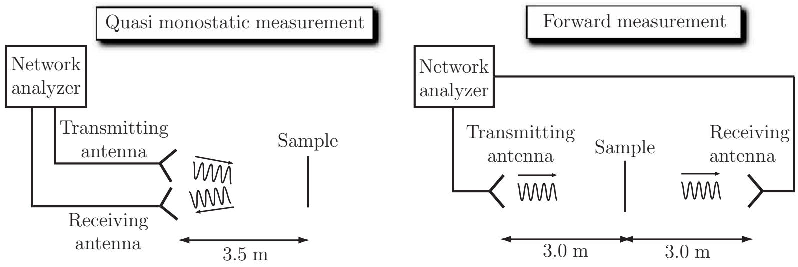


**Fig. 5** The experimental setups for quasi monostatic (*left figure*) and forward RCS (*right figure*) measurements.

processed by a coherent subtraction of the background. The frequency domain data were then transformed to the range domain, where the response from the sample was selected from the range profile using a 1.1 m spatial gate. Finally, the selected data were transformed back to the frequency domain.

The background subtraction combined with the time gating gave a background level of better than $-50$ dBsm (decibel square meters) for the frequency range above 5 GHz and $-40$ to $-30$ dBsm for the lowest part of the frequency range. The high background level at the lower frequencies is a consequence of the wideband horn illumination of the walls at these frequencies. This background level can be maintained for hours by using a single background measurement.

Forward RCS measurements were performed using a different setup with ridged waveguide horns in an ordinary laboratory area. The antennas were positioned facing each other at a distance of 6.0 m with the sample at the midpoint between the antennas, see the right-hand side of Fig. 5. The frequency interval $[2.5, 16]$ GHz was sampled with 5,086 equidistant points corresponding to an unambiguous time range of 378 ns. The unambiguous time range was sufficient to avoid influence of room reverberations such as delayed scattering from the floor and the walls in the laboratory area.

Calibration including both amplitude and phase was performed using a high precision sphere with radius 6.00 cm. The raw data from the calibration were then processed by a coherent subtraction of the background. The fabricated sample was then measured. A new measurement of the background was coherently subtracted from the sample measurement. The repeated background measurements were important in order to increase the efficiency of the background subtraction and to obtain the background levels. We performed the background measurements within less than 2 min after each sample (calibration) measurement.

The calibrated frequency domain data were transformed to the time domain, where the response from the sample was selected from the time profile using a 1.7 ns time gate. The size of the gate was chosen to minimize the influence from the background. Finally, the selected data were transformed back to the frequency domain. The background subtraction combined with the time gating gave a background level of less than $-40$ dBsm.

### 5.2 Validation of the monostatic method and experimental verification of the sum rule

The left graph in Fig. 6 shows a comparison between measurements of the monostatic RCS and the forward RCS. The agreement is better than 0.5 dB except for the minimum at 10.7 GHz where the discrepancy is 2.5 dB. The measured differences are well within experimental error limits. It is therefore validated that the monostatic RCS and the forward RCS are equal within good accuracy for this thin and non-magnetic sample.

However, the phase of the RCS amplitude is also important since the extinction cross section is determined from the imaginary part of the RCS amplitude, cf., the optical theorem (1). The right part[2] of Fig. 6 shows the extinction cross section determined from the optical theorem using both the monostatic and forward RCS amplitudes. The phase of the forward RCS amplitude is shifted according to the procedure described below in order to compare the two curves. The maximum discrepancy between the curves is 35 cm$^2$ at 15 GHz after an adjustment of the phase.

The real and imaginary parts of $A(f;\hat{\mathbf{k}},\hat{\mathbf{e}})/f^2$ are shown in Fig. 7. The phase of $A(f;\hat{\mathbf{k}},\hat{\mathbf{e}})/f^2$ obtained from the forward scattering experiment is adjusted using a time delay of 3.1 ps. We believe that the largest contribution to this phase shift is the time delay of the wave as it passes the 0.3 mm FR4 substrate and the 48 mm expanded polystyrene (EPS) sample support. Small alignment differences between the calibration plate and the sample in the monostatic case can also account for the observed phase difference. The difference between the two measurement methods is small which means that it is validated that conventional monostatic RCS measurements can be used to determine the extinction cross section for this class of thin and non-magnetic samples.

Different methods are used to experimentally verify (7). First the extinction cross section is integrated to obtain a lower bound of $\lim_{f\to 0} A(f;\hat{\mathbf{k}},\hat{\mathbf{e}})/f^2$. By integrating

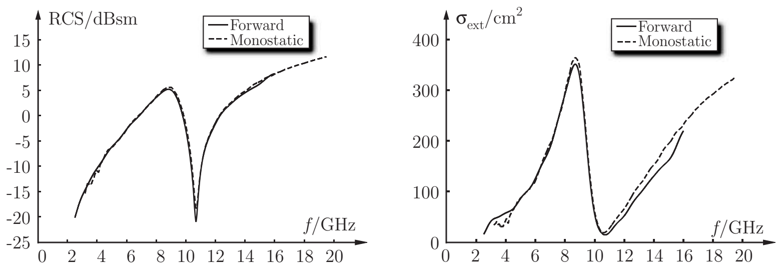


**Fig. 6** The forward and monostatic RCS (*left figure*) and the extinction cross section (*right figure*) determined from the RCS amplitude in the forward and backward directions.

[2] For convenience, we use the frequency $f$ instead of the wavenumber $k = 2\pi f/c_0$ in the discussion of the experimental verification.

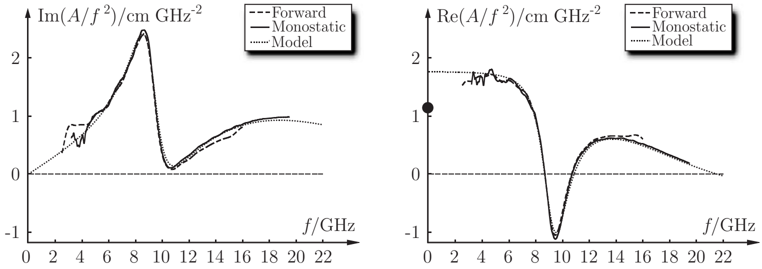


**Fig. 7** The imaginary part (*left figure*) and the real part (*right figure*) of $A/f^2$ determined from the RCS amplitude in the forward and backward directions. The dot for zero frequency indicates a lower bound of $\lim_{f\to 0} A(f;\hat{\mathbf{k}},\hat{\mathbf{e}})/f^2$ obtained by integrating the extinction cross section. The dotted lines are given by the approximation (8).

the measured data in the graph on the right-hand side of Fig. 6a lower bound of $1.1\,\mathrm{cm/GHz}^2$ is obtained using either the forward or the monostatic data.

A method to approximate $A(k;\hat{\mathbf{k}},\hat{\mathbf{e}})/k^2$ is to use a meromorphic function with roots and zeros in the lower half of the complex $k$-plane. Numerical tests using the algorithm in [6] indicate that it is sufficient to consider a rational function with a numerator and a denominator of second and fourth degree polynomials, respectively. This function can be represented by a sum of two Lorentz resonance models, *viz.*,

$$\frac{A^{(\mathrm{appr})}(k,\hat{\mathbf{k}},\hat{\mathbf{e}})}{k^2} = \sum_{n=1}^{2} a_n \frac{k_n^2 - \mathrm{i}k\nu_n}{k_n^2 - 2\mathrm{i}kk_n/Q_n - k^2} \tag{8}$$

The optical theorem, (1), can be used to determine an approximation to the extinction cross section, $\sigma_{\mathrm{ext}}^{(\mathrm{appr})}(k)$, from $A^{(\mathrm{appr})}(k,\hat{\mathbf{k}},\hat{\mathbf{e}})$,

$$\sigma_{\mathrm{ext}}^{(\mathrm{appr})}(k) = \frac{2\sqrt{\pi}}{k} \operatorname{Im} A^{(\mathrm{appr})}(k,\hat{\mathbf{k}},\hat{\mathbf{e}}) \tag{9}$$

The approximations (8) and (9) are depicted by the dotted lines in Fig. 7. It is concluded that the approximations are in good agreement with the experimental results.

A more accurate value for the quantity $\lim_{k\to 0} A(k;\hat{\mathbf{k}},\hat{\mathbf{e}})/k^2$ on the right-hand side of (7) is determined from (8). In fact, the lower bound $1.1\,\mathrm{cm/GHz}^2$ should be compared with the corresponding value $1.5\,\mathrm{cm/GHz}^2$ obtained by integrating $\sigma_{\mathrm{ext}}^{(\mathrm{appr})}(k)$ over the range $[0,22]$ GHz. The lower bound $1.5\,\mathrm{cm/GHz}^2$ is quite close to the static limit $1.8\,\mathrm{cm/GHz}^2$, which is predicted by the parameters in the Lorentz resonance model (8).

## 6 Conclusions

This paper exploits a sum rule for the extinction cross section to find bounds on scattering of electromagnetic waves by an object. The theory is both numerically and experimentally verified. The integrated extinction, which exclusively is determined by the static properties of the object, limits the total scattering properties of the object. Specifically, it is found that large scattering effects always have to be compensated by a loss of bandwidth. This loss of bandwidth can be quantified.

Moreover, we show that monostatic RCS amplitude measurements can be used to determine the extinction cross section for thin and non-magnetic samples by validating the experimental method with a forward RCS measurement. The experimental results show that the sum rule (7) is in good agreement with the measurements.

**Acknowledgements** The financial support by the Swedish Research Council and the Swedish Foundation for Strategic Research is gratefully acknowledged. The authors also thank Saab Bofors Dynamics, Linköping, Sweden, and in particular Carl-Gustaf Svensson and Mats Andersson for generous hospitality and practical assistance in the measurement campaigns.

## References

1. C. F. Bohren and D. R. Huffman. *Absorption and Scattering of Light by Small Particles*. Wiley, New York, 1983.
2. M. Gustafsson, C. Sohl, and G. Kristensson. Physical limitations on antennas of arbitrary shape. *Proc. R. Soc. A*, **463**, 2589–2607, 2007.
3. R. E. Kleinman and T. B. A. Senior. Rayleigh scattering. In V. V. Varadan and V. K. Varadan, editors, *Low and High Frequency Asymptotics*, volume 2 of *Handbook on Acoustic, Electromagnetic and Elastic Wave Scattering*, chapter 1, pages 1–70. Elsevier Science, Amsterdam, 1986.
4. E. F. Knott, J. F. Shaeffer, and M. T. Tuley. *Radar Cross Section*. SciTech, 5601 N. Hawthorne Way, Raleigh, NC 27613, 2004.
5. L. D. Landau and E. M. Lifshitz. *Statistical Physics, Part 1*. Butterworth-Heinemann, Oxford, third edition, 1980.
6. E. C. Levi. Complex-curve fitting. *IRE Trans. on Automatic Control*, **4**, 37–44, 1969.
7. R. G. Newton. *Scattering Theory of Waves and Particles*. Dover Publications, New York, second edition, 2002.
8. H. M. Nussenzveig. *Causality and Dispersion Relations*. Academic, London, 1972.
9. W. K. Panofsky and M. Phillips. *Classical Electricity and Magnetism*. Addison-Wesley, Reading, MA, second edition, 1962.
10. B. Peterson and S. Ström. T-matrix for electromagnetic scattering from an arbitrary number of scatterers and representations of E(3). *Phys. Rev. D*, **8**, 3661–3678, 1973.
11. E. M. Purcell. On the absorption and emission of light by interstellar grains. *J. Astrophys.*, **158**, 433–440, 1969.
12. G. T. Ruck, D. E. Barrick, W. D. Stuart, and C. K. Krichbaum. *Radar Cross-Section Handbook*, volumes 1 and 2. Plenum Press, New York, 1970.
13. D. Schurig, J. J. Mock, and D. R. Smith. Electric-field-coupled resonators for negative permittivity metamaterials. *Appl. Phys. Lett.*, **88**, 041109, 2006.
14. C. Sohl and M. Gustafsson. A priori estimates on the partial realized gain of Ultra-Wideband (UWB) antennas. *Quart. J. Mech. Appl. Math.*, **61**(3), 415–430, 2008.
15. C. Sohl, M. Gustafsson, and G. Kristensson. Physical limitations on broadband scattering by heterogeneous obstacles. *J. Phys. A: Math. Theor.*, **40**, 11165–11182, 2007.
16. C. Sohl, M. Gustafsson, and G. Kristensson. Physical limitations on metamaterials: Restrictions on scattering and absorption over a frequency interval. *J. Phys. D: Applied Phys.*, **40**, 7146–7151, 2007.

17. C. Sohl, C. Larsson, M. Gustafsson, and G. Kristensson. A scattering and absorption identity for metamaterials: experimental results and comparison with theory. *J. Appl. Phys.*, **103**(5), 054906, 2008.
18. J. Van Bladel. *Electromagnetic Fields*. IEEE Press, Piscataway, NJ, second edition, 2007.
19. H. Wallén and A. Sihvola. Polarizability of conducting sphere-doublets using series of images. *J. Appl. Phys.*, **96**(4), 2330–2335, 2004.

# Plasmonic Cloaks

**Andrea Alù[1,2] and Nader Engheta[1]**

[1]University of Pennsylvania, Department of Electrical and Systems Engineering
200 South 33rd St., Philadelphia, PA 19104, U.S.A.
andreaal@ee.upenn.edu, engheta@ee.upenn.edu
[2]University of Texas at Austin, Department of Electrical and Computer Engineering,
1 University Station C0803, Austin, TX, 78712, U.S.A.

**Abstract** The use of metamaterials and artificial media for cloaking applications has been shown to potentially lead to exciting developments in the fields of electromagnetics, microwaves, and optics. Plasmonic covers, in particular, have been shown to provide a local negative polarizability capable of canceling or reducing the dominant scattering from an isolated object and/or a cluster of objects. Here we provide an overview of the recent theoretical and numerical results related to our plasmonic cloaking technique, based on scattering cancellation, that may provide an overall invisibility effect by using plasmonic metamaterial covers.

## 1 Introduction

In recent years, the interest in applications of special materials has steadily increased worldwide. One such application deals with the possible use of metamaterials and plasmonic media for cloaking and "invisibility". In particular, since our proposal for employing such materials to significantly reduce the total scattering from a given object [1], other different techniques [2–19] have shown, theoretically and for some even experimentally, how metamaterials may be designed to operate as novel cloaks. Here we review our recent findings in this plasmonic cloaking, discussing and highlighting the total scattering reduction provided by a suitably designed plasmonic material or metamaterial that constitutes a "plasmonic cloak" surrounding a given object.

Our studies have revealed that the dominant multipolar contribution to the scattering from a given object of moderate size may be potentially suppressed by a suitably designed plasmonic metamaterial with low or negative permittivity. We have also underlined the intrinsic robustness of this phenomenon, which is inherently non-resonant, and therefore robust to variations in shape, design parameters, losses, wave polarization and source and observer position [20–21]. In [22], we have observed how this cloaking effect may not be limited to an isolated

S. Zouhdi et al. (eds.), *Metamaterials and Plasmonics: Fundamentals, Modelling, Applications*,

particle of moderate size, but it may be applied to combination and clusters of dielectric or conducting objects on a larger scale. In [23], moreover, we have proposed a realistic metamaterial design for the plasmonic cloak at microwave frequencies, applied to a cylindrical geometry. We have extended these concepts in [24–25] to optical frequencies and multi-frequency operation. The interested reader may find reviews of our recent findings in [26–28], where we have compared this cloaking technique to several other techniques that are currently available. In particular, in [26] we have reported an updated list of references on metamaterial cloaking. In the following, we will briefly highlight the main concepts related to this plasmonic cloaking technique, underlining the physical insights, benefits and possible limitations.

## 2 Isolated Objects

As we have shown in [1], the use of a plasmonic material surrounding a dielectric or conducting particle may dramatically suppress the total scattering from the object, by cancelling the dominant scattering contribution due to the local negative polarizability of plasmonic materials with low permittivity.

Figure 1, as a first numerical example compares the near-field distribution on the two planes for the conducting object, whose geometry has been first considered in [20], with radius $a = \lambda_0 / 5$, with $\lambda_0$ being the free-space wavelength. The figure compares the cases of presence and absence of a suitably designed plasmonic cloak, having permittivity $\varepsilon = 0.1\varepsilon_0$, permeability $\mu = 5.1\mu_0$ and outer radius $a_c = 1.09\,a$. The spheres are excited by a plane wave impinging from the left on the sphere. It is evident how the presence of the cloak may significantly reduce the unwanted scattering from the sphere, despite its total size may support resonant scattering. The cloaking effect, which is even more striking in the Poynting vector plots of Fig. 1, works on both planes of polarization, independent on the polarization of the impinging plane wave or the position of the source and of the observer. These results are consistent with our findings in [1, 20]. It should be underlined that the sketches of Fig. 1 and following figures related to the uncloaked cases present a mathematical line representing the outer boundary of the cloak. This mathematical line has been added for consistency in the numerical simulations of the uncloaked cases, but it is understood that it represents just a mathematical line (or a cover made of the same material as the background region in these uncloaked cases).

Figure 2 reports the far-field scattering patterns for the two geometries, highlighting the drastic scattering reduction over all the visible angles at the design frequency $f_0$. The drastic scale difference between the two plots should be noted, which results in a tiny shadow on the back of the cloaked object. The total scattering reduction is over 99% for this geometry, as noticed in [20].

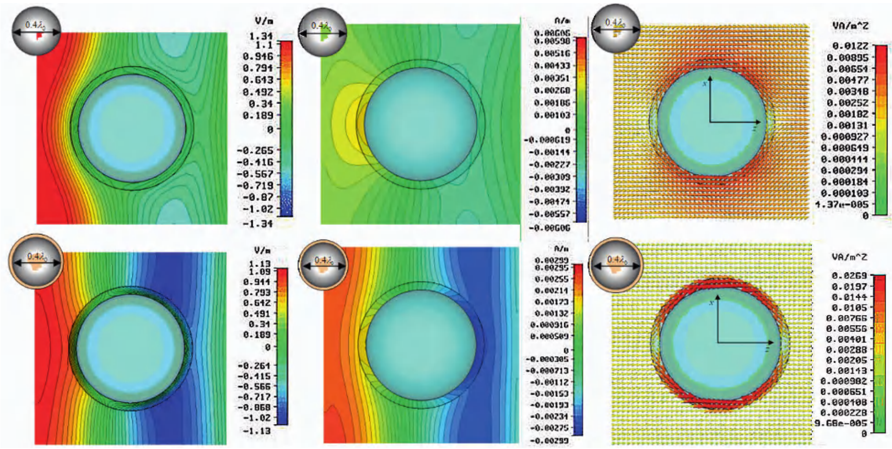


**Fig. 1** Comparison between the near-field electric field distribution in the H-plane (*left column*), magnetic field in the E-plane (*central column*) and the real part of the Poynting vector (i.e., the time-averaged energy flow) in the H-plane (*right column*) of a bare conducting sphere (*top row*) and of a cloaked conducting sphere of the same size (*bottom row*). The field distributions are snapshots in time. (Adapted from [20], Copyright (2007) by the Optical Society of America.)

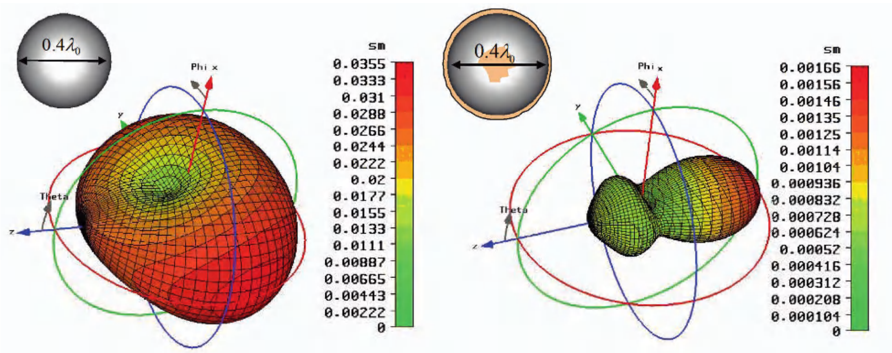


**Fig. 2** Comparison between the far-field scattering pattern between the bare conducting sphere (*left*) and the cloaked conducting sphere (*right*) of Fig. 1. Notice the different scale in the two plots. (Adapted from [20], Copyright (2007) by the Optical Society of America.)

Figure 3 shows the response of the two spheres of Figs. 1–2 for a different excitation, in the form of a short electric dipole antenna placed very close to the surface of the object, consistent with [20]. It is evident how, despite the drastic change in the excitation and position of the source, and despite the possible near-field coupling, the performance of the cloak in terms of total scattering reduction is effectively unchanged. This is particularly relevant due to the fact that the cloak does not require to be optimized or modified for the presence of nearby active source or drastic change in the position or form of the illumination.

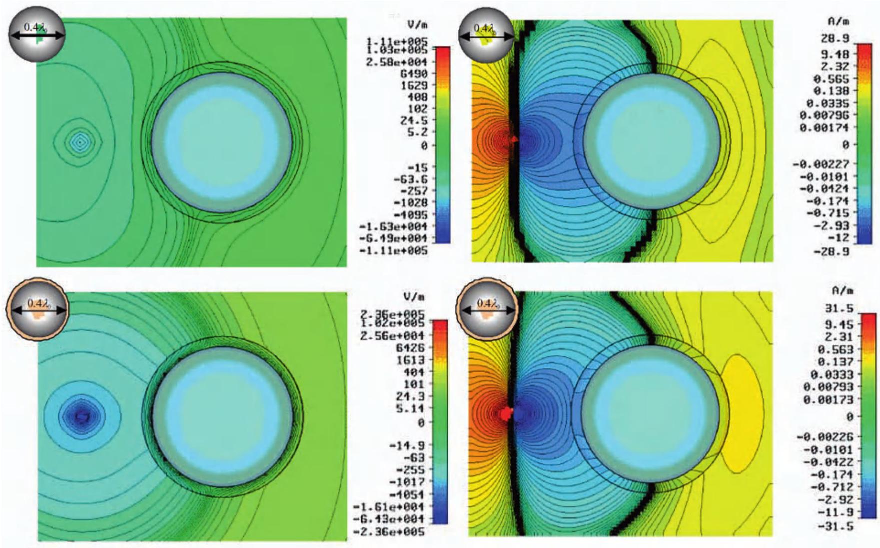


**Fig. 3** Comparison between the total near-field in the two planes of polarization between the bare conducting sphere (*top*) and the cloaked conducting sphere (*bottom*) of Figs. 1–2. The excitation now is given by a closely spaced short electric dipole. (Adapted from [20], Copyright (2007) by the Optical Society of America.)

## 3 Multilayered Cloak

As we have widely discussed in [1, 20], this plasmonic cloaking technique operates over a relatively less narrow range of frequencies, due to its inherent non-resonant features. Being an integrative effect, its dispersion is mainly associated with the material dispersion of the cloak, required of being plasmonic, and not as much with the dispersion of the geometry and the phenomenon, particularly for objects that are comparable in size with a fraction of the operating wavelength. It is interesting to verify that this inherent material dispersion, required by causality, may be used to our advantage to realize multi-frequency cloaks [24].

As with the geometry we analyzed in [24], for instance, a dielectric nanoparticle may be cloaked at two distinct optical frequencies by surrounding it with a two-layered plasmonic cover that may operate as a cloak at two distinct wavelengths. In this case, the dielectric particle has $\varepsilon = 3\varepsilon_0$ and radius $a = 100\,nm$, whereas the two-layered cloak has radii $a_1 = 107.5\,nm$ and $a_2 = 131.5\,nm$. Figures 4 and 5 show the electric near-field distributions on the H-plane for such a sphere, comparing the cases with and without cloak at the two distinct design frequencies of $\lambda_0 = 625\,nm$ and $\lambda_0 = 500\,nm$. Each one of the two layers of the cloak is supposed to have a permittivity dispersion that ensures $\mathrm{Re}[\varepsilon_c] = \varepsilon_0 / 5$ at one at one of the two distinct frequencies of operation, both following a classic Drude dispersion model.

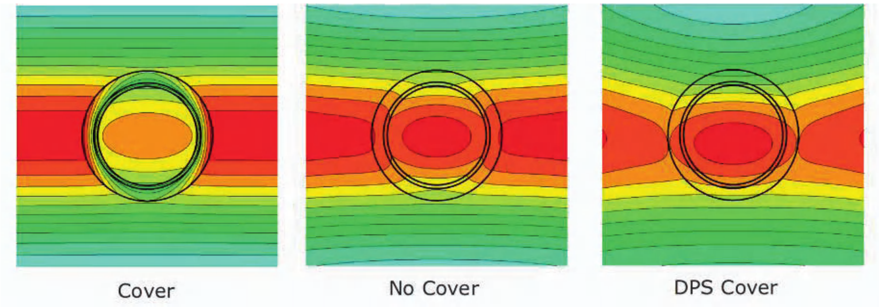


**Fig. 4** Comparison among the electric near-field distributions in the H-plane in the case of a cloaked dielectric sphere (*left*) the same bare sphere (*center*) and the same sphere covered by a dielectric cover with the same thickness as the cloak. The excitation now is given by a plane wave impinging from the bottom. These plots refer to the free-space wavelength $\lambda_0 = 625\,nm$. (Adapted from [24], Copyright (2008) by the American Physical Society.)

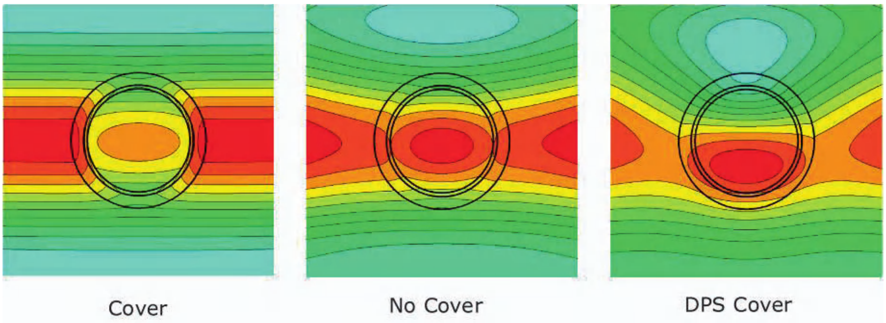


**Fig. 5** Similar to Fig. 4, but for the free-space wavelength $\lambda_0 = 500\,nm$. (Adapted from [24], Copyright (2008) by the American Physical Society.)

It can be seen that the cloak is capable of suppressing the scattering from the particle simultaneously at the two design frequencies, restoring the impinging planar phase fronts right outside the cloak surface. In this example, the field distributions are snapshots in time.

## 4 Cloaking Near an Obstacle

We have discussed in the previous sections how the plasmonic cloaking technique is robust to variations of the excitation and frequency variations near the design frequency. Here we report our numerical results on the case in which the impenetrable sphere considered in the previous section is tightly coupled with an impenetrable small cube with side $l = 2a/3 = 2\lambda_0/15$. We have considered this geometry in [21]. Consider, for instance, Fig. 6, i.e., an impenetrable sphere with the same geometry as the one of Fig. 1 placed in close proximity to a conducting small cube. The system is illuminated from the left with a plane wave.

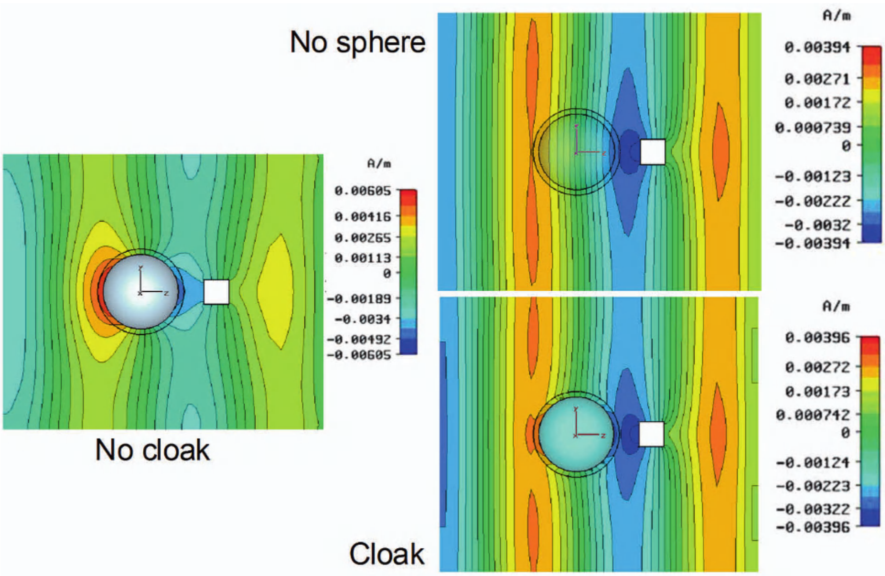


**Fig. 6** Near-zone magnetic field distribution (snapshot in time) for a system composed of the impenetrable sphere of Fig. 1 and a small closely spaced cube. Comparison between the cases of no cloak, absence of the sphere and cloaked sphere. (Adapted from [21], Copyright (2008) by the American Geophysical Union.)

Figure 6 reports the near-zone magnetic field distribution on the E-plane for three cases: (left) when the sphere is bare, showing strong coupling in the scattered fields from the two objects; (top right) absence of the sphere; (bottom right) the sphere is cloaked. It is evident how in the last two scenarios the scattered field is very similar to each other, i.e., not only does the cloak effectively cancel the scattering from the sphere, but it also reduces significantly the coupling between the two elements. For an observer placed anywhere in the near-field of the system, the presence of the sphere is undetectable when cloaked. In other words, an observer placed behind the sphere may be able to perceive the presence of the small cube placed in the sphere's shadow as if the sphere were not present.

Figure 7 reports similar results for an excitation with orthogonal polarization. It can be clearly seen how the cloak performs very well on both planes of polarization. It should be underlined that the case of a conducting or impenetrable sphere is the most challenging in terms of plasmonic cloaking, since it does not allow the wave to penetrate through the object. Dielectric particles, as those considered in the previous section, may perform even better than this scenario, in terms of reduced scattering and wider bandwidth of operation.

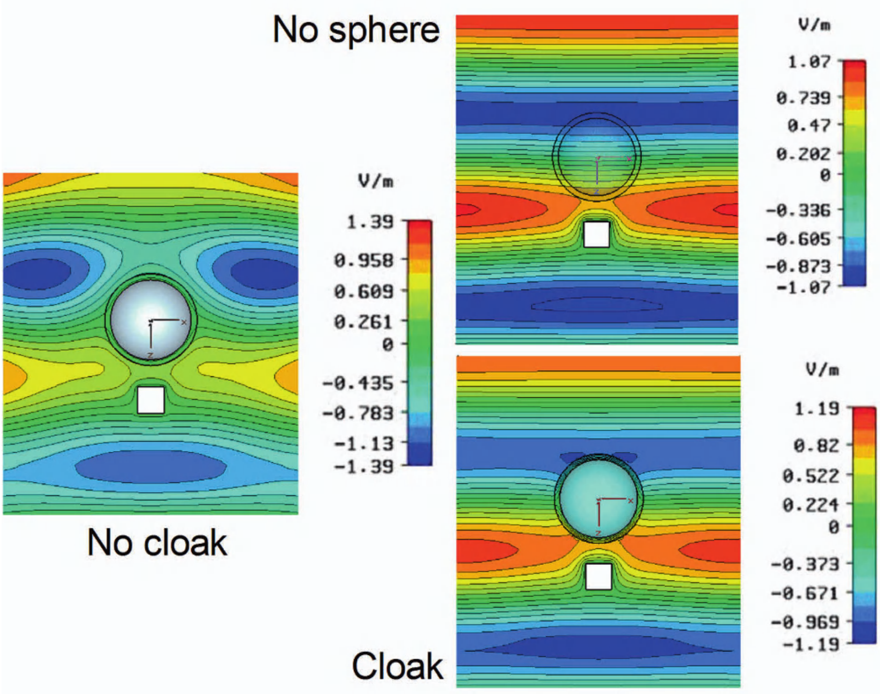


**Fig. 7** Similar to Fig. 6, but for excitation on the orthogonal plane of polarization. (Adapted from [21], Copyright (2008) by the American Geophysical Union.)

Figure 8 considers the case of a different type of excitation. In this case, we have simulated the case of a short electric dipole placed behind the conducting sphere. It is evident that this is an even more extreme case, due to the mutual coupling among the sphere, the cube and the nearby source. Still, the cloak performs very well in drastically reducing the unwanted scattering and coupling from the sphere.

## 5 Cloaking Clusters of Objects

As we have extensively studied in [22], and consistent with the findings in the previous section, collections and clusters of particles may be cloaked following

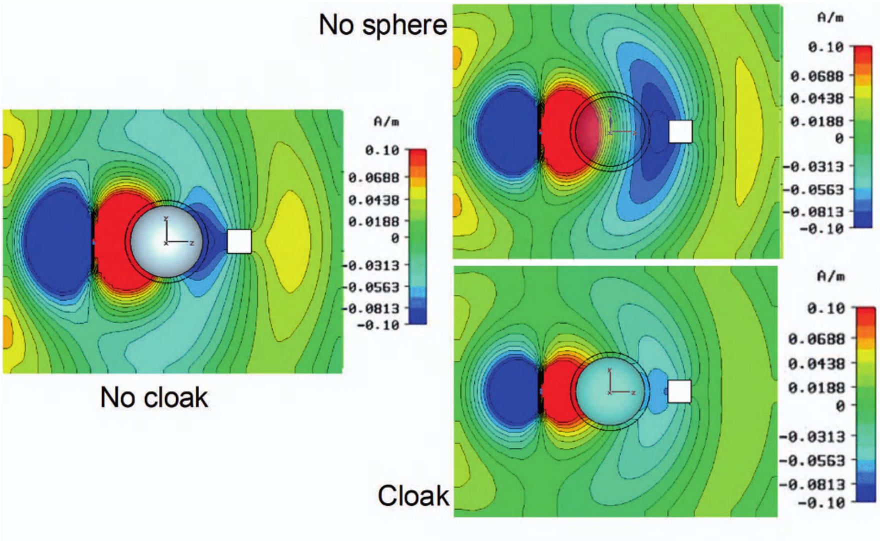


**Fig. 8** Similar to Figs. 6–7, but for a different type of excitation, consisting of a nearby short electric dipole. (Adapted from [21], Copyright (2008) by the American Geophysical Union.)

the same guidelines and design adopted for a single isolated object, due to absence (or significant reduction) of coupling among the cloaked elements.

Consider, for instance, the geometry of Figs. 9–11, i.e., an array of closely spaced impenetrable spheres, each of which with the same geometry and parameters of the sphere of Fig. 1. The figures compare the near-field magnetic distribution on the E-plane (which is the plane more challenging for cloaking, due to the orientation of the electric field parallel to the array axis) for three different orientation of the impinging plane wave. It is evident that, despite the complexity of the problem and the large electrical size of the overall cluster (over two wavelengths), the cloaks drastically suppress the unwanted scattering and coupling among the spheres, restoring the impinging planar wave fronts almost independent from the orientation of the impinging plane wave.

The results are consistent, and complement, those reported in [22], where it was also shown how the same cloaking design may be adopted for touching objects, or to some degree even to elements that merge together into a single larger obstacle. This is associated with the inherent non-resonant features and robustness of this cloaking mechanism.

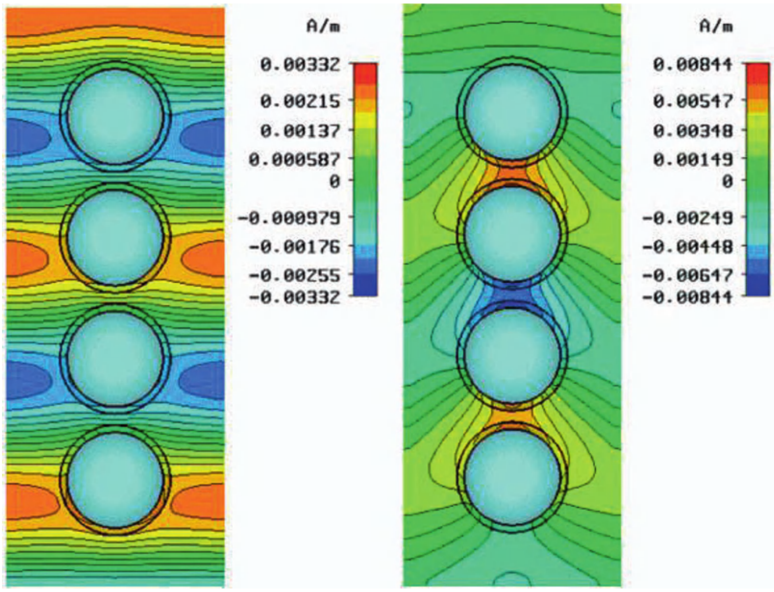


**Fig. 9** Cloaking an array of four closely spaced impenetrable spheres. Near-field magnetic field distribution on the E-plane for the cases of cloaked (*left*) and uncloaked (*right*) spheres for plane wave incidence impinging from the top of the figure. (Adapted from [22], Copyright (2007) by the Optical Society of America.)

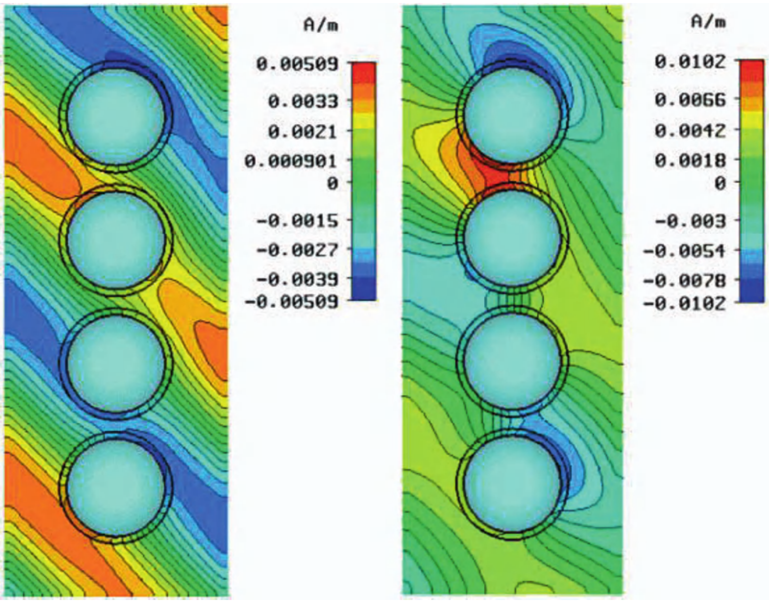


**Fig. 10** Similar to Fig. 9, but for 45° plane wave incidence. (Adapted from [22], Copyright (2007) by the Optical Society of America.)

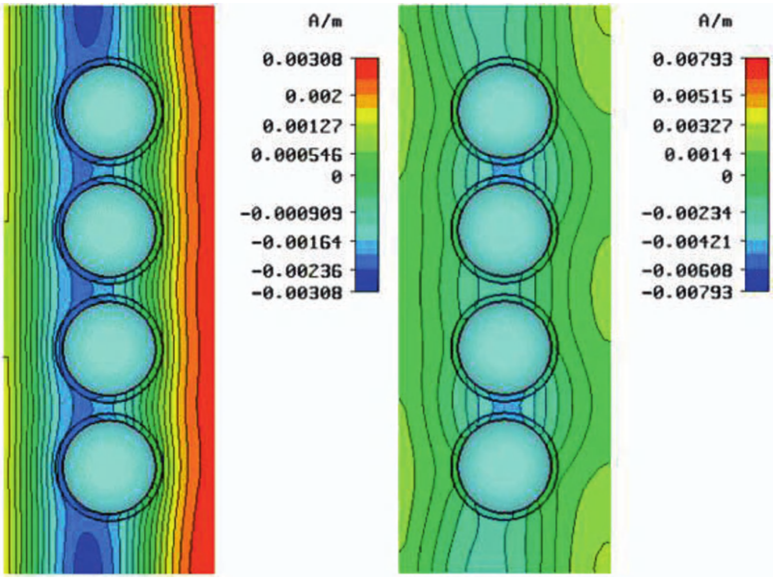


**Fig. 11** Similar to Figs. 9–10, but for 90° plane wave incidence. (Adapted from [22], Copyright (2008) by the Optical Society of America.)

## 6 Conclusions

To conclude, we have reported here an overview of our recent theoretical and numerical results for plasmonic cloaking, reporting our recent findings and numerical simulations on this exciting electromagnetic problem. The interested reader may refer to the list of references for additional information and insights.

## References

1. Alù, A., Engheta, N.: Achieving transparency with plasmonic and metamaterial coatings. Phys. Rev. E **72**, 016623 (2005).
2. Pendry, J. B., Schurig, D., Smith, D. R.: Controlling electromagnetic fields. Science **312**, 1780–1782 (2006).
3. Schurig, D., Mock, J. J., Justice, B. J., Cummer, S. A., Pendry, J. B., Starr, A. F., Smith, D. R.: Metamaterial electromagnetic cloak at microwave frequencies. Science **314**, 977–980 (2006).
4. Cummer, S. A., Popa, B. I., Schurig, D., Smith, D. R., Pendry, J. B.: Full-wave simulations of electromagnetic cloaking structures. Phys. Rev. E **74**, 036621 (2006).

5. Cai, W., Chettiar, U. K., Kildishev, A. V., Shalaev, V. M.: Optical cloaking with metamaterials. Nat. Photonic. **1**, 224–227 (2007).
6. Cai, W., Chettiar, U. K., Kildishev, A. V., Milton, G. W., Shalaev, V. M.: Nonmagnetic cloak with minimized scattering. Appl. Phys. Lett. **91** (2007).
7. Jacob Z., Narimanov, E. E.: Semiclassical description of non magnetic cloaking. Opt. Express **16**, 4597–4604 (2008).
8. Milton, G. W., Nicorovici, N. A., McPhedran, R. C., Podolskiy, V. A.: A proof of superlensing in the quasistatic regime, and limitations of superlenses in this regime due to anomalous localized resonance. Proc. Roy. Soc. Lond. **461**, 3999–4034 (2005).
9. Milton, G. W., Nicorovici, N. A.: On the cloaking effects associated with anomalous localized resonance. Proc. R. Soc. Lond. A: Math. Phys. Sci. **462**, 3027–3059 (2006).
10. Leonhardt, U.: Optical conformal mapping. Science **312**, 1777–1780 (2006).
11. Leonhardt, U.: Notes on conformal invisibility devices. New J. Phys. **8**, 118 (2006).
12. Greenleaf, A., Kurylev, Y., Lassas, M., Uhlmann, G.: Full-wave invisibility of active devices at all frequencies. Comm. Math. Phys. **275**, 749–789 (2007).
13. Chen, H., Jiang, X., Chan, C. T.: Extending the bandwidth of electromagnetic cloaks. Phys. Rev. B **76**, 241104 (2007).
14. Yan, M., Ruan, Z., Qiu, M.: Cylindrical invisibility cloak with simplified material parameters is inherently visible. Phys. Rev. Lett. **99**, 233901 (2007).
15. Ruan, Z., Yan, M., Neff, C. W., Qiu, M.: Ideal cylindrical cloak: perfect but sensitive to tiny perturbations. Phys. Rev. Lett. **99**, 113903 (2007).
16. Miller, D. A. B.: On perfect cloaking. Opt. Express **14**, 12457–12466 (2006).
17. Torrent, D., Sánchez-Dehesa, J.: Acoustic Cloaking in two dimensions: a feasible approach. New J. Phys. **10**, 063015 (2008).
18. Yaghjian, A., Maci, S.: Alternative derivation of electromagnetic cloaks and concentrators. Online at: arXiv:0710.2933v4.
19. Alitalo, P., Luukkonen, O., Jylhä, L., Venermo, J., Tretyakov, S.A.: Transmission-line networks cloaking objects from electromagnetic fields. IEEE Trans. Antenn. Propag. **56**, 416–424 (2008).
20. Alù, A., Engheta, N.: Plasmonic materials in transparency and cloaking problems: mechanism, robustness, and physical insights. Opt. Express **15**, 3318–3332 (2007).
21. Alù, A., Engheta, N.: Robustness in design and background variations in metamaterial/plasmonic cloaking. Radio Sci. **43**, RS4S01 (2008).
22. Alù, A., Engheta, N.: Cloaking and transparency for collections of particles with metamaterial and plasmonic covers. Opt. Express **15**, 7578–7590 (2007).
23. Silveirinha, M. G., Alù, A., Engheta, N.: Parallel plate metamaterials for cloaking structures. Phys. Rev. E **75**, 036603 (2007).
24. Alù, A., Engheta, N., Multifrequency optical cloaking with layered plasmonic shells. Phys. Rev. Lett. **100**, 113901 (2008).
25. Silveirinha, M. G., Alù, A., Engheta, N.: Infrared and optical invisibility cloak with plasmonic implants based on scattering cancellation. Phys. Rev. B **78**, 075107 (August 11, 2008).
26. Alù, A., Engheta, N.: Plasmonic and metamaterial cloaking: physical mechanisms and potentials. J. Opt. A: Pure Appl. Opt. **10**, 093002 (August 19, 2008).
27. Alù, A., Engheta, N.: Dispersion characteristics of metamaterial cloaking structures. In S. Zouhdi and S. Tretyakov, guest editors, Electromagnetics, Special Issue for Metamaterials 2007, **28** (7), 464–475 (October 2008).
28. Alù, A., Engheta, N.: Metamaterial and plasmonic cloaking. Handbook of Artificial Materials, F. Capolino, ed., Taylor & Francis/CRC Press, Vol. 2, in press.

# Geometrical Transformations for Numerical Modelling and for New Material Design in Photonics

**André Nicolet[1], Frédéric Zolla[1], Yacoub Ould Agha[1], and Sébastien Guenneau[2]**

[1] Institut Fresnel (UMR CNRS 6133) - Aix-Marseille Université,
Domaine Universitaire de Saint-Jérôme, F13397 Marseille cedex 20, France
andre.nicolet@fresnel.fr

[2] Department of Mathematical Sciences, University of Liverpool, Peach Street,
Liverpool L69 3BX, UK

**Abstract** This paper is a review of various techniques used in computational electromagnetism such as the treatment of leaky modes in waveguides, helicoidal geometries for microstructured optical fibres and the design of arbitrarily shaped invisibility cloaks. This seemingly heterogeneous list is unified by the concept of geometrical transformation that leads to equivalent materials, i.e., the change of coordinates is completely encapsulated in the material properties. The practical set up is conveniently made via the finite element method (FEM).

## 1 Geometrical Transformations and Equivalent Materials

Beside Cartesian coordinates, cylindrical and spherical coordinates, and even the other orthogonal systems [1], have been commonly used to set up electromagnetic problems. In this paper, much more general coordinate systems are discussed since they do not need to be orthogonal (and not even real valued). A modern approach is to write the equations of electromagnetism in the language of exterior calculus that is covariant, i.e. independent of the choice of the coordinate system (see e.g. [2]). In this way, the Maxwell equations involve only the exterior derivative and are purely topological and differential while all the metric information is contained in the material properties via a Hodge star operator. This looks rather abstract but can nevertheless be encapsulated in a very simple and practical equivalence rule [3–5]:

When you change your coordinate system, all you have to do is to replace your initial material (electric permittivity tensor $\underline{\underline{\varepsilon}}$ and magnetic permeability tensor $\underline{\underline{\mu}}$) properties by equivalent material properties given by the following rule:

$$\underline{\underline{\varepsilon}}' = \mathbf{J}^{-1}\underline{\underline{\varepsilon}}\mathbf{J}^{-T}\det(\mathbf{J}) \quad \text{and} \quad \underline{\underline{\mu}}' = \mathbf{J}^{-1}\underline{\underline{\mu}}\mathbf{J}^{-T}\det(\mathbf{J}), \tag{1}$$



S. Zouhdi et al. (eds.), *Metamaterials and Plasmonics: Fundamentals, Modelling, Applications*,

where $\mathbf{J}$ is the Jacobian matrix of the coordinate transformation consisting of the partial derivatives of the new coordinates with respect to the original ones ($\mathbf{J}^{-T}$ is the transposed of its inverse).

In Eq. (1), the right hand sides involve matrix products where the matrix associated with a second rank tensor involves the coefficients of its representation in the initial Cartesian coordinate system. The obtained matrix provides the new coefficients of the tensor corresponding to the equivalent material.

Explicitly, a map from a coordinate system $\{u,v,w\}$ to the coordinate system $\{x,y,z\}$ is given by the transformation characterized by $x(u,v,w)$, $y(u,v,w)$ and $z(u,v,w)$. As we start with a given set of equations in a given coordinate system, it seems at first sight that we have to map these coordinates on the new ones. Nevertheless it is the opposite that has to be done: the new coordinate system is mapped on the initial one (i.e. the new coordinates are defined as explicit functions of the initial coordinates) and the equations are then pulled back, according to differential geometry [2], on the new coordinates. This provides directly the functions whose derivatives are involved in the computation of the Jacobian matrix. The Jacobian is directly given by:

$$\mathbf{J}_{xu} \equiv \begin{pmatrix} \frac{\partial x}{\partial u} & \frac{\partial x}{\partial v} & \frac{\partial x}{\partial w} \\ \frac{\partial y}{\partial u} & \frac{\partial y}{\partial v} & \frac{\partial y}{\partial w} \\ \frac{\partial z}{\partial u} & \frac{\partial z}{\partial v} & \frac{\partial z}{\partial w} \end{pmatrix} . \tag{2}$$

The equivalence rule (1) can be extended to more general material properties such as local Ohm's law and bianisotropic materials [3]. Moreover, the rule given by Eq. (1) may be easily applied to a composition of transformations. Let us consider three coordinate systems $\{u,v,w\}$, $\{X,Y,Z\}$, and $\{x,y,z\}$. The two successive changes of coordinates are given by the sets of functions $\{X(u,v,w),Y(u,v,w), Z(u,v,w)\}$ and $\{x(X,Y,Z),y(X,Y,Z),z(X,Y,Z)\}$. They lead to the Jacobians $\mathbf{J}_{Xu}$ and $\mathbf{J}_{xX}$ so that the global Jacobian $\mathbf{J}_{xu} = \mathbf{J}_{xX}\mathbf{J}_{Xu}$. The compound transformation can therefore be considered either as involving this global Jacobian or as successive applications of Eq. (1). This rule naturally applies for an arbitrary number of coordinate systems. Note that the maps are defined from the final $u,v,w$ to the original $x,y,z$ coordinate system and that the product of the Jacobians, corresponding to the composition of the pull back maps, is in the opposite order.

When the initial material properties $\varepsilon$ and $\mu$ are isotropic and described by a scalar, they generally lead to anisotropic properties and are given via a transformation matrix $\mathbf{T} = \mathbf{J}^T\mathbf{J}/\det(\mathbf{J})$ related to the metric expressed in the new coordinates so that the equivalence rule (1) becomes

$$\underline{\underline{\varepsilon'}} = \varepsilon\mathbf{T}^{-1}\,, \quad \text{and} \quad \underline{\underline{\mu'}} = \mu\mathbf{T}^{-1}\,. \tag{3}$$

We note that there is no change in the impedance of the media since the permittivity and permeability suffer the same transformation.

As for the vector analysis operators and products, everything works as if we were in Cartesian coordinates. It means that once the material properties have been set to their equivalent values, all the computations are performed as if the coordinates were Cartesian. Once the solution has been obtained in the new coordinate system, e.g. the electric field $\mathbf{E}'$, its components in the original Cartesian coordinate system, $\mathbf{E}$, are given by (in the rest of this section, the vectors are represented by $3 \times 1$ column matrices):

$$\mathbf{E} = \begin{pmatrix} E_x \\ E_y \\ E_z \end{pmatrix} = \mathbf{J}^{-T} \begin{pmatrix} E'_u \\ E'_v \\ E'_w \end{pmatrix} = \mathbf{J}^{-T}\mathbf{E}'. \tag{4}$$

It must be emphasized here that $\mathbf{E}$ and $\mathbf{E}'$ are the same field expressed in two different coordinate systems. The direct interpretation of $\mathbf{E}'$ is difficult since it is expressed in a possibly non orthogonal and not normed basis. Other vector fields corresponding to 1-forms such as $\mathbf{H}$ or $\mathbf{A}$ are transformed in the same way while the vector fields corresponding to 2-forms (flux densities) such as $\mathbf{D}$, $\mathbf{B}$, and $\mathbf{J}$ are transformed according to

$$\mathbf{D} = \mathbf{J}\,\mathbf{D}'/\det(\mathbf{J}). \tag{5}$$

It may be checked that these transformations are compatible with the equivalence rule (1) telling that $\mathbf{D} = \underline{\underline{\varepsilon}}\mathbf{E}$ is replaced by $\mathbf{D}' = \underline{\underline{\varepsilon}}'\mathbf{E}'$ in the equivalent formulation. They also preserve the form of energy densities since, for instance, $\int_\Omega \mathbf{E}^T\mathbf{D}dxdydz = \int_{\Omega'} \mathbf{E}'^T\mathbf{D}'dudvdw$ where $\Omega'$ is the image of the domain $\Omega$ by the coordinate transformation and $\mathbf{E}^T\mathbf{D}$ is the matrix notation for the dot product.

As inhomogeneous and anisotropic equivalent materials are obtained and as the theoretical framework is the exterior calculus, the (Whitney) finite element method (FEM) is perfectly adapted to the numerical algorithm implementation [6–9].

In fact, this goes beyond simple change of coordinates as we will also consider active transformations, i.e. changes of space (i.e. of manifold) where the equations are written.

It is very often useful to use radial transformations. In this case, the most simple way is to first perform a transformation to cylindrical or spherical coordinates and to perform the inverse transformation once the radial transformation has been made. First, the classical transformation from Cartesian coordinates $\{x,y,z\}$ to polar coordinates $\{\rho,\theta,z\}$ is introduced via a map from $\rho,\theta$ to $x,y$:

$$\begin{cases} x(\rho,\theta) = \rho\cos\theta \\ y(\rho,\theta) = \rho\sin\theta. \end{cases} \tag{6}$$

The associated Jacobian is

$$\mathbf{J}_{x\rho}(\rho,\theta) = \frac{\partial(x,y,z)}{\partial(\rho,\theta,z)} = \begin{pmatrix} \cos\theta & -\rho\sin\theta & 0 \\ \sin\theta & \rho\cos\theta & 0 \\ 0 & 0 & 1 \end{pmatrix} = \mathbf{R}(\theta)\,\mathbf{diag}(1,\rho,1), \tag{7}$$

with

$$\mathbf{R}(\theta) = \begin{pmatrix} \cos\theta & -\sin\theta & 0 \\ \sin\theta & \cos\theta & 0 \\ 0 & 0 & 1 \end{pmatrix} \text{ and } \mathbf{diag}(1,\rho,1) = \begin{pmatrix} 1 & 0 & 0 \\ 0 & \rho & 0 \\ 0 & 0 & 1 \end{pmatrix}.$$

$\mathbf{R}(\theta)$ has the well known properties: $\mathbf{R}(\theta)^{-1} = \mathbf{R}(\theta)^T = \mathbf{R}(-\theta)$.

Furthermore, the inverse transformation is given by the map:

$$\begin{cases} \rho(x,y) = \sqrt{x^2+y^2} \\ \theta(x,y) = 2\arctan\left(\frac{y}{x+\sqrt{x^2+y^2}}\right), \end{cases} \tag{8}$$

and is associated with the Jacobian:

$$\mathbf{J}_{\rho x}(x,y) = \mathbf{J}_{x\rho}^{-1}(\rho(x,y),\theta(x,y)) = \mathbf{diag}(1,\frac{1}{\rho(x,y)},1)\,\mathbf{R}(-\theta(x,y)). \tag{9}$$

Similarly, the spherical coordinates are described via a map from $\rho,\theta,\varphi$ to $x,y,z$:

$$\begin{cases} x = \rho\cos\theta\sin\varphi \\ y = \rho\sin\theta\sin\varphi \\ z = \rho\cos\varphi. \end{cases} \tag{10}$$

The spherical Jacobian:

$$\mathbf{J}_{x\rho}(\rho,\theta,\varphi) = \begin{pmatrix} \cos\theta\sin\varphi & -\rho\sin\theta\sin\varphi & \rho\cos\theta\cos\varphi \\ \sin\theta\sin\varphi & \rho\cos\theta\sin\varphi & \rho\sin\theta\cos\varphi \\ \cos\varphi & 0 & -\rho\sin\varphi \end{pmatrix}, \tag{11}$$

can be written as $\mathbf{J}_{x\rho} = \mathbf{R}(\theta)\mathbf{M}_2(\varphi)\mathbf{diag}(1,\rho\sin\varphi,\rho)$ still involving the $\mathbf{R}(\theta)$ matrix together with:

$$\mathbf{M_2}(\varphi) = \begin{pmatrix} \sin\varphi & 0 & \cos\varphi \\ 0 & 1 & 0 \\ \cos\varphi & 0 & -\sin\varphi \end{pmatrix}, \tag{12}$$

with the properties: $\mathbf{M}_2^{-1}(\varphi) = \mathbf{M}_2^T(\varphi) = \mathbf{M}_2(\varphi)$.

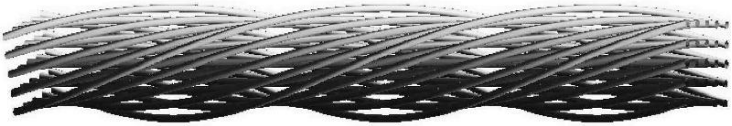

**Fig. 1** A twisted structure that may be described by the helicoidal coordinates.

## 2 Helicoidal Geometries and Leaky Modes in Twisted Optical Fibres

The purpose of this section is to show how the equivalence rule (1) can be used to study the propagation of modes in twisted waveguides via a two-dimensional model though the translational invariance of the geometry is lost (see Fig. 1).

Let us introduce an helicoidal coordinate system [14–16] $\{\xi_1, \xi_2, \xi_3\}$ deduced from rectangular Cartesian coordinates $\{x, y, z\}$ in the following way

$$x = \xi_1 \cos(\alpha\xi_3) + \xi_2 \sin(\alpha\xi_3),\ y = -\xi_1 \sin(\alpha\xi_3) + \xi_2 \cos(\alpha\xi_3),\ z = \xi_3\ , \quad (13)$$

where $\alpha$ is a parameter which characterizes the torsion of the structure. A twisted structure is a structure for which both geometrical and physical characteristics (here the permittivity $\varepsilon$ and the permeability $\mu$) together with the boundary conditions only depend on $\xi_1$ and $\xi_2$. Note that such a structure is invariant along $\xi_3$ but $\frac{2\pi}{\alpha}$-periodic along $z$ (the period may be shorter depending on the symmetry of the cross section).

This general coordinate system is characterized by the Jacobian of the transformation (13):

$$\mathbf{J}_{hel}(\xi_1, \xi_2, \xi_3) = \quad (14)$$

$$\begin{pmatrix} \cos(\alpha\xi_3) & \sin(\alpha\xi_3) & \alpha\xi_2 \cos(\alpha\xi_3) - \alpha\xi_1 \sin(\alpha\xi_3) \\ -\sin(\alpha\xi_3) & \cos(\alpha\xi_3) & -\alpha\xi_1 \cos(\alpha\xi_3) - \alpha\xi_2 \sin(\alpha\xi_3) \\ 0 & 0 & 1 \end{pmatrix}, \quad (15)$$

which does depend on the three variables $\xi_1$, $\xi_2$ and $\xi_3$. On the contrary, the transformation matrix $\mathbf{T}_{hel}$ :

$$\mathbf{T}_{hel}(\xi_1, \xi_2) = \frac{\mathbf{J}_{hel}^T \mathbf{J}_{hel}}{det(\mathbf{J}_{hel})} = \begin{pmatrix} 1 & 0 & \alpha\xi_2 \\ 0 & 1 & -\alpha\xi_1 \\ \alpha\xi_2 & -\alpha\xi_1 & 1 + \alpha^2(\xi_1^2 + \xi_2^2) \end{pmatrix}, \quad (16)$$

which describes the change in the material properties, only depends on the first two variables $\xi_1$ and $\xi_2$ [17–19]. This matrix may also conveniently be expressed in terms of twisted cylindrical coordinates:

$$\mathbf{R}(\varphi)\begin{pmatrix} 1 & 0 & 0 \\ 0 & 1 & -\rho\alpha \\ 0 & -\rho\alpha & 1+\rho^2\alpha^2 \end{pmatrix}\mathbf{R}(-\varphi) = \begin{pmatrix} 1 & 0 & \alpha\rho\sin(\varphi) \\ 0 & 1 & -\alpha\rho\cos(\varphi) \\ \alpha\rho\sin(\varphi) & -\alpha\rho\cos(\varphi) & 1+\rho^2\alpha^2 \end{pmatrix},$$

with $\varphi = 2\arctan\left(\frac{\xi_2}{\xi_1+\sqrt{\xi_1^2+\xi_2^2}}\right)$, $\rho = \sqrt{\xi_1^2+\xi_2^2}$.

It may be also interesting to consider leaky modes corresponding to complex propagation constants $\beta$ [5, 10]. A very efficient approach to compute the leaky modes is to introduce Perfectly Matched Layers (PML). Such regions have been introduced by Berenger [11] in the FDTD method. Nowadays, in the time harmonic case, the most natural way to introduce PML is to consider them as maps on a complex space [12] so that the corresponding change of (complex) coordinates leads to equivalent $\varepsilon$ and $\mu$ (that are complex (lossy), anisotropic, and inhomogeneous even if the original ones were real, isotropic, and homogeneous).

A remarkable property of the PML is that they provide the correct extension to non-Hermitian operators (since the associated $\mathbf{T}$ matrix is complex and symmetric) that allows the computation of the leaky modes in waveguides [13] and this may be obtained via a correct choice of the PML parameters, namely $R^*$, $R^{trunc}$ such that $R^* < \rho < R^{trunc}$, and the complex valued function of a real variable $s_\rho(\rho)$ (see Fig. 2 and Eq. 17) [10].

Helicoidal coordinates have thus been combined with PML to compute the leaky modes in twisted microstructured optical fibres [13]:

$$\mathbf{T}_{hPML} = \mathbf{R}(\varphi)\begin{pmatrix} \frac{\rho s_\rho}{\tilde{\rho}} & 0 & 0 \\ 0 & \frac{\tilde{\rho}}{\rho s_\rho} & -\alpha\frac{\tilde{\rho}}{s_\rho} \\ 0 & -\alpha\frac{\tilde{\rho}}{s_\rho} & \frac{\rho(1+\alpha^2\tilde{\rho}^2)}{\tilde{\rho}s_\rho} \end{pmatrix}\mathbf{R}(-\varphi). \tag{17}$$

This is the expression of the “twisted cylindrical PML tensor” in “helicoidal Cartesian modelling coordinates” $\xi_1, \xi_2$ and all the quantities involved in the previous expression can be given as explicit functions of these two variables, joining $s_\rho(\rho) = s_\rho(\sqrt{\xi_1^2+\xi_2^2})$ and $\tilde{\rho} = \int_0^{\sqrt{\xi_1^2+\xi_2^2}} s_\rho(\rho')d\rho'$ to the expressions for $\rho$ and $\varphi$ given here above. This is in fact the description of the “radial complex stretch”.

The fact that the equivalent materials are independent from the longitudinal coordinate $\xi_3$ allows a two-dimensional model for the determination of the propagation modes and of the leaky modes via a classical model provided it allows completely anisotropic and inhomogeneous media. Luckily, the finite element method (FEM) allows such a numerical computation.

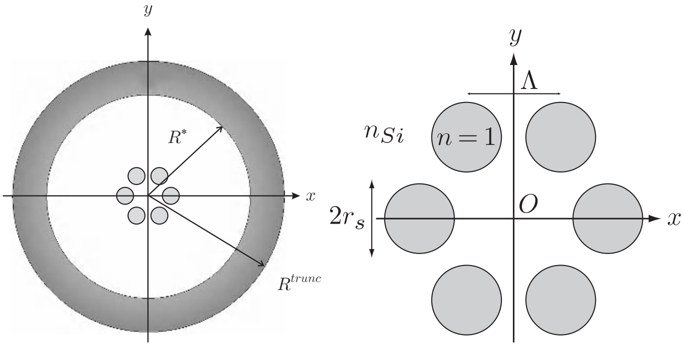


**Fig. 2** Cross section of a twisted six hole MOF structure together with the surrounding annulus used to set up the PML ($R^* = 30\,\mu\text{m}, R^{trunc} = 40\,\mu\text{m}$). On the right, a magnification of the hole structure with $\Lambda = 6.75\,\mu\text{m}$, $r_s = 2.5\,\mu\text{m}$, and $n_{\text{Si}} = 1.444024$.

As an illustrating example, we consider the hexagonal structure depicted in Fig. 2: this structure is a six hole microstructured optical fibre or MOF [5, 20–23] made up of a bulk of silica drilled by six air holes distant each other from $\Lambda = 6.75\,\mu\text{m}$. Each hole is circular with a radius equal to $r_s = 2.5\,\mu\text{m}$. A given wavelength $\lambda_0 = 1.55\,\mu\text{m}$ is considered for which the index of silica is about $\sqrt{\varepsilon_{\text{Si}}} = n_{\text{Si}} = 1.444024$. Note that for this structure no propagating mode can be found and the fundamental mode is a leaky mode. In order to check the validity of the FEM + PML combination for the leaky mode computation, the value of the complex propagating constant in the not twisted case is compared with the one obtained by using the multipole method. The philosophy of this latest method is completely different from the FEM + PML approach and the reader can refer to [5] for a comprehensive review of this method. The corresponding complex effective index, namely $n_{\text{eff}} = \beta/k_0$ for the two different methods is $1.4387741 + 4.3257457\,10^{-8}i$ for the multipole method and $1.43877448 + 4.325885\,10^{-8}i$ for the finite element method. The practical implementation of the finite element model has been performed with COMSOL Multiphysics® software using a mesh of about 16,800 second order triangular elements and the computation takes about 150 s on a Pentium M 1.86 GHz with 1Go memory laptop computer. Note that regarding its smallness with respect to the real part, the imaginary part is computed with an amazing accuracy: it is obtained with four figures though its value is smaller than the absolute error on the real part. The twisted problem is now considered to see how the fundamental leaky mode varies with respect to the torsion of the fibre. Still for the fundamental leaky mode and for a fixed $k_0$ corresponding to $\lambda_0 = 1.55\,\mu\text{m}$, two curves are plotted representing $\Re e\{\beta/k_0\}$ and $\Im m\{\beta/k_0\}$ (Fig. 3) versus $\alpha$, the parameter of torsion. It can be noticed that the relative influence of the torsion on the imaginary part is stronger than on the real part. The maximum torsion corresponds to $\alpha = 3{,}000\ \text{m}^{-1}$ so that the torsion length is $2\pi/\alpha = 2{,}090\ \mu\text{m}$ and taking into account the symmetry of the cross section, the period of the torsion is in fact $\pi/3\alpha = 349\ \mu\text{m}$. This

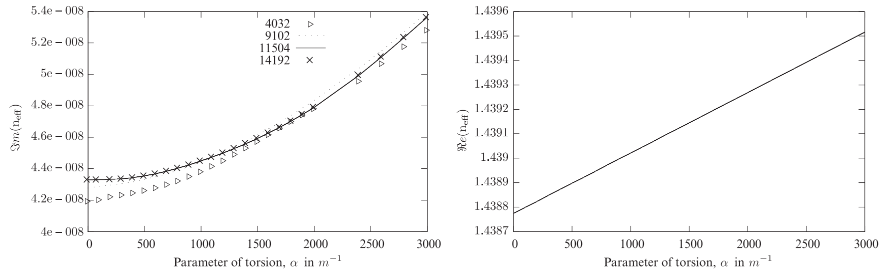


**Fig. 3** On the left, imaginary part of the effective index $n_{\rm eff} = \beta/k_0$ for the fundamental mode versus the parameter of torsion $\alpha$ ($\mathrm{m}^{-1}$) for various meshes. The results are good even for the coarser meshes ($\triangleright$ = 4,032 elements and the dotted line = 9,102 elements) and the discrepancy is unnoticeable between the curves for the finer meshes (the continuous line = 11,504 elements and $\times$ = 14,192 elements) indicating the mesh refinement is numerically convergent. On the right, real part of the effective index $n_{\rm eff} = \beta/k_0$ for the fundamental mode versus the parameter of torsion $\alpha$ ($\mathrm{m}^{-1}$).

maximum torsion is weak with respect to the wavelength and the size of the cross section pattern but strong with respect to the length of a real fibre.

This technique has been recently extended to alternative helicoidal coordinate systems with similar properties [24].

## 3 Cylindrical Cloaks of Arbitrary Cross Section

The geometrical transformations can also be used in the reverse sense to design new materials. In this case, a geometrical transformation is applied to free space to guess interesting material properties given by the equivalence rule. A new device can be built if the new material properties may be approximated, e.g. using electromagnetical metamaterials [25]. For instance, as proposed by Pendry [26, 28] a convex domain is mapped on a holey domain with the same exterior boundary. The structure made of the transformed equivalent material is an invisibility cloak and any object can be perfectly hidden in the central hole.

A quite more general situation is now considered here, where the shape of the cloak is no more circular and even possibly non convex but described by two arbitrary functions $R_1(\theta)$ and $R_2(\theta)$ giving an angle dependent distance from the origin corresponding respectively to the interior and exterior boundary of the cloak [29].

The geometric transformation which maps the field within the full domain $\rho \leq R_2(\theta)$ onto the hollow domain $R_1(\theta) \leq \rho \leq R_2(\theta)$ can be expressed as:

$$\rho'(\rho,\theta) = R_1(\theta) + \rho(R_2(\theta) - R_1(\theta))/R_2(\theta)\ ,\ 0 \leq \rho \leq R_2(\theta) \tag{18}$$

with also $\theta' = \theta\ ,\ 0 < \theta \leq 2\pi$ and $z' = z\ ,\ z \in \mathbb{R}$. Note that the transformation maps the field for $\rho \geq R_2(\theta)$ onto itself through the identity transformation. This leads to

$$\mathbf{J}_{\rho\rho'}(\rho',\theta') = \frac{\partial(\rho(\rho',\theta'),\theta,z)}{\partial(\rho',\theta',z')} = \begin{pmatrix} c_{11}(\theta') & c_{12}(\rho',\theta') & 0 \\ 0 & 1 & 0 \\ 0 & 0 & 1 \end{pmatrix}, \tag{19}$$

where

$$c_{11}(\theta') = R_2(\theta')/(R_2(\theta') - R_1(\theta')) \tag{20}$$

for $0 \le \rho' \le R_2(\theta')$ and $c_{11} = 1$ for $\rho' > R_2(\theta')$ and

$$c_{12}(\rho',\theta') = (\rho' - R_2(\theta'))R_2(\theta')\frac{dR_1(\theta')}{d\theta'} - \frac{(\rho' - R_1(\theta'))R_1(\theta')\frac{dR_2(\theta')}{d\theta'}}{(R_2(\theta') - R_1(\theta'))^2} \tag{21}$$

for $0 \le r' \le R_2(\theta')$, and $c_{12} = 0$ for $\rho' > R_2(\theta')$.

Finally, the properties of the cloak are given by:

$$\mathbf{T}^{-1} = \mathbf{R}(\theta')\begin{pmatrix} \frac{c_{12}^2 + f_\rho^2}{c_{11} f_\rho \rho'} & -\frac{c_{12}}{f_\rho} & 0 \\ -\frac{c_{12}}{f_\rho} & \frac{c_{11}\rho'}{f_\rho} & 0 \\ 0 & 0 & \frac{c_{11} f_\rho}{\rho'} \end{pmatrix}\mathbf{R}(\theta')^T, \tag{22}$$

with

$$f_\rho = \frac{(\rho' - R_1)R_2}{(R_2 - R_1)}.$$

The parametric representation of the ellipse $\rho(\theta) = \frac{ab}{\sqrt{a^2\cos(\theta)^2 + b^2\sin(\theta)^2}}$ corresponds to cloaks of elliptical cross section and it has been checked that it provides exactly the same result as in [29] where similar results have been obtained by a space dilatation.

To obtain general shapes, Fourier series

$$\rho(\theta) = a_0 + \sum_{k=1}^{n}(a_k\cos(k\theta) + b_k\sin(k\theta))$$

may be used. An example of such a general cloak is shown on Fig. 4: a source made of a wire of circular cross section (radius $= 0.25$) centered at point $\mathbf{r}_s = (2.5, 2)$ with a constant $E_z$ imposed on its boundary, radiating in a vacuum with wavelength $\lambda = 1$ (Note that all lengths are given in arbitrary units, micrometer for instance for near infrared). The electric field $E_z$ is therefore a cylindrical wave (Note that the electric field is given in arbitrary units, V/m for instance, and $E_z = J_0(2\pi 0.25) - iY_0(2\pi 0.25) = 0.472001 - i0.410004$ on the boundary of the source wire) and is not perturbed at all by a F-shaped scattering (lossy) obstacle of relative permittivity $1 + 4i$ placed near the origin $(0, 0)$ and surrounded by the cloak. Note also that the unbounded space is simulated via a circular PML. Figure 5 shows the corresponding analytical model.

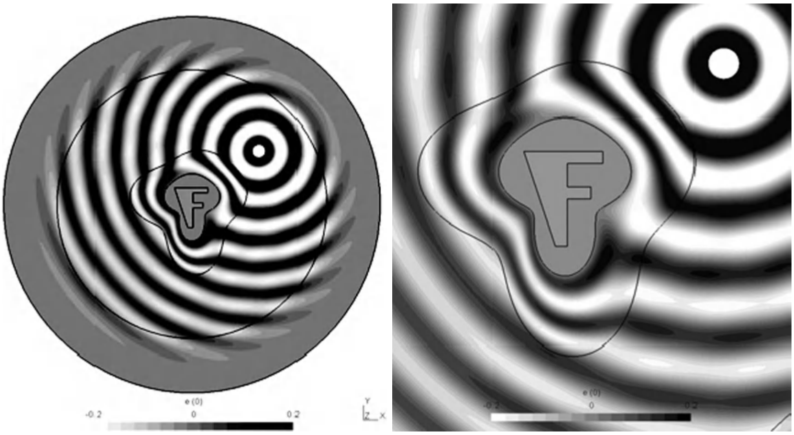

**Fig. 4** Cloak with a general shape given by Fourier series: $R_1(\theta)$ is with $a_0 = 1, b_1 = 0.1, a_2 = -0.15, b_3 = 0.2, a_4 = 0.1$, $R_2(\theta)$ is with $a_0 = 2, a_2 = -0.1, a_3 = -0.15, b_3 = 0.3, a_4 = 0.2$, all the other coefficients $= 0$. The real part of the electric field $E_z$ scattered by the cloak is represented here. Some residual interferences are due to numerical deviation mainly caused by the singular behavior of the equivalent material properties on the inner boundary of the cloak. Computation has been performed with GetDP [27].

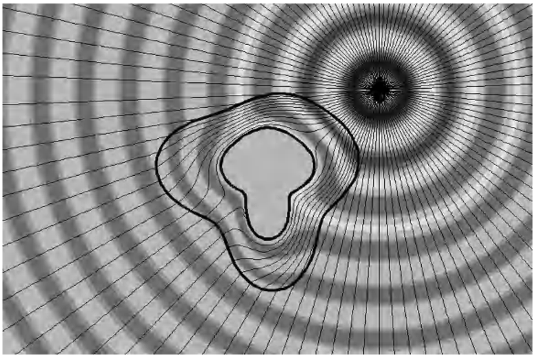

**Fig. 5** Analytical computation (with Mathematica®) of the field (and of associated rays) by directly applying the coordinate transformation to the source field: $E'_z(\rho', \theta') = E_z(\rho(\rho', \theta'), \theta = \theta'))$ with $\rho(\rho', \theta')$ obtained by inversion of the map defined by Eq. (18).

## *3.1 Three dimensional cloaks*

The three-dimensional cloaks may be determined following the same guidelines but using the spherical coordinates. For a spherical cloak, the Jacobian of the radial contraction is $\mathbf{J}_{\rho\rho'} = \mathbf{diag}(c_{11}, 1, 1)$ ($\rho$ is now the radius of a sphere). The total Jacobian is

$$\mathbf{R}(\theta)\mathbf{M}_2(\varphi)\mathbf{diag}(c_{11}, \rho/\rho', \rho/\rho')\mathbf{M}_2(\varphi)\mathbf{R}^T(\theta).$$

The matrix for the equivalent media is finally:

$$\mathbf{T}^{-1} = \mathbf{R}(\theta)\mathbf{M}_2(\varphi)\mathbf{diag}(\frac{\rho^2}{c_{11}\rho'^2}, c_{11}, c_{11})\mathbf{M}_2(\varphi)\mathbf{R}^T(\theta). \quad (23)$$

Three-dimensional arbitrary cloaks can be found by varying their interior and exterior radii with respect to the angular coordinates: $R_1(\theta,\varphi), R_2(\theta,\varphi)$.

## 4 Conclusion

The geometrical transformations may be viewed as a unifying point of view bridging several techniques in electromagnetism: treatment of unbounded domains and of twisted structures, design of invisibility cloaks... The cornerstone of the method is to remark that the Maxwell equations can be written in a covariant form such that all the metric properties are only involved in the material properties. The change of coordinates may therefore be encapsulated in exotic equivalent material properties, via the equivalence rule (1), and the rest of the computation is dealt with just as if rectangular Cartesian coordinates were used. Though this technique is completely general, the fact that the obtained material are usually anisotropic and inhomogeneous makes it of particular interest in the context of the finite element method where it provides very interesting models that do not require a modification of the existing code (if this one is general enough). It also provides a tool to design new electromagnetic devices such as the invisibility cloaks. It gives also an interpretation of negative refractive index materials together with a pictural view of the perfect lens that corresponds to a “folding” of the space [31–33]. Nevertheless, it should be emphasized that the space transformations that do not correspond to a diffeomorphism lead to material properties that are, if not impossible to obtain, at least challenging for the optical metamaterial science (even in a small frequency range). Thus far, experimental verification of invisibility cloaks was chiefly achieved for microwaves [34].

This work has been performed in the framework of the POEM project – ANR-06-NANO-008.

## References

1. Stratton, J.A.: Electromagnetic Theory. McGraw-Hill, New York (1941)
2. Bossavit, A.: Notions de géométrie differentielle pour l’étude des courants de Foucault et des méthodes numériques en Electromagnétisme. In: A. Bossavit, C. Emson, I. Mayergoyz (eds) Méthodes numériques en électromagnétisme, pp. 1–147. Eyrolles, Paris (1991) http://www.lgep.supelec.fr/mse/perso/ab/DGSNME.pdf.
3. Milton, G.W., Briane, M., Willis, J.R.: On the cloaking for elasticity and physical equations with a transformation invariant form. New J. Phys., **8**, 248, 1–20 (2006)

4. Nicolet, A., Zolla, F., Ould Agha, Y., Guenneau, S.: Geometrical transformations and equivalent materials in computational electromagnetism. COMPEL, **27**, 4, pp. 806–819 (2008)
5. Zolla, F. , Renversez, G., Nicolet, A., Khulmey, B., Guenneau, S., Felbacq, D.: Foundations of Photonic Crystal Fibres. Imperial College Press, London (2005)
6. Bossavit, A.: A rationale for 'edge-elements' in 3-D fields computations. IEEE Trans. Mag., **24**, 1, 74–79 (1998)
7. Dular, P., Hody, J.-Y., Nicolet, A., Genon, A., Legros, W.: Mixed finite elements associated with a collection of tetrahedra, hexahedra and prisms. IEEE Trans. Mag., **30**, 5, 2980–2983 (1994)
8. Dular, P., Nicolet, A., Genon, A., Legros, W.: A discrete sequence associated with mixed finite elements and its gauge condition for vector potentials. IEEE Trans. Mag., **31**, 3, 1356–1359 (1995)
9. Nicolet, A., Remacle, J.-F., Meys, B., Genon, A., Legros, W.: Transformation methods in computational electromagnetics. J. Appl. Phys. **75**, 10, 6036–6038 (1994)
10. Ould Agha, Y. ,Zolla, F., Nicolet, A., Guenneau, S.: On the use of PML for the computation of leaky modes: an application to microstructured optical fibres. COMPEL, **27**, 1, 95–109 (2008)
11. Berenger, J.-P.: A perfectly matched layer for the absorption of electromagnetic waves. J. Comput. Phys., **114**, 185–200 (1994)
12. Lassas, M., Somersalo, E., "Analysis of the PML equations in general convex geometry. Proc. Roy. Soc. Edinburgh, Sect. A. Math., **131**, 5, 1183–1207 (2001)
13. Nicolet, A., Zolla, F., Ould Agha, Y.,Guenneau, S.: Leaky modes in twisted microstructured optical fibres. Wave Complex Random Media, **17**, 4, 559–570 (2007) doi: 10.1080/17455030701481849.
14. Lewin, L., Ruehle, T.: Propagation in twisted square waveguide. IEEE Trans. MTT, **28**, 1, 44–48 (1980)
15. Yabe, H., Mushiake, Y.: An analysis of a hybrid-mode in a twisted rectangular waveguide. IEEE Trans. MTT, **32**, 1, 65–71 (1984)
16. Igarashi, H., Honma, T.: A finite element analysis of TE modes in twisted waveguides. IEEE Trans. Mag., **27**, 5, 4052–4055 (1991)
17. Nicolet, A., Zolla, F., Guenneau, S.: Modelling of twisted optical waveguides with edge elements. Eur. Phys. J. Appl. Phys., **28**, 153–157, (2004) doi: 10.1051/epjap:2004189.
18. Nicolet, A., Movchan, A.B., Guenneau, S., Zolla, F.: Asymptotic modelling of weakly twisted electrostatic problems. C. R. Mecanique, **334**, 2, 91–97 (2006)
19. Nicolet, A., Zolla, F.: Finite element analysis of helicoidal waveguides. IET Sci., Meas. Technol., **1**, 1, 67–70 (2007) doi: 10.1049/iet- smt:20060042.
20. Guenneau, S., Nicolet, A., Zolla, F., Geuzaine, C., Meys, B.: A finite element formulation for spectral problems in optical fibers. COMPEL, **20**, 1, 120–131 (2001)
21. Guenneau, S., Nicolet, A., Zolla, F., Lasquellec, S.: Modeling of photonic crystal optical fibers with finite elements. IEEE Trans. Mag., **38**, 2, 1261–1264 (2002)
22. Guenneau, S., Lasquellec, S., Nicolet, A., Zolla, F.: Design of photonic band gap optical fibers using finite elements. COMPEL, **21**, 4, 534–539 (2002)
23. Guenneau, S., Nicolet, A., Zolla, F., Lasquellec, S.: Theoretical and numerical study of photonic crystal fibers. Prog. Electromagn. Res., **41**, 271–305 (2003)
24. Shyroki, D. M.: Exact equivalent straight waveguide model for bent and twisted waveguides. IEEE Trans. MTT, **56**, 2, 414–419 (2008)
25. Ramakrishna, S.A.: Physics of negative refractive index materials. Rep. Prog. Phys., **68**, 2, 449–521 (2005)
26. Pendry, J.B., Shurig, D., Smith, D.R.: Controlling electromagnetic fields. Science **312**, 1780–1782 (2006)
27. Dular, P., Geuzaine, C., Henrotte F., Legros W.: A general environment for the treatment of discrete problems and its application to the finite element method. IEEE Trans. Mag., **34**, 5, 3395–3398 (1998) http://www.geuz.org/getdp/
28. Zolla, F., Guenneau, S., Nicolet, A., Pendry, J. B.: Electromagnetic analysis of cylindrical invisibility cloaks and the mirage effect. Opt. Lett., **32**, 9, 1069–1071 (2007)

29. Nicolet, A., Zolla, F., Guenneau, S.: Electromagnetic analysis of cylindrical cloaks of an arbitrary cross section. Opt. Lett., **33**, 14, 1584–1586 (2008)
30. Nicolet, A., Zolla, F., Guenneau, S.: Finite element analysis of cylindrical invisibility cloaks of elliptical cross section. IEEE Trans. Mag., **44**, 4, 1150–1153 (2008) doi: 10.1109/TMAG.2007.914865.
31. Leonhardt, U., Philbin, T. G.: General relativity in electrical engineering. New J. Phys. **8**, 10, 247 (2006) doi: 10.1088/1367-2630/8/10/247
32. Pendry, J.B., Smith, D.R.: Reversing light with negative refraction. Physics Today, **57**, 6, 37–43 (2004)
33. Schurig, D., Pendry, J. B., Smith, D.R.: Transformation-designed optical elements. Opt. Express, **15**, 22, 14772–14782 (2007)
34. Schurig, D., Mock, J.J., Justice, B.J., Cummer, S. A., Pendry, J.B., Starr, A.F., Smith, D.R.: Metamaterial electromagnetic cloak at microwave frequency Science, **314**, 5801, 977–980 (2006)

# Transformation and Moving Media: A Unified Approach Using Geometric Algebra

**Marco A. Ribeiro and Carlos R. Paiva**

Instituto de Telecomunicações and Department of Electrical and Computer Engineering, Instituto Superior Técnico
Av. Rovisco Pais 1, 1049-001 Lisboa, Portugal
marco.ribeiro@lx.it.pt

**Abstract** Using a previously derived framework that we have called the equivalence principle for electromagnetics, we analyze both transformation and moving media through a unified approach. Special emphasis is given to the application of this new method that uses the two geometric algebras defined over the tangent and cotangent bundles of space-time and is based on a technique that we have called the vacuum form reduction: the space-time constitutive relation of a class of bianisotropic media in a rigid metric is reduced, through this transformation, to a space-time constitutive relation which has the same form of vacuum and leads to a fictitious space-time with a flexible metric. As an example of transformation media we analyze an elliptic cloak with a drag effect. Negative refraction in moving media is the other example that we have chosen to illustrate the applicability of the general framework.

## 1 Introduction

Usually, to tackle a specific problem in electromagnetism, one has to adopt local coordinates. However, to uncover its intrinsic (or geometric) significance, we must check that it has the same meaning in all coordinate systems. That is why a coordinate-free approach may render the core physics easier to grasp by providing solutions in their greater generality. According to William Burke [1]: "The emphasis on the structures themselves rather than on their representations leads us naturally to use the coordinate-free language of modern mathematics." The evolution of Maxwell equations in the course of history [2] may reveal yet another important aspect: the use of a specific mathematical formalism is not a mere question of taste, elegance, conciseness or appropriateness – it is, above all, a question of intelligibility and insight, of being able to see further when the fog lifts, unmasking the inner structure that was hidden underneath archaic formalisms, thereby disclosing relationships that, otherwise, would remain obnubilated [3]. Quoting

S. Zouhdi et al. (eds.), *Metamaterials and Plasmonics: Fundamentals, Modelling, Applications*,

David Hestenes [4]: "The possibility that mathematical tools used today were invented to solve problems in the past and might not be well suited for current problems is never considered."

In a bare (or naked) four-dimensional manifold – one that carries neither a metric nor a connection – and using exterior differential forms, it is possible to build a metric-free approach to electrodynamics where the two Maxwell equations (homogeneous and inhomogeneous) are clearly separated from the metric structure of space-time [5]. This pre-metric electrodynamics, though not a complete framework, is able to accommodate a possible violation of Lorentz invariance. Furthermore, the two Maxwell equations are preserved by any diffeomorphism over the four-dimensional space-time: we can pull and stretch space-time, thereby modifying its metric, without any effect on the form of these two equations. Actually, only the constitutive relation, which characterizes the electromagnetic medium, will change. Through this apparently contrived mathematical construction, we are able to shed light on what we have called the equivalence principle for electromagnetics [6]: a given electromagnetic medium creates an effective geometry and a given geometry creates an effective medium. Hence, from this mathematical vantage point, the active transformations generated by metamaterials – appropriately called, in this context, transformation media and analyzed in [7, 8] – become crystal clear. This description of the interaction between a material medium and the electromagnetic field as a geometric effect has a simple physical explanation: according to Fermat's principle, light rays follow the stationary optical path in media – due either to a flexible metric (topological interpretation) or to a rigid metric filled with a metamaterial (materials interpretation). It is the fact that, in the topological interpretation, a space-time that corresponds to free space is permeated by a flexible (or curved) metric that resembles the kinematic aspects of general relativity [8].

The main goal of this paper is to show how the formalism presented in [6] can be used, as a unified approach, to handle two different problems of electromagnetism: transformation and moving media. Nevertheless, our «topological» interpretation is not identical to a flexible metric having a Euclidean three-dimensional space [7], or to a Minkowski four-dimensional space-time [8], as its background. Indeed our «topological» interpretation is, actually, a fictitious space-time – that we have called the *geometric* interpretation – and corresponds to an isotropic medium with a constant index of refraction [6]. Only when this isotropic medium reduces to vacuum, do we recover the topological interpretation considered in [8]. This new equivalence is made possible by what we have called a *vacuum form reduction* [6]: using Clifford's geometric algebras (either in the tangent or cotangent bundles of the space-time manifold) we were able to express, in that geometric interpretation, our constitutive space-time relation in a form that is equivalent to vacuum. One should stress that this form, although formally equivalent to vacuum (but not actually vacuum, in general), corresponds – in the materials interpretation – to a class of media that we have called *simple* media and constitutes a special class of bianisotropic media [6]. However, these simple media are not, necessarily, matched to free space as in [8].

Simple media are mathematically described in the usual form of constitutive relations for a bianisotropic medium as [6]

$$\mathrm{D} = \varepsilon_0\, \varepsilon(E) + \sqrt{\varepsilon_0 \mu_0}\; \xi(H), \quad \mathrm{B} = \mu_0\, \mu(H) + \sqrt{\varepsilon_0 \mu_0}\; \zeta(E). \tag{1}$$

The notation is the same as in [6]: we use italic fonts for forms defined over the cotangent bundle (e.g., $E$ and $H$) and regular fonts for vectors defined over the tangent bundle (e.g., $\mathrm{B}$ and $\mathrm{D}$). The parameters $\varepsilon$, $\xi$, $\mu$ and $\zeta$ are linear $h_\sigma$ – bundle maps which exhibit the following dependence on the space-time geometry:[1]

$$\begin{aligned} \varepsilon(E) &= -\frac{y}{y_0}\frac{\sqrt{-\mathrm{g}}}{g_{00}}\, g^{*}_{\perp}(E), \quad \xi(H) = \frac{1}{g_{00}}\,\mathrm{e}_{123} \llcorner \left(H \wedge g_{\perp}(\mathrm{e}_0)\right), \\ \mu(H) &= -\frac{y_0}{y}\frac{\sqrt{-\mathrm{g}}}{g_{00}}\, g^{*}_{\perp}(H), \quad \zeta(E) = -\frac{1}{g_{00}}\,\mathrm{e}_{123} \llcorner \left(E \wedge g_{\perp}(\mathrm{e}_0)\right). \end{aligned} \tag{2}$$

One should stress that our discussion is restricted to vector bundles, in which case the $h_\sigma$ – bundle maps reveal themselves in the simple form of linear functions between the tangent and dual spaces of $h_\sigma$. For more details about this mathematical framework we refer the reader to [6] and references therein.

To demonstrate the applicability of the theoretical framework described in [6], two different problems are worked out in some detail: (i) an elliptic cloaking, as an example of transformation media, with an additional drag effect; (ii) the occurrence of negative refraction in moving media.

Although counterposition and negative refraction are two distinct effects, we don't agree with the definition of negative refraction given in [9]: negative refraction concerns precisely the orientation of the refracted ray vector (i.e., the normalized time-averaged Poynting vector) [10]; the orientation of the refracted wave vector is irrelevant to whether or not the refraction is positive or negative (Willebrord Snel van Royen did not know Maxwell equations). Anyway, Byzantine quarrels about taxonomy should be dismissed when discussing actual physics – provided that the adopted nomenclature is disclosed from start.

[1] The space-time manifold $M$ has a $(1+3)$ – foliation characterized by a set of nonintersecting three-dimensional hypersurfaces $h_\sigma \subset M$ which are parameterized by a variable $\sigma$ with the dimensions of time [5].

## 2 Transformation Media According to Geometric Algebra

In this section we analyze transformation media [7] in the context of Clifford's geometric algebras through the hybrid mathematical framework introduced in [6]. The design of invisibility cloaking devices is addressed. Namely, we study elliptic cylinder shaped cloaks that have the ability to drag the electromagnetic field inside them. To assess the accuracy of this modeling, we also provide full wave numerical simulations.

### 2.1 Permeability and permittivity functions

As the medium to be designed is matched to free space and exhibits no magneto-electric coupling, we may write $g_{\perp}(\mathrm{e}_0)=0$, $g_{00}=-1$ and $y=y_0$. Hence, from (2) we get

$$\varepsilon=\mu=\left(\mathrm{g}^*\right)^{-\frac{1}{2}} g^* . \tag{3}$$

To simplify the notation we have dropped the subscript $\perp$ in $g^*$. One should stress that, in this context, $g^*$ is a three-dimensional metric and $\mathrm{g}^*$ its determinant.

To design an invisibility cloak, a simply connected manifold is required. However, elliptic cylinder coordinates are not appropriate due to singularities. In practice, it is more convenient to consider a single coordinate system $(u,v,z)$ whose transformation equations into orthogonal Cartesian coordinates are

$$x=u\cos v, \quad y=u\sqrt{1-e^2}\sin v, \quad z=z . \tag{4}$$

A careful examination of these expressions reveals that cylinders are in fact mapped into elliptic cylinders in a non-conformal way as one increases the eccentricity $e$ $(0\le e<1)$. The transformation $v\mapsto v+a$ in the present context corresponds to dragging rather than rotating. Nevertheless, one can always think of $v$ as the angle that is obtained by mapping the elliptic cylinders back into the cylinders again.

Let $\{\mathrm{e}^u,\mathrm{e}^v,\mathrm{e}^z\}$ and $\{\mathrm{e}_u,\mathrm{e}_v,\mathrm{e}_z\}$ be the bases for the tangent and dual spaces, respectively, which are related to each other through the orthonormal relations $e^a \rfloor e_b=\delta^a{}_b$ [2]. The transformation rules for vectors and co-vectors are easily derived from (4) and accordingly free space is characterized in the $(u,v,z)$ frame by the optical metric function

$$g^*\left(\mathrm{e}^u\right)=\alpha\,\mathrm{e}_u+\frac{\eta}{u}\,\mathrm{e}_v,\quad g^*\left(\mathrm{e}^v\right)=\frac{\eta}{u}\,\mathrm{e}_u+\frac{\beta}{u^2}\mathrm{e}_v,\quad g^*\left(\mathrm{e}^z\right)=\mathrm{e}_z, \tag{5}$$

where $\alpha$ , $\beta$ and $\eta$ are normalized metric coefficients given by

$$\alpha=1+\frac{e^2}{1-e^2}\sin^2 v,\quad \beta=1+\frac{e^2}{1-e^2}\cos^2 v,\quad \eta=\frac{e^2}{1-e^2}\cos v\sin v. \tag{6}$$

The desired transformation effect is obtained by compressing $\left(u\mapsto f(u)\right)$ and dragging $\left(v\mapsto v+h(u)\right)$ the $(u,v,z)$ coordinate system. One should note however that, in our simplified model, $f$ and $h$ are differentiable functions that do not depend on $v$. As a consequence, points with the same value of $u$ will be compressed and dragged by equal amounts. To determine the optic metric in transformed space it is worthwhile to define the auxiliary functions

$$\chi(u)=f^{-1}(u)\cdot f'\circ f^{-1}(u),\quad \phi(u)=f^{-1}(u)\cdot h'\circ f^{-1}(u). \tag{7}$$

Furthermore, (5) transforms into

$$\begin{aligned} g^*\left(\mathrm{e}^u\right)&=\frac{\chi(u)}{\left(f^{-1}(u)\right)^2}\left[\alpha\,\chi(u)\,\mathrm{e}_u+\left(\alpha\,\phi(u)+\eta\right)\mathrm{e}_v\right],\quad g^*\left(\mathrm{e}^z\right)=\mathrm{e}_z,\\ g^*\left(\mathrm{e}^v\right)&=\frac{\chi(u)}{\left(f^{-1}(u)\right)^2}\left[\left(\alpha\,\phi(u)+\eta\right)\mathrm{e}_u+\frac{\alpha\,\phi^2(u)+2\eta\,\phi(u)+\beta}{u\,\chi(u)}\mathrm{e}_v\right], \end{aligned} \tag{8}$$

where the metric coefficients $\alpha$ , $\beta$ and $\eta$ are determined as before but taking into account that $v\mapsto v-h\circ f^{-1}(u)$.

Introducing the unit pseudoscalars $\mathrm{e}^{123}=\mathrm{e}^1\wedge\mathrm{e}^2\wedge\mathrm{e}^3$ and $\mathrm{e}_{123}=\mathrm{e}_1\wedge\mathrm{e}_2\wedge\mathrm{e}_3$, where $(\mathrm{e}_1,\mathrm{e}_2,\mathrm{e}_3)$ and $\left(\mathrm{e}^1,\mathrm{e}^2,\mathrm{e}^3\right)$ are arbitrary orthonormal bases of the tangent and dual spaces, we define the determinants of $g$ and $g^*$ as

$$g\left(\mathrm{e}_{123}\right)=\mathrm{g}\,\mathrm{e}^{123},\quad g^*\left(\mathrm{e}^{123}\right)=\mathrm{g}^*\,\mathrm{e}_{123}. \tag{9}$$

These expressions are compact and intuitive when compared to the usual matrix definitions. For example, as $g^*\circ g=\mathrm{id}$, then according to (9), $\mathrm{g}^*=\mathrm{g}^{-1}$. This is a clear example of how functions in geometric algebra can be clearer then tensors. In fact, we have made use of this result in (3).

The pseudoscalar of any geometric algebra is unique up to scaling. Also, as $g^*$ is an outer-morphism, then from (9) we get

$$g^*\left(\mathrm{e}^{uvz}\right) = \frac{\mathrm{g}^*}{u^2\left(1-e^2\right)}\mathrm{e}_{uvz} \quad \Rightarrow \quad \left(g^*\right)^{-\frac{1}{2}} = \frac{1}{u}\frac{\left(f^{-1}(u)\right)^2}{\chi(u)}. \tag{10}$$

However, we are dealing with active transformations. Hence, when computing the equation to the left side of the arrow in (10), we have used (5) whereas the rest of the derivation was computed in the transformed space. With explicit expressions for the metric function and its determinant (8) and (10) can be used to derive the medium parameters directly from (3):

$$\begin{aligned}
\varepsilon\left(\mathrm{e}^u\right) &= \mu\left(\mathrm{e}^u\right) = \alpha\frac{\chi(u)}{u}\mathrm{e}_u + \frac{\alpha\,\phi(u)+\eta}{u}\mathrm{e}_v, \\
\varepsilon\left(\mathrm{e}^v\right) &= \mu\left(\mathrm{e}^v\right) = \frac{\alpha\,\phi(u)+\eta}{u}\mathrm{e}_u + \frac{\alpha\,\phi^2(u)+2\eta\,\phi(u)+\beta}{u\,\chi(u)}\mathrm{e}_v, \\
\varepsilon\left(\mathrm{e}^z\right) &= \mu\left(\mathrm{e}^z\right) = \frac{1}{u}\frac{\left(f^{-1}(u)\right)^2}{\chi(u)}\mathrm{e}_z.
\end{aligned} \tag{11}$$

## 2.2 *Full-wave numerical simulation*

Next we present the results of full-wave numerical simulations to assess the accuracy of our geometric modeling. Our results demonstrate the effect of elliptic cloaking devices which are capable of dragging the electromagnetic field inside them. The materials are characterized by the profile functions

$$f(u) = \frac{u_2 - u_1}{u_2}u + u_1, \quad h(u) = \frac{u_2 - u}{u_2}\theta_0, \quad 0 < u < u_2, \tag{12}$$

according to which an object placed inside region $u < u_1$ will not be seen from the outside ($u > u_2$). The cloaking material in between creates, at the same time, the desired drag effect (the amount of which is controlled by the drag coefficient $\theta_0$).

The corresponding permeability and permittivity functions are easily determined from (11). However, they are too long to be included here. They are obtained taking into account that $v \mapsto v - \theta_0\left(u_2 - u\right)/\left(u_2 - u_1\right)$ and

$$f^{-1}(u) = u_2 \frac{u - u_1}{u_2 - u_1}, \quad \chi(u) = u - u_1, \quad \phi(u) = -\frac{\theta_0 f^{-1}(u)}{u_2}. \tag{13}$$

In Fig. 1a we show how the total magnetic field is affected when a 2 GHz TM time-harmonic uniform plane wave (traveling from left to right) strikes an elliptically shaped ( $e = 0.7$ ) perfect magnetic conductor (PMC) with semi-major axis 0.1 m.

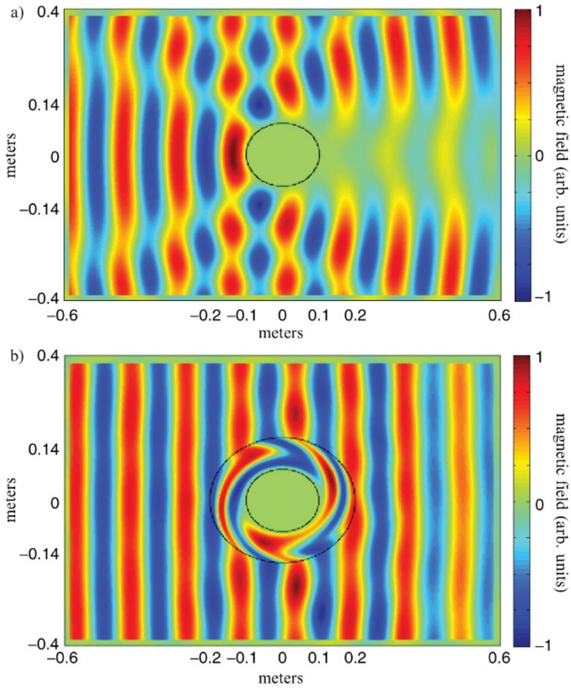


**Fig. 1** The magnetic field distribution obtained from simulations of a 2 GHz TM time-harmonic uniform plane wave striking a PMC with the shape of an elliptic cylinder ( $e = 0.7$ ) with semi-major axis $0.1\,\mathrm{m}$ : (**a**) without cloaking material; (**b**) with cloaking material ( $\theta_0 = -\pi/2$ ). The cloaking occupies the region $0.1\,\mathrm{m} < u < 0.2\,\mathrm{m}$.

When we enclose the PMC with the cloaking material we obtain the results shown in Fig. 1b. Apart from invisibility the extra drag effect can be observed, thus showing the flexibility of this geometric approach. The simulations have been preformed using the FDTD method with a rectangular grid of 1.2 m (eight wavelengths) by 0.8 m (2.67 wavelengths). We have used material average optimization (nine subcells) in order to reduce the effect of abrupt transitions. An incremental step of $\Delta = 125\ \mu\mathrm{m}$ was adopted. The domain was bounded with PMLs to reduce scattering into the simulation domain.

## 3 Optics of Moving Media

In this section we address a classic topic in electromagnetic theory: ray propagation in moving media. We show how negative refraction, in this context, can be easily analyzed using our mathematical framework.

### *3.1 The optical metric of a moving medium*

Let $\eta$ be the metric function of Minkowski space-time $M$ given by

$$\eta(\mathrm{e}_0) = \mathrm{e}^0, \quad \eta(\mathrm{e}_i) = -\,\mathrm{e}^i, \quad i = 1, 2, 3, \tag{14}$$

where $\{\mathrm{e}_0, \mathrm{e}_1, \mathrm{e}_2, \mathrm{e}_3\}$ and $\{\mathrm{e}^0, \mathrm{e}^1, \mathrm{e}^2, \mathrm{e}^3\}$ are bases for the tangent and dual spaces of $M$ respectively. The metric of Minkowski space-time is also the optic metric of free space: $g = \eta$ and $y = y_0$ in (2). Likewise, the optic metric of an isotropic medium, with index of refraction $n$, is

$$\overline{g} = \eta_{\parallel} + n^2 \eta_{\perp}, \tag{15}$$

where $\eta_{\parallel} = (\eta \llcorner \mathrm{e}_0) \wedge \mathrm{e}^0$ and $\eta_{\perp} = (\eta \wedge \mathrm{e}^0) \llcorner \mathrm{e}_0$ are, respectively, the parallel and perpendicular components of $\eta$ to $\mathrm{e}^0$.

A moving medium that is isotropic in its rest frame has an optical metric $g$ which is obtained from a boost of $\overline{g}$. Let us consider that the medium has a normalized velocity $\vec{\beta} = \beta\, \hat{\mathrm{v}}$. Then, introducing the rotor $\mathrm{R} = \exp(\rho\, \hat{\mathrm{v}}\, \mathrm{e}_0 / 2)$, with $\rho = \tanh^{-1}(\beta)$, we may write

$$L(\mathrm{a}) = \mathrm{R}\,\mathrm{a}\,\tilde{\mathrm{R}}, \quad L^{-1}(\mathrm{a}) = \tilde{L}(\mathrm{a}) = \tilde{\mathrm{R}}\,\mathrm{a}\,\mathrm{R}, \quad L^* = \eta L, \tag{16}$$

where $L$ is the boost function, $L^*$ its dual, $L^{-1}$ its inverse and $\mathrm{a} \in TM$ is an arbitrary 4-vector. But then

$$g = L^* \overline{g}\, L^{-1}. \tag{17}$$

We can separate (17) into parallel and perpendicular components, $g = g_{\parallel} + g_{\perp}$, as in (15). Using (15)–(17) together with the rules introduced in [6], we get

$$g_{\parallel}(\mathrm{a}) = \xi(\beta)\eta_{\parallel}(\mathrm{a}) + \xi\left(\eta_{\perp}(\mathrm{a})\middle|\vec{\beta}\right)\mathrm{e}^{0},$$
$$g_{\perp}(\mathrm{a}) = n^{2}\,\eta_{\perp}(\mathrm{a}) + \xi\left(\eta_{\parallel}(\mathrm{a})\middle|\mathrm{e}_{0} + \eta_{\perp}(\mathrm{a})\middle|\vec{\beta}\right)\eta_{\perp}(\vec{\beta}), \tag{18}$$

where $\xi(\beta) = \gamma^{2}\left(1 - n^{2}\beta^{2}\right)$, $\xi = \xi(1)$ and $\gamma = \left(1 - \beta^{2}\right)^{-1/2}$.

## 3.2 Negative refraction in moving media

To address negative refraction in moving media we analyze the problem shown in Fig. 2. This figure shows a plane boundary surface separating two homogeneous isotropic media with indices of refraction $n_1$ and $n_2$. The upper half-space is moving with normalized velocity $\beta$ as seen in rest frame of the lower half-space. One should read this figure in following way (geometric interpretation): the plane boundary separates two half-spaces filled with two different fictitious homogeneous space-times characterized by $g_1(n_1, \beta_1 = 0)$ and $g_2(n_2, \beta_2 = \beta)$. It is the abrupt change in the metric at the interface that is responsible for the deflection of the ray in refraction.

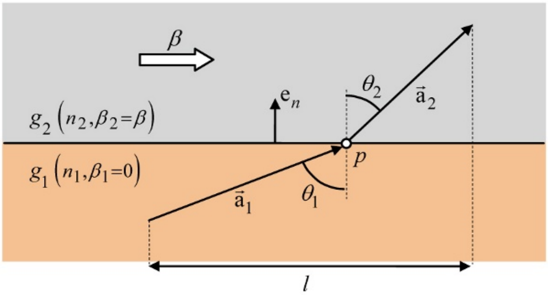


**Fig. 2** The interface between two fictitious space-times: the upper half region (with metric $g_2$) corresponds to a moving medium with normalized velocity $\beta$.

Let us define, in each half-space ($k = 1,2$), 4-vectors $\mathrm{a}_k = a_{0k}\,\mathrm{e}_0 + \vec{\mathrm{a}}_k$ such that $\vec{\mathrm{a}}_k$ are three-dimensional (relative) vectors pointing in the ray direction. Furthermore, $a_{0k} = ct_k$ ($c$ is the speed of light in vacuum). In fictitious space-time, $\mathrm{a}_k$ ($k = 1,2$) are null vectors. The corresponding quadratic forms can be solved to obtain $a_{0k}$ in terms of $g_k$ and $\vec{\mathrm{a}}_k$ as follows

$$g_k(\mathrm{a}_k)\big|\mathrm{a}_k = 0 \quad \Rightarrow \quad a_{0k} = \frac{-g_k(\mathrm{e}_0)\big|\vec{\mathrm{a}}_k \pm \sqrt{g_k(\mathrm{e}_0 \wedge \vec{\mathrm{a}}_k)\big|(\mathrm{e}_0 \wedge \vec{\mathrm{a}}_k)}}{g_k(\mathrm{e}_0)\big|\mathrm{e}_0}. \tag{19}$$

In general, if half-space $k$ represents a medium in Minkowski space-time moving parallel to the interface with a normalized velocity $\beta_k$, then from (17) or (18) we get

$$\begin{aligned} &g_k\left(\mathrm{e}_0\right)\middle|\mathrm{e}_0=\gamma_k^2\left(1-n_k^2\beta_k^2\right), \quad g_k\left(\mathrm{e}_0\right)\middle|\vec{\mathrm{a}}_k=a_k\,\gamma_k^2\,\beta_k\left(n_k^2-1\right)\sin\theta_k, \\ &\sqrt{g_k\left(\mathrm{e}_0\wedge\vec{\mathrm{a}}_k\right)\middle|\left(\mathrm{e}_0\wedge\vec{\mathrm{a}}_k\right)}=a_k\,\gamma_k^3\,n_k\sqrt{\left(1-\beta_k^2\right)\sin^2\theta_k+\left(1-n_k^2\beta_k^2\right)\cos^2\theta_k}. \end{aligned} \tag{20}$$

If Fig. 2 we have to find the stationary point, with respect to variations of the angle $\theta_1$, subject to the additional constraint $a_1\sin\theta_1+a_2\sin\theta_2=l$:

$$\left(\partial/\partial\theta_1\right)\left(a_{01}+a_{02}\right)=0\,. \tag{21}$$

For $\beta_1=0$ and $\beta_2=\beta$, which is the situation in Fig. 2, and from (19)–(21) we then obtain

$$\sin\theta_2=\pm\sqrt{\frac{1-\beta^2\xi_2}{m^2-\beta^2\xi_2}}, \quad m=\frac{n_2}{n_1\left(1-\beta^2\xi_2\right)\sin\theta_1+\beta\xi_2}, \tag{22}$$

where $\xi_2=\gamma^2\left(1-n_2^2\beta^2\right)$. Equation (22) is Snell's law for the refraction of light into a moving medium derived from the geometric interpretation in fictitious space-time. As the power is dragged towards the direction of motion in a moving medium one should take the positive sign for $\beta>\beta_n$ and the negative otherwise. We have introduced $\beta_n$ as the normalized velocity for negative refraction:

$$\beta_n=\frac{\left(n_2^2-1\right)-\sqrt{\left(n_2^2-1\right)^2+\left(2n_1n_2\sin\theta_1\right)^2}}{2n_1n_2^2\sin\theta_1}\le 0\,. \tag{23}$$

In Fig. 3, with $n_1=1.3$ and $n_2=1.4$, the transmitted angle is shown as a function of the normalized velocity $\beta$. Negative refraction takes place for $\beta<\beta_n$ and occurs even for small values of $\beta$. When $\theta_1>\sin^{-1}\left(1/n_1\right)$ and for $\beta_-\le\beta\le\beta_+$ the ray is totally reflected (see the curve $\theta_1=3\pi/8$ in Fig. 3), where

$$\beta_\pm=\frac{n_1\sin\theta_1\pm n_2}{1\pm n_1n_2\sin\theta_1}. \tag{24}$$

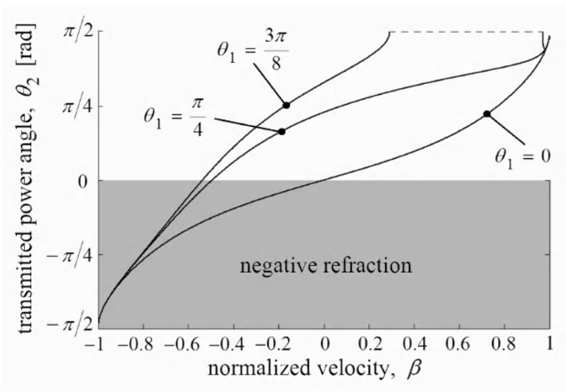


**Fig. 3** Negative refraction in moving media. The transmitted angle $\theta_2$ as a function of $\beta$ for different values of the incident angle.

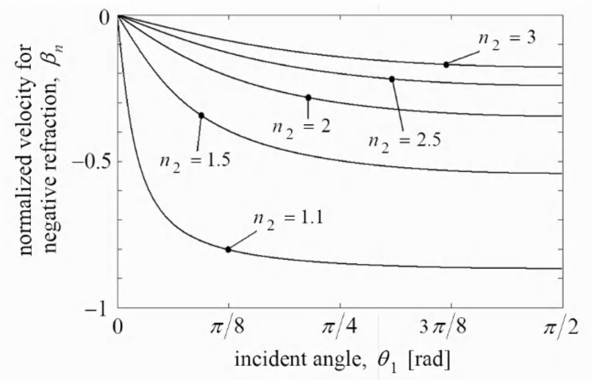


**Fig. 4** The minimum velocity to observe negative refraction as a function of the incident angle for $n_1 = 2$ and several values of $n_2$.

Fig. 4 reveals that negative refraction takes place for relatively small values of $|\beta|$ when $n_2$ increases.

# 4 Conclusions

Transformation and moving media were analyzed through the unifying perspective provided by the equivalence principle for electromagnetics previously presented in [6]. As an example of transformation media, an elliptic cloaking with a drag effect was analyzed. Full wave numerical simulations, to assess the accuracy, have confirmed the approach. Negative refraction in moving media was also analyzed as another example of application. These two different problems of classical electrodynamics should provide enough evidence to convince the skeptical reader, probably bemused by such an abstract framework, that – although this approach cannot be considered the most appropriate formalism for every problem in electromagnetics – it is certainly a new theoretical tool worth considering by researchers when dealing with specific problems such as those two analyzed herein. However, the fertility of the method cannot be reduced to those two problems: the class of simple media, corresponding to what we have called a fictitious space-time, provides enough generality to tackle a wide range of problems, namely those related to a new and active research area – the electromagnetics of metamaterials.

**Acknowledgments** This work was partially funded by FCT (Fundação para a Ciência e a Tecnologia), Portugal.

## References

1. Burke, W.L.: Applied Differential Geometry, p. xii. Cambridge University Press, Cambridge (1985)
2. Lindell, I.V.: Differential Forms in Electromagnetics, pp. 1–5. IEEE/Wiley, Piscataway, NJ (2004)
3. Thirring, W.: Classical Mathematical Physics – Dynamical Systems and Field Theories, 3rd ed., pp. 312–328. Springer, New York (1997)
4. Hestenes, D.: Oersted Medal Lecture 2002: Reforming the mathematical language of physics. Am. J. Phys. **71**, 104–121 (2003)
5. Hehl F.W., Obukhov, Yu. N.: Foundations of Classical Electrodynamics. Birkhäuser, Boston, MA (2003)
6. Ribeiro, M.A., Paiva, C.R.: An equivalence principle for electromagnetics through Clifford's geometric algebras. Metamaterials (2008), doi: 10.1016/j.metmat.2008.03.002
7. Schurig, D., Pendry, J.B., Smith, D.R.: Calculation of material properties and ray tracing in transformation media. Opt. Express **14**, 9794–9804 (2006)
8. Leonhardt, U., Philbin, T.G.: General relativity in electrical engineering. New J. Phys. **8**, 247 (2006)
9. Mackay, T.G., Lakhtakia, A.: Counterposition and negative refraction due to uniform motion. Microwave Opt. Technol. Lett. **49**, 874–876 (2007)
10. Grzegorczyk, T.M., Kong, J.A.: Electrodynamics of moving media inducing positive and negative refraction. Phys. Rev. B **74**, 033102 (2006)

# Homogenization of Split-Ring Arrays, Seen as the Exploitation of Translational Symmetry

**Alain Bossavit**

LGEP (CNRS, Univ. Paris Sud), 11 Rue Joliot-Curie, 91192 Gif-sur-Yvette, France
bossavit@lgep.supelec.fr

**Abstract** Homogenization, which reduces the cost of numerical simulations in materials with repetitive structure, is a promising approach to the design of metamaterials. This cost reduction stems from the possibility to compute effective permeability and permittivity of an equivalent homogenized material by solving an auxiliary "cell problem" on the generating cell of the metamaterial. The first part of this paper is a tutorial, where the procedure is described in the context of the exploitation of symmetry via harmonic analysis, and justified by an appropriate asymptotic result when the size of the cell is small enough. The second part argues that this standard approach can fail, and explains how it does, when a second small parameter, besides the cell's size, is present in the physical situation. This is precisely what happens in the case of an array of split rings, where the slit's width competes, so to speak, with the cell's size in the passage to the limit that leads to the cell problem. We show how this competition must be arbitrated in order to recover the negative effective permeability one may expect, on physical grounds, near some resonant frequency, in the case of a split-rings array. A simplified model, amenable to analytical computation, illustrates this "frequency dependent homogenization" procedure.

## 1 Introduction

When a regular, crystal-like, array of small split rings (Fig. 1, left) is immersed in an AC magnetic field, the metamaterial thus obtained can behave in surprising ways [1]. For instance, the spatial average B of magnetic induction b (at a large enough scale with respect to the size of the "cell" C of Fig. 1), and the spatial average P of the reactive power inside the material relate by $P = i\omega\,(\nu_{eff}\,B)^* \cdot B$ (that is to say, $P = i\omega H^* \cdot B$, if one sets $H = \nu_{eff} B$), with an effective reluctivity $\nu_{eff}$ that is not only anisotropic (i.e., a tensor), and complex-valued (because of inevitable Joule losses), but can exhibit a *negative* real part in some directions (here, vertically) in some narrow window $[\omega_1, \omega_2]$ of angular frequencies. This is due to an "internal resonance" when $LC \sim \omega^{-2}$, where L is the ring inductance and C the slit capacitance. All it takes is a near-perfect conductor (or dielectric), in order to have $e \sim 0$ in the ring. Then, by Faraday's law, a displacement current

S. Zouhdi et al. (eds.), *Metamaterials and Plasmonics: Fundamentals, Modelling, Applications*,

must cross the slit, hence a large electric field there, whose average energy can offset the cell's magnetic energy if $\omega$ is slightly above the resonant frequency.

Our objective is to define a so-called "cell problem", a boundary value problem whose equations are those of Maxwell, but set on C only instead of being set on the entire space, which once solved would provide $\nu_{\text{eff}}$, or its inverse $\mu_{\text{eff}}$, and also (though we shall not go into this in detail) the analogous effective permittivity $\varepsilon_{\text{eff}}$. From this point on, one would be free to solve the macroscopic problem at hand (with a specific shape for the metamaterial-filled region(s), specific source currents, etc.) by using the effective coefficients only, ignoring the microstructure that has already been dealt with when solving the cell problem(s). This will allow a cheaper numerical simulation (by allowing the use of much coarser finite element nets, for instance), and perhaps more importantly, serve in *designing* metamaterials by repetitively solving the cell problem inside some iterative procedure which makes the cell's structure evolve towards some optimal one.

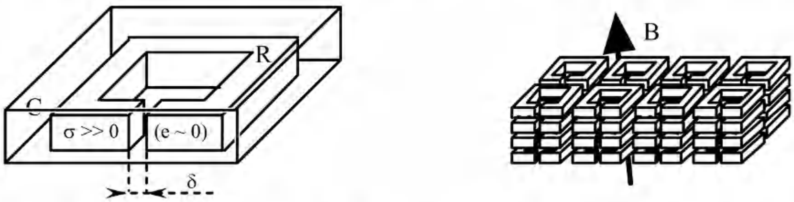


**Fig. 1** A "split ring" R in its symmetry cell C (*left*), and a stack of such cells, making a metamaterial (*right*). An oversimplistic design, as such materials go, but enough to demonstrate our frequency-dependent homogenization technique. Later, the thin slit of width $\delta$ is replaced by a surface $\Sigma$, and the air region $C - (R \cup \Sigma)$ is denoted A.

This procedure – solve a micro-scale cell problem, or several, then address a macro-scale problem where all materials are homogeneous, with effective co-efficients as found – is called *homogenization* [2]. As an approximation technique (which it is: one replaces the original problem by a different one, deemed close to it), it requires a justification, that only some appropriate convergence theorem can provide. This is our main concern in this work. But let it be clear that *which* theorem to prove (a matter of asking the right question, that is, an act in *modelling*), is more important here than *proving* it, a technical matter.

The first part of the paper is devoted to this proof, which we shall be able to keep simpler than in other approaches to homogenization (such as matched asymptotic expansions [2], or Gamma-convergence [3]) by assuming *linearity* of the constitutive laws. This allows one to use standard harmonic analysis mechanisms such as (spatial) Fourier transform and Floquet–Bloch decomposition [4], whose relatively involved interrelations provide the gist of the proof technique. Shortly said, one designs a family of *virtual* problems $P^\alpha$, in which the *actual*, physical one is embedded (we make it correspond to $\alpha = 1$), and one proves convergence, in some weak sense, of the solution $u^\alpha$ of $P^\alpha$ to the solution $u^0$ of some limit problem $P^0$, an inspection of which exposes the cell problem.

When $\alpha$ models the cell size, $P^0$ can be shown to correspond to a homogeneous medium, which can then be substituted for the periodic array if $u^1$ (the actual solution) and $u^0$ are close enough, which one may usually assume for small-grained arrays.

But this very assumption must be questioned in the case of metamaterials, as we shall see. It remains possible to embed the real problem $P^1$ in a (different) family $\underline{P}^\alpha$ of virtual ones, and to ensure the closeness between $u^1$ and $\underline{u}^0$, but for this one must account for the relation that must exist, at the intended working frequency, between cell's size and slit's width for the internal resonance to occur. Hence the introduction in the asymptotic analysis of a second small parameter, that must be linked with the cell's size in a way we shall discover, thus making the $\underline{P}^\alpha$ family – and the cell problem derived from its limit $\underline{P}^0$ – different from the $P^\alpha$ and $P^0$, and the corresponding cell problem, that fit a low-frequency situation. A convergence result still holds, and can be proven by similar means, but the final result – effective coefficients, and how they depend on $\omega$ – is radically different. These modelling issues make the second part of the paper.

The organization is as follows: Section 2, recalling elements of harmonic analysis on groups [5], shows how the use of both spatial Fourier transform and Bloch–Floquet transform pertains to the exploitation of symmetry (translational symmetry, complete or partial) and explains their shared features by this commonality. Section 3 addresses their differences and how they relate nonetheless, suggesting that Fourier analysis is a limit case of Floquet–Bloch, as obtained when the size of the symmetry cell tends to 0. Section 4 uses this to establish the main convergence result about homogenization in magnetostatics. In Section 5, the same kind of result is obtained for the full Maxwell system (in steady-state regime at angular frequency $\omega$), but is found, though correct, inadequate as regards modelling. Section 6 solves the conundrum this raises in the case of the split-ring metamaterial by introducing a second parameter, besides the cell's size, in the analysis, namely the slit's width. A summing-up discussion of such "two small-parameter" problems makes Section 7.

About notation: We shall distinguish *vectors*, elements of the 3D vector space $V_3$, and *points*, elements of the associated affine space, denoted $A_3$. If x is a point and v a vector, x + v denotes a point, the *translate* of x by v. This way, $V_3$ is an additive group, which thus *acts* on $A_3$ "by translations". (Italics, when not used for emphasis, signal that some implicit definition is being given, or suggested, as it is the case here.) $L^2(M)$ denotes the Hilbert space of square-integrable functions over the measure space M. Complex conjugation is indicated by a star.

## 2 Harmonic Analysis and the Exploitation of Symmetry

Homogenization is the exploitation of symmetry, namely translational symmetry of the crystal-like structure, taking account of the smallness of the symmetry cell.

These are two distinct issues. The present Section addresses the first one of these, leaving smallness of the cell to be considered later in Section 3.

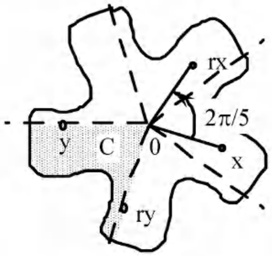


**Fig. 2** Domain D with fivefold symmetry, generated by rotations $r^k$ of the symmetry cell C. Note how r relates pairs of "new boundary" points, like here y and ry.

Let us begin with a case of rotational symmetry (Fig. 2), where the number of symmetry operations is finite, before moving to translational symmetry, where the group of symmetry operations is infinite (which will raise technical, if not essential, difficulties). In domain D with n–fold rotational symmetry (n = 5 here), one wishes to solve the problem $-\mathrm{div}(\mu \text{ grad } \varphi) = q$, for a given magnetic charge q, with $\varphi = 0$ on $\partial D$. We shall call this "problem P". (Charge q is fictitious, physically. The source of the field is rather a current density, or a magnetization. But there is always an equivalent charge, then, which is the one we deal with.) Let r denote the $2\pi/n$ rotation around the axis, rx the rotated image of a point x, note that rD = D, and that there is a "symmetry cell" C (which can be carved out in many different ways) such that D be the union, with minimum overlap, of its transforms $r^k C$, k = 0 to 4. Assume that $\mu(rx) = \mu(x)$ for all x (apart, possibly, from those of some zero-measure set: we shall gloss over this, which raises no difficulty). These identities also hold for all elements $g = r^k$, k = 0 to 4, of the group G generated by r. We shall use these peculiarities to replace problem P by five problems $P_k$, independent, all set on C instead of D (which makes each $P_k$ "simpler" than P, in an obvious way), each with its own set of boundary conditions on the "new boundary" $\partial C - \partial D$. The trade-off (five "small" problems instead of a single "big" one), is obviously favorable in the case of, e.g., finite element computations. The method requires the following machinery. (See [6] for further details, and for how this transposes to discrete formulations, using finite elements.)

One calls *characters* of G the complex-valued functions $\chi$ such that $\chi(gh) = \chi(g)\chi(h)$ for all g, h in G and $\chi(id) = 1$ for the identity transform. Since $r^5$ is the identity, this implies, as easily verified, that there are five characters $\chi_k$, for integers k from 0 to 4, fully determined by $\chi_k(r) = \exp(2i\pi k/5)$. Note that $\chi_j \chi_k = \chi_{j+k}$, if one counts j + k modulo 5, so that characters form themselves a group $\Gamma$, called the *dual* of G. (The dual of $\Gamma$ is of course G.) Given a function $\varphi$, denote by $U_g\varphi$ the function defined by $(U_g\varphi)(gx) = \varphi(x)$. Then form, for each k, the *projector*

$\Pi_k = n^{-1} \sum_{g \in G} \chi_k^*(g)\, U_g$, thus called because $\Pi_k \Pi_k = \Pi_k$ and $\Pi_j \Pi_k = 0$ if $j \neq k$. We note that $\varphi = \sum_k \Pi_k \varphi$, and that $\mathrm{div}(\mu\, \nabla \Pi_k \varphi) = \Pi_k[\mathrm{div}(\mu\, \nabla\varphi)]$, the property known as G-*equivariance* of the differential operator div($\mu$ grad). All this shows that "problem $Q_k$", that is, solving $-\mathrm{div}(\mu\, \nabla\varphi) = \Pi_k q$ over all D with $\varphi = 0$ on $\partial D$, has $\Pi_k \varphi$ for its solution. Moreover, $\Pi_k \varphi$ transforms in a particular way under rotation, owing to the obvious equality $U_r \Pi_k = \chi_k(r) \Pi_k$: one has $(\Pi_k\varphi)(rx) = \chi_k(r)(\Pi_k\varphi)(x)$, which shows that $\Pi_k\varphi$ is determined by its restriction $\varphi_k$ to the symmetry cell, and that $\varphi_k$ satisfies "problem $P_k$": $-\mathrm{div}(\mu\, \nabla\varphi) = -\Pi_k q$ over C, with $\varphi = 0$ on $\partial D$ and $\varphi(rx) = \chi_k(r)\varphi(x)$ for pairs of points $\{x, rx\}$ that belong to the new boundary.

Hence the recipe: (1) Form the right-hand sides $\Pi_k q$ by computing $\Pi_k q(x) = n^{-1} \sum_j \exp(-2i\pi kj/n)\, q(r^j x)$ for points x of C, the step called "(discrete) Fourier analysis", (2) Solve each problem $P_k$ over C, using on the new boundary the "pseudo-periodic boundary condition" (p.p.b.c., from now on) $\varphi(rx) = \exp(2i\pi k/n)\, \varphi(x)$, (3) Extend the solution $\varphi_k$ of $P_k$ to all D, using $\varphi_k(rx) = \exp(2i\pi k/n)\, \varphi_k(x)$, hence $\Pi_k\varphi$, and sum up to recover $\varphi = \sum_k \Pi_k\varphi$. (In particular, $\varphi = \sum_k \varphi_k$ over C.) This step is "(discrete) Fourier synthesis".

Let us now test the power of this method by considering the case of crystal-like symmetry. This time, $-\mathrm{div}(\mu\, \nabla\varphi) = q$ is to be solved over all space (a well-posed problem if $q \in L^2(A_3)$ has bounded support), and $\mu(x + \tau) = \mu(x)$ for all points x and all translation vectors $\tau$ of the form $\sum z^i v_i$, where $v_1$, $v_2$, $v_3$ are three fixed independent vectors and the $z^i$ are relative integers. The set T of such translation vectors, which do form a group of mappings from $A_3$ to itself (a subgroup of $V_3$, isomorphic to $Z^3$), is called the *Bravais lattice.* There is no unique, or even preferred choice for the cell C: We select an arbitrary spatial point c (for *center*) and take for C the set of points $x = c + \sum_i \lambda^i v_i$ for all $\lambda^i$ such that $|\lambda^i| \leq 1/2$. The translates of C by all vectors $\tau$ of T pave space, with overlap at their boundaries. Characters are here functions $\chi_\kappa(\tau) = \exp(i\, \kappa \cdot \tau)$, where $\kappa$ is a 3D vector, but not all such vectors are needed: Let's call $w_1$, $w_2$, $w_3$ the *dual* vectors to the $v_i$s, defined by $w_i \cdot v_i = 2\pi$ and $w_j \cdot v_i = 0$ if $i \neq j$, and B (akin to the "Brillouin zone" of crystallography) the set of vectors $\sum_i \lambda^i w_i$ with $|\lambda^i| \leq 1/2$. Translates of B by vectors $\theta = \sum_i z^i w_i$, with integer weights $z^i$, pave $V_3$. Since $\exp(i\kappa \cdot \tau) = \exp(i(\kappa + \theta) \cdot \tau)$ for such vectors $\theta$, one gets all the characters by letting $\kappa$ span B only. Moreover, pairs of points of $\partial B$ that are related by such $\theta$-translations yield the same character. Therefore, the dual group of T is B "wrapped around", with identification of such points, a 3D *torus* (which we still call B). This time, group T and its dual are very different: Both have an infinity of elements, but T is discrete, topologically speaking, whereas B is continuous and compact. (Predictably, the dual of B is T: The corresponding Fourier technique, which shall not be detailed here, is that of *Fourier series*, as applied to functions living on the torus T, that is to say, to triply periodic functions of three variables.)

The order of T being infinite mandates minor adjustments with respect to the above example (no division by n). For x in C, set

$$(\Pi_\kappa\varphi)(x) = \mathrm{vol}(C) \sum_{\tau \in T} \exp(-i\kappa \cdot \tau)\, \varphi(x + \tau).$$

Since $(\Pi_\kappa\varphi)(x + \tau) = \exp(i\kappa \cdot \tau)\,(\Pi_\kappa\varphi)(x)$, as easily checked, this is a pseudo-C-periodic function. Then $\varphi = (2\pi)^{-3} \int_B d\kappa\, \Pi_\kappa\varphi$, which suggests the same kind of approach as in the case of cyclic symmetry: Since equivariance obviously holds, form the functions $\Pi_\kappa q$ on C, solve

$$-\operatorname{div}(\mu \nabla\varphi) = \Pi_\kappa q, \quad \text{with p.p.b.c.}, \tag{1}$$

for all $\kappa$, hence $\varphi_\kappa$ on C, then integrate in $\kappa$ to recover $\varphi$. This is *Floquet–Bloch* analysis.

But now prospects to save on computation look grim: What is the point of replacing a single partial differential equation (even though its domain is the whole space), by an infinity of boundary value problems on C which – depending on $\kappa$ by their boundary conditions, as they do – are all different? We note that the treatment by the Fourier transform, when applicable, that is, when $\mu$ is invariant by all translations, does not suffer from the same shortcomings, because it replaces the original equation by an infinity of *algebraic* ones (namely, $\kappa \cdot (\mu\, \hat{\varphi}(\kappa)\, \kappa) = \hat{j}(\kappa)$, for all $\kappa \in V_3$, where the Fourier components $\hat{j}(\kappa)$ and $\hat{\varphi}(\kappa)$ of j and $\varphi$ are complex *numbers*, rather than *functions*). These equations can be solved in one stroke, hence the solution $\varphi$ by inverse Fourier transform. What homogenization does, as we shall see, is reduce the complexity of the Floquet–Bloch treatment by solving (approximately, of course) all problems (1) in one stroke.

## 3 Bloch and Fourier

To make easier the comparison between Bloch and Fourier analyses, and also to make formulas look more familiar, we take point c as origin of a reference frame based on the $v_i$s, and reuse symbol x to denote the translation vector $x - c$. Set

$$\hat{\varphi}_\kappa(x) = \exp(-i\,\kappa \cdot x)\,(\Pi_\kappa\varphi)(x).$$

This way, the "Bloch mode" $\hat{\varphi}_\kappa$ is C-periodic and is obtained by the summation

$$\hat{\varphi}_\kappa(x) = \mathrm{vol}(C) \sum_{\tau \in T} \exp(-i\kappa \cdot (x + \tau))\, \varphi(x + \tau). \tag{2}$$

The inverse transform formula becomes, accordingly,

$$\varphi(x) = (2\pi)^{-3} \int_B d\kappa\, \exp(i\,\kappa \cdot x)\, \hat{\varphi}_\kappa(x). \tag{3}$$

These formulas compare with the direct Fourier transform,

$$\hat{\varphi}(\kappa) = \int_{V_3} d\tau \exp(-i\,\kappa \cdot \tau)\, \varphi(\tau), \tag{4}$$

and the inverse one:

$$\varphi(x) = (2\pi)^{-3} \int_{V_3} d\kappa \exp(i\,\kappa \cdot x)\, \hat{\varphi}(\kappa). \tag{5}$$

The right-hand side (r.h.s.) of (2) looks like an approximate quadrature formula for the r.h.s. of (4), and (5) looks like what (3) would be, should the cell C reduce to a point and B grow up to fill space entirely.

To make rigorous sense of these observations, let us consider a family of Bravais lattices $T_\alpha$, indexed by a real $\alpha > 0$, generated by the translation vectors $\alpha v_1$, $\alpha v_2$, $\alpha v_3$, and look at what happens when $\alpha \to 0$. The homothetic image $C_\alpha$ of C, with center c and ratio $\alpha$, makes a symmetry cell for $T_\alpha$, and the corresponding set of characters is the torus formed from $B_\alpha = \alpha^{-1}$ B. We denote by $\langle \hat{\varphi}_\kappa \rangle_\alpha$ the average of $\hat{\varphi}_\kappa$ over $C_\alpha$. One easily proves that

**Lemma 1.** *Given* $\varphi$ *in* $L^2(A_3)$, $\langle \hat{\varphi}_\kappa \rangle_\alpha \to \hat{\varphi}(\kappa)$ *as* $\alpha \to 0$.

In words: For a *fixed* value of the "wavevector" $\kappa$, the cell-average of the Bloch mode of a well-behaved function $\varphi$ converges to its Fourier coefficient $\hat{\varphi}(\kappa)$. There is a kind of reciprocal result, the technical proof of which we omit:

**Lemma 2.** *Given* $\varphi$ *and a bounded family* $\{\varphi^\alpha : \alpha > 0\}$ *of functions in* $L^2(A_3)$, *assume that* $\langle \hat{\varphi}^\alpha_\kappa \rangle_\alpha \to \hat{\varphi}(\kappa)$ *for all* $\kappa$ *when* $\alpha \to 0$. *Then* $\varphi^\alpha$ weakly *converges to* $\varphi$ *when* $\alpha \to 0$.

In words: If cell averages of Bloch modes of $\varphi^\alpha$ converge towards Fourier coefficients of $\varphi$, for all values of $\kappa$, then $\int \varphi^\alpha \psi \to \int \varphi \psi$ for all $\psi$ (this is what weak convergence means), so weighted averages of $\varphi^\alpha$ converge towards those of $\varphi$. Remark than no more is expected from homogenization than good approximation of spatial *averages* of fields, so this looks fine.

# 4 Static Homogenization: Magnetostatics

Rather than committing ourselves to the use of a scalar magnetic potential $\varphi$ as we did thus far, it will be more convenient to deal with the problem in the following symmetric form: Given $\mu$, invariant by all translations of T, and given the compactly supported source current j, find fields h and b such that

$$\text{div } b = 0, \qquad b = \mu h, \qquad \text{rot } h = j. \tag{6}$$

This is "problem P". We shall search for the Floquet–Bloch decompositions of b and h, that is, for fields $\hat{h}_\kappa$, $\hat{b}_\kappa$, living on the symmetry cell C, such that $h(x) = (2\pi)^{-3} \int_{V_3} d\kappa \exp(i\,\kappa \cdot x)\, \hat{h}_\kappa(x)$, etc. Since $\text{rot}[\exp(i\kappa \cdot x)\, \hat{h}_\kappa(x)]$ equals

$\exp(i\kappa\cdot x)$ [rot + i $\kappa\times$] $\hat{h}_\kappa(x)$, with obvious notation, and since a similar relation holds about div, one has "problem $P_\kappa$" to solve,

$$(\mathrm{div} + i\,\kappa\,\cdot)\ \hat{b}_\kappa = 0, \quad \hat{b}_\kappa = \mu\ \hat{h}_\kappa, \quad (\mathrm{rot} + i\,\kappa\,\times)\ \hat{h}_\kappa = \hat{j}_\kappa, \tag{7}$$

for each $\kappa \in B$, on C, with periodic boundary conditions, where the $\hat{j}_\kappa$'s are the Bloch modes of j. Notice how the multiplication by $\exp(-\,i\,\kappa\cdot x)$, while uniformizing the boundary conditions for this $\kappa$-indexed infinity of cell problems, moved the dependence on $\kappa$ into the differential operators. Thus (7) is by no means simpler than (6), quite the contrary.

But now comes the decisive move, by which we exploit the smallness of the cell C. Let us embed problem P into a family $P^\alpha$ of similar ones, but with $C_\alpha$-periodicity of $\mu$ instead of C-periodicity, so that (6) is problem $P^1$, one among the family. The corresponding cell problems $P^\alpha_\kappa$ are the same as in (7), apart from the $\alpha$ indexes, and their $C_\alpha$- instead of C-periodicity. As this last feature prohibits a comparison between the $P^\alpha_\kappa$'s for a fixed $\kappa$ and different $\alpha$'s, we "pull back" problems $P^\alpha_\kappa$ onto C by the transform $x \to c + (x - c)/\alpha$, which blows up $C_\alpha$ to C. Denoting by $b^\alpha_\kappa$, $h^\alpha_\kappa$, etc., hats dropped, the pullbacks (e.g.: $b^\alpha_\kappa(y) = \hat{b}^\alpha_\kappa(c + \alpha(y - c))$, thus living on C, and C-periodic), one sees that

$$(\mathrm{div} + i\,\alpha\kappa\,\cdot)\, b^\alpha_\kappa = 0, \ \ b^\alpha_\kappa = \mu\, h^\alpha_\kappa, \ \ (\mathrm{rot} + i\,\alpha\kappa\,\times)\, h^\alpha_\kappa = \alpha\, j^\alpha_\kappa, \tag{8}$$

with now the same $\mu$ for all (it's the original $\mu$, C-periodic), and the prospect to see all these $\kappa$-subproblems become "the same" when $\alpha \to 0$.

**Proposition 1.** *When* $\alpha \to 0$, *the solution* $\{b^\alpha_\kappa, h^\alpha_\kappa\}$ *of* (8) *converges* (in the strong sense of $L^2(C)$) *towards the solution* $\{b_\kappa, h_\kappa\}$ *of*

$$\mathrm{div}\, b = 0, \qquad b = \mu h, \qquad \mathrm{rot}\, h = 0 \tag{9}$$

$$i\,\kappa\cdot\langle b\rangle = 0, \qquad i\,\kappa\times\langle h\rangle = \hat{j}(\kappa). \tag{10}$$

*where* $\langle\ \rangle$ *denotes averaging over* C.

*Proof* (sketched). Terms in $\alpha$ vanish, hence (9). Since $b^\alpha_\kappa$ and $h^\alpha_\kappa$ are C-periodic, the integrals $\int_C \mathrm{div}\, b^\alpha_\kappa$ and $\int_C \mathrm{rot}\, h^\alpha_\kappa$ are null. Integrate the first line of (8) over C, and use Lemma 1 to find the right-hand side $\hat{j}(\kappa)$ in (10). ◊

Now look at (9, 10). This problem still depends on $\kappa$, but it splits into two parts. One is "find the relation $B = \mu_{\mathrm{eff}} H$ that must exist between vectors B and H for

$$\mathrm{div}\, b = 0, \ \ \langle b\rangle = B, \ \ b = \mu h, \ \ \mathrm{rot}\, h = 0, \ \ \langle h\rangle = H \tag{11}$$

to have a solution", and this is the expected *cell-problem*, from which $\kappa$ has disappeared. The second part consists in finding, for each $\kappa$, vectors $\langle b\rangle$ and $\langle h\rangle$

(complex valued) such that $i\kappa \cdot \langle b\rangle = 0$, $\langle b\rangle = \mu_{eff}\langle h\rangle$, $i\kappa \times \langle h\rangle = \hat{j}(\kappa)$, and here we recognize the $\kappa$-indexed algebraic problems associated with the Fourier method of solving

$$\operatorname{div} b = 0, \quad b = \mu_{eff} h, \quad \operatorname{rot} h = j. \tag{12}$$

Thanks to Lemma 2 (and the fact that the averages of a field over $C_\alpha$ and of its pullback over C are equal), we may conclude as follows:

**Theorem 1.** *When* $\alpha \to 0$, *the solution* $\{b^\alpha, h^\alpha\}$ *of problem* $P^\alpha$ *weakly converges towards the solution* $\{b, h\}$ *of* (12), *where the homogenized permeability* $\mu_{eff}$ *is the one obtained by solving the cell problem* (11).

Such an asymptotic result was a precondition to replacing problem $P^1$, the original one, by $P^0$, if we so label problem (12), so this is satisfying. But does it *justify* this replacement? As with all perturbative techniques, this depends on the magnitude of the terms thus neglected in the Taylor expansion in $\alpha$ of $\{b^\alpha, h^\alpha\}$ near $\alpha = 0$. It can be shown (but this is another issue than what Thm 1 addresses) that this is so if the spectral content of the spatial Fourier transform of j is poor in "small spatial wavelengths", where small refers to the size L of cell C, i.e., if $\hat{j}(\kappa)$ is small enough to be neglected when $L|\kappa| \ll 1$ does not hold. To appreciate whether this is so belongs to the "modelling" part of the procedure.

## 5 Homogenizing the Full Maxwell System

Let us now try the same approach on the Maxwell equations, $-i\omega\varepsilon e + \operatorname{rot} h = j$ and $i\omega\mu h + \operatorname{rot} e = 0$, where $\varepsilon$ integrates the conductivity $\sigma$ by the usual trick of setting $\varepsilon = \varepsilon_0 - i\sigma/\omega$. Our work is cut out for us: Proceeding exactly as above, we find this instead of (8):

$$-i\omega\alpha d^\alpha_\kappa + (\operatorname{rot} + i\,\alpha\kappa\,\times)h^\alpha_\kappa = \alpha\, j^\alpha_\kappa, \qquad d^\alpha_\kappa = \varepsilon\, e^\alpha_\kappa,$$

$$i\omega\alpha b^\alpha_\kappa + (\operatorname{rot} + i\,\alpha\kappa\,\times)e^\alpha_\kappa = 0, \qquad b^\alpha_\kappa = \mu\, h^\alpha_\kappa,$$

and the $\alpha = 0$ limit is characterized by

$$\operatorname{div} b = 0, \qquad b = \mu h, \qquad \operatorname{rot} h = 0,$$

$$\operatorname{div} d = 0, \qquad d = \varepsilon\varepsilon, \qquad \operatorname{rot} e = 0,$$

$$-i\omega\langle d\rangle + i\,\kappa \times \langle h\rangle = \hat{j}(\kappa), \quad i\omega\langle b\rangle + i\,\kappa \times \langle e\rangle = 0. \tag{13}$$

The weak limit, the same theorem tells us, will satisfy (13) with constitutive relations $\langle b\rangle = \mu_{eff}\langle h\rangle$ and $\langle d\rangle = \varepsilon_{eff}\langle e\rangle$, which are the image in Fourier space of the Maxwell equations for a material with effective coefficients $\mu_{eff}$ and $\varepsilon_{eff}$, as given by solving the cell problem (11) and its electrostatic counterpart.

But this is a big disappointment! We *don't* expect the effective coefficients for a metamaterial to be independent of frequency, as this result would tend to suggest, especially not in the case of Fig. 1. What went wrong? Not the logic underlying the theorem, but the modelling: The choice of problems $P^\alpha$ in which to embed $P^1$ cannot be the same as in statics, because it must take into account the existence, besides the cell's size, of a second small parameter, the width of the slit (to say nothing of the penetration depth, which we take null from the onset by assuming $e = 0$ in the bulk of the ring).

## 6 Homogenizing the Split-Ring Metamaterial

Indeed, since the resonance condition $LC \sim \omega^{-2}$ is essential, it should be an invariant feature of all problems $P^\alpha$ in order to be preserved at the limit. When $\alpha \to 0$, both L and C scale like $\alpha$ if the cell is shrunk by homothetic contraction, hence the resonance is lost, so one should imagine a family of problems $P^\alpha$ that make the slit capacitance behave in $1/\alpha$. This is easy: Take the slit width in $P^\alpha$ equal to $\alpha^3\delta$. Let us now look for the $\alpha = 0$ limit under these conditions.

To keep things simple, we start from a modelling of problem $P^1$ that already acknowledges the high conductivity of the ring (this is done by assuming $e = 0$ in R) and the smallness of $\delta$ (this is done by modelling the slit by a surface $\Sigma$ that bears a capacitive layer). Cell C is made of the ring R, the slit $\Sigma$, and the "air part" A around. With hopefully little risk of confusion, we also denote by R, $\Sigma$, A the set-unions of all translates of these cell parts in the given lattice. The same conventions apply, with index $\alpha$ appended, for problems $P^\alpha$. Now, the version of problem $P^\alpha$ we propose ourselves is, in weak form, *find* $h^\alpha$ *such that*

$$\int_{A_\alpha} i\omega\mu\, h^\alpha \cdot h' + \int_{A_\alpha} (i\omega\varepsilon)^{-1} (\text{rot}\, h^\alpha - j) \cdot \text{rot}\, h' \tag{14}$$

$$\ldots + \int_{\Sigma_\alpha} (i\omega\varepsilon)^{-1} \alpha^3\, \delta\, (n \cdot \text{rot}\, h^\alpha)\, (n \cdot \text{rot}\, h') = 0$$

*for all test fields* h', where n denotes the unit normal on $\Sigma_\alpha$. Notice how (in the case $\alpha = 1$) the third term accounts for the capacitive effect across $\Sigma$.

We proceed as above, by throwing the Bloch decomposition of h into (14), hence the $\kappa$-indexed cell problems, then scaling to pull them back to the reference cell C. This results in *find* $h^\alpha_\kappa$ (a Bloch mode, now), C-*periodic*, *such that*

$$\alpha^3 \int_A i\omega\mu\, h^\alpha \cdot h' + \alpha \int_A (i\omega\varepsilon)^{-1} ((\text{rot} + i\alpha\kappa\, \times)\, h^\alpha - \alpha j) \cdot (\text{rot} + i\alpha\kappa\, \times)\, h'$$

$$\ldots + \alpha^3 \int_\Sigma (i\omega\varepsilon)^{-1}\, \delta\, [n \cdot (\text{rot} + i\alpha\kappa\, \times)\, h^\alpha][n \cdot (\text{rot} + i\alpha\kappa\, \times)\, h'] = 0$$

*for all test fields* h', where one clearly sees how the $\alpha^3$ term in front of $\delta$ maintains the balance between inductive and capacitive reactive powers. The second term acts like a penalty one, making rot h equal to 0 in the $\alpha = 0$ limit.

Let us now, leaving intermediate details aside, describe this limit. Since rot h = 0 in A, we write it h = grad $\varphi$, with $\varphi$ possibly multivalued, since a current I will flow in the ring across $\Sigma$. Let us therefore introduce a "cut" S (cf. Fig. 3) across which $\varphi$ may have a jump $[\varphi]$, equal to I. Jumps can also exist on $\partial C$, because although h is C-periodic, $\varphi$ need not be: What one must have is just $\varphi(x + v_i) - \varphi(x)$ equal to some constant $c_i$ for pairs of boundary points x and $x + v_i$. Call $\Phi$ the space of admissible potentials on these conditions. The weak form of the cell problem then turns out to be, *find* $\varphi$ *in* $\Phi$ *such that, for all test functions* $\varphi'$ *in* $\Phi$,

$$\int_A i\omega\mu \, \nabla\varphi \cdot \nabla\varphi' + (i\omega C)^{-1} \, [\varphi][\varphi'] = \int_A i\omega \, B \cdot \nabla\varphi', \tag{15}$$

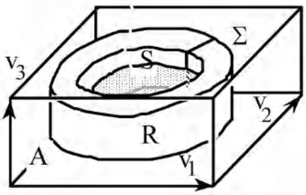


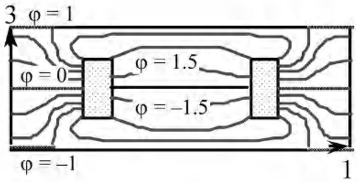


**Fig. 3** *Left*: Surface $\Sigma$ modelling the slit, and cutting surface S. *Right*: Typical behavior of the solution $\varphi$ of the cell problem in an axial plane (arbitrary figures). Notice the jump of $\varphi$ across the cut and the opposite directions of the magnetic field inside and outside the ring.

where C, the capacitance of the slit, is taken equal to $\int_\Sigma \varepsilon_0/\delta$, and B, a given vector parameter, can be recognized as the average induction. To find the effective reluctivity, as suggested in the Introduction, we then set $\nu_{\text{eff}} \, B \cdot B = \int_A \mu \, |\nabla\varphi|^2 - 1/(C\omega^2) \, [\varphi]^2$. Note how $\nu_{\text{eff}}$ can change sign. It is *real*, here, owing to our perfect conductor assumption, which excludes losses, but it would be easy to correct (15) to account for these: Just add a "boundary impedance" term, in $(1 + i)(\sigma d)^{-1} \, h \cdot h'$, where d is the skin depth, on $\partial R$.

This is a mildly exotic variant of the magnetostatics problem, easy to solve by using nodal elements for $\varphi$ in A (and node-doubling on the cut S). If one focuses interest on the vertical part of $\nu_{\text{eff}}$ (B then being vertical), and if the height of the ring almost matches that of the cell, the two-dimensional situation that results is amenable to analytical calculation (Fig. 4). One finds $\nu_{\text{eff}}(\omega) = \nu_0 (1 - \omega^2 \mu_0 \, aC)/[a + a'(1 - \omega^2 \mu_0 \, aC)]$, where a and a' are the *relative* (to the cross section) areas of the two parts of the air region and C the slit's capacitance. Hence a window $\omega_1 = \nu_0/aC$ to $\omega_2 = \nu_0 (a + a')/aa'C$ of negative effective reluctivity. For $\sigma$ finite but very large, correcting for skin effect as explained above, one can expect the result plotted on Fig. 4, right.

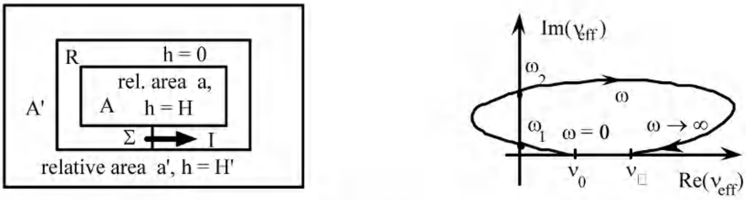


**Fig. 4** *Left*: Horizontal cross section of C. The ring current I is H – H' (by Ampère), one has I = iωCV, where V is the voltage drop across the gap, and V relates to H by Faraday. Hence the formula for $\nu_{eff}(\omega)$ given below. *Right*: Plot of $\nu_{eff}$ in the complex plane, parameterized by the angular frequency, if Joule losses are accounted for.

# 7 Discussion

Attentive readers may well have suspected a sleight-of-hand in what precedes: I first embedded the physical problem P in a family $P_\alpha$, indexed by the cell-size-related parameter $\alpha$, searched for the limit $P_0$, and then... threw away the result as non-satisfactory, just to select, seemingly out of the blue, *another* family of problems, which I decided was more suitable! What's going on?

This is a delicate issue, but one that is not special to homogenization techniques (see e.g. [7], or the book [8]), and it can be discussed in non-specific terms. Suppose we have at hand a real-life problem where two small parameters a and b make numerical simulations difficult, but are also, both of them, good candidates to perturbative treatment. To formalize such an approach, let us consider the family of problems $P_{\alpha\beta}$ where a and b are replaced, all other things equal, by $\alpha$a and $\beta$b, and where $q_{\alpha\beta}$ denotes the value of some quantity of interest, a function of the solution $u_{\alpha\beta}$. The latter may behave wildly when both $\alpha$ and $\beta$ go to zero, but *if* we can prove, by mathematical arguments, that $q_{\alpha\beta}$ has a limit $q_{00}$, which can be computed from the solution $u_{00}$ of some limit problem $P_{00}$, and that q is smooth in $\{\alpha, \beta\}$ near $\{0, 0\}$, then solving $P_{00}$ instead of the real-life problem $P_{11}$ can be a smart move. We just need to make sure that the derivatives $\partial_\alpha q$ and $\partial_\beta q$ at $\alpha = 0$ and $\beta = 0$ are small enough to justify the neglect of all terms except the very first one in the Taylor expansion $q_{\alpha\beta} = q_{00} + \alpha\, \partial_\alpha\, q + \beta\, \partial_\beta\, q + \ldots$ when $\alpha = 1$ and $\beta = 1$.

In the case of the split-ring problem, a is the cell's size and b the slit's width, and q can be, say, the average magnetic energy density (or rather, since it's complex-valued, its imaginary part, which yields the real part of $\mu_{eff}$). But it's clear, on physical grounds, that q is *not* smooth, not even continuous, at point $\{0, 0\}$, which forbids the simple-minded perturbative approach in which $\{\alpha, \beta\}$ would be treated as a single, if two-dimensional, parameter.

On the other hand, perturbation with respect to $\alpha$ alone, or to $\beta$ alone, is possible. The latter consists in replacing the slit by a surface $\Sigma$ bearing the capacitance $C = \int_\Sigma \varepsilon_0/\delta$, and letting $\alpha$ stay equal to 1, which ignores the repetitive

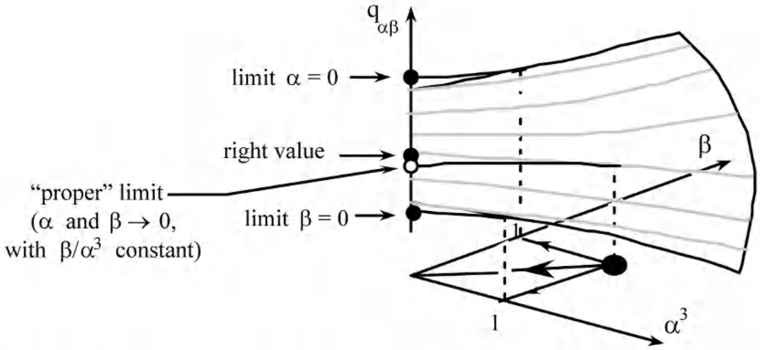


**Fig. 5** Graph of the observable parameter q. Though q smoothly depends on $\alpha$ and $\beta$, the limits $q_{10}$ and $q_{01}$ can be very different, because of the discontinuity at the origin in parameter space.

structure of the metamaterial: No homogenization, therefore. The other option, keeping $\beta = 1$ and letting $\alpha$ go to 0, which ignores the resonance condition LC ~ $\omega^{-2}$, corresponds to the "static" homogenization performed in Section 5, and found wanting. Figure 5 is meant to suggest why these perturbative approaches, *"justified" by a convergence theorem as they may be*, will fail in practice: The derivatives $\partial_{\alpha\beta}q$ at $\{1, 0\}$ and $\{0, 1\}$ are just too large. The correct perturbative approach is suggested by the figure: Find a path $\beta = \psi(\alpha)$, in the $\{\alpha, \beta\}$-plane, that follows, as closely as possible, the projection of the level line passing through $\{1, 1, q_{11}\}$, find the $\alpha = 0$ limit of this family of problems, solve that. Of course we have no way to predetermine this optimal path, but the one we did choose, $\beta = \alpha^3$, is our best guess, because it preserves the feature of problem $P_{11}$ that we know is responsible for the global behavior of the metamaterial, namely the internal resonance within each cell that occurs when LC ~ $\omega^{-2}$. Again, a detailed computation of the derivative $\partial_{\alpha\beta}q$ at the origin, along the curve $\beta = \alpha^3$, would give a posteriori justification, should we need it.

So the homogenization of metamaterials at high frequencies, as a numerical technique, rests on two pillars: Correct modelling, which suggests *which* convergence result is required to justify the derivation of the cell problem to be solved, and mathematical analysis to establish this convergence. We have seen how misleading the neglect of the former in favor of the latter could be, so it's only fair to insist on the necessity of a convergence theorem: This is, to say things rapidly, what guarantees the smoothness, *outside the singular point at the origin*, of the graph of q, on Fig. 5. Owing to the fact that only *weak* convergence was proven, not all observable quantities will behave that smoothly. For instance – a trivial counter-example – the value of the electric field at point c, or any other fixed spatial point, stands no chance to converge when $\{\alpha\ \beta\}$ tends to $\{0, 0\}$, whichever way. Only those observables that are spatial averages of some local function of the actual, highly oscillatory field, will have such a smooth graph. Only parameters of this kind, which fortunately includes the effective coefficients we are after, can legitimately be approximated by homogenization techniques.

## References


1. S. Zouhdi, A. Sihvola, M. Arsalane (eds): Advances in Electromagnetics of Complex Media and Metamaterials, NATO Science Series II, 89, Kluwer (Dordrecht), 2002.
2. A. Bensoussan, J.L. Lions, G. Papanicolaou: Asymptotic Methods for Periodic Structures, North Holland (Amsterdam), 1978.
3. A. Braides: "Introduction to Homogeneization and Gamma-convergence", in A. Braides and A. Defranceschi (eds.): Homogenization of Multiple Integrals, Oxford U.P. (Oxford), 1998.
4. D. Sjöberg, C. Engström, G. Kristensson, D.J.N. Wall, N. Wellander: "A Floquet–Bloch Decomposition of Maxwell's Equations Applied to Homogenization", Multiscale Model. Simul., **4**, 1 (2005), pp. 149–71.
5. G.W. Mackey: "Harmonic Analysis as the Exploitation of Symmetry – A Historical Survey", Bull. AMS, **3**, 1, Pt. 1 (1980), pp. 543–698.
6. A. Bossavit: "Boundary Value Problems with Symmetry, and Their Approximation by Finite Elements", SIAM J. Appl. Math., **53**, 5 (1993), pp. 1352–1380.
7. S. Richardson: "How Not to Tackle Some Singular Perturbation Problems", SIAM Rev., **32**, 3 (1990), pp. 471–473.
8. W. Eckhaus: Asymptotic Analysis of Singular Perturbations, North-Holland (Amsterdam), 1979.

# Mixing Formulas and Plasmonic Composites

**Henrik Wallén, Henrik Kettunen, and Ari Sihvola**

Department of Radio Science and Engineering
Helsinki University of Technology (TKK)
P.O. Box 3000, FI-02015 TKK, Finland
henrik.wallen@tkk.fi

**Abstract** Composites with plasmonic inclusions or holes in a plasmonic host medium can exhibit very interesting, or even extreme, properties. We compare the predicted effective permittivities of plasmonic composites using the classical mixing rules of Maxwell Garnett, Lord Rayleigh and Bruggeman with quasistatic numerical simulations and a series solution in two dimensions. The Maxwell Garnett and Rayleigh rules are reasonably accurate for small or modest volume-fractions of inclusions in a regular or almost regular lattice, while the Bruggeman rule is clearly less useful in this case. Finally, we also consider transparency, near-field superlensing and extreme anisotropy as possible applications using silver–air composites, using the Drude model for the complex permittivity of silver.

## 1 Introduction

The effective permittivity of ordinary dielectric composites can be successfully estimated using a large variety of different mixing rules [15]. Each rule provides one estimate, and depending on the microstructure of the composite, different rules can give the best approximation for the effective permittivity. For a two-phase mixture with lossless positive-permittivity constituents, the effective permittivity must be between the permittivities of the constituents. However, if one of the constituents has negative permittivity, the situation is radically different, since surface plasmon resonances can be excited at the interfaces between the positive- and negative-permittivity components.

Classical mixing formulas have, to some extent, been used also for plasmonic mixtures [7, 12, 14, 16, 17], but their predictions may deviate strongly and qualitatively from each other. It has been critically pointed out [8] that the Maxwell Garnett formula predicts infinities and Bruggeman complex results for real-valued component permittivities. Recently, some purely numerical results [11] and finally also comparisons between numerical results and mixing rules [4] have been presented, but the topic is by no means exhaustively documented.

S. Zouhdi et al. (eds.), *Metamaterials and Plasmonics: Fundamentals, Modelling, Applications*,

In this paper, we consider the classical Maxwell Garnett, Lord Rayleigh and Bruggeman mixing rules in two dimensions and discuss their limitations and applicability for plasmonic composites. To evaluate the accuracy of the mixing rules, we also compute the effective (quasistatic) permittivity using the finite element method (FEM) and a series solution for a square lattice of circular cylinders [10]. In addition to the regular lattice, we also consider one slightly disordered composite, and finally present three silver–air mixtures with interesting properties. A preliminary version of this paper appeared in the META'08 proceedings [18].

## 2 Mixing Formulas and Their Limitations

Consider a plasmonic two-phase mixture where the plasmonic constituent (or inclusion) with relative permittivity $\varepsilon_\mathrm{r}$ occupies the volume fraction $p$. For simplicity, we assume that the other constituent has relative permittivity 1. The task is to estimate the effective permittivity $\varepsilon_\mathrm{eff} = \varepsilon_\mathrm{eff}(\varepsilon_\mathrm{r}, p)$. The classical mixing formulas by Maxwell Garnett, Bruggeman and Lord Rayleigh are available for both two- and three-dimensional mixtures, but we only consider the 2D case in this paper.

For mixtures with cylindrical inclusions, the Maxwell Garnett formula [9] predicts the effective relative permittivity

$$\varepsilon_\mathrm{eff} = 1 + \frac{2p(\varepsilon_\mathrm{r} - 1)}{\varepsilon_\mathrm{r} + 1 - p(\varepsilon_\mathrm{r} - 1)} , \tag{1}$$

while the Bruggeman (symmetric) formula [1] gives

$$\varepsilon_\mathrm{eff} = \frac{1}{2}\left(B \pm \sqrt{B^2 + 4\varepsilon_\mathrm{r}}\right), \quad B = 1 - \varepsilon_\mathrm{r} + 2p(\varepsilon_\mathrm{r} - 1) , \tag{2}$$

where the branch of the (complex) square root yielding the physically more reasonable result should be chosen; see also the more thorough analysis in [17].

The 2D Rayleigh formula [6] gives the estimate

$$\varepsilon_\mathrm{eff} = 1 + \frac{2p}{\dfrac{\varepsilon_\mathrm{r} + 1}{\varepsilon_\mathrm{r} - 1} - p - \dfrac{\varepsilon_\mathrm{r} - 1}{\varepsilon_\mathrm{r} + 1}\left(0.3058\, p^4 + 0.0134\, p^8\right)} , \tag{3}$$

which can be understood as a refinement of the Maxwell Garnett formula, taking some higher order interactions between the cylindrical inclusions in a square lattice into account.

For each mixing rule $\varepsilon_\mathrm{eff}(\varepsilon_\mathrm{r}, p)$ we can define a complementary rule

$$\varepsilon^c_\mathrm{eff}(\varepsilon_\mathrm{r}, p) = \varepsilon_\mathrm{r}\, \varepsilon_\mathrm{eff}(1/\varepsilon_\mathrm{r}, 1 - p) , \tag{4}$$

by exchanging the roles of the inclusion and environment. In principle, the Maxwell Garnett and Rayleigh formulas are valid for separated cylindrical inclusions (small $p$), while the corresponding complementary rules are valid for cylindrical holes in a plasmonic material (large $p$). The Bruggeman formula (2) is symmetric with respect to the inclusion and environment, i.e., it is its own complement.

For a square lattice of cylindrical inclusions, the volume fraction must be smaller than $p_{\max} = \pi/4 = 78.5\%$, if the cylinders are not allowed to overlap. This can be seen as one upper bound for the Maxwell Garnett and Rayleigh formulas. To get good estimates for the effective permittivity, the volume fraction should be somewhat smaller for the Rayleigh formula, and significantly smaller for the Maxwell Garnett formula.

A 2D-cylinder can support plasmonic resonances when $\varepsilon_\mathrm{r} = -1$. Therefore, the effective permittivity $\varepsilon_\mathrm{eff}$ of a mixture with cylindrical inclusions should be singular near $\varepsilon_\mathrm{r} = -1$ if the volume fraction $p$ is small. This is correctly predicted by the Maxwell Garnett and Rayleigh formulas (1) and (3). As shown in Fig. 1, the Maxwell Garnett formula predicts one singularity and the Rayleigh formula predicts two singularities with good accuracy, compared with the series solution for a square lattice from [10], as long as the volume fraction is not too large. The effective permittivity $\varepsilon_\mathrm{eff}$ as a function of $\varepsilon_\mathrm{r}$ has an infinite number of discrete singularities, with an accumulation point at $\varepsilon_\mathrm{r} = -1$, as shown in [10]. However, it appears that one or two singularities are enough to capture the overall behavior of $\varepsilon_\mathrm{eff}(\varepsilon_\mathrm{r})$ everywhere except near the essential singularity at $\varepsilon_\mathrm{r} = -1$, when the volume fraction $p$ is not too large: say $p < 25\%$ or $p < 50\%$.

The Bruggeman formula (2) does not predict any singularities, but instead a region where the effective permittivity is complex, shown in Fig. 2. This is certainly incorrect for a square lattice of cylinders with real permittivity, and the symmetric

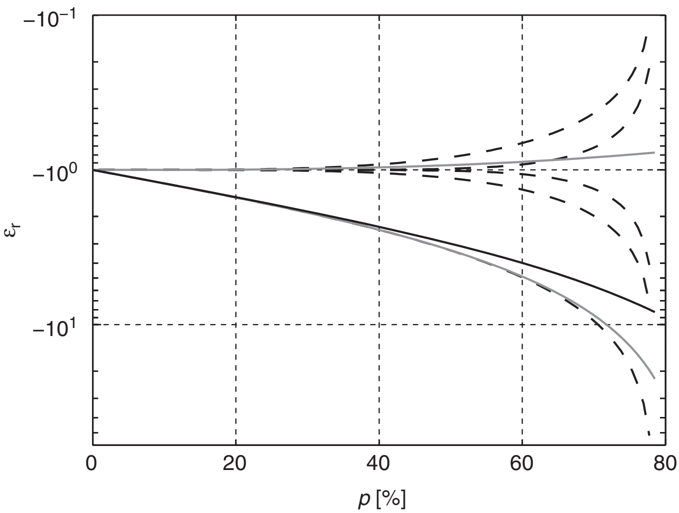


**Fig. 1** Singularity locations for the Maxwell Garnett formula (*black line*) and Rayleigh formula (*gray lines*), compared with the five most significant singularities for a square lattice [10] (*dashed black lines*).

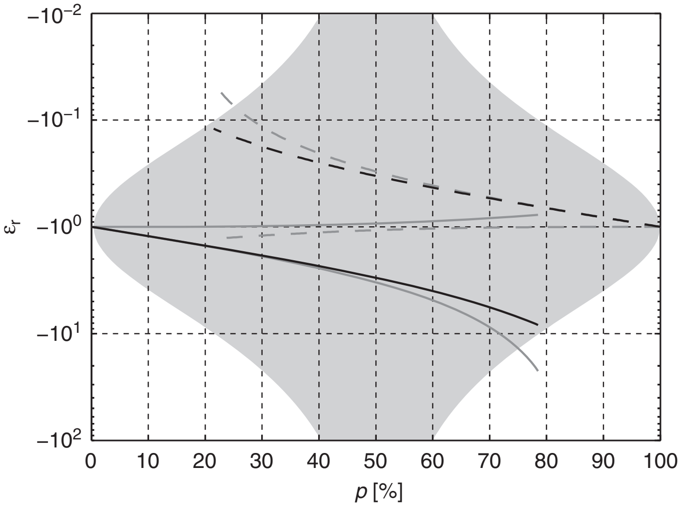


**Fig. 2** Singularity locations for the Maxwell Garnett formula (*black line*) and Rayleigh formula (*gray lines*), and their complementary formulas (*dashed lines*). In the shaded region, the Bruggeman formula gives complex results.

treatment of the inclusion and environment has been argued as one reason why the Bruggeman formula is inappropriate [4]. However, if we interpret the complex region as a region where the Bruggeman formula fails to predict a numerical value – due to one or several singularities – then the formula might be appropriate for plasmonic composites that are geometrically more symmetric with respect to the inclusion and environment.

In this paper, we have only considered composites with non-overlapping inclusions, i.e., without percolation. This can also be one explanation why the Bruggeman formula (2) is less accurate, since it has a percolation threshold $p_c = 50\%$, which is clearly not consistent with the geometrical structure of the composites we consider here.

## 3 Quasistatic Verification

The electrostatic effective permittivity of a periodic mixture can easily be computed using the finite element method (FEM). In particular, we use COMSOL MULTIPHYSICS 3.4 and the geometry shown in Fig. 3 to compute the effective permittivity of a regular lattice ($a \times a$) with cylindrical inclusions (radius $R$). The volume fraction is then $p = \pi R^2/a^2$, with $R < a/2$. The unknown is the potential $\phi(\mathbf{r})$ that satisfies the (generalized) Laplace equation,

$$\nabla \cdot \left[\varepsilon_\mathrm{r}(\mathbf{r})\,\nabla\phi(\mathbf{r})\right] = 0\,, \tag{5}$$

**Fig. 3** Geometry and boundary conditions for the computational setup for the regular lattice.

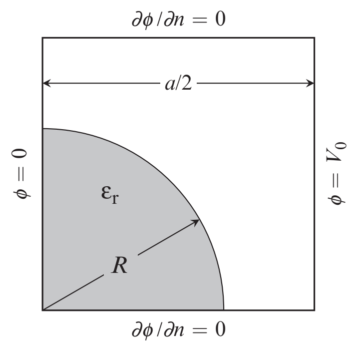


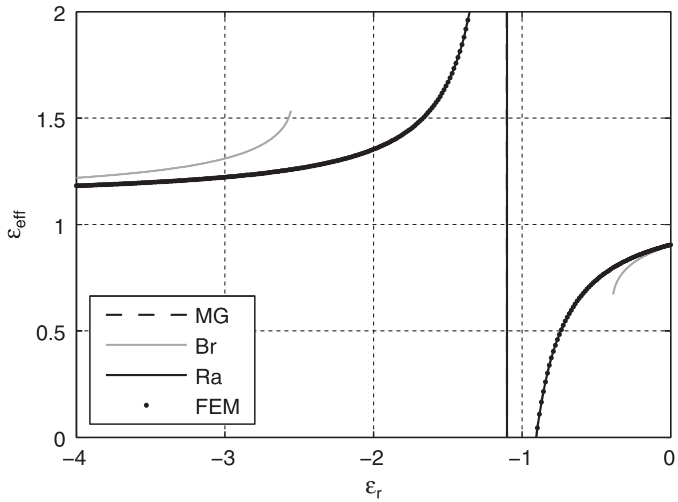


**Fig. 4** Effective permittivity for a regular lattice with $p = 5\%$ negative-permittivity rods in air using the Maxwell Garnett (MG), Bruggeman (Br) and Rayleigh (Ra) formulas and FEM.

and the boundary conditions shown in Fig. 3. Using a plate-capacitor model, the effective permittivity can be expressed as

$$\varepsilon_{\text{eff}} = \frac{1}{V_0^2} \int_S \varepsilon_{\text{r}}(\mathbf{r})\, \nabla\phi(\mathbf{r}) \cdot \nabla\phi(\mathbf{r})\, dS \,, \tag{6}$$

where $V_0$ is the applied voltage and the integral is over the whole computational domain in Fig. 3. The relative permittivity $\varepsilon_{\text{r}}(\mathbf{r})$ is $\varepsilon_{\text{r}}$ in the cylinder and one outside.

A representative selection of numerical results for the effective permittivity $\varepsilon_{\text{eff}}$ of regular lattices is shown in Figs. 4–7. The series solution in Fig. 6 is computed using the formulas in [10]. In general, the Maxwell Garnett formula gives accurate results for low volume fractions, and the Rayleigh formula gives accurate results also for larger volume fractions. The Bruggeman formula, where applicable, is clearly less

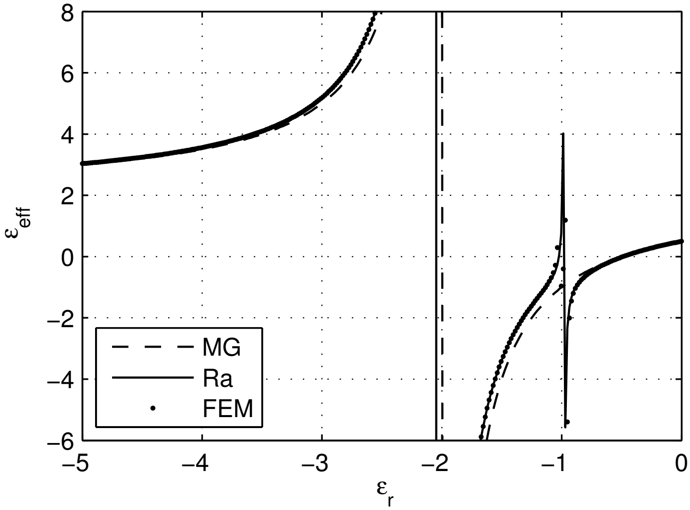


**Fig. 5** Effective permittivity, as in Fig. 4, but with the higher volume fraction $p = 1/3$. (The Bruggeman prediction is omitted, since it gives a reasonable estimate only for $\varepsilon_r \approx 0$ in this case.)

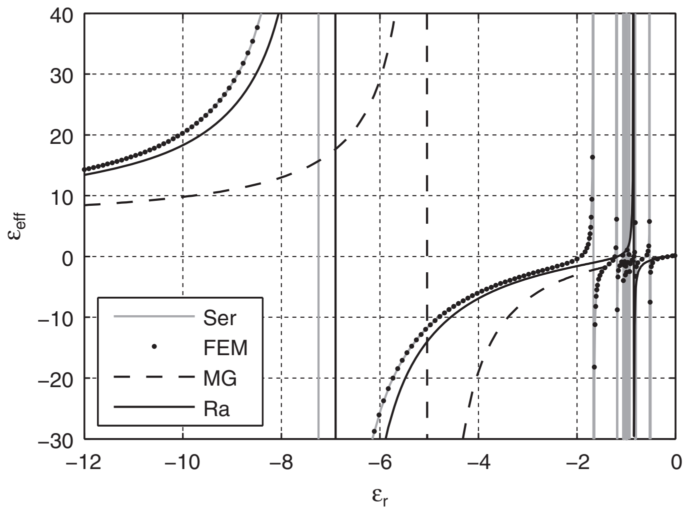


**Fig. 6** Effective permittivity for a dense composite with $p = 2/3$ negative permittivity rods in a square lattice using the Maxwell Garnett (MG) and Rayleigh (Ra) mixing formulas compared with the FEM-result and the series solution (Ser). The accuracy of the mixing formulas are clearly not very useful for this high volume fraction, but the series solution and FEM agree very well.

accurate in this case. None of the mixing formulas are accurate when the cylinders are almost touching, since many singularities or higher order interactions should be taken into account, but the FEM and series solutions agree almost perfectly as shown in Fig. 6.

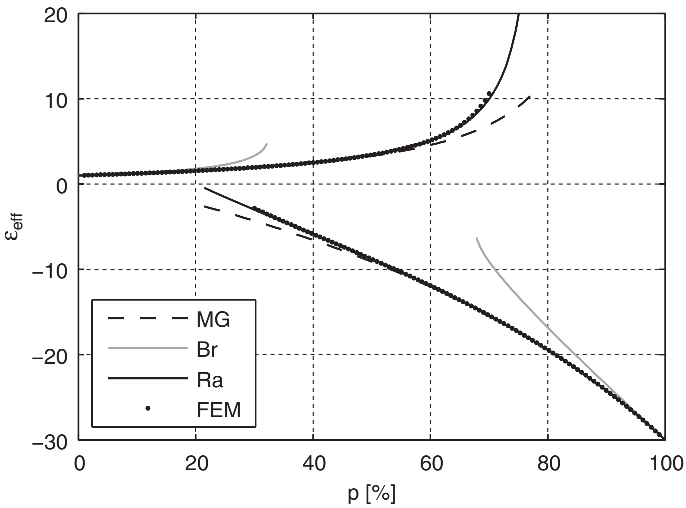


**Fig. 7** Effective permittivity for a mixture of air and a plasmonic material with $\varepsilon_r = -30$. The curves starting at $p = 0\%$ is for a mixture with plasmonic rods in air, while the curves ending at $p = 100\%$ is for a mixture with holes in a plasmonic material. The complementary version of the Maxwell Garnett and Rayleigh formulas are used in the latter case, and $p$ is always the volume fraction of the plasmonic material.

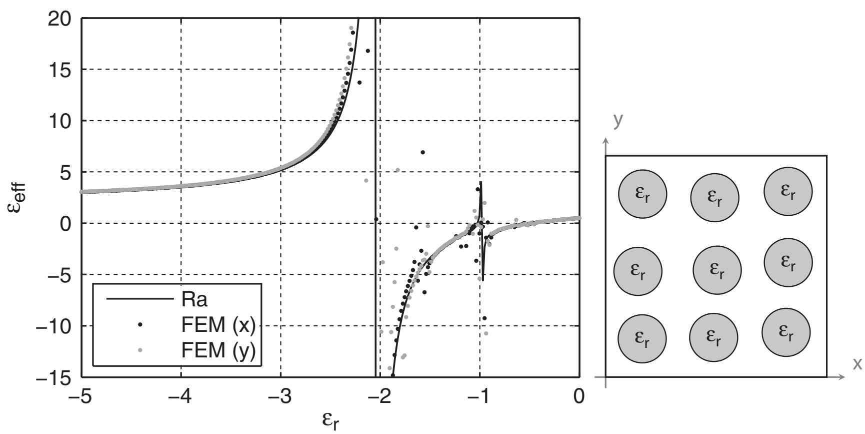


**Fig. 8** Effective permittivity for one slightly disordered sample with $p = 1/3$. The material is anisotropic, with different $\varepsilon_{\text{eff}}$-components in the $x$- and $y$-directions, and several additional singularities appear. The Rayleigh formula is not as accurate as for the regular lattice in Fig. 5, but it still gives a very useful estimate, especially for $\varepsilon_r < -2.5$ and $\varepsilon_r > -0.5$.

Even a small deviation from a regular lattice can have a large impact near the plasmonic resonances, as shown in Fig. 8. However, as long as the cylinders are not allowed to be too close to each other, the Maxwell Garnett and Rayleigh formulas seem to give useful estimates for large ranges of $\varepsilon_r < 0$.

## 4 Possible Applications Using Silver–Air Mixtures

Above, we have ignored losses and silently assumed that the mixtures can be homogenized using a static effective permittivity. In the following, we consider more realistic silver–air mixtures, either cylindrical silver-nanorods in air (small $p$) or silver with cylindrical nanoholes (large $p$). We still assume that the geometrical details are small enough compared with the wavelength, so that a quasistatic approximation is reasonable. For the complex relative permittivity of silver, we use the Drude model

$$\varepsilon_\mathrm{r}(\lambda) = \varepsilon_\mathrm{r}' - \mathrm{j}\,\varepsilon_\mathrm{r}'' = \varepsilon_\infty - \frac{(\lambda/\lambda_\mathrm{p})^2}{1-\mathrm{j}\lambda/\lambda_\mathrm{d}} \,, \qquad \begin{cases} \varepsilon_\infty = 5.5 \\ \lambda_\mathrm{p} = 130\,\mathrm{nm} \\ \lambda_\mathrm{d} = 30\,\mu\mathrm{m} \end{cases} , \tag{7}$$

where the parameters are optimized to match the measured values in [5] for ultraviolet A and visible wavelengths. For these wavelengths, $320\,\mathrm{nm} < \lambda < 700\,\mathrm{nm}$, the real part of the permittivity is negative, $-24 < \varepsilon_\mathrm{r}' < 0$, while the imaginary part is relatively small, $\varepsilon_\mathrm{r}'' \ll \varepsilon_\mathrm{r}'$.

The considered mixtures are anisotropic, with dyadic effective permittivity

$$\overline{\overline{\varepsilon}}_\mathrm{eff} = \varepsilon_\mathrm{eff,t}(\mathbf{u}_x\mathbf{u}_x + \mathbf{u}_y\mathbf{u}_y) + \varepsilon_\mathrm{eff,z}\mathbf{u}_z\mathbf{u}_z \,, \tag{8}$$

if we assume that the cylinders or holes are parallel with the $z$-axis. The axial permittivity is obviously the weighted average of the components

$$\varepsilon_\mathrm{eff,z} = p\,\varepsilon_\mathrm{r} + (1-p) \,, \tag{9}$$

while the transversal permittivity $\varepsilon_\mathrm{eff,t}$ can be estimated using the above mixing rules.

### 4.1 Transparency

To get perfect transparency, the effective permittivity should be $\varepsilon_\mathrm{eff} = +1$, which seems to be impossible unless $p = 0$, but we can at least try to obtain $\varepsilon_\mathrm{eff,t} \approx +1$. Considering the above mixing rules, the most promising possibility seems to be to use a mixture with large enough holes in silver, and $\varepsilon_\mathrm{r}$ near $-1$. The complementary Maxwell Garnett formula predicts $\varepsilon_\mathrm{eff,t} = +1$ for any $p > 0$ if $\varepsilon_\mathrm{r} = -1$, which is clearly wrong. However, using the Rayleigh formula we see that, at both sides of the singularity near $\varepsilon_\mathrm{r} = -1$, we could get $\varepsilon_\mathrm{eff,t} \approx +1$, as shown in Fig. 9.

### 4.2 Near-field superlens

A perfect lens [13] needs $\varepsilon_\mathrm{eff} = \mu_\mathrm{eff} = -1$, but for a near-field superlens (NFSL) it is sufficient to obtain $\varepsilon_\mathrm{eff} = -1$. Pure silver has $\varepsilon_\mathrm{r} = -1 - \mathrm{j}0.07$ at $\lambda = 331\,\mathrm{nm}$

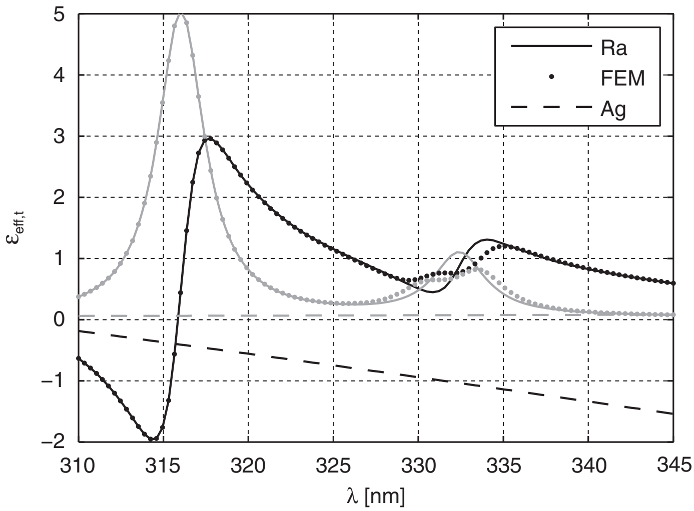


**Fig. 9** Effective permittivity, as a function of free-space wavelength, for a mixture with $p = 60\%$ silver and 40% air-holes. The Rayleigh estimate (Ra) and quasistatic FEM-result for a periodic lattice are shown, compared with the permittivity of pure silver (Ag). The real parts are shown in black and the imaginary part in gray. Near 326 nm and 338 nm, the effective permittivity $\varepsilon_{\text{eff,t}}$ is close to $+1$.

according to the Drude model (7). It would be highly useful to tune the wavelength of the superlens, as suggested in [2], using a suitable mixture of silver and an ordinary dielectric.

According to the complementary Maxwell Garnett rule, the effective relative permittivity $\varepsilon_{\text{eff,t}} = -1$ when

$$p = 1 - \frac{(1+\varepsilon_r)^2}{(1-\varepsilon_r)^2}\,, \tag{10}$$

which is also plotted in Fig. 10 along with the (numerically solved) corresponding value using the complementary Rayleigh rule.

For instance, using a mixture with $p = 50\%$ silver and 50% air-holes and operating at the free-space wavelength $\lambda = 444\,\text{nm}$, which is in the visible violet/blue-region, we get

$$\varepsilon_r = -6.16 - \mathrm{j}0.17 \quad \text{and} \quad \varepsilon_{\text{eff,t}} = -1.00 - \mathrm{j}0.058\,, \tag{11}$$

using the Drude model and the complementary Rayleigh formula. For a regular lattice, the quasistatic FEM-solution as well as the series solution gives the same $\varepsilon_{\text{eff,t}}$ with three digits accuracy. The axial effective permittivity is not $-1$ but instead $\varepsilon_{\text{eff,z}} = -2.58 - \mathrm{j}0.086$, but this is not necessarily a problem for a NFSL that works for only one polarization (TM). If we choose the orientation so that the TM-fields are

$$\mathbf{H} \parallel \mathbf{u}_z \qquad \text{and} \qquad \mathbf{E} \perp \mathbf{u}_z\,, \tag{12}$$

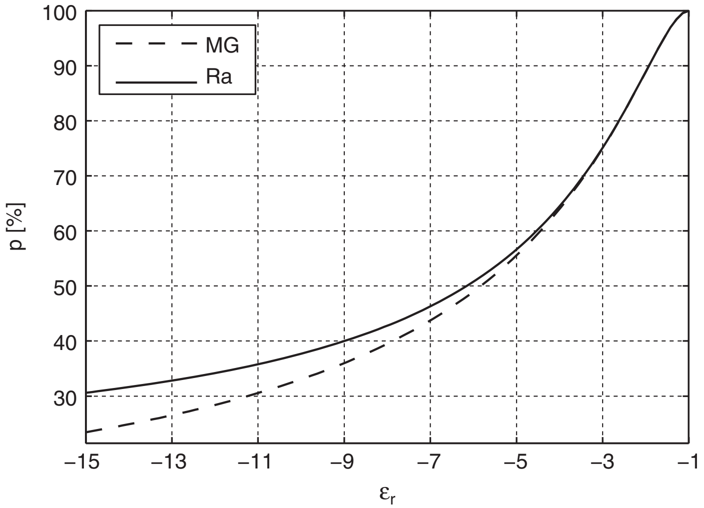


**Fig. 10** Mixture with holes with $\varepsilon_{\mathrm{eff,t}} = -1$ according to the Maxwell Garnett (MG) and Rayleigh (Ra) formulas.

then $\varepsilon_{\mathrm{eff,z}}$ can have any value and only $\varepsilon_{\mathrm{eff,t}}$ is significant for the superlensing effect. However, the composite is then a silver slab with cylindrical holes inside the slab – instead of holes through the slab, which would certainly be easier to manufacture.

## *4.3 Extreme Anisotropy*

The final example is a mixture with very large transversal permittivity and near-zero axial permittivity. The Maxwell Garnett formula (1) predicts infinite transversal permittivity $\varepsilon_{\mathrm{eff,t}}$ when

$$p = \frac{\varepsilon_{\mathrm{r}} + 1}{\varepsilon_{\mathrm{r}} - 1}\,, \tag{13}$$

while the axial permittivity $\varepsilon_{\mathrm{eff,z}}$ is zero when

$$p = \frac{1}{1 - \varepsilon_{\mathrm{r}}}\,. \tag{14}$$

These two coincide when $p = 1/3$ and $\varepsilon_{\mathrm{r}} = -2$. Similarly, the Rayleigh formula gives the numerical values $p = 33.0\%$ and $\varepsilon_{\mathrm{r}} = -2.03$.

Using a mixture with $p = 33.0\%$ silver rods in air and operating at the free-space wavelength $\lambda = 357\,\mathrm{nm}$, we get

$$\varepsilon_{\mathrm{r}} = -2.03 - \mathrm{j}0.09, \quad \varepsilon_{\mathrm{eff,t}} = -\mathrm{j}33, \quad \text{and} \quad \varepsilon_{\mathrm{eff,z}} = -\mathrm{j}0.03, \tag{15}$$

where the anisotropy is finite, but still very large: $\varepsilon_{\mathrm{eff,t}}/\varepsilon_{\mathrm{eff,z}} = 1100$.

## 5 Conclusion

In this paper, we have considered the quasistatic effective permittivity of plasmonic mixtures with cylindrical inclusions (or holes) in a regular or almost regular lattice. For these composites, the mixing formulas by Maxwell Garnett and Lord Rayleigh give surprisingly accurate results. The Maxwell Garnett formula predicts the location and effect of one plasmonic resonance, while the more accurate Rayleigh formula predicts two plasmonic resonances, which seems to be sufficient to predict the effective permittivity when the volume fraction is $p < 25\%$ and $p < 50\%$, respectively, and $\varepsilon_r \neq -1$. The Bruggeman formula is clearly not useful for this particular kind of mixture.

Among the considered possible applications, the extremely anisotropic composite seems to be the most promising one. Ideally, the effective permittivity would be given by (8) with $\varepsilon_{\text{eff,t}} \to \infty$ and $\varepsilon_{\text{eff,z}} = 0$. The effective permittivity becomes finite and nonzero for a silver–air composite, but the anisotropy-contrast $\varepsilon_{\text{eff,t}}/\varepsilon_{\text{eff,z}}$ can still very large. This could perhaps be useful for optical nanocircuits [3], where materials with $\varepsilon_{\text{eff}} \approx 0$ and $|\varepsilon_{\text{eff}}| \gg 1$ are needed. Also the composite near-field superlens could be useful, since the tunability range (in terms of $\varepsilon_r$ or $\lambda$) is quite large, unless the structure is too difficult to manufacture in practice.

**Acknowledgements** This work was supported by the Academy of Finland.

## References

1. Bruggeman DAG (1935) Berechnung verschiedener physikalischer Konstanten von heterogenen Substanzen. I. Dielektrizitätskonstanten und Leitfähigkeiten der Mischkörper aus isotropen Substanzen. Ann Physik 24:636–679
2. Cai W, Genov DA, Shalaev VM (2005) Superlens based on metal-dielectric composites. Phys Rev B 72(19):193101
3. Engheta N (2007) Circuits with light at nanoscales: Optical nanocircuits inspired by metamaterials. Science 317:1698–1702
4. Fourn C, Brosseau C (2008) Electrostatic resonances of heterostructures with negative permittivity: Homogenization formalisms versus finite-element modeling. Phys Rev E 77(1):016603
5. Johnson PB, Christy RW (1972) Optical constants of the noble metals. Phys Rev B 6(12):4370–4379
6. Lord Rayleigh (1892) On the influence of obstacles arranged in rectangular order upon the properties of a medium. Phil Mag 34:481–502
7. Mackay TG (2007) On the effective permittivity of silver–insulator nanocomposites. J Nanophotonics 1:019501
8. Mackay TG, Lakhtakia A (2004) A limitation of the Bruggeman formalism for homogenization. Opt Comm 234:35–42
9. Maxwell Garnett JC (1904) Colours in metal glasses and metal films. Trans Royal Soc (London) 203:385–420
10. McPhedran RC, McKenzie DR (1980) Electrostatic and optical resonances of arrays of cylinders. Appl Phys 23:223–235
11. Mejdoubi A, Brosseau C (2007) Numerical calculations of the intrinsic electrostatic resonances of artificial dielectric heterostructures. J Appl Phys 101:084109

12. Nonaka S, Kawajiri K, Yasuba H, Sugiyama T, Ivanov ST (2002) Novel optical surface plasmon propagating along a planar metal with nano-dielectric particles. Jpn J Appl Phys 41:4798–4801
13. Pendry JB (2000) Negative refraction makes a perfect lens. Phys Rev Lett 85(18):3966–3969
14. Shi L, Gao L, He S, Li B (2007) Superlens from metal-dielectric composites of nonspherical particles. Phys Rev B 76(4):045116
15. Sihvola A (1999) Electromagnetic mixing formulas and applications. The Institution of Electrical Engineers, London
16. Stefanou N, Modinos A, Yannopapas V (2001) Optical transparency of mesoporous metals. Solid State Commun 118:69–73
17. Vinogradov AP, Dorofeenko AV, Zouhdi S (2008) On the effective constitutive parameters of metamaterials. Phys Usp 51(5) [In Russian: Usp Fiz Nauk 178(5):511–518]
18. Wallén H, Kettunen H, Sihvola A (2008) Mixing formulas and plasmonic composites. In: NATO ARW and META'08, Marrakesh, Morocco, pp. 485–491

# Applications of EBG in Low Profile Antenna Designs: What Have We Learned?

**Yahya Rahmat-Samii[1] and Fan Yang[2]**

[1]Department of Electrical Engineering, University of California at Los Angeles, Los Angeles, CA 90095, USA
[2]Department of Electrical Engineering, The University of Mississippi, University, MS 38677, USA

**Abstract** This chapter reviews some unique properties and applications of electromagnetic band gap (EBG) structures in antenna engineering. Advanced computation and optimization techniques are utilized to characterize and design EBG and antennas. An insight into operational physics of the EBG structures has been presented. Representative antenna examples are illustrated to show our current knowledge on the potential applications of the EBG metamaterials.

## 1 Introduction

In 1864, James Clark Maxwell documented his four famous Maxwell's equations, as shown in (1), which established the fundamental features of electromagnetic waves.

$$\begin{aligned} \nabla \times \vec{E} &= -\frac{\partial \mu \vec{H}}{\partial t} \\ \nabla \times \vec{H} &= \frac{\partial \varepsilon \vec{E}}{\partial t} + \vec{J} \\ \nabla \cdot \vec{D} &= \rho \\ \nabla \cdot \vec{B} &= 0 \end{aligned} \tag{1}$$

Tremendous amount of knowledge is hidden in these four equations. In particular, recent research advancement on metamaterials focuses on the critical roles of constitutive parameters: the permittivity $\varepsilon$ and the permeability $\mu$.

The ancient Greek prefix, *meta* (means "beyond"), has been used to describe the composite materials with unique features that do not exist in the nature [1]. Reviewing the literature, it appears that various terminologies have been used to classify metamaterials depending on their applications. As an example, "double negative (DNG) material" refers to those materials with effective negative permittivity and permeability, which results into properties such as left-handed

S. Zouhdi et al. (eds.), *Metamaterials and Plasmonics: Fundamentals, Modelling, Applications*,

(LH) wave propagation and negative index of refraction (NIR). Periodic structures that prohibit the propagation of electromagnetic waves in a certain frequency band for certain arrival angles and polarization senses are classified as electromagnetic band-gap (EBG) structures. Another important category of metamaterials consist of ground planes that exhibit unique reflection characteristics other than conventional PEC, and are defined as "artificial complex ground planes". Figure 1 shows the three basic categories of metamaterials, with some representative applications illustrated.

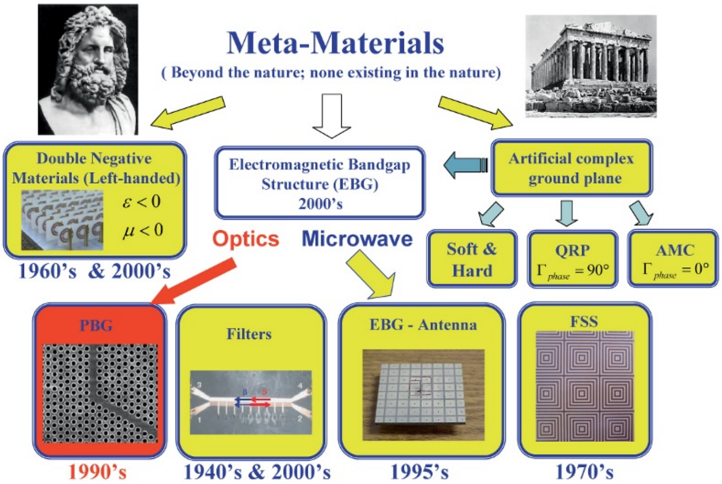


**Fig. 1** Classification of metamaterials and some representative applications.

This chapter summarizes the results published by the authors on this subject, with ample examples addressed on the analysis, designs, and applications of EBG structures in antenna engineering.

## 2 Advanced Computation and Optimization Techniques

Various structures and geometries have been proposed to achieve the exciting EBG properties. For example, Fig. 2a shows an EBG transmission line with periodic holes on the ground plane [2], Fig. 2b depicts a mushroom-like EBG surface [3], and Fig. 2c sketches a woodpile EBG structure consisting of square dielectric bars [4]. Advanced computation and optimization techniques are essential for proper designs and characterizations of these EBG structures. There are several numerical methods with various degrees of sophistication and accuracy, including plane-wave expansion and spherical-wave expansion, transfer matrix method, finite difference time domain (FDTD) method, finite element method (FEM), and method of moment (MoM). In this chapter, our focus will be on the FDTD method, because it is flexible enough to model various media and provides a broad band characterization in one single simulation [5].

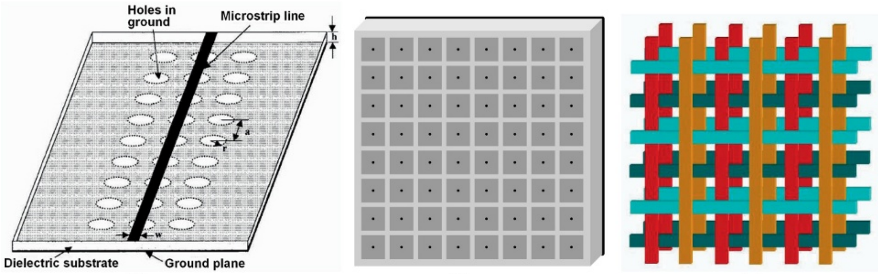


(a) (b) (c)

**Fig. 2** Various electromagnetic band gap (EBG) structures: (**a**) a one-dimensional EBG transmission line, (**b**) a two-dimensional mushroom-like EBG surface, and (**c**) a three-dimensional woodpile EBG structure.

## 2.1 *FDTD engine*

As shown in Fig. 3, a powerful FDTD computational engine has been developed at UCLA Antenna Lab to analyze various antennas and electromagnetic objects, including the EBG structures [6–9]. The FDTD engine is built based on Yee's cells, and the computational domain is truncated by the perfectly matched layers (PML). The total field/scattered field technique is implemented to simulate the plane wave incidence. Since most EBG structures are periodic composites, periodic boundary conditions (PBC) are also developed using the split field technique as well as constant $k_x$ method (Spectral FDTD). To increase the computational efficiency, some post-processing approaches are adopted, such as the Prony method and auto-regressive moving-average (ARMA) estimator.

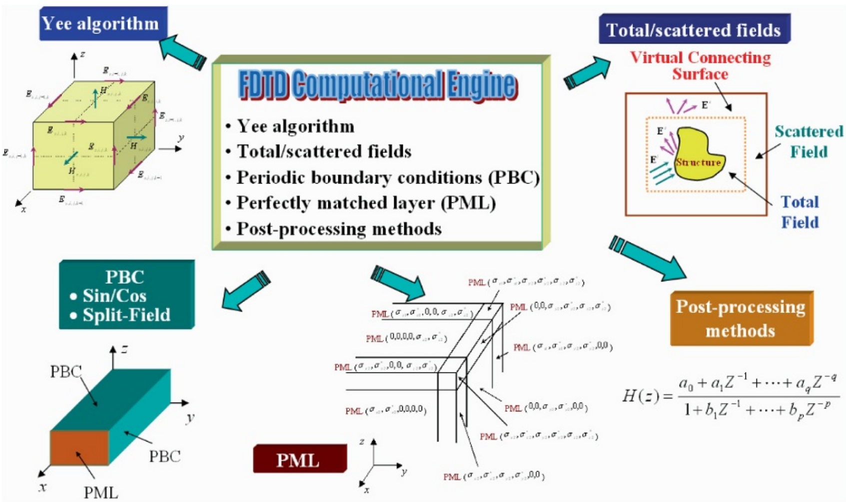


**Fig. 3** An FDTD computational engine developed at UCLA.

## *2.2 Spectral FDTD method*

In many applications, an EM structure extends to infinity in a periodic manner, such as electromagnetic band gap structures and double negative metamaterials. In this situation, periodic boundary condition (PBC) that models the effect of periodic replication is introduced to truncate the computational domain so that only a single unit cell needs to be simulated [10]. Here, a spectral FDTD method is presented, which is capable to analyze arbitrary incidence angles in a simple, efficient, and accurate manner.

*Fundamental challenge in PBC.* Periodic boundary conditions are developed based on the Floquet theory [11]. For a periodic structure with periodicity $p$ along the $x$ direction, electromagnetic fields at two boundaries $x = 0$ and $x = p$ satisfy the following equations in the frequency domain:

$$\begin{aligned}\vec{\mathrm{E}}(x=0,y,z) &= \vec{\mathrm{E}}(x=p,y,z)e^{jk_x p}\\ \vec{\mathrm{H}}(x=0,y,z) &= \vec{\mathrm{H}}(x=p,y,z)e^{jk_x p}\end{aligned} \tag{2}$$

The exponential term represents a propagation phase delay, which is determined by the propagation constant $k_x$ and the periodicity $p$. For a plane wave incidence, the propagation constant $k_x$ is determined by the frequency and incident angle:

$$k_x = k_0 \cdot \sin\theta = 2\pi f \sqrt{\varepsilon_0 \mu_0} \cdot \sin\theta \tag{3}$$

where $k_0$ is the free space wave number. However, when (3) is converted to the time domain using the Fourier transformation, one obtains:

$$\begin{aligned}\vec{E}(x=0,y,z,t) &= \vec{E}(x=p,y,z,t+p\sin\theta/C)\\ \vec{H}(x=0,y,z,t) &= \vec{H}(x=p,y,z,t+p\sin\theta/C)\end{aligned} \tag{4}$$

where $C = 1/\sqrt{\varepsilon_0\mu_0}$ is the speed of light in free space. It is noticed that when updating electric and magnetic fields in the ***current time*** ($t$), the field data in the ***future time*** ($t + p\sin\theta/C$) are needed. It opposes the causal relation in the time domain simulation.

*Spectral FDTD method.* Various PBCs have been proposed to address this challenge in the past decade, including the normal incidence method, Sin–Cosine method, split-field method, etc. It is instructive to compare these methods on a $k_x$-frequency plane, as shown in Fig. 4. For a normal incident case, $\theta = 0$ and $k_x = 0$. The reflection coefficient is calculated on the leftmost dashed line in Fig. 4. The Sin–Cosine method, which is developed to calculate the reflection coefficient at oblique incidence but only at a single frequency, is indicated by a plus sign. The wideband split field method calculates the reflection coefficient at a given incident angle, as represented by the tilted dashed line.

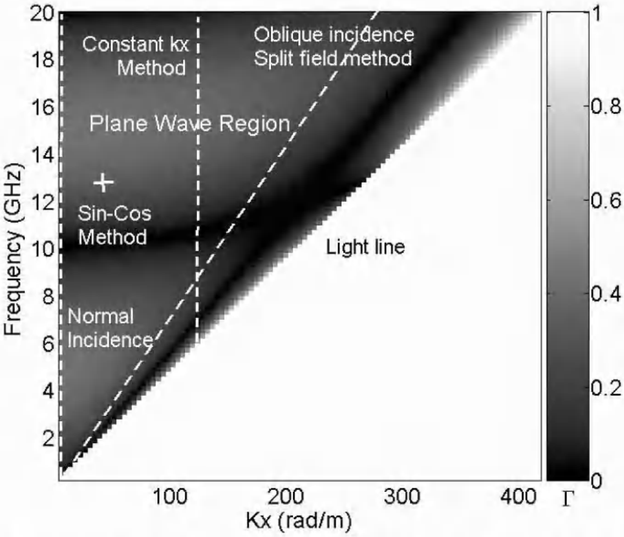


**Fig. 4** Comparison of various PBCs on a $k_x$-frequency plane. The reflection coefficient (Γ) of a dielectric slab is plotted in grayscale at different frequencies and horizontal wave numbers ($k_x$).

Alternatively, one can also calculate the reflection coefficient on a vertical line in the $k_x$-frequency plane, as represented by the middle dashed one in Fig. 4. On this line, the horizontal wave number $k_x$ is a constant. The relationship of the horizontal wave number, frequency, and incident angle is described in (3). When a constant $k_x$ is chosen, change of frequency leads to correlated change of the incident angle. Therefore, FDTD simulation is performed based on a constant $k_x$ but a variant incident angle $\theta$, which distinguishes the proposed method from the early PBC approaches.

The reason of choosing a constant $k_x$ is recognized from the transformation of (2) into the time domain, where a very simple periodic boundary condition (PBC) can be obtained:

$$\begin{aligned} \vec{E}(x=0,y,z,t) &= \vec{E}(x=p,y,z,t)e^{jk_x p} \\ \vec{H}(x=0,y,z,t) &= \vec{H}(x=p,y,z,t)e^{jk_x p} \end{aligned} \tag{5}$$

No time delay or advancement is required in this equation. Therefore, it can be directly used to update the field values on the periodic boundary. One should notice that $e^{jk_x p}$ in (5) is a complex constant number, resulting in complex E and H values in the FDTD simulation.

*Numerical example.* To demonstrate the validity of this spectral FDTD method, a periodic patch array example is illustrated here. The patch size is 5 mm and the periodicity is 10 mm. Figure 5 shows the FDTD computed reflection coefficients at different incident angles. The results obtained by the spectral FDTD method using a constant $k_x$ PBC shows a good agreement with the split field method. It is important to point out that spectral FDTD works well for large incident angles such as 85° whereas the split field method cannot give a converged result because of the prohibitive long simulation time.

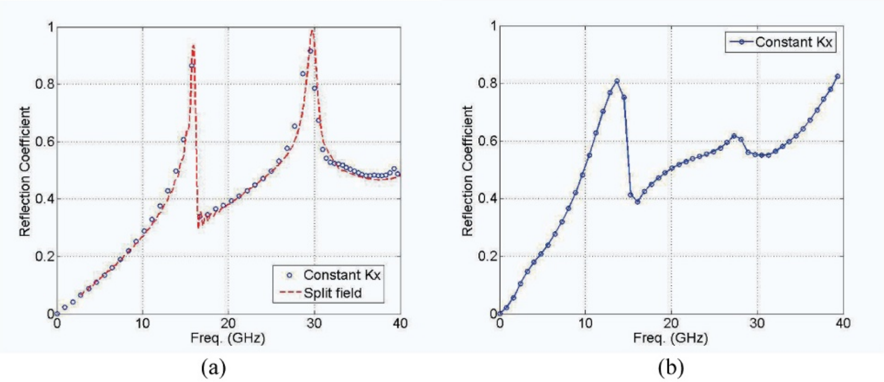


**Fig. 5** FDTD simulated results of a periodic patch array: (**a**) 60° TE incidence and (**b**) 85° TE incidence.

It is worthwhile to highlight several advantages of the spectral FDTD method. First, this algorithm is very easy to implement. In contrast to the split field method [8] that uses auxiliary fields *P* and *Q*, this approach computes *E* and *H* fields directly. Thus, no complicated formulas need to be derived and the traditional Yee's updating scheme is used. The perfectly matched layers also remain unchanged, which helps to simplify the implementation procedure. Secondly, this algorithm is efficient in calculating the scattering at large incident angles. When the split field method is used to calculate the oblique incidence, the time step size ($\Delta t$) needs to be decreased as the incident angle ($\theta$) increases. Thus the simulation time becomes prohibitively long for large incidence angles. In contrast, the spectral FDTD method uses a standard Yee's scheme to update the E and H fields. The stability condition remains unchanged regardless of the horizontal wave number ($k_x$) or incident angle.

## *2.3 Optimization methods*

To obtain desired electromagnetic properties, some evolutionary optimization algorithms, such as genetic algorithm (GA) and particle swarm optimization (PSO), are used in EBG designs and optimizations. In [12], a multi-band EBG surface is obtained using GA optimization. In [13], the PSO algorithm is linked with an FDTD kernel to optimize the performance of EBG designs. In particular, it is utilized to determine the unit cell topology of an EBG structure, in order to obtain a desired reflection phase and also achieve an equivalently miniaturized design. As a result, a compact EBG surface is obtained for low profile antenna applications. The interested readers are referred to [12–13] for in-depth discussions on this very exciting topic and additional references.

# 3 EBG Characteristics

## *3.1 Various FDTD models*

EBG structures exhibit unique electromagnetic properties, which are identified through a variety of FDTD models. Figure 6a shows a transmission line model. A microstrip line is located above an EBG surface and the transmission coefficient is computed using the FDTD method. Without the EBG surface, the transmission coefficient equals to one and all energy can pass through. When the EBG surface is used, a stop band similar to a filter is observed. This model is suitable for microwave circuit applications. Figure 6b illustrates a surface wave model. An infinitesimal dipole source is positioned in the middle of a grounded slab to excite surface waves. Without the EBG cells, strong electromagnetic fields can be observed at a reference plane. When the source is surrounded by the EBG cells, surface waves will be inhibited in a certain frequency range and weak fields are recorded at the reference plane. Figure 6c shows a dipole antenna model, where a horizontal dipole is positioned near the EBG ground plane for a low profile configuration. The resonant frequency of the antenna varies depending on the dipole length. When the frequency is within a certain range, the EBG ground provides a proper reflection phase which enhances the radiation efficiency of the antenna.

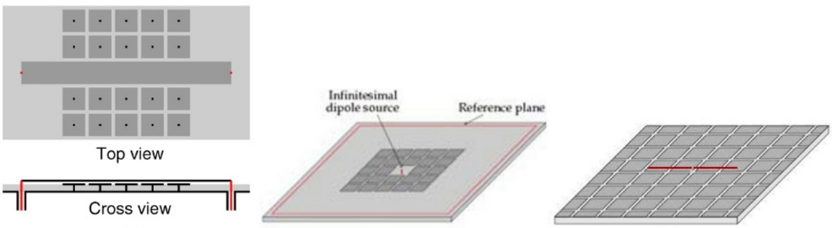


(a) (b) (c)

**Fig. 6** Various FDTD models have been used to characterize the EBG properties: (**a**) a suspended microstrip line above an EBG surface, (**b**) an infinitesimal dipole source surrounded by EBG cells, and (**c**) a horizontal dipole near an EBG ground plane.

## *3.2 From a PEC surface to an EBG surface: understanding the underlying physics*

To better understand the EBG properties, it is helpful to observe the evolution from a PEC surface to the EBG surface, as shown in Fig. 7. For a PEC surface, the frequency of 0° reflection phase, referred to as the 0°-reflection-phase frequency afterwards, starts at h = $\lambda/4$ for both TE and TM waves and shifts up to higher frequencies when the incident angle increases. When a via loaded PEC surface is considered, the 0°-reflection-phase frequency also starts at h = $\lambda/4$ for both polarizations. As the incident angles increases, TM frequency is stable whereas

TE frequency increases. For a patch loaded PEC, the 0°-reflection-phase frequency for TE polarization is angular independent, but TM frequency still vary with incident angles. When the EBG structure that includes both vias and patches is used, the 0°-reflection-phase frequency becomes stable for both TE and TM polarizations [14].

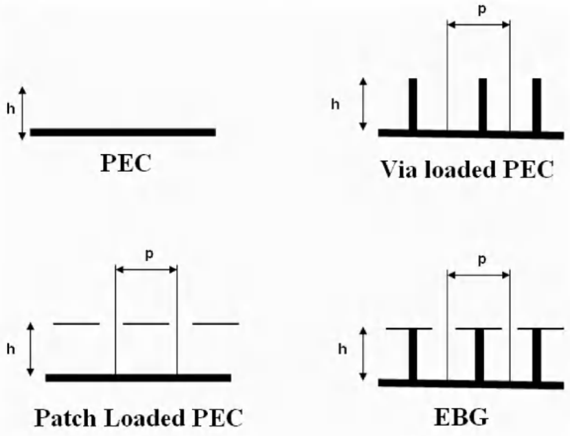


**Fig. 7** Evolution of electromagnetic band gap (EBG) surface: from a PEC to a via loaded PEC, a patch loaded PEC, and finally an EBG surface.

## *3.3 Band gap and reflection phase properties*

Two unique electromagnetic features of EBG structures can be summarized in accordance to the incident electromagnetic waves:

- When the incident wave is a surface wave ($k_x^2 + k_y^2 \geq k_0^2$), the EBG structure shows a *frequency band gap* through which the surface wave cannot propagate for any incident angles and any polarization states, resulting in an ideal isolator for electromagnetic waves.
- When the incident wave is a plane wave ($k_x^2 + k_y^2 < k_0^2$), the EBG structure has an *in-phase reflection coefficient* of +1 at a certain frequency, which resembles an ideal perfect magnetic conductor (PMC) that does not exist in nature.

In the above equations, $k_x$ and $k_y$ denote the wave numbers in the horizontal directions, while $k_0$ is the free-space wave number.

To illustrate these properties, a mushroom-like EBG structure (shown in Fig. 2b) has been analyzed and the results are presented here. The dimensions of the EBG structure are:

$$W = 0.10\lambda,\ g = 0.02\lambda,\ h = 0.04\lambda,\ \varepsilon_r = 2.94 \tag{6}$$

where $W$ is the width of the square patch, $g$ is the gap width, $h$ is the substrate thickness, and $\varepsilon_r$ is the dielectric constant of the substrate. The vias' radius in the EBG structure is $0.005\lambda$. The free-space wavelength at 4 GHz, $\lambda = 75$ mm, is used as a reference length to define the physical dimensions of the EBG structure. It is worthwhile to point out that the periodicity of the EBG structure ($0.12\lambda$) is much smaller than the wavelength.

Figure 8a shows the dispersion diagram of the EBG structure, where the vertical axis is the frequency and the horizontal axis represents the values of the horizontal wave numbers ($k_x$, $k_y$) in the Brillouin zone. Each point in the dispersion diagram represents a certain surface wave mode. It is observed that no surface waves can exist in the frequency range from 3.5 to 5.9 GHz. Thus, this frequency region is defined as a surface wave band gap of the EBG structure.

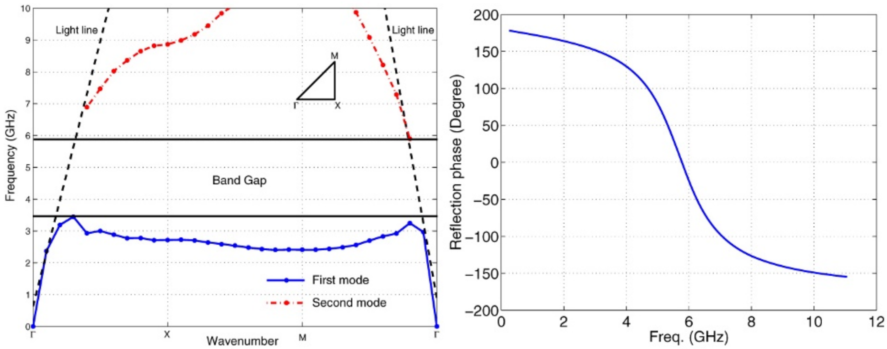

(a) (b)

**Fig. 8** Electromagnetic properties of an EBG structure characterized using FDTD method with periodic boundary conditions (PBC): (**a**) the dispersion diagram and (**b**) the reflection phase. The EBG structure exhibits a frequency band gap for surface waves and an in-phase reflection coefficient for plane-wave incidence.

Figure 8b shows the reflection phase of the EBG structure for normal incidence. The reflection phase is defined as the phase of the reflected E field normalized to the phase of the incident E field on the reflecting surface. It is well known that a perfect electric conductor (PEC) has a 180° reflection phase and a perfect magnetic conductor (PMC) has a 0° reflection phase. In contrast, the reflection phase of the EBG surface decreases monotonically from 180° to −180° as frequency increases. For example, the EBG surface exhibits a 90° reflection phase around 4.6 GHz and a 0° reflection phase at 5.8 GHz. It is important to note that the reflection phase varies with incident angles and polarization states depending on the physical structures of the EBG.

# 4 EBG Applications in Antenna Engineering

## 4.1 Patch antennas and EBG structures

Patch antennas residing on high dielectric constant substrates are broadly used due to their compact size and conformability with monolithic microwave integrated circuits (MMICs). Unfortunately, utilization of high dielectric constant substrates results in a narrow bandwidth and pronounced surface waves. The bandwidth can be improved using a thick substrate; however, this excites severe surface waves, which will decrease the antenna efficiency, degrade the antenna pattern, and increase the mutual coupling between the elements in a patch antenna array.

The mushroom-like EBG structure exhibits a surface wave band gap feature, which is utilized in patch antenna designs. Some beneficial effects are reported in [15]. Figure 9a shows the photo of a patch antenna surrounded by four rows of EBG cells. The radiation pattern of the antenna has been measured and compared to a conventional patch antenna. It is noticed that the antenna with EBG outperforms the conventional design: its front radiation is 3 dB higher while its back lobe is more than 15 dB lower than the one without EBG.

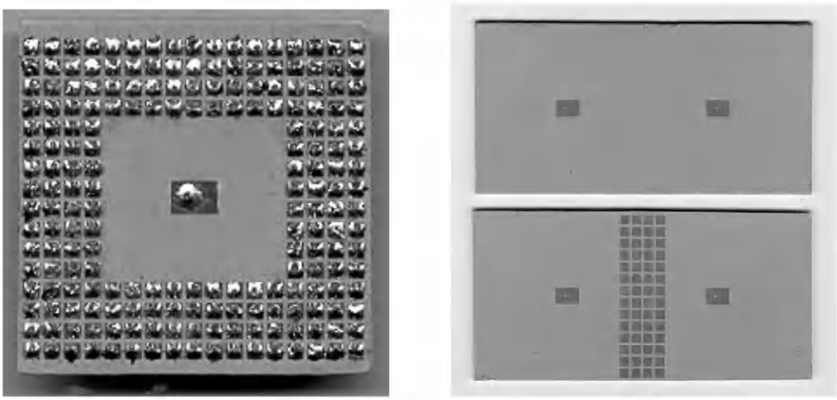

(a) (b)

**Fig. 9** Photos of (**a**) a microstrip patch antenna surrounded by an EBG structure and (**b**) microstrip antenna arrays without EBG (*above*) and with EBG (*below*).

This approach has also been extended to array applications to reduce the mutual coupling between antenna elements. Figure 9b shows photographs of the fabricated antenna arrays with and without EBG structure in between. It has been observed that both antennas resonate at 5.86 GHz with return losses better than −10 dB. For the antenna array without EBG structure, the mutual coupling at 5.86 GHz is −16.8 dB. As a comparison, the mutual coupling of the antenna array with EBG in between is only −24.6 dB. An about 8 dB reduction in the mutual coupling is achieved due to the EBG structure [15].

## *4.2 Low profile antennas*

Another EBG application is to design low profile wire antennas, which is favorable in modern wireless communication systems. To illustrate the fundamental principle, Fig. 10 compares the EBG with the traditional PEC ground plane in antenna designs. When an electric current is vertical to a PEC ground plane, the image current has the same direction and reinforces the radiation from the original current. This antenna has good radiation efficiency, but suffers from relative large height due to the vertical placement of the current. To realize a low profile configuration, one may position a wire antenna horizontally close to the ground plane. However, the problem in this structure is the poor radiation efficiency because the opposite image current cancels the radiation from the original current. Traditionally, equivalent magnetic currents near a PEC ground plane have been used, which has lead to a profusion of microstrip antennas. Recently, it has been shown that the EBG surface is capable in generating a constructive image for the electric current within a certain frequency band, resulting in a good efficiency of low profile wire antenna. Therefore, the wire-EBG antenna becomes a new frontier in antenna area, which could provide a useful alternative to microstrip antennas.

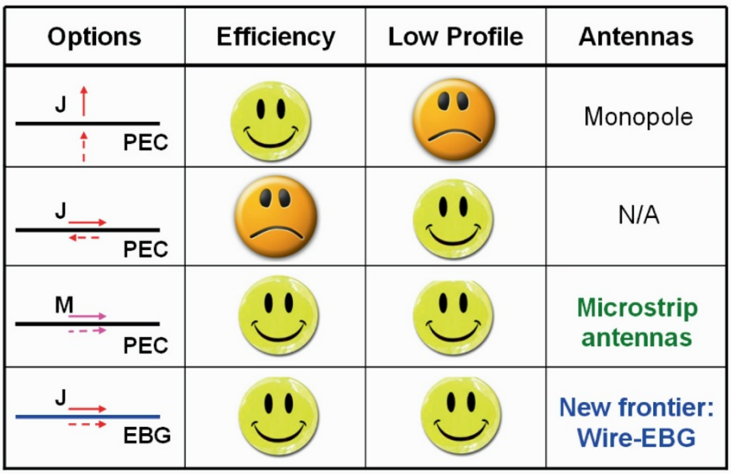


**Fig. 10** Comparisons of conventional PEC and EBG ground planes in antenna designs. The wire-EBG antenna is a new type of low profile antennas.

*Circularly polarized (CP) antennas.* Various low profile wire-EBG antennas have been developed to realize diverse radiation performance. Circularly polarized (CP) antennas are desired in many communication systems such as the Global Positioning System (GPS) and satellite links. The EBG ground plane is implemented in low profile CP wire antenna designs. The first approach is to replace the PEC ground of a curl antenna with an EBG ground, as shown in Fig. 11a. The circular polarization is generated by the traveling current along the curl and the EBG ground plane helps to improve the radiation efficiency of the curl in a low profile configuration [16]. It is noticed that the overall antenna height (0.07λ) is much smaller than that of a conventional curl design on a PEC ground plane (0.25λ). Figure 11b presents the second approach for low profile CP wire antenna design where a linearly polarized dipole is used instead of the CP curl [17]. The circular polarization pattern of the overall antenna is realized by the superposition of the directly radiating wave from the dipole and the reflected wave from the EBG ground plane. A polarization-dependent EBG (PDEBG) ground plane has been uniquely designed and implemented so that the reflected wave has a perpendicular polarization direction to the directly radiating wave as well as a 90° phase shift [18].

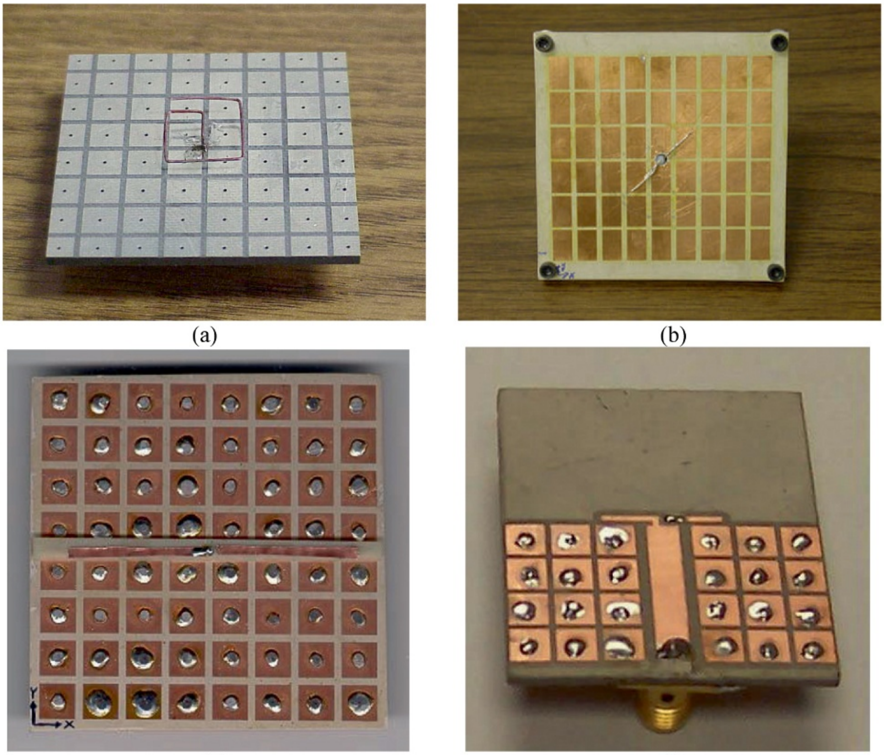

(a) (b) (c) (d)

**Fig. 11** Various EBG applications in low profile antenna designs: (**a**) a CP curl antenna, (**b**) a dipole antenna on a PDEBG surface for CP performance, (**c**) a reconfigurable bent monopole antenna with radiation pattern diversity, (**d**) a dipole antenna near a semi-EBG ground for WLAN application.

*Reconfigurable antenna with radiation pattern diversity.* Reconfigurable antennas are desirable in modern wireless communication systems because they can provide more functionalities than ordinary antennas by reconfiguring their operating frequencies, polarizations, and radiation patterns. Figure 11c shows the photo of a reconfigurable wire-EBG antenna, where a feeding probe is connected to two metal strips through two switches [19]. When the left switch is ON and the right switch is OFF, the probe has an electrical connection to the left strip, resulting in a bent monopole oriented along the $-x$ direction. When the left switch is OFF and the right switch is ON, a bent monopole oriented along the $+x$ direction is obtained. As a consequence, the direction of the antenna beam can be switched in space and the diversity in the radiation pattern is realized. The measured radiation patterns reveal that the antenna beam can be switched between ±26°.

*Dipole antenna for WLAN applications.* Figure 11d shows the photo a printed dipole antenna design with a semi-EBG ground plane [20]. The radiation efficiency of the dipole antenna is significantly improved when a PEC ground plane is replaced by the EBG ground plane. This antenna prototype realizes a 9.4% bandwidth and an omni-directional pattern. This design is particularly useful for the internal wireless local area network (WLAN) antennas of laptop computers.

## 4.3 Surface wave antenna

The concept of surface wave antenna (SWA) [21] was proposed in 1950s. To trap and guide surface waves, a commonly used structure in SWA is the corrugated metal surface. However, the quarter-wavelength height of the corrugated structure, which is relatively large for many wireless communication systems, limits the SWA applications. The recent advancement on metamaterials [22] and artificial electromagnetic surfaces [23] have provided new opportunities for novel SWA designs. In particular, a patch loaded slab (no vias) can support a tightly bounded surface wave within a thin substrate [24].

In this section, a recently reported patch-fed surface wave antenna (PFSWA) is presented. The objective is to realize a monopole like radiation pattern, which is widely used in wireless communications such as radio broadcast and wireless local area network (WLAN). Since the vertical monopole antenna is not recommended in low profile applications, an alternative approach is to use higher order modes of circular or annular-ring microstrip antennas [25–26]. However, the

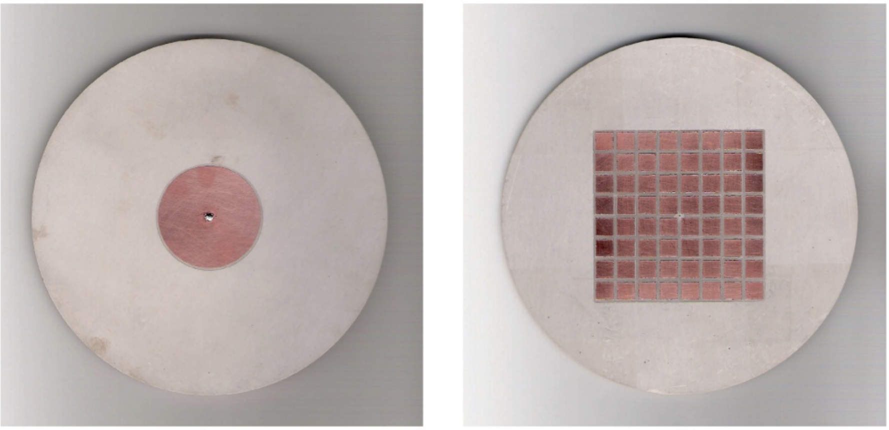

(a) (b)

**Fig. 12** Photos of a fabricated PFSWA: (**a**) a center-fed circular patch in the middle layer, and (**b**) periodic square patch array on the top layer.

microstrip antennas usually suffer from a narrow impedance bandwidth because of the high Q resonance. The proposed PFSWA utilizes the diffractions of surface waves at the boundary of the ground plane to form a monopole like pattern [27]. An attracting feature of this PFSWA design is the low profile geometry of the entire antenna structure, which is realized by a thin grounded slab with periodic patch loading.

An antenna prototype has been fabricated and tested to demonstrate the PFSWA concept. Figure 12a shows the photo of the excitation circular patch fabricated on a 60 mil (1.524 mm) thick RT/duroid 6002 high frequency laminate ($\varepsilon_r = 2.94 \pm 0.04$). A 50 Ω SMA connector is soldered to the center of the circular patch. Figure 12b is a photo of 8 × 8 periodic patches loading fabricated on another dielectric slab. These two layers are stacked together to form a complete PFSWA structure.

The return loss of the PFSWA has been measured and compared with a conventional center fed patch antenna. The patch antenna has large input impedance and high Q factor, resulting in a poor return loss of only −6 dB. In contrast, the PFSWA has achieved a good return loss near −30 dB because of the efficient launching of the surface waves in the artificial ground plane. The periodic square patches successfully convert the electromagnetic fields underneath the circular patch into the surface waves propagating along the ground plane. Thus, the Q factor of the entire radiating structure is reduced and a better return loss is obtained.

The radiation patterns of the PFSWA have also been measured at the resonant frequency, which resemble a monopole pattern [27]. The xz plane ($\varphi = 0°$) and diagonal plane ($\varphi = 45°$) patterns are almost identical to each other. It has a deep null in the broad side direction and the antenna beam is at $\theta = 47°$ direction with a gain of 5.6 dBi. The co-polarization is along the $\theta$ direction, and the cross polarization is 25 dB lower than the co-polarization in the front side.

## 5 Conclusions

This invited chapter highlights and summarizes some of the recent research activities and experiences of the authors in the area of electromagnetic band gap structures for antenna applications. The underlying operational physics of the EBG structures are discussed. Advanced computation and optimization techniques are referred to for realistic EBG and antenna designs. Furthermore, representative examples are presented to demonstrate the potential utility of the EBG metamaterials.

As a forecast for the future EBG metamaterial research, the following topics are suggested to challenge the researchers and engineers:

- Seeking miniaturizations in all three dimensions by searching for evolutionary concepts
- Sorting out what are truly unique and novel developments vs. just another hypothetical exercise

- Identifying real-life applications and potential users
- Developing cost effective implementations and manufacturing

We hope this chapter will stimulate discussions and pave the way for new avenues of research in EBG metamaterials.

## References


1. N. Engheta and R. Ziolkowski, *Metamaterials: Physics and Engineering Explorations*, New York: Wiley, 2006.
2. V. Radisic, Y. Qian, R. Coccioli, and T. Itoh, "Novel 2-D photonic bandgap structure for microstrip lines," *IEEE Microw. Guided Wave Lett.*, vol. 8, no. 2, pp. 69–71, Feb. 1998.
3. D. Sievenpiper, L. Zhang, R. F. J. Broas, N. G. Alexopolus, and E. Yablonovitch, "High-impedance electromagnetic surfaces with a forbidden frequency band," *IEEE Trans. Microw. Theory Tech.*, vol. 47, pp. 2059–2074, Nov. 1999.
4. E. Ozbay, A. Abeyta, G. Tuttle, M. Tringides, R. Biswas, T. Chan, C. M. Soukoulis, and K. M. Ho, "Measurement of a three-dimensional photonic band gap in a crystal structure made of dielectric rods," *Phys. Rev. B, Condens. Matt.*, vol. 50, no. 3, pp. 1945–1948, July 1994.
5. A. Taflove and S. Hagness, *Computational Electrodynamics: The Finite Difference Time Domain Method*, 2nd Ed., Artech House, Boston, MA, 2000.
6. M. A. Jensen, *Time-Domain Finite-Difference Methods in Electromagnetics: Application to Personal Communication*, Ph.D. dissertation at University of California, Los Angeles, CA, 1994.
7. H. Mosallaei and Y. Rahmat-Samii, "Periodic bandgap and effective dielectric materials in electromagnetics: characterization and applications in nanocavities and waveguides," *IEEE Trans. Antenn. Propag.*, vol. 51, no. 3, 549–563, Mar. 2003.
8. A. Aminian, F. Yang, and Y. Rahmat-Samii, "Bandwidth determination for soft and hard ground planes by spectral FDTD: a unified approach in visible and surface wave regions," *IEEE Trans. Antenn. Propag.*, vol. 53, no. 1, pp. 18–28, Jan. 2005.
9. Y. Rahmat-Samii and H. Mosallaei, "Electromagnetic band-gap structures: classification, characterization and applications," *Proceeding of the IEE-ICAP Symposium*, pp. 560–564, April 2001.
10. J. Maloney and M. P. Kesler, "Chapter 13: Analysis of periodic structures," *Computational Electrodynamics: The Finite Difference Time Domain Method*, 2nd Ed., A. Taflove and S. Hagness, Artech House, Boston, MA, 2000.
11. L. Brillouin, *Wave Propagation in Periodic Structures*, 2nd Ed., Dover, New York, 2003.
12. D. J. Kern, D. H. Werner, A. Monorchio, L. Lanuzza, and M. J. Wilhelm, "The design synthesis of multiband artificial magnetic conductors using high impedance frequency selective surfaces," *IEEE Trans. Antenn. Propag.*, vol. 53, no. 1, Part 1, pp. 8–17, Jan. 2005.
13. N. Jin and Y. Rahmat-Samii, "Particle swarm optimization of miniaturized quadrature reflection phase structure for low-profile antenna applications," *2005 IEEE AP-S Int. Symp. Dig.*, vol. 2B, pp. 255–258, July 2005.
14. Y. Rahmat-Samii, "Metamaterials in antenna applications: classifications, designs and applications," *IWAT Proc.*, 2006.
15. F. Yang and Y. Rahmat-Samii, "Microstrip antennas integrated with electromagnetic band-gap (EBG) structures: a low mutual coupling design for array applications," *IEEE Trans. Antenn. Propag.*, vol. 51, no. 10, pp. 2936–2946, Oct. 2003.
16. F. Yang and Y. Rahmat-Samii, "A low profile circularly polarized curl antenna over electromagnetic band-gap (EBG) surface," *Microw. Opt. Technol. Lett.*, vol. 31, no. 3, pp. 165–168, 2001.

17. F. Yang and Y. Rahmat-Samii, "A low profile single dipole antenna radiating circularly polarized waves," *IEEE Trans. Antenn. Propag.*, vol. 53, no. 9, pp. 3083–3086, Sep. 2005.
18. F. Yang and Y. Rahmat-Samii, "Polarization dependent electromagnetic band gap (PDEBG) structures: designs and applications," *Microw. Opt. Technol. Lett.*, vol. 41, no. 6, pp. 439–444, July 2004.
19. F. Yang and Y. Rahmat-Samii, "Bent monopole antennas on EBG ground plane with reconfigurable radiation patterns," *2004 IEEE APS Inter. Symp. Digest*, vol. 2, pp. 1819–1822, June 20–26, 2004.
20. F. Yang, V. Demir, D. Elsherbeni, A. Elsherbeni, and A. Eldek, "Enhancement of printed dipole antennas characteristics using semi-EBG ground plane," *J. Electromagnet. Wave. Appl.*, vol. 20, no. 8, pp. 993–1006, June 2006.
21. F. J. Zucker, "Surface-wave antennas," Chapter 12 of *Antenna Engineering Handbook*, 3rd Ed., Richard C. Johnson, McGraw-Hill, New York, 1993.
22. IEEE Trans. Antenn. Propag., Special Issue on Meta-materials, vol. 51, no. 10, Oct. 2003.
23. IEEE Trans. Antenn. Propag., Special Issue on Artificial Magnetic Conductors, Soft/Hard Surfaces and other Complex Surfaces, vol. 53, no. 1, Jan. 2005.
24. A. Al-Zoubi, F. Yang, and A. Kishk, "A low profile dual band surface wave antenna with a monopole like pattern," *IEEE Trans. Antenn. Propag.*, pp. 3404–3412, Dec. 2007.
25. J. Huang, "Circularly polarized conical patterns from circular microstrip antennas," *IEEE Trans. Antenn. Propag.*, vol. 32, pp. 991–994, Sep. 1984.
26. L. Economou and R. J. Langley, "Patch antenna equivalent to simple monopole," *Electronic Lett.*, vol. 33, no. 9, pp. 727–729, Nov. 1999.
27. F. Yang, Y. Rahmat-Samii, and A. Kishk, "A low profile surface wave antenna for wireless communications," *IET Proc. Microw. Antenn. Propag.*, vol. 1, no. 1, pp. 261–266, Feb. 2007.

# Negative Index Metamaterial Lens for the Scanning Angle Enhancement of Phased-Array Antennas

**Tai Lam, Claudio Parazzoli, and Minas Tanielian**

The Boeing Company, M/C 3W-50, P.O. Box 3707, Seattle, Washington, USA
tai.a.lam@boeing.com

**Abstract** The unique electromagnetic properties of negative index metamaterials (NIM) provide enormous flexibility in lens design resulting in lenses with better performance and lighter weight. This work presents the design and full wave simulations of a NIM lens to enable a Phased-Array Antenna (PAA) to scan to the horizon. Simulation and optimization techniques are discussed in detail with fabrication issues considered along the way. Simplified 2D effective medium simulations are used to explore the design space and optimize lens geometry and material makeup. More computationally intensive effective medium simulations in 3D are then performed for a better assessment of the antenna performance. Material an-isotropy is then explored to find the lowest order material for easier fabrication while maintaining desired beam characteristics. The conformal mapping technique of transformation optics is used to convert lens shapes into contours that are easier to fabricate. We also discuss on going investigations of alternative NIM materials with higher level isotropy.

## 1 Introduction

It has been only about a decade ago since Pendry proposed the realization of NIM by using split resonance rings (SRR's) and wires [1, 2]. The SRR's provide negative magnetic permeability while the wires provide negative electric permittivity. Combined together, the SRR's and the wires generate a medium with negative index of refraction and new propagation properties that were predicted by Veselago in 1968 [3]. In 2000 Smith et al. demonstrated the first practical realization of NIM in the microwave frequencies [4].

NIM allows independent design and control of the permittivity and permeability and proves to be the ultimate electromagnetic 'designer material.' Since its

S. Zouhdi et al. (eds.), *Metamaterials and Plasmonics: Fundamentals, Modelling, Applications*,

experimental verification NIM has seen many practical applications in antenna miniaturization [5], flat gradient index lenses [6, 7], invisibility cloaking devices [8], and superlenses that could overcome the diffraction limits [9], to name but a few major examples. The properties of NIM that makes it beneficial for lenses are the focusing of evanescent fields, negative Snell's law, and the ability to match impedance to that of free space to minimize reflections and scattering.

This work presents the design and simulation of a NIM lens to enhance the scanning angle of a Phased-Array Antenna (PAA). A major limitation of PAA's is the inability to scan the beam close to the horizon. Most available PAA systems have a maximum usable scanning angle of about 60° from the vertical axis [10]. One method of increasing the scanning angle is the utilization of mechanical augmentations, such as gimbaled systems. Mechanical augmentations sacrifice the main benefit of a PAA, which is the ability to electronically scan without the mechanical time delay and overshoot. Mechanical augmentations also increase system size and weight making it undesirable for airplanes and satellites platforms, where the latter would also require more utilization of the inertial correction system.

In Section 2 we describe the NIM lens design and simulation techniques. A working prototype PAA is simulated in 3D using full wave simulations. The resulting beam is subsequently used to illuminate the lens being designed. To speed up the optimization process another PAA and lens simulation setup is performed in 2D to allow for faster exploration of the design space. The optimized lens design found in 2D is then be re-analyzed in 3D for more accurate results. 3D simulation is also used as a virtual prototyping tool to explore NIM material anisotropy and fabrication issues.

In Section 3 we discuss the various challenges faced while trying to fabricate the lens. Most of the difficulties are due to the geometry limitations of SRR's and wires, where unit cells with a cubic lattice are mapped to spherical domain. To acquire a lens shape that is easier to fabricate, conformal transformation technique is used to map a lens from one shape to another. Due to material limitations mentioned a partial lens is being fabricated in our lab. It is challenging to build a fully isotropic material from SRR's and wires, therefore alternative isotropic NIM materials are being explored.

## 2 Simulation and Design Optimization

In this section we describe 3D full wave simulations of an actual PAA. The resulting beam is then used for the lens design. The simulation techniques are described in detail and the beam is characterized and compared to known results. As an intermediate step in lens design, numerous 2D simulations are performed to speed up the design space exploration and optimization process.

The optimized lenses found using 2D simulations are used as starting points for 3D lens designs. From a practical standpoint isotropic NIM materials are very difficult to fabricate, especially if using the SRR's and wires medium. To alleviate fabrication issues lenses using NIM with reduced material isotropy are explored. The electric permittivity and magnetic permeability dyadics of the anisotropic materials are transformed from spherical coordinates, which is required by the lens, to Cartesian coordinates required by the simulation software. Far-field intensities and polarization ratios are compared between the various lenses.

## 2.1 Simulation geometry and setup

Lens design work requires the ability to simulate the full PAA beam output. Since the lens is located in the near-field of the PAA, geometrical ray tracing approximations cannot be used. Full wave 3D simulations are carried out modeling an actual PAA built by the Boeing Phased-Array Antenna Group. This particular PAA will be used later for lens measurement and performance characterization once it is fabricated.

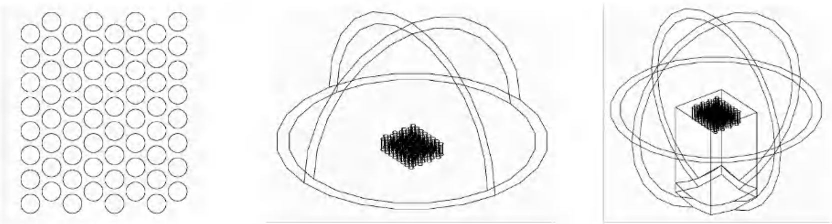

(a) (b) (c)

**Fig. 1** (**a**) Waveguide elements layout of an 8 × 8 PAA and simulation domains using (**b**) a hemisphere and (**c**) a sphere.

The specific PAA mentioned has 8 × 8 elements, arranged in a triangular lattice, and operates at 14.25 GHz center frequency in the Ku-Band. Figure 1a shows the layout of the 64 waveguide elements. The simulation domain shown in Fig. 1b consists of a hemisphere whose radius is ten free space wavelengths $\lambda_0$, and lies directly on top of the waveguide output ports. To reduce backscattering a perfectly matched layer (PML) one $\lambda_0$ thick is wrapped around the hemisphere domain. The outer boundaries of the PML are set as scattering boundary to further emulate an open boundary. The equatorial plane of the hemisphere is described as perfect electric conductor (PEC) except at the waveguide output ports.

Figure 1c shows a variation of Fig. 1b where the simulation space takes the shape of a near complete sphere. This setup, while computationally more intensive with almost twice the volume, is useful for below horizon beam steering investigations.

The ground plane for this setup is the small square shown encompassing the waveguides. The hemisphere layout is limited to half-space investigations because the beam, even if the lens is able to steer it below the horizon, would scatter off the ground plane and bounce back to above the horizon.

For waveguide mode numerical accuracy each waveguide element is drawn and filled with dielectric, and excited by the Port boundary condition with the $TE_{11}$ mode. This is as opposed to using just Port excitations on 2D waveguide cross-sections without extrusions into 3D objects. Following the operation mode of the actual PAA, the array elements are uniformly illuminated, i.e. each waveguide input port is given the same input power. The waveguide elements are fed with ideal phase delays calculated from the relative distances between the centers of the waveguides. For a given beam scanning direction $(\theta, \varphi)$ the ideal phase delay for a particular waveguide element in the array is given as

$$\psi_i = -k_0 (u x_i + v y_i) \tag{1}$$

where $k_0 = 2\pi / \lambda_0$ is the free space wave number, $u = \sin\theta\cos\varphi$ and $v = \sin\theta\sin\varphi$ are the direction cosines, and $(x_i, y_i)$ is the coordinate of the waveguide element with respect to an arbitrary coordinate system. The geometric center of the array is chosen as the natural origin of the coordinate system.

## 2.2 Beam characterization

Simulations of the PAA described above are performed using Comsol's Multiphysics 3.4 finite element analysis software package with the RF module [11]. Figure 2a shows an example of the resulting intensity far-field pattern in 3D for a beam scanned at 30°. Note that the plot is in dB scale so the sidelobes seem prominent. The main beam and sidelobes characteristics match reasonably well to the far-field intensity calculations in Fig. 2b obtained independently using Discrete Fourier Transform (DFT) on the array without accounting for waveguides mutual impedance coupling.

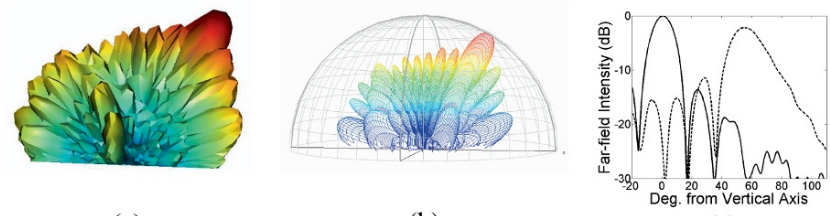


(a) (b) (c)

**Fig. 2** Far-field intensity pattern of a 30° beam using (**a**) 3D full wave simulations and (**b**) ideal DFT method showing reasonable agreement. (**c**) Far-field intensity plots of a broadside (solid) and a 60° beam (dashed).

The far-field intensity is calculated along the circumference of the circle on a meridian plane, at the interface between the air domain and the PML layer. Figure 2c shows the far-field intensities of a broadside beam, i.e. $\theta = 0^{\circ}$, and a $\theta = 60^{\circ}$ beam.

The broadside beam's primary sidelobe has a power intensity that is −13 dB compared to the beam's maximum intensity. This is as expected for a PAA that is uniformly illuminated. For a nominal 60° scanned beam, the maximum intensity is slightly lower than that of the broadside beam and it occurs at 55° rather than 60°. This under-scan phenomenon is well known for PAA; it is just the effect of the element factor on the array factor. In the rest of this paper we always refer to a nominal 60° beam.

Another prominent feature of the 60° beam is the smearing of the beam towards the horizon. This could be an artifact of far-field calculations using the Fast Fourier Transform (FFT) techniques when the edges of the ground plane are not sufficiently far away from the active elements. This same artifact is also observed in the lab when planar near-field scanners do not scan far enough from the active elements, and the data is subsequently used for far-field intensity calculations. This numerical artifact should have minimal effect on our results since the intensity of the smeared section is very small compared to the peak intensity.

## *2.3 Lens optimization*

With the PAA beam simulated and well characterized one could, in principle, start putting a NIM lens on top of the PAA and start doing lens design and optimization. However because 3D full wave simulation is intensive in computer memory, CPU, and time requirements, it is not practical to explore the design space by doing successive simulations. A 2D version of the PAA is used instead to speed up the design optimization process.

The 2D version of the PAA is implemented in Comsol's 2D domain with TE waves. Figure 3a shows the simulation results of an 8 × 1 PAA in 2D with the beam steering angle of 60°. This initial beam with a nominal steering angle of 60° is used in all subsequent simulations to search for the desired lens properties. For the PAA, line sources are used with segment lengths equaling the diameter of the original cylindrical waveguides and separated by the original lattice spacing in one dimension. The simulation domain circle radius is $\sim 25\lambda_0$; such a large domain is used to minimize the effect of the vertical offset of the beam-lens intersection point when doing automated calculation of the intensity far-field pattern and final steering angle determination. A PML layer one $\lambda_0$ thick is again used to better represent an open boundary.

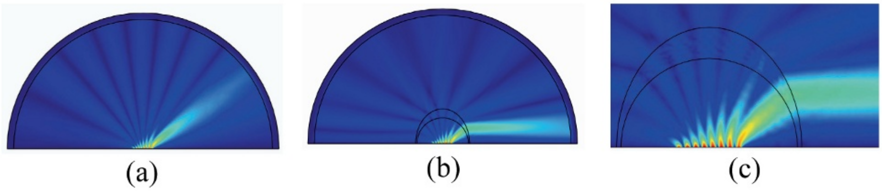


**Fig. 3** Plots of the magnitude of the E-field of a 2D PAA beam with an original steering angle of 60° propagating through (**a**) free space and (**b**) an optimized lens steering the beam to the horizon. (**c**) A close up view of (**b**) in the near-field of the PAA.

As a demonstration of the NIM lens performance, Fig. 3b shows the same nominal 60° beam going through an optimized NIM lens. The beam gets steered sideway to the horizon. Figure 3c is a close up view of Fig. 3b showing more detailed features of the PAA output and beam-lens interaction. The lens shown consists of the area between an inner circle of radius $R$ = 4 in., and an outer ellipse with semimajor axis $a$ = 5.4 in. and semiminor axis $b$ = 4.2 in.. The material of the NIM lens is impedance matched to free space with $\varepsilon_r = -1.8$ and $\mu_r = -1.8$ giving an index of refraction of $n = -1.8$.

The optimization process starts with building and running a model in Comsol and performing all the necessary post-processing analysis. The model is then exported to Matlab for scripting and modification. For parametric study the lens is designed as a shell resulting from the area between two ellipses. The script is ran scanning over various sizes and eccentricities of the inner and outer ellipses and NIM index of refraction values. The far-field intensity is extracted and the peak intensity and the angle of occurrence are used as the figure of merit for that particular geometry and material setting.

Over 8,000 FEM runs in 2D were performed to explore the design space and search for the optimized geometry and material. Figure 4a shows a limited example output of the script where the lens geometry is fixed and the material index of refraction is varied. The results clearly demonstrate a NIM lens with a range of index of refraction capable of steering a 60° beam close to the horizon. Figure 4b shows the corresponding final beam intensity in the far-field. In fact, upon closer inspection, some lenses are able to steer the beam below the horizon. Notice the sharp dips in Fig. 4a and b at $n = -2.1$. For lenses with $n < -2.1$ the beam actually gets steered below the horizon and scatters off the ground plane, giving a false reading of the actual steering power of the lens. Figure 4c demonstrates such a case when $n = -2.4$.

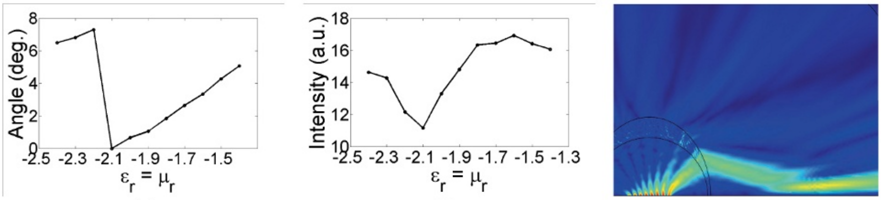


(a) (b) (c)

**Fig. 4** An example of the outputs of an optimization run showing (**a**) the final steering angle as a function of lens material index of refraction and (**b**) the corresponding peak far-field intensity. (**c**) A case where the beam is steered below the horizon and scatters off the ground plane.

Regardless of antennas' scanning ability, most applications are limited to above horizon scanning either because of the platforms they are mounted on or the extended operating environment. With this factor in mind a lens design that just scans to the horizon is identified for further development. From Fig. 4a and b a lens with an index of refraction $n = -1.8$ is chosen as it steers a 60° beam almost to the horizon and still retains a relatively high power intensity in the far-field.

With an optimized lens shape found we are ready to simulate the whole antenna in 3D for more accurate results. In 3D the lens is formed by rotating the 2D cross section in Fig. 3c about the central axis resulting in a dome structure. From this perspective the PAA lens is a specialized radome that enhances the performance of the PAA.

## 2.4 3D full wave simulation

Fully isotropic NIM material in the microwave frequencies is not available at this time. There are special cases of material slabs built but the fabrication techniques and material configurations are not easily transferable to the spherical symmetry of the PAA lens [12–14]. In order to find the most easily manufactured PAA lens, we have to simulate the lens using materials with reduced isotropy, i.e. materials that only respond to some of the electric and magnetic fields components, but not to all three. The design problem statement is now reduced to finding a material with limited isotropy that is easy to fabricate, capable of steering a $60^{\circ}$ beam to the horizon, and also preserves the polarization of the beam.

The PAA lens has spherical symmetry and the beam phase front and polarization components are spherical in nature, so we need the NIM materials to respond to the relevant spherical components of the antenna field. For anisotropic materials simulations Comsol requires the permittivity and permeability dyadics $\overline{\overline{\varepsilon}}$ and $\overline{\overline{\mu}}$ in the Cartesian coordinate system, so we need to transorm the dyadics from a spherical coordinate system to a Cartesian one.

$$\overline{\overline{\varepsilon}} = \begin{bmatrix} \varepsilon_r & 0 & 0 \\ 0 & \varepsilon_\theta & 0 \\ 0 & 0 & \varepsilon_\varphi \end{bmatrix} \longrightarrow \begin{bmatrix} \varepsilon_{xx} & \varepsilon_{xy} & \varepsilon_{xz} \\ \varepsilon_{yx} & \varepsilon_{yy} & \varepsilon_{yz} \\ \varepsilon_{zx} & \varepsilon_{zy} & \varepsilon_{zz} \end{bmatrix} \tag{2}$$

The transformation above is done by direct substitution of the constitutive relations in the two coordinate systems. Assuming $\overline{\overline{\varepsilon}}$ is diagonal in the spherical coordinate system,

$$\begin{bmatrix} D_r \\ D_\theta \\ D_\varphi \end{bmatrix} = \begin{bmatrix} \varepsilon_r & 0 & 0 \\ 0 & \varepsilon_\theta & 0 \\ 0 & 0 & \varepsilon_\varphi \end{bmatrix} \begin{bmatrix} E_r \\ E_\theta \\ E_\varphi \end{bmatrix} \tag{3}$$

where $\vec{D}$ and $\vec{E}$ are the electric displacement and electric field vectors, respectively. In the Cartesian coordinate system (3) assumes the following form

$$\begin{bmatrix} D_x \\ D_y \\ D_z \end{bmatrix} = \begin{bmatrix} \varepsilon_{xx} & \varepsilon_{xy} & \varepsilon_{xz} \\ \varepsilon_{yx} & \varepsilon_{yy} & \varepsilon_{yz} \\ \varepsilon_{zx} & \varepsilon_{zy} & \varepsilon_{zz} \end{bmatrix} \begin{bmatrix} E_x \\ E_y \\ E_z \end{bmatrix} \tag{4}$$

Writing the components of the vectors $\vec{D}$ and $\vec{E}$ in terms of projections from the transformed coordinate systems with

$$\begin{aligned} E_r &= E_x \sin\theta\cos\varphi + E_y \sin\theta\sin\varphi + E_z \cos\theta \\ E_\theta &= E_x \cos\theta\cos\varphi + E_y \cos\theta\sin\varphi - E_z \sin\theta \\ E_\varphi &= -E_x \sin\varphi + E_y \cos\varphi \end{aligned} \tag{5}$$

and

$$\begin{aligned} D_x &= D_r \sin\theta\cos\varphi + D_\theta \cos\theta\cos\varphi - D_\varphi \sin\varphi \\ D_y &= D_r \sin\theta\sin\varphi + D_\theta \cos\theta\sin\varphi + D_\varphi \cos\varphi \\ D_z &= D_r \cos\theta - D_\theta \sin\theta \end{aligned} \tag{6}$$

Substituting (5) into (3), then substitute the results into (6) and comparing the final results with (4) gives the desired permittivity tensor in the Cartesian coordinate system. With a little algebraic manipulation the permittivity dyadic $\overline{\overline{\varepsilon}}$ has the following component values in Cartesian coordinates

$$
\begin{aligned}
\varepsilon_{xx} &= \varepsilon_r \sin^2\theta\cos^2\varphi + \varepsilon_\theta \cos^2\theta\cos^2\varphi + \varepsilon_\varphi \sin^2\varphi \\
\varepsilon_{yy} &= \varepsilon_r \sin^2\theta\sin^2\varphi + \varepsilon_\theta \cos^2\theta\sin^2\varphi + \varepsilon_\varphi \cos^2\varphi \\
\varepsilon_{zz} &= \varepsilon_r \cos^2\theta + \varepsilon_\theta \sin^2\theta \\
\varepsilon_{xy} &= \varepsilon_{yx} = \left(\varepsilon_r \sin^2\theta + \varepsilon_\theta \cos^2\theta - \varepsilon_\varphi\right)\sin\varphi\cos\varphi \\
\varepsilon_{xz} &= \varepsilon_{zx} = \left(\varepsilon_\varphi - \varepsilon_\theta\right)\sin\theta\cos\theta\cos\varphi \\
\varepsilon_{yz} &= \varepsilon_{zy} = \left(\varepsilon_r - \varepsilon_\theta\right)\sin\theta\cos\theta\sin\varphi
\end{aligned}
\tag{7}
$$

The transformation for the permeability dyadic $\overline{\overline{\mu}}$ is exactly the same as above. The relations in (7) and its equivalent version for the permeability dyadic are entered into Comsol's subdomain expressions and material property settings. The same technique is also used to transform material dyadics from the cylindrical coordinates into Cartesian coordinates to explore additional NIM material configurations and realization possibilities. Figure 5a shows the far-field intensity results for a 60° beam going through the different lenses. The far-field intensities of the broadside beam and the nominal 60° beam without a lens from Fig. 2c are included for reference. Through many simulations four lens materials are identified to be able to bend a nominal 60° beam to the horizon: (1) isotropic material, (2) $\varepsilon_{\varphi,z}$ and $\mu_{\varphi,z}$ in the cylindrical coordinates, (3) $\varepsilon_\varphi$ and $\mu_z$ in the cylindrical coordinates, and (4) $\varepsilon_{\theta,\varphi}$ and $\mu_{\theta,\varphi}$ in the spherical coordinates. Typical NIM unit cell material losses are included in the simulations, so in some cases lenses with reduced isotropy materials actually lead to higher peak intensities than isotropic material because of lower losses. All the materials have impedance matching to that of free space, i.e. the magnitudes of the corresponding $\varepsilon$ and $\mu$ dyadic components are equal, except for case 3. Using the full sphere simulation domain, all the lenses are shown to be able to scan a 60° beam past 90° to below the horizon.

For the PAA and lens system to have more utility in both radar and communication applications, the lens must preserve the polarization of the original beam. Figure 5b compares the polarization ratios $E_\theta / E_\varphi$ of the different lenses. For better clarity, only the polarization ratios around the peaks in Fig. 5a are plotted. Since the software does not allow independent control of the TE11 polarization of the different circular waveguide ports, this is a relative comparison rather than an absolute quantification of the cross-polarization discrimination ratio (XPD). Using the characteristic shape of the 60° beam without the lens as the standard, we see that all lenses with 2D and 3D materials preserve the polarization of the original beam. However, 1D material in case 3 loses the original polarization as there is not enough components in the permittivity and permeability dyadics to preserve the polarization. Hence the minimum material anisotropy we can use is 2D materials. Material case 4 is the most desirable because it is in the spherical coordinates and should be able to the preserve the polarization for an original beam steered at any angle. Material case 2, while it seems to work fine for a nominal 60° beam, would not work very well for lower angle beams because the *z*-component of the material would decouple from the dominant $\theta$-component of the fields.

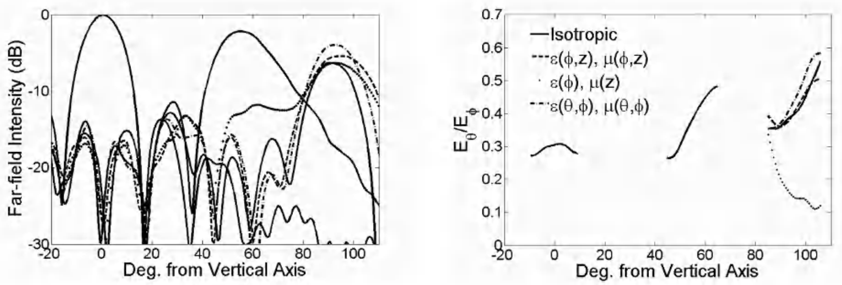


(a) (b)

**Fig. 5** (**a**) The far-field intensities of a 60° beam going through a NIM lens with various material anisotropy and (**b**) the corresponding polarization ratios. The legend is common to both figures.

# 3 Fabrication and Design Considerations

This section presents fabrication and design issues faced while working on the realization of the PAA lens. SRR's and wires have been used almost exclusively as the NIM material of choice in the microwave frequencies. The optimized lens geometry of an ellipsoidal shell in Section 2 presents several fabrication issues. Firstly the NIM unit cells composed of SRR's and wires would start to crowd together at higher latitudes and eventually meet at a single point at the north pole. In principle one could amorphize the unit cells and deviate from the spherical coordinate system lattice, i.e. to have a smaller number of unit cells as we go up in latitude. Previous work by Boeing and university team members on electrically small antennas (ESA) shows that amorphizing SRR unit cells lead to very high material losses [15]. Even if we can tolerate the higher material losses, only the SRR's can be amorphized and not the wires. The wires running in the θ direction need to be continuous and cannot be cut; shortened wires deviate from the infinite wire assumption during NIM unit cell simulations and do not provide the negative permittivity required.

As the latitude increases the unit cell size decreases and the SRR's and wires parameter have to be redesigned to give the desired negative permittivity and permeability. The unit cells size decreases to a point that no parameters can be found for SRR's and wires to give the desired material properties.

The second issue is non-uniform lens thickness. The lens is thicker at the top than the bottom in the radial direction so a higher numbers of NIM layers are needed at the pole than at the equator. The ellipsoidal lens could be built up by NIM layers one unit cell thick. A staircase approximation is used to hug the curvature of the ellipse, so the top layers successfully get cut off at higher and higher latitudes. The wires in the $\theta$ direction on these top layers would be cut and are not grounded properly, again running into the cut-wire problem. The staircase approximation also introduces additional losses.

The issues just discussed above show that SRR's and wires, inherently a planar technology with cubic symmetry, face their greatest limitations in the spherical coordinate system of the lens. To alleviate some of the geometry and fabrication issues, conformal transformation techniques is used to map an ellipsoidal shell lens into a spherical shell lens. Even with a uniform thickness the spherical shell lens does not resolve the issue of unit cell crowding at higher latitudes of the lens. To solve this issue a truncated lens design is investigated which leads to some other material matching requirements. Finally, while the fabrication of a truncated lens using SRR's and wires is in progress, alternative NIM materials realization using other methods are investigated as a long term solution.

## *3.1 Conformal transformation*

The optimized lens configuration found in Section 2 is an ellipsoidal shell with constant index. As mentioned earlier, a non-constant thickness gives rise to fabrication issues and losses when using SRR and wire medium. A spherical shell of constant thickness is a more natural geometry for the lens. Recently, empowered by the flexibility of metamaterials, transformation optics techniques have been introduced for applications such as the invisibility cloaking device and material transformation [16, 17]. This technique makes use of the coordinate transformation invariance of Maxwell's Equations. We apply this technique to transform a NIM lens with an elliptical cross section to one with a circular cross section.

Consider the general case of an ellipsoidal shell lens in Fig. 6a with an inner radius $R_1(\theta)$ and outer radius $R_2(\theta)$. We like to map this region and its permittivity and permeability tensors into another ellipsoidal shell lens with inner radius $R_3(\theta)$ and outer radius $R_4(\theta)$. When we take away the $\theta$ dependence of $R_3$

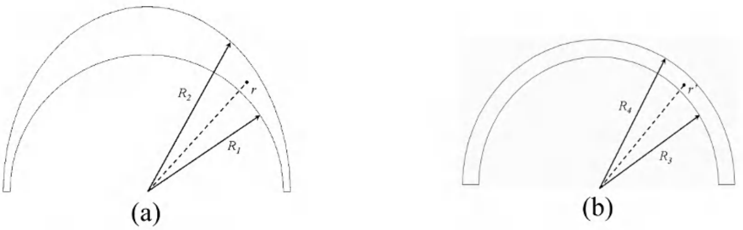


**Fig. 6** A lens with (**a**) elliptical cross section gets mapped into (**b**) a lens with circular cross section using conformal transformation.

and $R_4$ we end up with the desired spherical shell lens shown in Fig. 6b. The mapping could be achieved with the straight forward transformation

$$\begin{aligned} r' &= R_3 + \frac{(R_4 - R_3)(r - R_1)}{(R_2 - R_1)} \\ \theta' &= \theta \\ \varphi' &= \varphi \end{aligned} \tag{8}$$

where the primed axes are in the transformed coordinate system. In Eq. (8) we purposely left out the explicit $\theta$ dependence of the four radii, but it is there implicitly. This transformation equation could also be applied to any two arbitrary regions with radii that are not smooth functions of $\theta$; it could be a piece-wise transformation where only the relative locations and thicknesses at a given $\theta$ is of relevance. Also useful is the inverse transformation for the radial direction

$$r = R_1 + \frac{(R_2 - R_1)(r' - R_3)}{(R_4 - R_3)} \tag{9}$$

Using transformation Eqs. (8) and (9) and the transformation technique prescribed in [16, 17], the permittivity dyadic takes the following form in the transformed coordinate system

$$
\begin{aligned}
\varepsilon_{r'} &= \frac{(R_4 - R_3)}{r'^2 (R_2 - R_1)} \left[ R_1 + \frac{(R_2 - R_1)(r' - R_3)}{(R_4 - R_3)} \right]^2 \varepsilon_r \\
\varepsilon_{\theta'} &= \frac{(R_2 - R_1)}{(R_4 - R_3)} \varepsilon_\theta \\
\varepsilon_{\varphi'} &= \frac{(R_2 - R_1)}{(R_4 - R_3)} \varepsilon_\varphi
\end{aligned} \tag{10}
$$

The permeability dyadic transformation takes the same exact form. The radial component is not used in our simulation and fabrication but is included here for completeness. With this transformation we have essentially traded geometry for material, going from a complex geometry with constant material properties to one of simple geometry with variable material properties. This transformation should not be confused with the one in Section 2.4; even with the new material properties in Eq. (10), we still need to transform it further using Section 2.4 to convert material dyadics in spherical coordinates into one in Cartesian coordinates that Comsol requires.

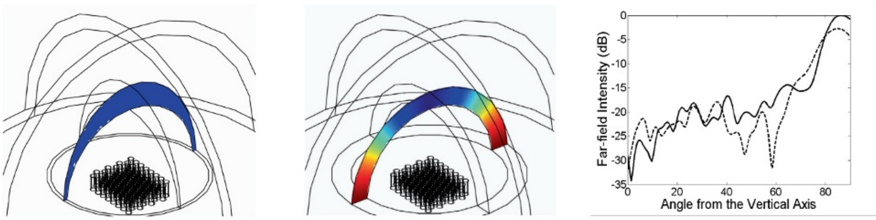


(a) (b) (c)

**Fig. 7** (**a**) The optimized lens with constant material and varied geometry gets mapped into (**b**) a lens with varied material and constant geometry for easier fabrication. (**c**) The comparison of the far-field intensities of the ellipsoidal (solid) and spherical (dashed) shells.

As a concrete example we transform the optimized lens found in Section 2 into a spherical shell lens. Figures 7a and b show the simulation domains and slice plots of the material properties for the two lens configurations. The ellipsoidal shell lens has constant index of refraction $n = -1.8$ while the spherical shell lens has a gradient index of refraction of $-2.5 < n(\theta) < -0.36$ for a shell one inch thick. The range of the index of refraction could be controlled by adjusting the spherical lens thickness with material losses taken into considerations. Figure 7c compares the intensity far-field patterns of the two configuration showing they closely match considering differences in meshing and material gradients.

The conformal transformation technique proves to be useful in lens geometry and material design. In this example it transforms a configuration that is easier to optimize into a configuration that is easier to fabricate, and resulting in a more desirable final shape. If we were to start out with the spherical shell lens, the gradient index of refraction required would have been very difficult to optimize because the design space seems unbounded.

## 3.2 Truncated lens

Even with a spherical shell lens we are still faced with the crowding of the SRR and wire unit cells in the $\varphi$ direction at higher latitudes and certainly at the pole. To build a limited proof-of-concept sample we are fabricating a truncated lens where the spherical shell only contains enough material to steer a 60° beam.

To determine the right amount of material to include the 60° beam near-field power intensity is plotted along the great inner circle of the spherical shell lens, shown in Fig. 8a. The −10 dB band width occurs at colatitudes of roughly 40–75°. Figure 8b shows the resulting truncated lens geometry within the simulation domain and a slice plot showing the index of refraction gradient.

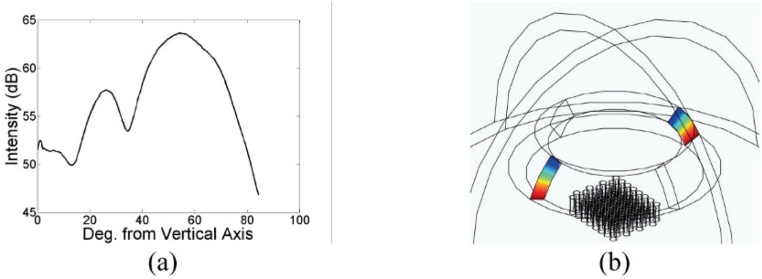


**Fig. 8** (**a**) The near-field power intensity along the inner shell of the spherical lens to extract −10 dB angles for lens truncation. (**b**) The geometry of the corresponding truncated lens.

The primary concern with a truncated lens is the performance of beams at mid scan angles. Broadside and low scan angle beams propagate in air, while a 60° beam gets most of its intensity intercepted by the lens. The mid-angled beams would get split between air and lens material. The part intercepting the lens would get scanned towards the horizon, while the part in air sees a material discontinuity at the lens truncation point. This discontinuity would scatter the beam at varying levels depending on the beam scanning angle.

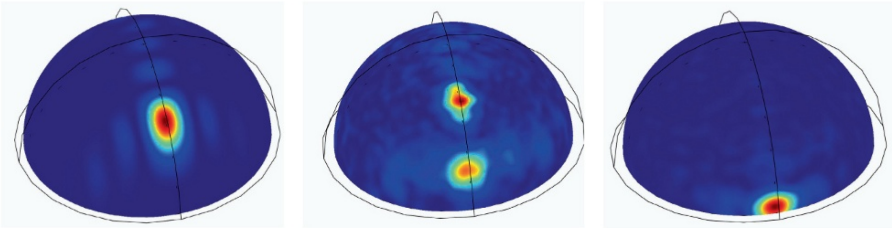


**Fig. 9** Far-field intensity plots of (**a**) a 45° beam without a lens and (**b**) a 45° beam and (**c**) a 60° beam going through a truncated lens.

Figure 9a shows the far-field intensity of a 45° beam without a lens. Figure 9b shows the far-field intensity for the same beam going through a truncated lens. We can clearly see that part of the beam gets steered to the horizon, while the other part gets scattered and deflected towards the pole. In this example the beam gets deflected up by 9° relative to its original trajectory. The far-field intensity of a 60° beam going through a lens is included in Fig. 9c for comparison.

For a proof-of-concept device, unit cells are being designed and fabrication details are being worked out for a spherical shell lens with truncation. The actual lens fabrication techniques and performance will be presented in a later work when available. Our group's previous NIM lens designs and fabrications show good agreement between simulations and experiments [7], so we expect similar agreements this time as well.

## *3.3 Alternative NIM*

The limitations of cubic SRR and wire unit cells to conform to an arbitrary geometry are obvious from the previous sections. While the truncated lens is being fabricated, other NIM materials are being investigated as long term solutions.

One candidate alternative NIM material is coated dielectric spheres, shown in Fig. 10a. Coated dielectric spheres have been investigated previously to achieve negative refractive index at microwave and infrared frequencies [18, 19]. To achieve negative index of refraction in coated dielectric spheres, Mie resonance in the core provides the negative $\mu_r$ and surface resonance of the coating provides the negative $\varepsilon_r$. The coated dielectric spheres would be truly an isotropic NIM if attainable. The material could be produced in bulk via batch processing, and the resulting 'powder' or 'block' could be moulded or milled into shape, respectively.

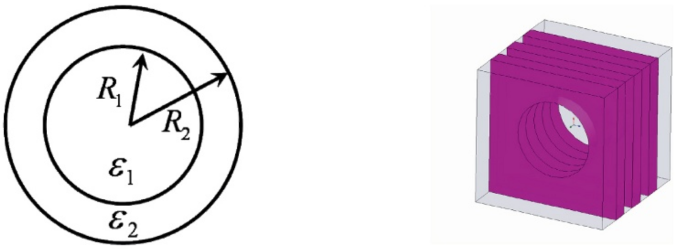


(a) (b)

**Fig. 10** (**a**) Coated dielectric spheres and (**b**) stacked hole arrays are being investigated to provide NIM materials at microwave frequencies.

The difficulty with coated dielectric spheres as a NIM at microwave frequencies is achieving negative $\varepsilon_r$. For the plasma frequency of the coating material to be at the microwave frequencies, materials with very low electron carrier densities are needed. It is still unclear if those materials would be sufficiently conductive to respond and interact with the incoming electric field to provide the negative $\varepsilon_r$. Further material and geometry investigations are still needed.

Another candidate alternative NIM material is stacked hole arrays. The stacked hole arrays medium consists of metal plates with holes drilled in a periodic fashion in two dimensions on a plane. The plates are stacked together with a gap between them. Figure 10b shows a unit cell simulation of the medium. Three plates are shown in this example but lower or higher numbers of plates could be used to attain the same effect. Periodic boundary conditions on the transverse boundaries are used to mimic a large array.

The mechanism for stacked hole arrays to achieve negative refractive index is the extraordinary optical transmission via surface plasmons [20]. Recently stacked hole arrays NIM material was used to build a planoconcave lens [21]. The material electromagnetic properties is essentially 2D with rotational symmetry about the axis of the holes, and exactly meets the requirements of the PAA lens. The periodicity of the holes, however, is on the order of one $\lambda_0$ and resembles photonic bandgap structures. For this material to be useful on the PAA lens, the array lattice spacing must be made much smaller than the radius of curvature of the spherical shell lens. This could be achieved by filling the gaps and holes with high dielectric materials. Once this relative size requirement is met the unit cell simulation with hole arrays on a flat plate should closely approximate hole arrays on a spherical surface. Concentric metallic spherical shells with hole arrays could then be used to fabricate the full dome lens.

## 4 Summary and Discussion

We have presented a complete methodology for designing and simulating a NIM lens that enhances the scanning angle of a PAA from a nominal 60° to the horizon. The lens design and optimization techniques are developed and 3D full wave simulations show the original goal is achieved. Along the design process fabrication issues have been taken into account and various techniques developed to circumvent the limitations of SRR's and wires medium.

One important result is the successful use of transformation optics to transform a lens that is easier to optimize into one that is easier to fabricate. Due to the limitation of SRR's and wires, only a truncated lens is being fabricated in our laboratory as a proof-of-concept device. The details of the fabrication process and measurement data will be presented elsewhere when available. As a long-term solution, dielectric coated spheres and stacked hole arrays are being investigated as NIM in the microwave frequencies.

**Acknowledgments** This work is funded by the United States Defense Advanced Research Projects Agency (DARPA) under contract #HR001-05-C-0068. U.S. Trademarks and Patent Office application pending.

## References

1. Pendry, J.B., Holden, A.J., Robbins, D.J., Stewart, W.J.: Magnetism from conductors and enhanced nonlinear phenomena. IEEE Trans. Micro. Theory Tech., Vol. 47, No. 11, pp. 2075–2084 (1999)
2. Pendry, J.B., Holden, A.J., Stewart, W.J., Youngs, I.: Extremely low frequency plasmons in metallic mesostructures. Phys. Rev. Lett., Vol. 76, No. 25, pp. 4773–4776 (1996)
3. Veselago, V.G.: The electrodynamics of substances with simultaneously negative values of $\varepsilon$ and $\mu$ . Sov. Phys. Usp., Vol. 47, pp. 509–514 (1968)
4. Smith, D.R., Padilla, W.J., Vier, D.C., Nemat-Nasser, S.C., Schultz, S.: Composite medium with mimulataneously negative permability and permittivity. Phys. Rev. Lett., Vol. 84, No. 18, pp. 4184–4187 (2000)
5. Ziolkowski, R.W., Kipple, A.D.: Application of double-negative materials to increase the power radiated by electrically small antennas. IEEE Trans. Antenn. Propag., Vol. 51, No. 10, pp. 2626–2640 (2003)
6. Parazzoli, C.G., Koltenbah, B.E.C., Greegor, R.B., Lam, T.A., Tanielian, M.H.: Eikonal equation for a general anisotropic or chiral medium: application to a negative-graded index-of-refraction lens with an anisotropic material. J. Opt. Soc. Am. B, Vol. 23, No. 3, pp. 439–450 (2006)
7. Greegor, R.B., Parazzoli, C.G., Nielsen, J.A., Thompson, M.A., Tanielian, M.H., Vier, D.C., Schultz, S., Smith, D.R., Schurig, D.: Microwave focusing and beam collimation using negative index of refraction lenses. IET Microw. Antenn. Propag., Vol. 1, No. 1, pp. 108–115 (2007)

8. Schurig, D., Mock, J.J., Justice, B.J., Cummer, S.A., Pendry, J.B., Starr, A.F., Smith, D.R.: Metamaterial electromagnetic cloak at microwave frequencies. Science, Vol. 314, pp. 977–980 (2006)
9. Pendry, J.B., Smith, D.R.: The quest for the superlens. Sci. Am., Vol. 295, No. 1, pp. 60–67, (July 2006)
10. Mailloux, R.J.: Phased Array Antenna Handbook, 2nd Ed. Artech House, Boston, MA (2005)
11. www.comsol.com
12. Vier, D.C., Schultz, S., Greegor, R.B., Parazzoli, C.G., Nielsen, J.A., Tanielian, M.H.: Three dimensional double negative (DNG) metamaterial resonating at 13.5 GHz. Submitted to IET Microw. Antenn. Propag.
13. Grbic, A., Eleftheriades, G.V.: An isotropic three-dimensional negative-refractive-index transmission-line metamaterial. J. Appl. Phys., Vol. 98, pp. 043106 (2005)
14. Alitalo, P., Maslovski, S., Tretyakov, S.: Experimental verification of the key properties of a three-dimensional isotropic transmission-line superlens. J. Appl. Phys., Vol. 99, pp. 124910 (2006)
15. Greegor, R.B., Parazzoli, C.G., Nielsen, J.A., Tanielian, M.H., Vier, D.C., Schultz, S., Ziolkowski, R.W., Holloway, C.L.: Electrically small antenna using a mu-negative (MNG) metamaterial hemisphere. Submitted to IEEE Antenn. Wire. Propag. Lett.
16. Schurig, D., Pendry, J.B., Smith, D.R.: Calculation of material properties and ray tracing in transformation media. Opt. Express, Vol. 14, No. 21, pp. 9794–9804 (2006)
17. Rahm, M., Schurig, D., Roberts, D.A., Cummer, S.A., Smith, D.R., Pendry, J.B.: Design of electromagnetic cloaks and concentrators using form-invariant coordinate transformations of Maxwell's equations. Photon. Nanostr.-Fund. Appl., Vol. 6, pp. 87–95 (2008)
18. Holloway, C.L., Kuester, E.F., Baker-Jarvis, J. Kabos, P.: A double negative (DNG) composite medium composed of magnetodielectric spherical particles embedded in a matrix. IEEE Trans. Antenn. Propag., Vol. 51, No. 10, pp. 2596–2603 (2003)
19. Wheeler, M.S., Aitchison, J.S., Mojahedi, M.: Coated nonmagnetic spheres with a negative index of refraction at infrared frequencies. Phys. Rev. B, Vol. 73, pp. 045105 (2006)
20. Beruete, M., Sorolla, M., Campillo, I.: Left-handed extraordinary optical transmission through a photonic crystal of subwavelength hole arrays. Opt. Express, Vol. 14, No. 12, pp. 5445–5455 (2006)
21. Beruete, M., Navarro-Cia, M., Sorolla, M., Campillo, I.: Planoconcave lens by negative refraction of stacked subwavelength hole arrays. Opt. Express, Vol. 16, No. 13, pp. 9677–9683 (2008)

# Application of Wire Media in Antenna Technology

**Silvio Hrabar**

Faculty of Electrical Engineering and Computing, University of Zagreb,
Unska 3, Zagreb, HR 10 000, Croatia
Silvio.Hrabar@fer.hr

**Abstract** This paper reviews the results of experimental investigation of radiating structures based on plasma-like wire media, undertaken at University of Zagreb. It is shown that all three regions of the dispersion curve of wire media, namely the Epsilon-NeGative (ENG) region, the Epsilon-Near-Zero (ENZ) region and the Epsilon-PoSitive (EPS) region, can be successfully utilized in antenna applications. The phenomenon of gain increase of an antenna embedded in wire medium, based on ultra-refraction in ENZ region, was investigated in 10 GHz band. The results revealed that the use of ultra-refraction may be a practical approach in the case of low-directivity radiators such as simple monopole antennas. Another example of the utilization of the ENZ region deals with the shortened horn antenna with embedded wire-medium-based ENZ slab operating in 10 GHz band. Two prototyped shortened horn antennas (labeled as horn I and horn II) had lengths of 52% and 33% of the length of the optimal horn, respectively. Measured gain was found to be very similar to the gain of the full length optimal horn (within 0.1 dB), but in a narrow band (12% for horn I and 8% for horn II). The last example deals with a scanning leaky-wave antenna operating at 10 GHz, based on a waveguide filled with double-wire medium operating in all three regions of the dispersion curve. These three regions correspond to three different modes of propagation in the waveguide: the backward-wave mode, the forward-wave mode and the mode with infinite wavelength. Experimental results revealed the possibility of main beam scanning within an angle of ±60° from broadside direction.

## 1 Introduction

It is well known [1, 2] that an array of parallel wires (Fig. 1a), the lattice constant ($d$) of which is *much smaller* than the wavelength ($d \ll \lambda$), can be thought of as a plasma-like material (ENG metamaterial) described by its relative permittivity [1, 2]:

S. Zouhdi et al. (eds.), *Metamaterials and Plasmonics: Fundamentals, Modelling, Applications*,

$$\varepsilon_{reff} = \varepsilon_{reff}^{'} - j\varepsilon_{reff}^{''} = 1 - \frac{f_p^2}{f^2 - j\gamma f}. \tag{1}$$

Here, $f$ and $f_p$ represent the frequency of the signal and the cut-off frequency of the array ('plasma frequency'), respectively, while factor $\gamma$ represents the losses (see the graph in Fig. 1b). The plasma frequency is dependent on the geometrical parameters of the array (lattice constant $a$ and wire radius) and several different equations for its prediction are available in the literature [2, 14]. Although the concept of an array of thin wires was introduced a long time ago [1], the interest in this structure has been revitalized after the first experimental DNG metamaterial was reported [3].

The operation of wire medium illuminated with a plane wave can be understood in an intuitive and simple way with the help of the transmission line theory (Fig. 1c.) The free space can be thought of a transmission line with a series distributed inductance and a shunt distributed capacitance representing the free-space permeability ($\mu_0$) and permittivity ($\varepsilon_0$), respectively. Since the wires are parallel to the electric field vector, they can be thought of the distributed inductance 'connected' in parallel with free-space permittivity ($\varepsilon_0$). These two elements form a parallel LC tank circuit that behaves as a shunt inductance below the resonant frequency ($f_p$). Thus, the whole structure behaves as a LL transmission line that can be interpreted as an Epsilon-NeGative metamaterial (ENG). It is important to notice that the losses of wire media operating in the ENG region are significantly lower than the losses of widely used Mu-NeGative (MNG) media based on Split-Ring Resonators (SRRs). Low losses are associated with the fact that very low current flows through the parallel tank circuit in the vicinity of the resonant frequency ($f_p$) (On the contrary, a SRR inclusion behaves as a series tank circuit associated with the high current density and therefore high losses in the vicinity of the resonant frequency). Slightly above the $f_p$, equivalent relative permittivity of the tank circuit is a small positive number very close to zero (the tank circuit behaves as a shunt capacitance smaller than free-space permittivity). Wire-medium operating in this frequency region is usually referred to as Epsilon-Near-Zero metamaterial (ENZ) [10]. If the frequency is increased further, the equivalent permittivity approaches unity and the wire medium operates like an ordinary Epsilon-PoSitive (EPS) material.

It was shown [14] that (1) applies only if no component of the wave vector is parallel to the wires. If this constraint is not met, the wire-medium exhibits spatial dispersion. In the case of lossless wires, the effective permittivity of wire medium with spatial dispersion is given by [14]:

$$\varepsilon_{reff} = 1 - \frac{f_p^2}{f^2 - \left(\frac{q \cdot c}{2\pi}\right)^2}. \tag{2}$$

Here, $c$ stands for the speed of light and $q$ is the component of a wave vector parallel to the wires. In a general case $q$ may also be dependent on the frequency and $\varepsilon_{reff}$ becomes a rather complicated function of both geometrical parameters of the array and frequency. However, even in this case it is possible to identify several different characteristic regions of the dispersion curve with the ENG behavior, the ENZ behavior and the EPS behavior.

This paper reviews some of the experimental results of utilization of all three characteristic regions of the dispersion curve of wire media in antenna technology, undertaken at University of Zagreb.

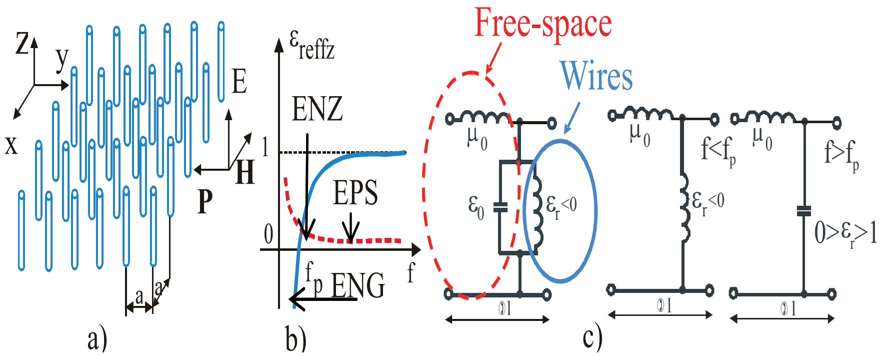


**Fig. 1** (**a**) A thin-wire-based metamaterial, (**b**) Effective permittivity; solid – real part, dashed – imaginary part (**c**) Transmission line equivalent circuit.

## 2 An Antenna Embedded in Wire Medium

One very interesting application of wire medium that operates just above the plasma frequency (in the ENZ region of the dispersion curve) was proposed recently in [4]. The authors embedded a simple omnidirectional radiator (a monopole antenna) into the wire medium and observed a significant increase in directivity. A very simple intuitive explanation, based on ultra-refraction, was given in [4] and is briefly reviewed here in Fig. 2a. If one represents the spherical waves emanating from the source by rays, the incident angle ($\theta_1$) and the refracted angle ($\theta_2$) are related by Snell's law (see ray 1 in Fig. 2a):

$$\theta_2 = \sin^{-1}\left(\sqrt{\varepsilon_r}\,\sin(\theta_1)\right). \tag{3}$$

If the relative permittivity of the ENG slab ($\varepsilon_r$) is a very small positive number, the angle $\theta_2$ will be close to 0°, i.e. all outgoing rays will be nearly perpendicular to the surface of the ENZ slab. This will cause a directive broadside radiation pattern similar to the radiation pattern of an aperture with uniform current distribution. It is important to notice that the basic principle of ultra-refraction is actually not novel at all. Similar experiments that mimic the behavior of radiators embedded in plasma were performed back in the sixties of the previous century [1]. However, the intuitive picture of rays is just a first approximation, while several different rigorous studies of wave propagation in the slab with vanishing permittivity have been presented in the last few years [8–10]. These studies revealed that the background physics of directivity increase is actually more complicated and it includes phenomena of tunneling, spatial filtering and even excitation of leaky-waves in the case of a realistic finite wire-medium slab.

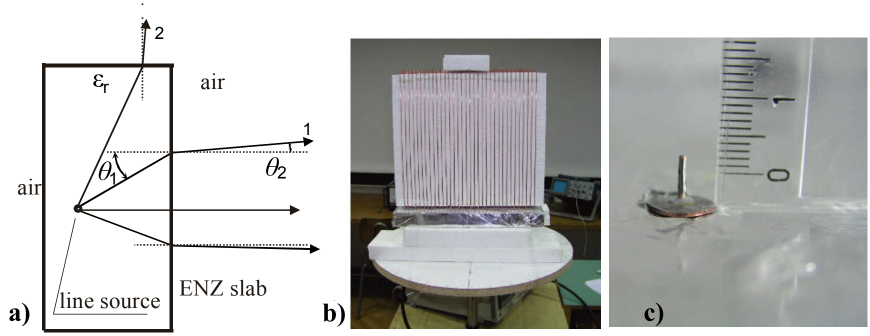


**Fig. 2** (**a**) A finite ENZ slab with embedded line source, (**b**) Wire-media ENZ slab used in the experiments with ultra-refraction (**c**) Experimental monopole antenna (ENZ slab removed).

We investigated the feasibility of the application of ultra-refraction with several simple experimental antennas in 10 GHz frequency band [5, 6]. The wire medium consisted of parallel copper wires (radius $r = 0.7$ mm) glued onto Styrofoam plates with $\varepsilon_r \approx 1$ (Fig. 2b). The lattice constant was $a = 9$ mm and the sample thickness varied from 2 to 14 layers of wires. Obviously, the fabricated wire-based metamaterial is anisotropic and it will show plasma-like behavior only for the wave whose electric field vector is parallel to the wires (this is a case different from those reported in [4, 7] where two mutually perpendicular sets of wires were used). Two samples were used in the experiments; the large sample (0.31 × 0.31 m, variable thickness) and the small sample (0.155 × 0.155 m, variable thickness). In the first series of experiments, a quarter-wavelength monopole (the length of 7.5 mm) over the ground plane was used as the radiating element (Fig. 2c). The monopole was placed in the center of the wire medium slab. Both the far-field radiation pattern (in H plane) and gain of these antennas have been measured at several frequencies and for different number of wire-layers. Samples of the obtained results are given in Figs. 3 and 4. It can be seen (Fig. 3a) that at the frequency slightly higher than the plasma frequency (10.25 GHz) the directive pattern is formed. Two main lobes in the direction of 0° and 180° and two major secondary lobes in the directions of +90° and −90° can be observed. These secondary lobes appear due to rays refracted at the slab sides (see ray 2 in Fig. 2a). By further increasing the frequency (Fig. 3b), the main lobe splits and two maxima in directions different from broadside (0°) appear. This effect was predicted by theoretical analysis in [8] and it shows that the background physics is indeed associated with the excitation of leaky waves. The measured gain, in comparison to the isotropic radiator at 10.50 GHz, as a function of the number of wire layers for both samples is shown in Fig 4. In the case of the large sample, the highest gain of 23.41 dB was obtained for eight wire-layers. Assuming a uniform current distribution on a 0.155 × 0.155 m physical aperture, and assuming that the gain is equal to the directivity, a gain of 25.7 dBi is calculated. Therefore the gain of the whole antenna system (monopole antenna embedded in the wire-based slab) approaches maximal theoretical gain for the given physical aperture.

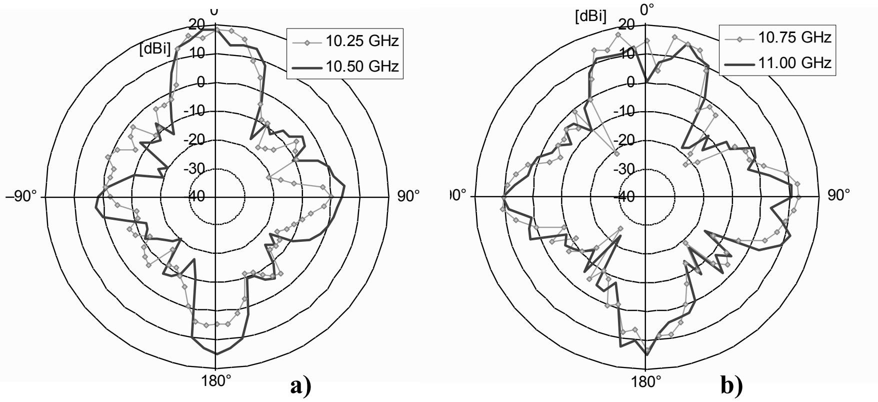


**Fig. 3** Measured radiation pattern of a monopole embedded into wire media (large sample, thickness of 14 layers).

The small sample had the physical aperture equal to one quarter of the aperture of the large sample. Thus, a 6 dB reduction in the gain could be expected. However, this was not the case (see Fig. 4). Both curves in Fig. 4 show the same behavior, but they reach their maxima at a different number of wire-layers. When the wire slab is thin, the obtained gain is almost the same in both cases, showing that only a small portion of the physical size is actually used to focus the radiated wave. In the case of the small sample some rays 'hit' the top plane of the metamaterial parallelepiped and do not contribute to the broadside radiation. This is the reason why the larger sample gives higher gain. On the other hand, when the metamaterial sample becomes thicker, there is a significant influence of the energy reflected from the interfaces between metamaterial and air, which builds up a complicated standing wave pattern inside the sample. Since the two samples have different dimensions, there are two different thicknesses at which the energy radiated through the top of the metamaterial parallelepiped becomes minimal, yielding optimal gain in broadside direction. Thus, the thickness of the wire-based ENZ layer is a critical design parameter.

The considered smaller sample (0.155 × 0.155 m) of the metamaterial was also used to increase the directivity of an aperture antenna. The aperture antenna was realized as an open-ended standard X-band rectangular waveguide (cross section with dimensions 22.86 × 10.16 mm). The measured gain of this antenna was between 3 and 4 dB in the considered frequency band (Fig. 5).

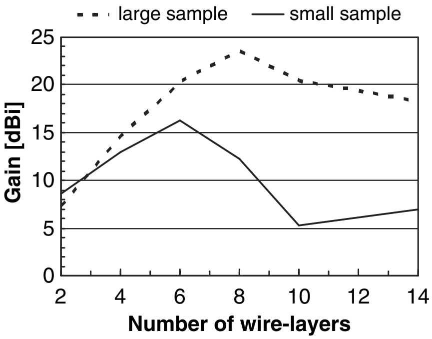


**Fig. 4** Comparison of the measured gain at 10.25 GHz and in 0° direction for the monopole antenna embedded in large (0.31 × 0.31 m) and small (0.155 × 0.155 m) wire slab.

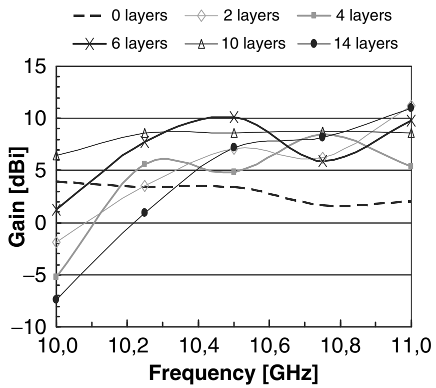


**Fig. 5** Measured gain of the open waveguide embedded in thin-wire based metamaterial in 0° direction.

Again, the wire-based metamaterial overlay produced increased directivity, but the relative improvement was not so pronounced as in the case of the quarter wave monopole. The maximum gain of 10.2 dBi at 10.5 GHz was obtained with the metamaterial consisting of six wire layers, while at 11 GHz the measured gain was 11.2 dBi for the sample with 2 and 14 layers (Fig. 5). The last antenna that was embedded in the metamaterial was the optimal pyramidal horn (gain of 12 dB) operating in 10 GHz band [5, 6]. The horn antenna aperture was embedded in the metamaterial with 0.155 × 0.155 m cross section, while the number of wire layers was changed between 2 and 14. In this experiment no gain improvement was observed. This is actually the expected result. A wire-based slab cannot improve the gain if the antenna aperture already has a (nearly) uniform distribution of equivalent currents. Thus, embedding an antenna into wire-based ENZ slab appears to be a convenient method of gain increase only in the case of low-directivity radiators.

## 3 Shortened Horn Antenna with Embedded Wire-Based Slab

It is very well known that the gain of the horn antenna depends both on aperture size and horn length. Maximal gain is associated with the optimal horn length that does not cause excessive phase variations of the wave front across the aperture (see the optimal horn sketched in the upper part of Fig. 6a). If one manufactures a shorter horn with the same aperture (lower part of Fig. 6a), it will have inherently lower gain due to pronounced phase variation caused by the spherical wave front. A very recent theoretical study [11] proposed a method of gain increase of such a horn by employing double-wire medium, operating in the ENZ region. The obtained simulation results showed gain equal to the gain of the full-length optimal horn within a finite bandwidth. One could say that the wire-medium straightens the wave front similarly to well-known metallic lenses [12]. However, the wire-medium slab is flat, so strictly speaking *it is not* a conventional lens. A more correct explanation of the physics of gain increase is angular filtering with the ENZ slab [10]. We performed experimental investigation [15, 16] that verified the theoretical predictions of the phenomenon of gain increase, published in [11].

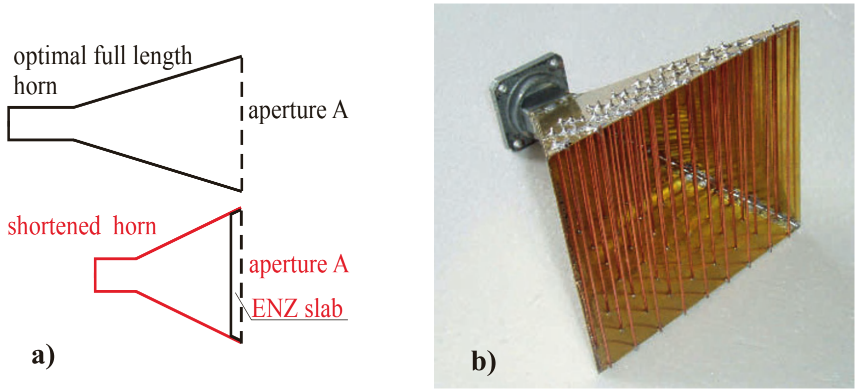


**Fig. 6** (**a**) Principle of shortening of the horn antenna (**b**) Example of realized experimental shortened horn antenna with embedded ENZ metamaterial lens.

At first, the optimal horn was designed for operation in 10 GHz band. It had an aperture of 125 × 112 mm and the length of 190 mm (flare angle of 15°), and it was fed with an X-band waveguide (22.5 × 10 mm). The gain of this reference horn, obtained by full-wave simulations using CST Microwave Studio™ [13] is plotted in Fig. 7 (curve a). The gain varies from 20 to 22 dBi in the band from 9 to 12 GHz. The curve (b) in the same figure shows simulated gain of the horn with *equal* aperture but with the shorter length of 99 mm (52% of the length of the optimal horn as suggested in [11]) and flare angle of 27°. As expected, this antenna showed significantly lower gain, varying between 16 to 17 dBi in the band from 9 to 12 GHz. In [11], a design with two perpendicular sets of wires (double-wire media) was suggested. However, it is clear that the vertical component of the electric field, associated with waveguide $TE_{01}$ mode, will be predominant inside the antenna. Thus, it appears that another (horizontal) set of wires has very little impact on the antenna parameters, and it is almost redundant. After verification of this hypothesis by full-wave simulations, it was decided to use only one set of wires aligned in vertical direction.

Experimental shortened horn was manufactured out of 1 mm thick brass plates and equipped with single-wire-based metamaterial with three layers of wires. The wire medium was based on bare copper wires (diameter of 0.7 mm) [15, 16]. The lattice constants were 14 and 8.5 mm in longitudinal and transversal directions, respectively. The slab comprised three layers with 16, 14 and 12 wires, respectively. The first and last wire in each layer were located at the distance of half of the unit cell from the horn inner wall. A number of holes that fit the described pattern of wires were drilled in the horn walls. The wires were stretched across the horn inner space and soldered onto the horn body (Fig. 4b). Gain, return loss, radiation pattern and cross-polarization level were measured using a standard horn and a HP 8720B network analyzer. Some of the measurement results are shown in Figs. 7 and 8.

It can be seen (curve denoted as c in Fig. 7) that the phenomenon of gain increase of more than 2 dB, predicted for double-wire medium filling in [11], was also observed here, for the case of the single-wire medium. The measured bandwidth was 12%, which is narrower than the bandwidth predicted by simulations in

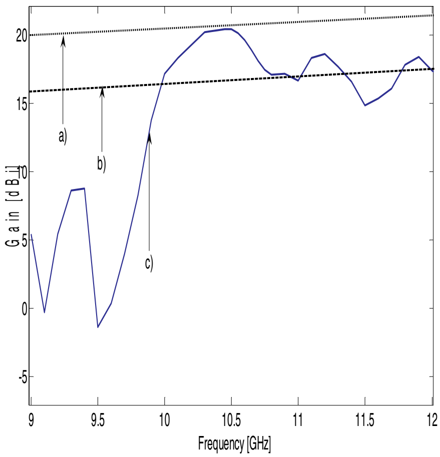


**Fig. 7** (**a**) Simulated gain of full length optimal horn (**b**) Simulated gain of shortened horn (**c**) Measured gain of shortened horn (52% of the length of an optimal horn) with embedded single-wire-based slab (wires aligned along vertical transversal direction).

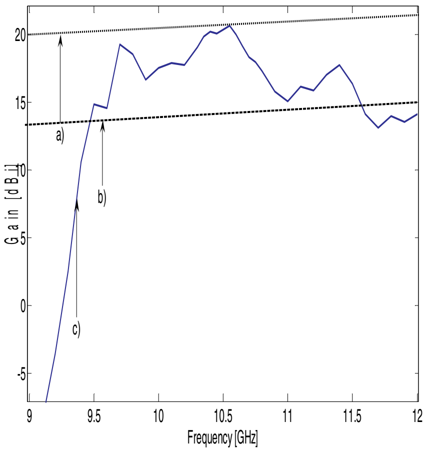


**Fig. 8** (**a**) Simulated gain of full length optimal horn (**b**) Simulated gain of shortened horn (**c**) Measured gain of shortened horn (33% of the length of an optimal horn) with embedded double-wire-based slab (wires aligned along vertical transversal direction and along horizontal longitudinal direction).

[11], but consistent with the first experimental results presented in [15]. The measured radiation patterns at the frequency of 9.7 GHz (not shown in figures, due to lack of space) revealed a 3 dB beam width of 16° with a side lobe level of −20 dB. The return loss and cross-polarization levels within the operating band were found to be better than −10 and −27 dB, respectively.

Finally, it was attempted to further decrease the length of the shortened horn. If the horn is very short, the wave front will be almost spherical with a pronounced longitudinal component of the electric field vector. Thus, it appears that the inclusion of wires in the longitudinal direction should improve the wave front straightening and eventually yield an even shorter antenna. A new experimental horn with two sets of wires and a length of only 66 mm (33% of the length of optimal horn) was prototyped. It had 10 × 6 wires with a lattice constant of 14 mm in transversal direction and 13 × 10 wires with a lattice constant of 8.5 mm in longitudinal direction. The measurement results (Fig. 8) revealed the gain increase of almost 7 dB comparing to the bare shortened horn, within 8% fractional bandwidth.

One concludes that with the help of a wire medium slab it is possible to construct a rather short horn antenna (down to 33% of the length of the optimal horn) that yields almost the same gain as the optimal horn, but in a narrow band.

## 4 Scanning Leaky-Wave Antenna

A leaky-wave antenna is a fast-wave guiding structure, in which the traveling wave continuously loses its energy owing to radiation [17] (see the waveguide example shown in Fig. 9a). The angle of maximum radiation $\theta_m$ (azimuth angle in Fig. 9a) is determined using the simple fact that free-space propagation vector $k_0$ is a sum of the transversal component of propagation vector in the space above the guiding structure $k_t$ and vector $k_l$ that describes propagation along the structure:

$$k_t^2 + k_l^2 = k_0^2 \Rightarrow \Theta_m = \sin^{-1}\left(k_l / k_0\right) \tag{4}$$

Recent introduction of a metamaterial-based leaky-wave antenna with back-fire to end-fire scanning capabilities has attracted considerable interest [19]. This antenna is based on a planar artificial transmission line that supports backward-wave propagation, propagation with infinite wavelength and forward-wave propagation. In our group, a similar idea was used for the construction of scanning leaky-wave antennas in wire-medium-based waveguide technology [24, 25].

A waveguide loaded with the wire medium was experimentally investigated for the first time in [18]. The authors used a waveguide with square cross-section and it contained an array of two perpendicular sets of wires (similar to the sketch in Fig. 9a). The double-wire medium was thought of as a simple waveguide filling with a uniaxial permittivity tensor:

$$\varepsilon(f)=\varepsilon_0\begin{bmatrix}\varepsilon_p(f) & 0 & 0\\ 0 & \varepsilon_p(f) & 0\\ 0 & 0 & 1\end{bmatrix}. \tag{5}$$

Here $\varepsilon_0$ stands for the free-space permittivity while $\varepsilon_p$ stands for two tensor components associated with relative permittivity in transversal directions. Relative transverse permittivity is considered to be described by the simple Drude model (1) (dielectric function $\varepsilon_p(f)$ with plasma frequency $f_p$ in (5)). If one fills a waveguide with such a material, the waveguide will support backward-wave propagation for frequencies either below $f_p$ (if $f_p < f_c$ ) or below $f_c$ (if $f_c < f_p$), $f_c$ being the cut-off frequency of $TM_{11}$ mode [18]. For frequencies located between $f_p$ and $f_c$, there will be no propagation (stop-band). For frequencies either above $f_c$ (if $f_p < f_c$ ) or above $f_p$ (if $f_c < f_p$), the propagation will take place in the form of forward waves. Experimental results presented in [18] appeared to be consistent with this simplified explanation. A similar approach was used in the experimental study conducted in our group [20, 21]. Additionally, it was shown possible to close that gap between the backward-wave mode ($k_l < 0$ mode that corresponds to ENG part of the dispersion curve) and the forward-wave mode ($k_l > 0$ mode that corresponds to EPS part of the dispersion curve). It could be achieved by a simple choice of the plasma frequency of wire medium that would be equal to the cut-off frequency of the $TM_{11}$ mode ($f_c = f_p$). At that frequency ($f_p$) the propagation should take place with infinite wavelength ($k_l = 0$ mode). At first sight, the results in [20, 21] again seemed to be consistent with the simple Drude model (1) of wire-medium.

However, in [20, 21] it was also noted that the measured plasma frequency of the wire medium in the waveguide was different from the value predicted by the simple Drude model by more than 30%. This difference was attributed to manufacturing errors. On the other side, the wave vector in TM operated waveguide has components parallel to the wires and according to the theory presented in [14, 22] the spatial dispersion should take place. Thus, it seems that one should use the corrected Drude model (2). The inconsistency between approaches [18, 20, 21] and [22] was resolved in the experimental investigation in [23]. It was found that the spatial dispersion indeed occurred in the TM operated waveguide and that the dispersion curve had both a pole and a zero (similarly to the Lorentz dispersion model). Above the frequency of the pole, the qualitative behavior is indeed similar to that predicted by the simple Drude model, but with an apparently shifted plasma frequency. Although the background physics of spatial dispersion is *fundamentally* different from the dispersionless case, it is again possible to identify the ENG, the ENZ and the EPS regions. Thus, it is possible to construct a waveguide with a smooth transition from the backward-wave propagation band, through the point with infinite wavelength, to the forward-wave propagation band. If one manufactures a longitudinal slot along such a waveguide, there will be leaky wave radiation from the structure. This new structure [24] is a waveguide analogous to the planar leaky-wave antenna introduced in [19].

The wire-based waveguide was manufactured from brass and it had dimensions of 22 × 22 × 80 mm (Figs. 9a and b). Twenty four copper wires (diameter of 0.5 mm) were used for the construction of filling. The wires were stretched between waveguide walls and soldered onto the waveguide body. Each 'layer' comprised four wires with a distance between two neighboring wires of 11 mm and a distance between the wire and neighboring waveguide wall of 5.5 mm. The distance between neighboring layers was also 11 mm. A slot with dimensions 56 × 2.5 mm, lying along the line of symmetry, was machined on the top waveguide wall. The waveguide ends were closed with two metallic hatches with N coaxial connectors. The connectors' pins lied along the waveguide line of symmetry. They actually acted as small monopole antennas, providing excitation of $TM_{11}$ mode. One waveguide end was used as the antenna feed, while the other end was simply terminated with a coaxial matched load. The far-field radiation pattern was measured at three different frequencies (7.9, 9.7 and 10.7 GHz). These three frequencies correspond to the backward-wave mode, k = 0 mode and the forward-wave mode of operation, respectively. The measured radiation patterns (Fig. 10) revealed scanning from −60° (back-fire) to +60° (end-fire). Also, the radiation in *k* = 0 mode in the broadside direction is clearly visible. One also notices the existence of one unexpected side lobe at the frequency of 7.9 GHz. This occurred due to poor matching of coaxial termination to the waveguide wave impedance, which in turn caused the standing wave. These matching problems have been overcome in the new design presented in [25].

Thus, the wire-based waveguide that operates in all three regions of the dispersion curve of the wire medium with spatial dispersion may be used for constructing a scanning leaky-wave antenna.

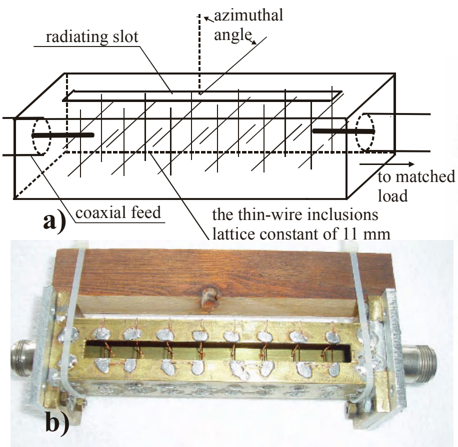


**Fig. 9** (**a**) A sketch of the experimental wire-based leaky-wave antenna; (**b**) A photo of the experimental wire-based leaky-wave antenna.

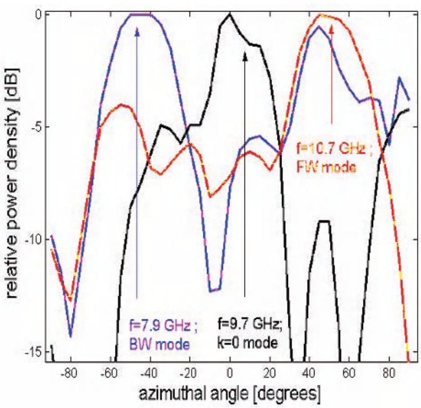


**Fig. 10** Measured radiation patterns of the experimental wire-based waveguide leaky-wave antenna.

## 5 Conclusions

It was shown experimentally that all three regions of the dispersion curve of wire media (the ENG region, the ENZ region and EPS region) can be successfully used in antenna technology. Possible applications include gain increase of simple low-directivity radiators, shortened horn antennas, and back-fire to end-fire scanning leaky wave antennas.

## References

1. Rotman, W., ‘Plasma simulation by artificial dielectrics and parallel-plate media’, IEEE Trans. Antenn. Prop., Vol. 10, No. 1, pp. 82–95, January 1962
2. Pendry, J. B., Holden A. J. et al., ‘Low frequency plasmons in thin-wire structures’, J. Phys.: Condens. Matter, Vol. 10, No. 22, pp. 4785–4809, June 1998
3. Smith, D. R., Willie J., et al., ‘A composite medium with simultaneously negative permeability and permittivity’, Phys. Rev. Lett., Vol. 84 , No. 18, pp. 4184–4187, May 2000
4. Enoch, S., Tayeb, G. et al., ‘A metamaterial for directive emission’, Phys. Rev. Lett., Vol. 89., No. 21, pp. 213902-1–213902-4, November 2002
5. Bonefacic, D., Hrabar, S. et al., ‘Experimental investigation of radiation properties of an antenna embedded in low-permittivity metamaterial’, Microw. Opt. Technol. Lett., Vol. 48, No. 12, pp. 2582–2586, 2006
6. Bonefacic, D., Hrabar, S. et al., ‘Some considerations on radiation properties of antennas embedded into low-permittivity metamaterial’, Proceedings on Metamaterials ’07, Rome, pp. 181–183, October 2007
7. Jun, H., Chun-Sheng, Y. et al., ‘A new patch antenna with metamaterial cover’, J. Zhejiang Univ., Sci. A, Vol. 7, No. 1, pp. 89–94, January 2006
8. Lovat, G., Burghignoli, P., et al., ‘Directive radiation from a line source in a metamaterial slab with low permittivity’, Proc. IEEE APS, Vol. 1B, pp. 260–263, 2005
9. Engheta, N., Ziolkowsky, R. (ed.), ‘Metamaterials: Physics and Engineering Explorations’, IEEE Press and Wiley Interscience, Piscataway, NJ, 2006
10. Alu, A., Silveirinha, M. et al., ‘Epsilon-near-zero (ENZ) metamaterials and electromagnetic Sources…’, Phy. Rev. B, Vol. 75, No. 155410, pp. 1-13, April 2007
11. Wu, Q., Pan, P., ‘A novel flat lens horn antenna designed based on zero refraction principle of metamaterials’, Appl. Phys., Vol. A 87, No. 2, pp. 151–156, May 2007
12. Schelkunoff, S.A., Friis, H. T., ‘Antennas, Theory and Practice’, Wiley, New York, 1952
13. CST Microwave Studio 2006, www.cst.com
14. Tretyakov, S., ‘Analytical Modeling in Applied Electromagnetics’, Artech House, Norwood, MA, 2003
15. Hrabar, S., Bonefacic, D., et al., ‘Analytical and experimental investigation of horn antenna…’, Proceedings on ICeCOM 2007, pp. 189–192, Dubrovnik 2007
16. Hrabar, S., Bonefacic, D., et al., ‘ENZ-based shortened horn antenna – an experimental study’, Proceedings on IEEE APS 2008, paper No. 503.4 in the conference CD, San Diego, CA, 2008
17. Walter, C. H., ‘Traveling Wave Antennas’, McGraw-Hill, New York, 1965.
18. Esteban, J., Camacho-Penalosa, C., Page, J. E., Martin-Guerrero, T. M., Marquez-Segura, E., ‘Simulation of negative permittivity and negative permeability by means…’, IEEE Trans. MTT. Vol. 53, No. 4, pp. 1506–1514, April 2005.
19. Liu, L., Caloz, C., et al., ‘Dominant mode leaky-wave antenna with backfire-to-endfire scanning capability’, Elect. Lett., Vol. 38, No. 23, pp. 1414–1416, November 2002.

20. Hrabar, S., Jankovic, G., et al., ‘Experimental investigation of waveguide filled with uniaxial thin-wire-based ENG metamaterial’, Proceedings on AP-S 2006, pp. 475–478, 2006
21. Hrabar, S., Jankovic, G., et al., ‘Basic radiation properties of waveguides filled with uniaxial single-negative metamaterials’, Microw. Opt. Technol. Lett., Vol. 48 , No. 12, pp. 2587–2591, December 2006
22. Nefedov, I. S., Dardenne, X., et al. ‘Backward waves in a waveguide, filled with wire media’, Microw. Opt. Technol. Lett., Vol. 48 , No. 12, pp. 2560–2564, December 2006
23. Hrabar, S., Vuckovic, A., et al., ‘Influence of spatial dispersion on properties of waveguide…’, Proceedings on Metamaterials 07, Rome, pp. 259–262, October 2007
24. Hrabar, S., Jankovic, G., ‘Scanning leaky-wave antenna based on a waveguide filled with plasma-like ENG Metamaterial’, Proceedings on MELECON 2006, pp. 280–283, Malaga 2006
25. Hrabar, S., Kumric, H., et al., ‘Towards high-power metamaterial-based scanning leaky-wave antenna for plasma physics applications’, Proceedings on Meta 08, pp. 81, Marrakech 2008

# Optimization of Radar Absorber Structures Using Genetic Algorithms

**Nadia Lassouaoui, Habiba Hafdallah Ouslimani, and Alain Priou**

University Paris X, Nanterre, Pôle Scientifique et Technique de Ville d'Avray, Groupe Electromagnétisme Appliqué, 50 rue de Sèvre 92410,Ville d'Avray, France
alain.priou@u-paris10.fr

**Abstract** In this paper, a real-valued genetic algorithm (GA) is implemented to construct Radar Absorbing Materials RAM by searching the characteristics (thickness *T,* permittivity $\varepsilon$ , permeability $\mu$ and conductivity σ) which ensure the minimization of the reflectivity on a frequency band. The genetic algorithms used the reflectivity in fitness function to direct the research to the best configuration. Here in, we dealt with the narrowband absorbers (Salisbury screen and circuit "Analog" RAM) and the broadband absorbers (Jaumann screen). Numerical results are presented and showed the efficiency of the methods.

## 1 Introduction

In electromagnetic applications, the problems are complex since there is no prior knowledge of the topology of the multidimensional research space, it is determined by the complex interdependence of Maxwell' equations. Several works exploit various theories and techniques to solve electromagnetic problems. The use of evolutionary techniques to automate the design of antennas is now intensively used; indeed, considerable research has been focused on the use of evolutionary techniques in electromagnetic [1–5].

Genetic algorithms GAs [6] are search procedures based on the mechanics of natural selection and genetics; they are increasingly being applied to difficult problems. In [2], the NASA Ames Research Center (Evolvable Systems Group) conducts research on antenna designs. Their approach is to encode antenna structure into a genome and to use GA to evolve the desired antenna performance as defined in a fitness function. In [3], the genetic optimization allows finding the electric properties of a number of layers positioned at either the center of an infinitely long rectangular waveguide, or adjacent to the perfectly conducting back plate of a semi-infinite shorted-out rectangular waveguide. The GA was used to minimize the reflectivity of the waveguides. In [4], the authors adopted the binary GAs with the finite element boundary integral method to optimize the geometry

S. Zouhdi et al. (eds.), *Metamaterials and Plasmonics: Fundamentals, Modelling, Applications*,

parameters of the periodical absorber structures. In [7], the GAs are used to find the geometrical and physical properties of a multilayer absorbing structure that can minimize the reflection coefficient on a X-band and for a wide incidence angle. The compute of the reflectivity is doing with the concept of impedance transformation [8, 9].

In [10], the GAs are associated with the differential theory [11] to analyze the scattering wave by rough surfaces, a stack constituted by a homogeneous layer, lamellar periodic structure and layer of Teflon on the upper is studied. A frequency selective surface (FSS) (A stack of metallic grating with homogeneous dielectric layer) is optimized [12], where the analysis of periodic metallic layer is doing with the curvilinear coordinate based method [13].

Here in, we explore the GAs for designing various types of absorbers: The narrowband absorbers (Salisbury screen and circuit "Analog" RAM) and the broadband absorbers (Jaumann absorbers).

In following section, we present briefly the GAs, after, we present the various studied structures and application results. Finally, we give our conclusion and perspectives.

## 2 Genetic Algorithm Optimizers

Genetic Algorithms GAs are stochastic search procedures modelled on the Darwinian concepts of natural selection and evolution. As an optimizer, the powerful heuristic of GAs is effective at solving complex, combinatorial and related problems. GA optimizers are particularly effective when the goal is to find an approximate global maximum in a high-dimension, multimodal function domain in a near-optimal manner.

In GAs, a set or population of potential solutions is caused to evolve toward a global optimal solution. This evolution (Fig. 1a) occurs as a result of pressure exerted by a fitness-weighted selection process and exploration of the solution space is accomplished by crossover and mutation of existing characteristics present in the current population.

Crossover involves the random selection of a crossover site(s) and the combining of the two parent's genetic information (Fig. 1b). The mutation [6] serves as a means for introducing new, unexplored points into the GA optimizer's search domain. It introduces the genetic material that is not present in the current population.

The GAs evolve according a fitness function which measures the ability of the solution candidate to adapt to the problem. The best solution will have the highest or lowest fitness function. Indeed, the fitness function is the link between the physical problem and the GA optimization process.

The GAs are stopped when either a design goal is reached, or no progress is observed in the population for several generations.

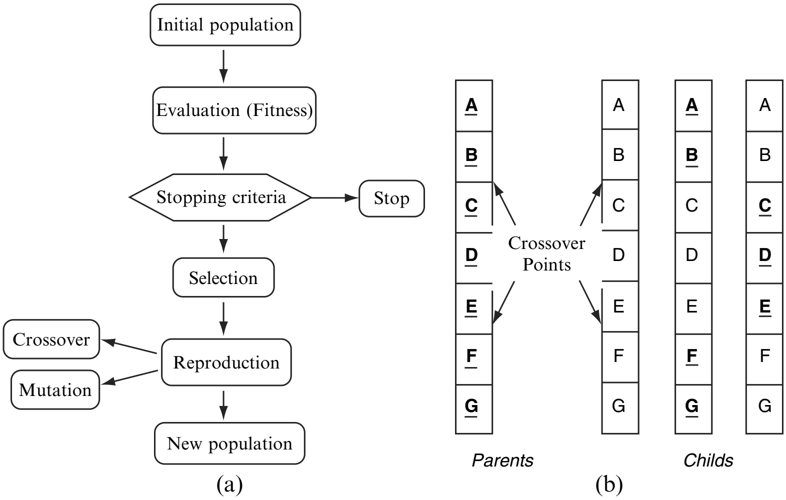


**Fig. 1** Various steps of genetic algorithms.

## 3 Studied Absorber Structures

The literature presents a great number of absorbers [8, 9, 14–17]. Here in, we present the applications of GAs in designing absorber structures. Firstly, we study the Radar Absorbing Materials which operate optimally only in narrow band about a resonant frequency (Salisbury screen and circuit analog RAM). Then, we present an absorber (Jaumann absorber) which operates on a broad band. We give the application results, and we analyze the absorbers according the electric and dimension characteristics of the layers.

### *3.1 Salisbury screen*

If a thin sheet is located as an intervening medium between the free space and a flat metallic surface, the input impedance $Z_{in}$ may be obtained by combining the effects of the sheet resistance $R_{sh}$ and the transformed impedance of the metallic surface, which act in parallel. The sheet material $R_{sh}$ is expressed by its conductivity $\sigma_{sh}$ and its thickness $t_{sh}$:

$$R_{sh} = \frac{1}{\sigma_{sh} . t_{sh}} \tag{1}$$

A Salisbury screen (Fig. 2) is defined by adjusting the spacing between the thin sheet and the metallic surface to $\lambda/4$; and for incidence normal to the sheet, the input impedance is identical to $R_{sh}$, hence the condition for zero reflection for such a thin screen shielding metallic surfaces is:

$$R_{sh}=Z_0 \tag{2}$$

With $Z_0$ is the characteristic impedance of the free space (377 Ω/square).


**Fig. 2** Salisbury screen.

With Eqs. (1) and (2), the exact thickness $t_{sh}$ of the resistive sheet is obtained:

$$t_{sh} = 1/(Z_0 \sigma_{sh}) \tag{3}$$

We use the GAs to search the characteristics of Salisbury screen which ensures the minimization of the reflectivity for a given frequency *f*. At each generation, the reflectivity (in dB) of the best solution in the population is taken as the fitness. We note that for the spacer, we take these characteristics:

The thickness $d_{sp} = \lambda/4$, the permeability $\mu_{sp} = 1$, the imaginary part of the permittivity is equal to zero.

By Fig. 3, we give the obtained results of optimization with normal incidence at frequency 5 GHz. The Fig. 3a gives the evolution of the fitness in genetic process. We check that it is doing in decreasing way, since the hope is the minimization of the reflectivity. We note that each level corresponds to a configuration; at final generation, the frequency response of the Salisbury screen is showed by Fig. 3b, we achieve −28 dB at 5 GHz and we note the periodicity of the frequency response, where the peaks appear at discrete frequencies of (2n + 1) × 4.25 GHz.

The obtained characteristics are:

– The permittivity, permeability, conductivity and thickness of the resistance sheet are respectively:

$\varepsilon_{sh} = 2.39$ $\mu_{sh} = 1$ $\sigma_{sh} = 43 s/m$ $t_{sh}$=61,1µm

– The permittivity of the spacer is: $\varepsilon_{sp} = 1.1$

Figure 4 gives the reflectivity according to the incidence angles at 4.25 GHz, the performances decrease in away from the normal, which is physically correct.

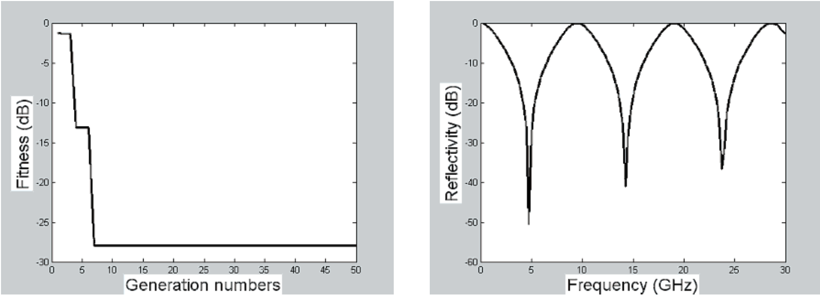


(a) (b)

**Fig. 3** Optimization of the Salisbury screen for normal incidence at 5 GHz (**a**) Fitness according the generations, (**b**) frequency response of the obtained configuration at final generation.

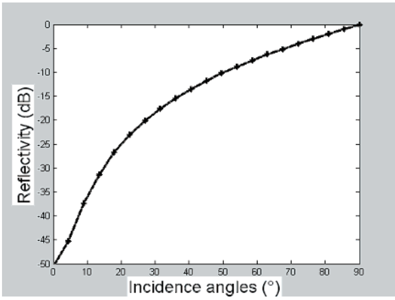


**Fig. 4** Reflectivity according incidence angles at frequency 4.25 GHz.

It is possible to replace the Salisbury screen by a Dallenbach absorber [8]. This latter is constituted by a finite layer of dielectric material backed on the conducting surface. It is analyzed as a function of both permittivity and permeability of the material. The results [8] in Fig. 5 are essentially that of a power reflection on the permittivity plane corresponding to each thickness. Unlike the Salisbury screen, the zero reflection condition can be satisfied also with a thickness smaller than $\lambda/4$ for more than one set of complex permittivity values.

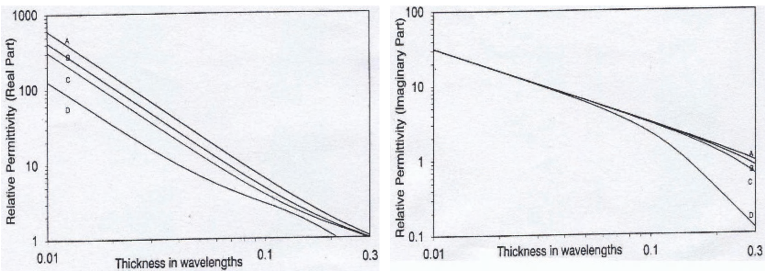


(a) (b)

**Fig. 5** Real and imaginary parts of the relative permittivity versus thickness of the Dallenbach layer, with the relative permeability values: 1.05 (A), 1.5 (B), 2 (C) and 5 (D).

## 3.2 Circuit analog RAM

When a layer of patterns of finite conductivity is deposed over the spacer, it modifies the effective input impedance [8]. In practice the layer is in the form of an array of two-dimensional patterns which have characteristics reactance associated with them. This constitutes yet another powerful method of designing a resonant absorber. The class of such absorbers is known as circuit “analog” absorber or CA radar absorbing materials. Some of the well-known CA-RAM are constructed with wires, strips, intersecting wires, crossed dipoles, etc.

CA-RAM patterns have the property of resonating at a characteristic frequency, which is function of geometry, orientation and patterns density. By adjusting these physical attributes, it is possible to obtain the resonance, and the reflection minima at any desired frequency. An example is an array of wire elements placed on a spacer (Fig. 6).

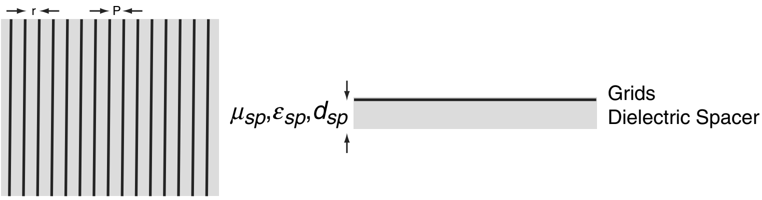


**Fig. 6** CA-RAM with wire grids of radius *r* and pitch *p*.

The metallic wires are assumed to be of radius *r* and placed parallel to each other at a pitch *p*. The effective impedance for such wires may be expressed for oblique incidence $\theta$ by [8]:

$$Z_{wires} = \frac{pZ_{\mathrm{int}}}{Z_0}\cos\theta + j\frac{p}{\lambda}\ln\left(\frac{p}{2\pi r}\right)\cos\theta \tag{4}$$

Where the internal impedance of the metallic wires in the microwave region is given as [8]:

$$Z_{\mathrm{int}} = \frac{1}{2\pi r}\sqrt{\frac{\mu_0\omega}{2\sigma}}(1+j) \tag{5}$$

The input impedance for a metal backed configuration with a spacer of thickness $d_{sp}$ is obtained by taking the parallel combination [8]:

$$Z_{in} = \frac{jZ_{wires}Z_{sp}\tan(\beta d_{sp}\cos\theta)}{Z_{wires} + jZ_{sp}an(\beta d_{sp}\cos\theta)} \tag{6}$$

The reflection coefficient for CA-RAM may be determined by:

$$\rho = \frac{Z_{in} - Z_0}{Z_{in} + Z_0} \tag{7}$$

$Z_0$ is the characteristic impedance of the free space.

By the following Fig. 7, we give the obtained results for normal incidence at the frequency 5 GHz. The evolution of the fitness in genetic process and the frequency response of the obtained solution at the generation 500 are respectively given by Fig. 7a and b. A minimum is found at 5 GHz where we reach almost −33 dB, and some local minima around −10 dB appear at frequencies up to 5 GHz. The obtained characteristics are:

– The permittivity, permeability and thickness of the spacer:

$\varepsilon_{sp} = 3.99$ $\mu_{sp} = 1$ $d_{sp}$=*9.845 mm*

– The conductivity, pitch and radius of the grids:

$\sigma = 1.73$ *s/m* *p=2 mm* *r=0.5 μm*

The frequency response and the characteristics of the solution at generation 100 are given by the Fig. 8, we obtain a pick about −19 dB at the frequency 5 GHz where the optimization is doing.

With the obtained configuration at generation 500, we analyze the dependence of the reflectivity according the incidence angles and the characteristics of the grids. With Fig. 9a, we note that more we approach the grazing incidence angle (90°), the performance decreases, what is physically correct since more we move away from the incidence normal, more the reflection decreases.

The electromagnetic absorption deteriorates rapidly on other side of the characteristics of the grids. Indeed, the reflectivity approaches zero (Fig. 9b–d) after some thresholds of the conductivity, the pitch and the radius of grids.

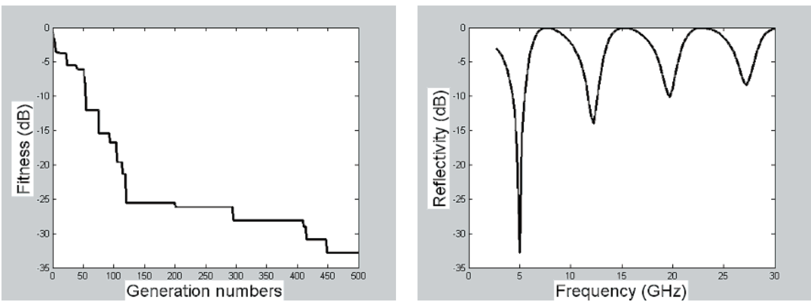


(a) (b)

**Fig. 7** Obtained results at generation 500 for normal incidence and optimization at 5 GHz.

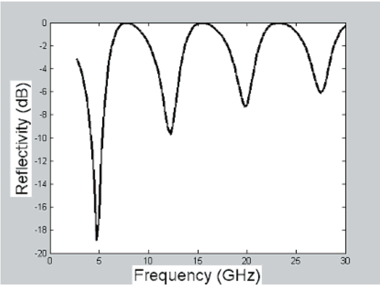


$\varepsilon_{sp} = 3.755$

$\mu_{sp} = 1$

$d_{sp} = 10\ mm$

$\sigma = 1 s/m$

$p = 2\ mm$

$r = 0.5\ \mu m$

**Fig. 8** Results at the generation 100 for normal incidence and optimization at 5 GHz.

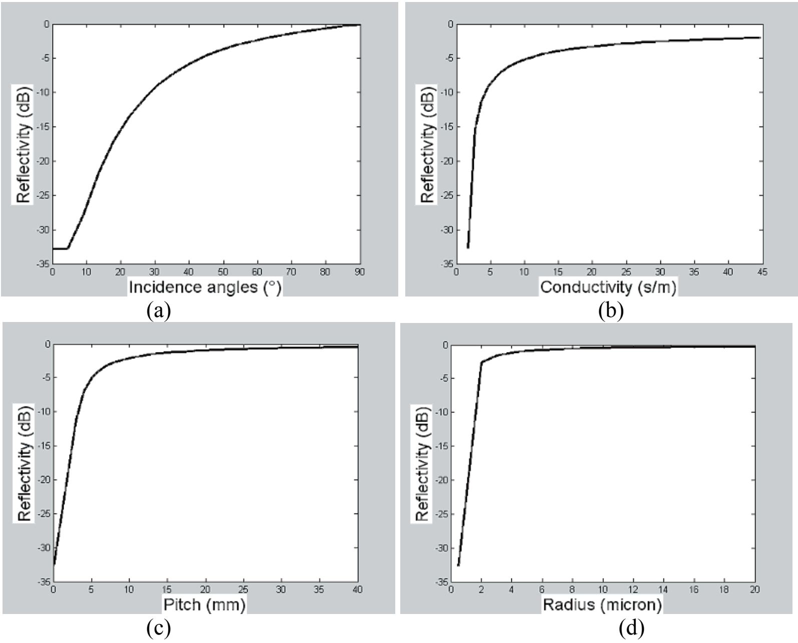


**Fig. 9** Reflectivity at $f$ = 5 GHz according to the: (**a**) incidence angles, (**b**) conductivity, (**c**) pitch, (**d**) radius of grids.

Now, we present absorbers with broadband characteristics, which are achieved by exploiting the multiple layers of narrowband absorbers.

## *3.3 Jaumann absorber screen*

A commonly used technique to obtain RAM with broadband radar cross section (RCS) reduction characteristics is to use multiple layers of narrowband absorbers [8]. A multilayer Salisbury screen uses several layers of suitably spaced resistive sheets defines the Jaumann screen. The net effect of this configuration is resonance at discrete sets of frequencies resulting in multiband absorber. The expression for the reflection coefficient [8, 9] of a multilayered Jaumann absorber is essentially simple but recursive in nature (Fig. 10).


**Fig. 10** Jaumann absorber with two resistive sheets.

By Fig. 11, we present the obtained results for optimization at frequency 5 GHz for normal incidence. With Fig. 11a, we check that the GAs allow the research towards the configurations which decrease the reflectivity. The frequency response of the solution at generation 100 presents various modes where the resonance is doing at various frequencies (Fig. 11b). The obtained configuration:

*1st sheet*: $\varepsilon_{sh1} = 1.1$ $\mu_{sh1} = 1$ $\sigma_{sh1} = 50 s/m$

$R_{sh1}$=379.8 $\Omega/square$ $t_{sh1}$=52.7 $\mu m$

*2nd sheet*: $\varepsilon_{sh2} = 2.06$ $\mu_{sh2} = 1$ $\sigma_{sh2} = 50 s/m$

$R_{sh2}$=250 $\Omega/square$ $t_{sh2}$=80 $\mu m$

*Dielectric spacers*: $\varepsilon_{sp} = 1.91$ $d_{sp} = \lambda/9.24$

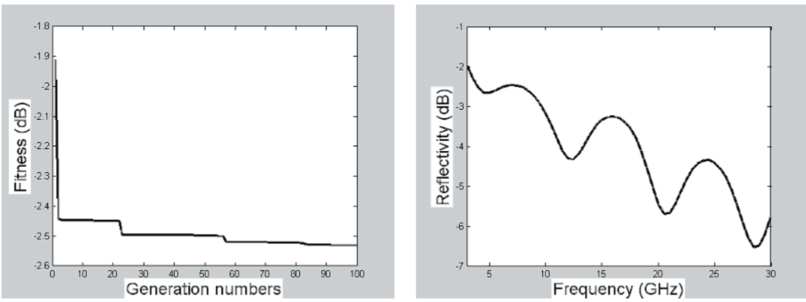


(a) (b)

**Fig. 11** Obtained results for the two layer Jaumann absorber for normal incidence.

In the case of a three layer Jaumann absorber, we give the results for normal incidence and at 5 GHz. By Fig. 12b, we see various modes where the reflectivity is minimal. The obtained characteristics are:

*1st sheet*: $\varepsilon_{sh1} = 3.04$ $\mu_{sh1} = 1$ $\sigma_{sh1} = 56 s/m$

$R_{sh1}$=561 $\Omega/square$ $t_{sh1}$=31,7 $\mu m$

*2nd sheet*: $\varepsilon_{sh2} = 1.58$ $\mu_{sh2} = 1$ $\sigma_{sh2} = 57 s/m$

$R_{sh2}$=371 $\Omega/square$ $t_{sh2}$=47.3 $\mu m$

*3rd sheet*: $\varepsilon_{sh3} = 1.44$ $\mu_{sh3} = 1$ $\sigma_{sh3} = 57 s/m$

$R_{sh3}$=$250\,\Omega/square$ $t_{sh3}$=$70.3\mu m$

*Dielectric spacers*: $\varepsilon_{sp} = 1.70$ $d_{sp}$=$\lambda/10$

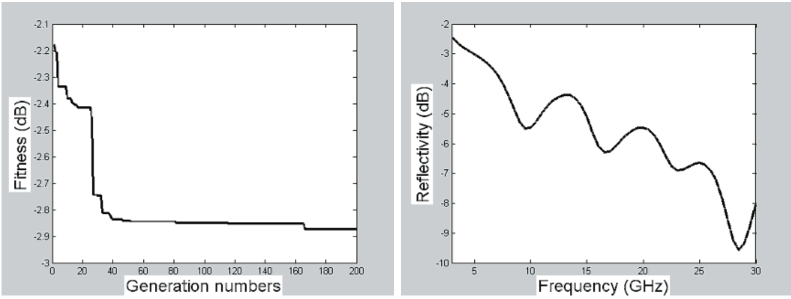


(a) (b)

**Fig. 12** Three layer Jaumann absorber.

We propose to analyse the Jaumann absorber according to the number of layers. Then, we compare between (Fig. 13):

– The Jaumann absorber with three layers by using the obtained configuration from the optimization for normal incidence at 5 GHz.
– The Jaumann absorber with two layers by using the same configuration of the two up layers of Jaumann absorber with three layers.

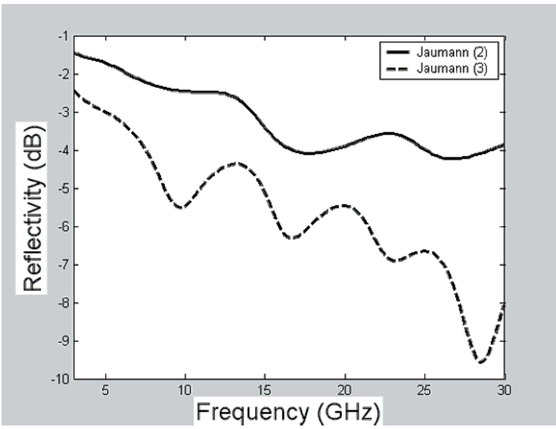


**Fig. 13** The reflectivity by Jaumann absorbers with three and two layers for normal incidence.

We can see that with three layers (Fig. 13), the reflectivity is better, since it is minimal, where at some frequencies; we have a difference of more −5 dB.

## 4 Conclusions

In this paper, we have studied the electromagnetic absorbers and used the genetic algorithms to search the characteristics which ensure the desired performances.

The main characteristic of the genetic algorithms is the ability to search in multidimensional space the combination of the material characteristics ($\varepsilon$, $\mu$, $\sigma$, *thickness*) of absorbers which ensure a better reflectivity on a frequency band.

In the genetic interface, the parameters (crossover and mutation rates, the replacement percentage) are computed in automatic ways by the program to allow an automatic research. We also supervise the diversity of the population to avoid the stagnation of the research and allow the best exploration of the research space.

In future works, we hope to study and use the statistical approaches for comparing the optimized materials with existing and well identified materials, and we explore the designed genetic interface to optimize various high-impedance surfaces and antennas.

## References

1. Rahmat-Samii, Y., Michielssen, E.: Electromagnetic Optimization by Genetic Algorithms. Wiley, New York (1999).
2. Lohn, J., Crawford, J., Globus, A., Hornby, G., Kraus, W., Larchev, G., Pryor, A., Srivastava, D.: Evolvable systems for space applications. Proceedings of International Conference on Space Mission Challenges for Information Technology (2003).
3. Hall, J.M.: A novel, real-valued genetic algorithm for optimizing radar absorbing materials. NASA/CR-2004-212669 (2004).
4. Cui, S., Weile, D.S.: Robust design of absorbers using genetic algorithms and the finite element-boundary integral method. IEEE Transactions on Antennas and Propagation. Vol. 51, No. 12, pp. 3249–3258 (2003).
5. Cui, S., Weile, D.S., Volakis, J.L.: Novel planar absorber designs using genetic algorithms. Antennas and Propagation Society International Symposium. Vol. 2B, pp. 271–274 (2005).
6. Goldberg, D.E.: Genetic Algorithms in Search, Optimization and Machine Learning. Addison-Wesley, Reading, MA (1989).
7. Lassouaoui, N., Ouslimani, H., Priou, A.: Genetic Algorithms for Automated Design of the Multilayer Absorbers in the X-Band and Incident Angle Range. Progress in Electromagnetics Research Symposium PIERS'08. Hangzhou (2008).
8. Vinoy, K. J., JHA, R. M.: Radar Absorbing Materials. Kluwer, Dordrecht (1996).
9. Petit, R.: Electromagnetic Waves in Radio Electricity and Optics. Masson Edition, Paris (1992).
10. Lassouaoui, N., Ouslimani, H., Priou, A.: Differential Theory with Genetic Algorithms in Design Periodic Absorbers. Progress in Electromagnetics Research Symposium PIERS'08. Hangzhou (2008).
11. Neviere, M., Popov, E.: Light Propagation in Periodic Media, Differential Theory and Design. Marcel Dekker, New York (2003).
12. Lassouaoui, N., Ouslimani, H., Priou, A.: Development of Genetic Algorithms and C-Method for Optimizing a Scattering by Rough Surface. European Computing Conference. Springer, Greece (2007).

13. Granet, G., Edee, K., Felbacq, D.: Scattering of a plane wave by rough surfaces: A new curvilinear coordinate system based approach. Progress in Electromagnetics Research, PIER. Vol. 37, pp. 235–250 (2002).
14. Rozanov, K. N.: Ultimate thickness to bandwidth ratio of radar absorbers. IEEE Transactions on Antennas and Propagation. Vol. 48, pp. 1230–1234 (2000).
15. Vinogradov, A. P., Lagar'kov, A. N., Sarchev, A. K., Sterlina, I. G.: Multilayer absorbing structures from composite materials. Journal of Communications Technology & Electronics. Vol. 41, pp. 142–145 (1996).
16. Kazantsev, Y. N., Krasnozhen, A. P., Tikhonravov, A. V.: Multilayered absorbing structures with Debye dispersion of the permittivity. Soviet Journal of Communications Technology & Electronics. Vol. 36, pp. 19–25 (1991).
17. Knott, E. F., Shaeffer, J. F.: Tuley, Radar Cross Section: Its Prediction, Measurement and Reduction, Artech House, Dedham, MA, pp. 413–442 (1985).

# Design of Metamaterial-Based Resonant Microwave Absorbers with Reduced Thickness and Absence of a Metallic Backing

**Filiberto Bilotti and Lucio Vegni**

University "Roma Tre" – Department of Applied Electronics,
Via della Vasca Navale, 84 – 00146 Rome – Italy
bilotti@uniroma3.it

**Abstract** In this chapter, we present a review of our research activities on resonant metamaterial absorbers. This research, leaded by our group, has been conducted during last years in close cooperation with other theoretical and experimental groups. The common idea behind all the layouts we present in this work is the possibility to strongly reduce the thickness and to avoid the metallic backing of regular absorbers by using metamaterials. The principles of operation of each proposed setup are reviewed and some numerical results are presented to show the application capabilities of resonant microwave absorbers without a metallic backing.

## 1 Introduction

Microwave absorbers find applications in several aspects of military and civil applications. The reduction of the radar signature of aircrafts, ships, tanks and other targets for stealth and camouflage purposes, is perhaps the most widely know application of microwave absorbers in the military framework. On the other hand, absorbers are also used in military and civil applications to reduce the electromagnetic interference among microwave components and/or electronic circuits mounted on the same platform. Microwave absorbers find interesting applications also in satellite and mobile phone terminals, in order to reduce the back-radiation of the radiators, which is a useful feature for both high-precision radio-navigation systems and mobile communications characterized by low electromagnetic pollution.

Whatever is the application for which the absorber is intended, it has to be, anyway, electrically thin, in order to minimize the space occupancy. In addition, especially for what concerns resonant absorbers (i.e. absorbers used to reduce the reflection in a narrow frequency band), which is the matter of the present work, at least another issue is to be considered. Most of the resonant absorbers are based on

S. Zouhdi et al. (eds.), *Metamaterials and Plasmonics: Fundamentals, Modelling, Applications*, 

the concept of the Salisbury screen [1], which is made of a metallic plate and a 377 Ohm resistive sheet placed a quarter of the wavelength apart from the plate. In this setup, the presence of the metallic plate governs the electromagnetic behavior of the component. The strong reduction of the power reflection at the design frequency, in fact, is due to the destructive interference between the incident wave and the reflected wave from the metallic screen itself. If the object to hide is a metallic one (e.g. planes, tanks, etc.), the presence of the metallic plate does not represent a problem. Anyway, the recent advances in material technology allow to replace most of the metallic parts of large objects with new non-metallic materials, exhibiting enhanced performances in terms of robustness and low weight. In this framework and for all the applications not involving metallic objects, resonant absorbers with a metallic backing would work properly at the design frequency, while behaving as regular conductors outside the operational band. The result is that the object to hide would be characterized by a low observability in the narrow frequency band of the absorber operation, while being much more visible at any other frequency.

Some of the electromagnetic properties of composite artificial materials, metamaterials and metasurfaces, have been shown to be very promising in order to design microwave absorbers with improved performances. The most interesting results refer to the employment of frequency selective [2] and high impedance surfaces [3]. Such setups can be split in two categories: one is characterized by electrically thin components employing a metallic backing [4–10], and the other one is characterized by regular quarter wavelength thicknesses and absence of the metallic backing plate [11–12]. Recently, an attempt to obtain both the advantages of the two categories (i.e. reduced thickness and absence of the metallic plate) has been proposed in [13], by employing two frequency selective surfaces sandwiching a regular dielectric slab.

Alternative ways to obtain *compact* absorbers *without the metallic backing* have been recently proposed by our research group and make use of different classes of metamaterials. Some of these approaches are reviewed in the present work, which is organized as follows. In Section 2, we review the design of microwave absorbers based on Single-NeGative (SNG) metamaterials (i.e. materials characterized by a negative real part of either permittivity or permeability). In Sections 3 and 4, we review the design of microwave absorbers based on Split-Ring Resonators (SRRs) and Multiple Split-Ring/Spiral Resonators (MSRRs/SRs), respectively. Finally, in Section 5 we present some alternative layouts, characterized by a simpler geometry and that can be easily fabricated. Part of the research activities on these topics has been conducted in close collaboration with the groups of the University of Pennsylvania (Professor N. Engheta) and Bilkent University (Professor E. Ozbay).

## 2 ENG–MNG Resonant Absorbers

In cooperation with Engheta's group, we have shown [14] how a regular 377 Ohm resistive sheet sandwiched by a properly designed slab pair consisting of a MuNeGative (MNG) and an Epsilon-NeGative (ENG) slab behaves as an effective sub-wavelength absorber working, in principle, for any polarization, angle of incidence and total thickness of the component (Fig. 1). The physical mechanism behind, is the compact resonance arising at the interface between the two metamaterial slabs, which is due to the flip of the sign of the constitutive parameters across the interface [15]. Under certain design rules presented in [14], the resistive sheet placed at the interface between the two materials, does not perturb the compact resonance and most of the power carried by the impinging wave is absorbed in the sheet itself.

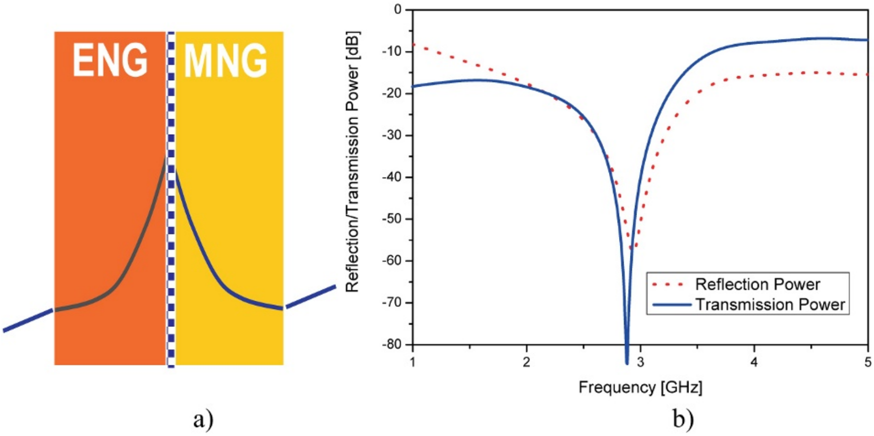


**Fig. 1** (**a**) Layout of a resonant absorber made of ENG and MNG slabs. (**b**) Full-wave simulated response in the case of normal incidence. *Data*. ENG slab thickness: 1 mm; MNG slab thickness: 11 mm; design frequency: 3 GHz; ENG relative permittivity at 3 GHz: −1; ENG relative permeability at 3 GHz: 1; MNG relative permittivity at 3 GHz: 0.1; MNG relative permeability at 3 GHz: −10. (From [14].)

In [14] it has been shown that the proposed absorber exhibits superior performances with respect to Salisbury's layout. In particular, the proposed structure does not need the metallic plate and can be made electrically thin, in principle, without any limit. In addition, angular and frequency bandwidths of operation are both greater than the ones of the Salisbury screen. Finally, it is recalled here that losses, which usually affect the performances of metamaterial based components, do not represent an issue here and, indeed, help to reduce the power reflected from the screen.

If we were able to fabricate through proper inclusions isotropic and homogeneous ENG and MNG slabs, the layout shown in Fig. 1a would work with the ideal performances recalled so far. Anyway, when dealing with real-life inclusions, the practical realization of such an absorber is not actually easy. The most challenging aspect resides in meeting the resonance condition at the interface between the two different inclusion-based metamaterials. The ENG slab, in fact, can be obtained at microwaves by using a regular wire medium [16], while the MNG slab through the employment of properly designed SRRs [17]. As long as the two slabs are supposed to be made of ideal isotropic materials, it is relatively easy to design the slabs to obtain a resonant mode confined at the interface in the presence of the resistive sheet. As soon as the inclusions are considered, instead, even in the easier case of the ENG–MNG pair of [15] without the resistive sheet, the actual interface between the two "effective" slabs disappears, since the materials are made by inclusions hosted in regular dielectrics (Fig. 2). In this case, especially when the resistive sheet is also considered, it is very challenging to optimize the setup in order to excite the resonant mode required for the operation of the absorber.

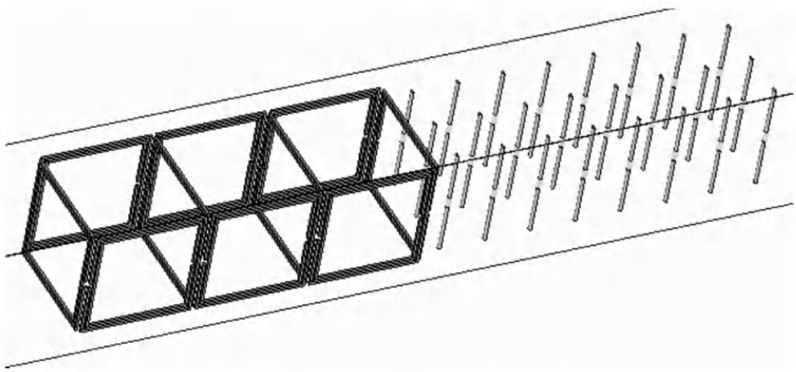

**Fig. 2** Sketch of a possible actual implementation of the ENG–MNG absorber presented in [15]. The ENG slab is implemented through a wire medium (*right side*), while the MNG slab through a proper set of SRRs (*left side*).

For this reason, we decided to consider different layouts, based on a different principle of operation.

## 3 SRR Based Microwave Absorbers

Keeping the constraints of having resonant microwave absorbers with sub-wavelength thicknesses and without any metallic backing, one interesting possibility is offered by the employment of a planar array of SRRs working at resonance [18]. In this case, at the collective resonant frequency of the SRRs, the planar array of

SRRs (Fig. 3a) would work as a Perfect Magnetic Conductor (PMC) and, thus, the 377 Ohm resistive sheet can be placed at a very small electrical distance from that. The principle of operation is, thus, the same as for any other compact absorber based on the employment of frequency-selective and high-impedance surfaces, but it does not require any metallic backing.

The typical thickness of this absorber layout depends only on the dimensions of the SRRs. The typical side length of an SRR inclusion is around λ/20 and, thus, the thickness of the absorber is of the same order. In Fig. 3b the response of the absorber as a function of the frequency is depicted in the case of a normal impinging plane wave with the magnetic field directed along the axes of the SRRs.

The actual fabrication of the absorber depicted in Fig. 3a is relatively easy and the resonance condition is easily met, since we do not have to excite a resonant interface mode any more. The inclusions resonate, in fact, all together at the same design frequency and the array behaves as a material with a very high real part of the permeability, returning, thus, the boundary condition of a PMC. It is worth noticing that in this case the losses are higher than in the layout presented in the previous Section, but, again, they do not affect the behavior of the absorber.

The setup in Fig. 3a is currently under fabrication by Ozbay's group at Bilkent University, in the frame of a collaboration started within the European Network of Excellence Metamorphose.[1]

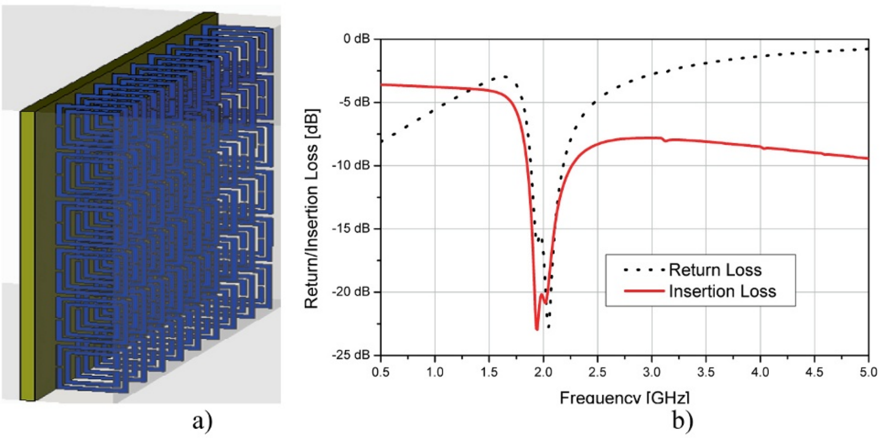


**Fig. 3** (**a**) Layout of a resonant absorber made of a planar array of split-ring resonators and a resistive sheet (377 Ohm) placed in close proximity. (**b**) Full-wave simulated response in the case of normal incidence. *Data*. SRR external side length: 5 mm; strip width: 0.1 mm; separation between adjacent strips: 0.1 mm; gap: 0.1 mm. (From [18].)

[1] www.metamorphose-eu.org

## 4 Microwave Absorbers Based on Miniaturized MSRR and SR Inclusions

In order to gain a further reduction of the absorber thickness, we need to find ever more miniaturized magnetic inclusions, such as MSRRs[2] and SRs.[3] In [19] and [20] our and Ozbay's groups have proposed new analytical models for the design of such miniaturized inclusions, in order to make the design of the absorber straightforward. The SRRs of Fig. 3a are basically replaced either by MSRRs (Fig. 4a) or by SRs (Fig. 4b).

The employment of MSRRs allows to obtain absorbers whose typical thickness is around $\lambda/40$, while the SRs are able to increase the miniaturization of the component up to $\lambda/100$ and even beyond.

The reflection and transmission properties of the absorbers based on such inclusions are not shown here for sake of brevity. They are very similar to the ones already presented in Fig. 3b in the case of the SRRs. The only difference is that, when increasing the number of the rings or turns, the bandwidth of operation, as expected, becomes narrower.

The configurations presented in Fig. 4 based on MSRRs and SRs are currently under fabrication at Bilkent University.

## 5 Microwave Absorbers: Fabrication Issues and Alternative Layouts

The layouts presented in Figs. 3–4 are based on magnetic inclusions only and, for this reason, they can be fabricated in a relatively easy way, with respect to the configuration depicted in Fig. 2. Nevertheless, the actual fabrication of the absorbers in Figs. 3–4 requires several steps and cannot be performed in a direct way. The reason of these difficulties resides in the specific polarization of the impinging field required to excite the magnetic inclusions. Since the magnetic field must be parallel to the axes of the magnetic inclusions, the magnetic inclusions cannot be placed on a plane. Therefore, in order to fabricate the absorbers depicted in Figs. 3–4, we need at first to print an $N \times M$ planar array of inclusions on a

[2] This magnetic resonator is basically a generalization of the SRR with multiple concentric rings. Increasing the number of the rings, the capacitive effects between two adjacent rings increase, as well. The result is the reduction of the resonant frequency of the inclusion with the number of the rings. In [19] it has been shown that a few rings are enough to obtain the maximum achievable reduction of the resonant frequency for a fixed length of the external side of the inclusion.

[3] In the SR the capacitive effects are much stronger, due to the asymmetric nature of the inclusion. Increasing the number of the turns, the capacitive effects between two adjacent turns increases. Even in this case, a few turns are enough to obtain the maximum achievable reduction of the resonant frequency for a fixed length of the external side of the inclusion [19].

dielectric board; then the board is cut in M slabs containing one column of N inclusions each; finally, in order to get the layouts depicted in Figs. 3–4, the M slabs are aligned and placed in a frame.

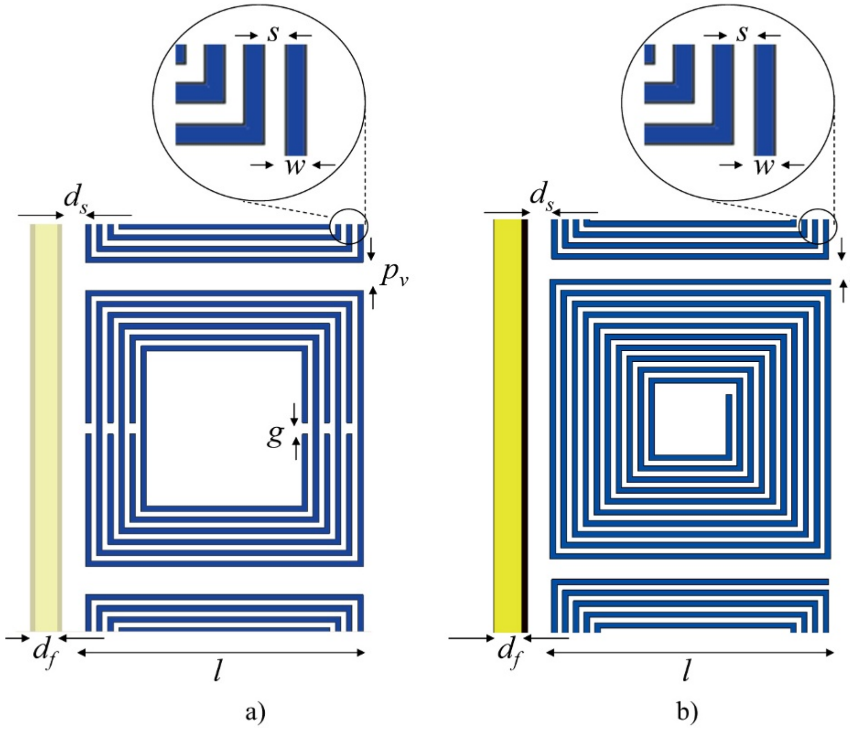


**Fig. 4** (**a**) Layout of a resonant absorber made of a planar array of MSRRs and a resistive sheet (377 Ohm) placed in close proximity. (**b**) Layout of a resonant absorber made of a planar array of SRs and a resistive sheet (377 Ohm) placed in close proximity.

In order to solve this problem, we have proposed the layout depicted in Fig. 5a. Following the latest advances of the metamaterial research in the IR and optical regimes [21], the magnetic resonance of either the SRR, or the MSRR, or the SR is replaced with the magnetic resonance of two parallel cut-wires printed on the two sides of the same thin dielectric board. The current densities in the two parallel wires are oppositely directed and the current loop is closed within the dielectric board through the displacement current. This inclusion is excited by a magnetic field parallel to the board. A planar array made of parallel cut-wires, thus, would behave in a similar way as the array of SRR depicted in Fig. 3a. The electromagnetic behavior of a microwave absorber based on this design is shown in Fig. 5b. The impinging wave is polarized as sketched in Fig. 5a.

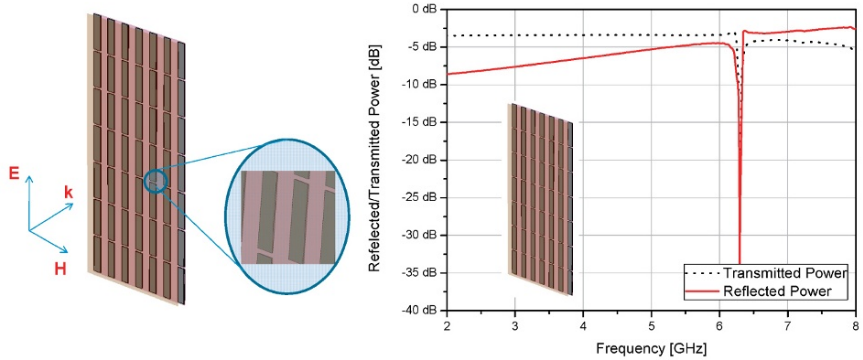


a) b)

**Fig. 5** (**a**) Layout of a resonant absorber made of a planar array of parallel cut-wires and a resistive sheet (377 Ohm) placed in close proximity. (**b**) Full-wave simulated response in the case of normal incidence.

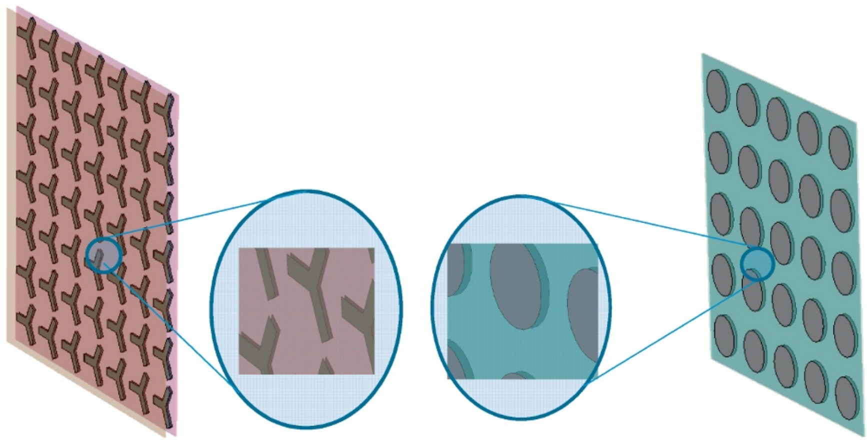

a) b)

**Fig. 6** (**a**) Layout of a resonant absorber made of a planar array of parallel tripod inclusions and a resistive sheet (377 Ohm) placed in close proximity. (**b**) Layout of a resonant absorber made of a planar array of parallel disk inclusions and a resistive sheet (377 Ohm) placed in close proximity.

Finally, in order to increase the isotropy of the absorber, we have proposed also the two layouts depicted in Fig. 6 [22]. In these configurations, the parallel cut-wires are replaced by two parallel tripod structures and two parallel disks, respectively.

# 6 Conclusions

In this chapter, we have presented a review of different resonant microwave absorber layouts based on the employment of metamaterials. The common features of these layouts are: (a) electrically small thickness; (b) absence of the metallic backing plate. For each of the proposed absorber configurations we have presented the operational principles and the possible limitations when going towards the actual fabrication of the components. Isotropy issues have been also considered and some solutions have been proposed.

**Acknowledgments** The authors would like to acknowledge all the co-authors of the research we have here reviewed: Professor Nader Engheta (University of Pennsylvania), Dr. Andrea Alù (University of Pennsylvania), Professor Ekmel Ozbay (Bilkent University), Dr. Koray Aydin (Bilkent University), Mr. Boratay Alici (Bilkent University), Mr. Luca Nucci (University “Roma Tre”), Mr. Luca Scorrano (University “Roma Tre”), Mr. Simone Tricarico (University “Roma Tre”).

The authors would like to acknowledge also the support of the following national and international projects: METAMORPHOSE Network of Excellence, funded under the 6th Framework Programme by the European Commission; PRIN 2006, funded by the Italian Ministry of the Research; ECONAM, funded under the 7th Framework Programme by the European Commission.

# References

1. Salisbury, W.W.: Absorbent body for electromagnetic waves, U.S. Patent 2 599 944, (1952)
2. Munk, B.A.: Frequency Selective Surfaces: Theory and Design. Wiley, New York (2000)
3. Sievenpiper, D., Zhang, L., Broas, R.F.J., Alexopolous, N.G., and Yablonovitch, E.: High-impedance electromagnetic surfaces with a forbidden frequency band. IEEE Trans. Microw Theor. Tech., **47**, 2059–2074 (1999)
4. Chakravarty, S., Mittra, R., Williams, N.R.: On the application of the microgenetic algorithm to the design of broad-band microwave absorbers comprising frequency-selective surfaces embedded in multilayered dielectric media. IEEE Trans. Microw Theory Tech., **49**, 1050–1059 (2001)
5. Liu, H., Chenga, H., Chua, Z., and Zhanga, D.: Absorbing properties of frequency selective surface absorbers with cross-shaped resistive patches. Mater. Des., **28**, 2166–2171 (2007)
6. Kern, D.J., Werner, D.H.: A genetic algorithm approach to the design of ultra-thin electromagnetic bandgap absorbers. Microw Opt. Technol. Lett., **38**, 61–64 (2003)
7. Gao, Q., Yin, Y., Yan, D.B., Yuan, N.C.: A novel radar-absorbing-material based on EBG structure. Microw. Opt. Technol. Lett., **47**, 228–230 (2005)
8. Zheng, B., Shen, Z.: Wideband radar absorbing material combining high-impedance transmission line and circuit analogue screen. Electron. Lett., **44** (2008)
9. Costa, F., Monorchio, A., Manara G.: Ultra-thin absorbers by using high impedance surfaces with resistive frequency selective surfaces. IEEE Antennas and Propagation International Symposium, 861–864 (2007)

10. Tretyakov S., Maslovski S.: Thin composite radar absorber operational for all incidence angles. Thirty-third European Microwave Conference, 1107–1110 (2003)
11. Itou, A., Ebara, H., Nakajima, H., Wada, K., Hashimoto, O.: An experimental study of a λ/4 wave absorber using a frequency-selective surface. Microw. Opt. Technol. Lett., **28**, 321–323 (2001)
12. Itou, A., Hashimoto, O., Yokokawa, H., Sumi, K.: A fundamental study of a thin λ/4 wave absorber using FSS technology. Electron. Commun. Jpn 1 (Part I: Communications), **87**, 77–86 (2004)
13. Kiani, G.I., Weily, A.R., Esselle, K.P.: Frequency Selective Surface Absorber using Resistive Cross-Dipoles. IEEE Antennas and Propagation Society International Symposium, 4199–4202 (2006)
14. Bilotti, F., Alù, A., Engheta, N., Vegni, L.: Compact Microwave Absorbers Utilizing Single Negative Metamaterial Layers. Proceedings of the USNC/CNC/URSI National Radio Science Meeting, 152, (2006)
15. Alù, A., Engheta, N.: Pairing an epsilon-negative slab with a mu-negative slab: anomalous tunneling and transparency. IEEE Trans. Antenn. Propag., **51**, 2558–2570 (2003)
16. Maslovski, S.I., Tretyakov, S.A., Belov, P.A.: Wire media with negative effective permittivity: a quasi-static model. Microw. Opt. Technol. Lett., **35**, 47–51 (2002)
17. Pendry, J.B., Holden, A.J., Robbins, D.J., Stewart, W.J.: Magnetism from conductors and enhanced nonlinear phenomena. IEEE Trans. Microw. Theory Tech., **47**, 2075–2081 (1999)
18. Bilotti, F., Nucci, L., Vegni, L.: An SRR based microwave absorber. Microw. Optic. Technol. Lett., **48**, 2171–2175 (2006)
19. Bilotti, F., Toscano, A., Vegni, L.: Design of spiral and multiple split-ring resonators for the the realization of miniaturized metamaterial samples. IEEE Trans. Antenn. Propag., **55**, 2258–2267 (2007)
20. Bilotti, F., Toscano, A., Vegni, L., Alici, K.B., Aydin, K., Ozbay, E.: Equivalent circuit models for the design of metamaterials based on artificial magnetic inclusions. IEEE Trans. Microw. Theory Tech., **55**, 2865–2873 (2007)
21. Dolling, G., Enkrich, C., Wegener, M., Zhou, J.F., Soukoulis, C.M., Linden, S.: Cut-wire pairs and plate pairs as magnetic atoms for optical metamaterials. Opt. Lett., **30**, 3198 (2005)
22. Bilotti, F., Vegni, L.: Resonant microwave absorbers without a metallic backing based on metamaterials. Proceedings of the NATO Advanced Research Workshop Metamaterials for Secure Information and Communication Technologies, 32–35 (2008)

# Dual-Mode Metamaterial-Based Microwave Components

**Darren S. Goshi[1], Anthony Lai[2], and Tatsuo Itoh[3]**

[1]Honeywell International Inc., Torrance, CA, USA
darren.goshi@honeywell.com
[2]HRL Laboratories LLC, Malibu, CA, USA
alai@hrl.com
[3]University of California, Los Angeles, CA, USA
itoh@ee.ucla.edu

**Abstract** This chapter reviews several examples of how the mode concepts of composite right/left-handed transmission line metamaterials can be utilized in the development of unique microwave components. These components are analyzed from a modal characteristic point of view and are based on the concept of both mode coupling and the variation of the field profiles associated with each mode. Both guided modes and resonant modes are discussed. Finally, an example of a system application based on a mode-based metamaterial structure is presented.

## 1 Introduction

This chapter focuses on the application of dual-mode metamaterial structures. Several examples of how mode concepts can be exploited in the development of unique microwave components based on composite right/left-handed (CRLH) transmission line (TL) metamaterials are presented. These components are developed from a modal characteristic perspective that makes use of the mode coupling or the difference of the electromagnetic fields associated with each mode.

The modal concept has proven to be very essential in microwave, millimeter-wave and optical engineering. Many passive components are based on the clever use of modes. For instance, the proximity directional coupler is based on the even and odd modes in a symmetrically configured coupled transmission lines or waveguide. The difference between the even and odd modes provides a coupling mechanism. The so-called dual mode filter makes use of the resolution of the degenerate modes along orthogonal directions so that the desired pass band characteristics can be obtained.

Metamaterials have been shown to provide very unique properties in electromagnetic engineering. Although there are several categories in metamaterials such

S. Zouhdi et al. (eds.), *Metamaterials and Plasmonics: Fundamentals, Modelling, Applications*,

as photonic crystals, high impedance surfaces, etc., this chapter deals with the negative index or left-handed (LH) metamaterials. It was demonstrated that the CRLH structure can achieve unique electromagnetic functionality beyond that of the originally proposed LH structures [1–6]. Microwave components based on the CRLH structure inspired by the mode concept have been demonstrated to have very unique characteristics and deserve some attention.

The chapter is organized in the following: The next section will review some of the basics and principles of the CRLH structure with a focus on the dual-mode applicability that will be discussed and applied throughout the chapter. The subsequent section presents a variety of dual-mode metamaterial structures ranging from couplers to antennas and concluding with a system application in the form of an integrated mixer front-end.

## 2 Review of CRLH Structure

The one-dimensional CRLH structure is fundamentally a transmission line [1]. This composite structure originates as a practical realization of a LH TL with the inclusion of unavoidable parasitic right-handed (RH) effects, occurring due to physical implementation. The CRLH is therefore analyzed as a periodic structure through its unit-cell properties. A generalized equivalent circuit of a CRLH unit-cell with a length $p$ is shown in Fig. 1 along with its dispersion characteristics. The red curve depicts the LH region and the blue curve indicates the RH region. In the RH region, the CRLH TL acts like the conventional TL which has positive propagation constant. In the LH region, a fundamental backward wave, which has negative propagation constant and phase advance phenomena is supported. The CRLH structure in its simplest form consists of a series LH capacitance ($C_L$), a series RH inductance ($L_R$), a shunt LH inductance ($L_L$), and a shunt RH capacitance ($C_R$). An effectively homogeneous CRLH TL can be realized by cascading this LC unit-cell under the condition that $p$ is much smaller than a wavelength. The uniqueness of this structure arises from the periodic loading of the (LH) components along the line. The solid curve of Fig. 1 is the case for an unbalanced structure in which the ratio $C_L/L_L \neq C_R/L_R$. There exists a spectral gap between these regions in which the structure becomes a single negative material so that no wave propagation takes place. This gap can be closed if the structure is designed under the balanced condition, where $C_L/L_L = C_R/L_R$. This balanced curve is indicated by the dashed line.

In the balanced case, the dispersion curve is continuous through the two regions. This feature has been exploited in frequency scanned antennas as the simplest means of realizing a single structure that can operate in both LH and RH regions.

In addition to changing the operating frequency, applying tunable components into the unit-cell parameters allows for dynamic switching between these operating modes. All of these components take advantage of the fact that different propagation regions occur at different frequency bands for a given CRLH unit-cell.

Another popular feature that has been exploited in CRLH metamaterial structures is the ease at which the phase response, or phase slope can be engineered. This technique has led to unique components with broadband and dual-band operation since specific phase characteristics at multiple frequencies can be designed. The CRLH TL can typically be realized with planar microwave technology such as microstrip line or coplanar waveguide.

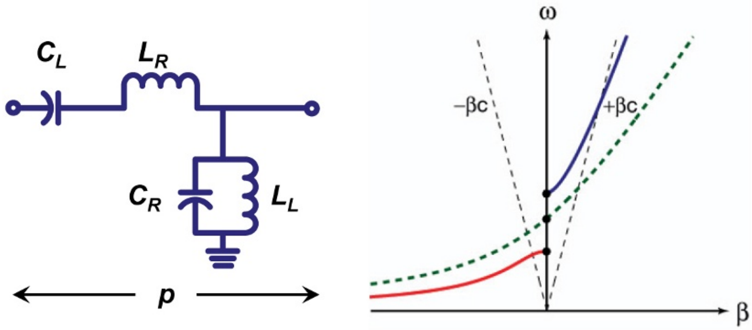


**Fig. 1** Generalized unit cell of CRLH structure (*left*) and associated dispersion diagram (*right*).

## 3 Dual Mode Metamaterial Structures

The recent innovation of novel metamaterial structures has led to the development of various components with enhanced features such as broadband and dual-band operation, as well as miniaturized circuits. Among these examples, many dual-band structures have been presented, in terms of mainly dual-band, and dynamically tunable components. Specifically, the phase response of CRLH structures have been shown to be engineerable to present desired responses at multiple specified frequencies, resulting in dual-frequency, or broadband components such as couplers and filters [6]. Also, it has been shown that by introducing tunable components into the unit-cell, the dispersion characteristics of a CRLH structure can be altered to operate in a chosen propagating mode, LH or RH guided or radiating regions [7]. In this section, the idea of dual-mode metamaterials based on even/odd mode for polarization selectivity and field profiling will be considered.

## 3.1 Proximity coupler based on CRLH even/odd mode analysis

The directional coupler is used for microwave signal processing and is indispensable for many applications. Among several types of couplers, the proximity coupler is made of two transmission lines placed in parallel with a small gap. This type of coupler cannot attain strong coupling due to mechanical limitation of fabrication and is typically used for 10 dB coupling and less. The basic coupling mechanism lies in the characteristic impedance difference of the even and odd modes in the coupler.

A directional coupler comprised of two identical CRLH lines placed in parallel was found to have a very interesting property [8]. Unlike the conventional microstrip coupler, it was discovered that up to 0-dB coupling is possible. This means that all input power to port 1 is delivered to port 3 while no output emerges at ports 2 and 4. The fabricated nine unit cell, 0-dB coupler circuit is shown in Fig. 2 as a reference.

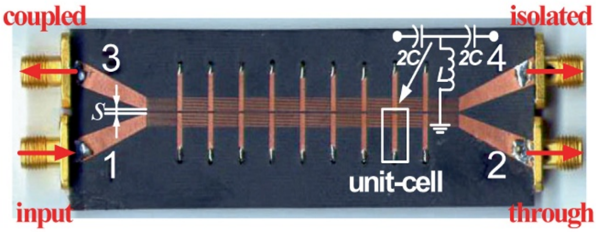


**Fig. 2** CRLH Proximity Coupler. From [8]: ©2004 IEEE. Reprinted with permission.

In this design, the first step was to realize an isolated balanced CRLH TL. When two identical balanced CRLH TLs are placed in proximity, there is an additional series inductance $L_m$ and additional shunt capacitance $C_m$ due to mutual coupling as shown in Fig. 3. Although the individual TL is designed under the balanced condition, due to this proximity coupling, it is seen in the even mode and odd mode equivalent circuits that neither mode satisfies the balanced condition. Therefore, the coupled line has a spectral gap and hence no wave can be delivered toward ports 2 and 4. The input impedance is found to be fairly constant and close to 50 ohms and hence, essentially all the power is delivered to port 3. Following this principle, a coupler with variable coupling levels can be designed by changing the size of the coupler so that the signal does not completely decay and reaches ports 2 and 4. Using the same design methodology, a three unit-cell, 3-dB coupler was demonstrated with a 2-dB amplitude imbalance over a wide 50% bandwidth from 3.5–5.8 GHz. This circuit also achieved a ±5 phase imbalance from 3–4 GHz. Both circuits were built on 1.57 mm, $\varepsilon_r$ = 2.2 Duroid substrate. It is clear that the even and odd modes in the coupled section are responsible for controlling the behavior for this extremely interesting and practical device.

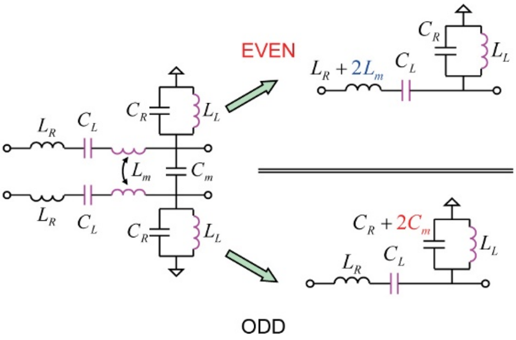


**Fig. 3** Equivalent unit-cell circuits for even and odd modes of the coupler. From [8]: ©2004. IEEE Reprinted with permission.

## *3.2 Dual-mode metamaterial with even/odd mode selectivity*

The general CRLH dispersion diagram shown in Fig. 1 suggests that the CRLH structure will support LH behavior at lower frequencies and RH behavior at higher frequencies. This simply implies that in order to utilize both regions of dispersion, the frequency must be changed. To operate in both modes at a fixed frequency, the entire dispersion curve of the structure can be shifted by electronic control through such means as a varactor diode [7]. The dual-mode CRLH TL structure proposed in [9] takes a different approach for mode selectivity. In this case, based on the mode field polarization of the excited wave, different engineerable propagation

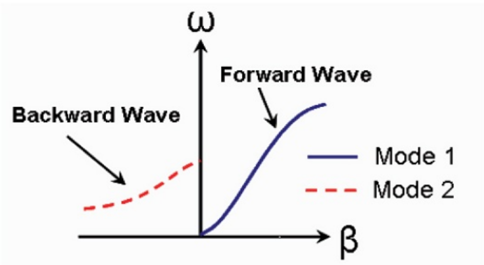


**Fig. 4** Proposed dispersion characteristics for a dual-mode CRLH-TL based on field polarization. From [9]: ©2007 IEEE. Reprinted with permission.

characteristics can be obtained. Specifically, at a given frequency, Mode 1 provides a forward propagation while Mode 2 accomplishes a backward or LH propagation. This idea is conceptually illustrated in Fig. 4.

Notice that the conventional CRLH structure consists of a series inductance $L_R$ and a shunt capacitance $C_R$ to represent the RH behavior and of a series capacitance $C_L$ and a shunt inductance $L_L$ for the LH behavior. To realize the mode selective dispersion (Mode 1 or Mode 2), the LH components $L_L$ and $C_L$ need to be eliminated for Mode 1 and introduced for Mode 2. The proposed dual-mode CRLH structure makes use of the symmetric unit cell excited by even mode and odd mode. The symmetry plane thus becomes a virtual ground for the odd excitation and an open for the even excitation. To this end, the equivalent circuit illustrated in Fig. 5 can be employed. For the odd mode excitation, the LH inductance $L_L$ is grounded to become a shunt element while the LH capacitance $C_L$ is inserted as a series element by means of the transformer. For the even excitation, both $L_L$ and $C_L$ are 'floating' and do not contribute to the circuit operation. In this way, the application of even and odd excitation is able to realize RH and LH operation, respectively.

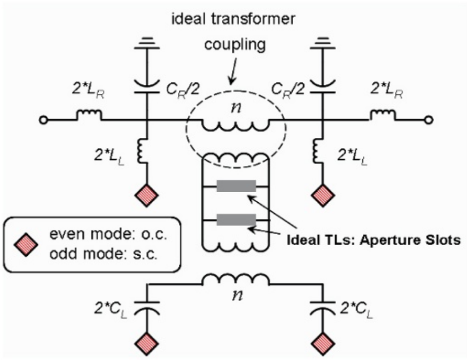


**Fig. 5** Equivalent half-circuit model of even- and odd-mode excited metamaterial for realization of dual-mode metamaterial. From [9]: ©2007 IEEE. Reprinted with permission.

The circuit is implemented in a double layered structure with a ground plane in-between the two substrates to accommodate coupling slots for realization of the transformers. The microstrip circuit is situated on the top surface with four access ports while the bottom surface has a microstrip circuit with surface mount (SMT) capacitors to realize $C_L$. This complex layered structure was required in order to achieve a series based coupling effect. The layout schematic and coupling procedure is illustrated in Fig. 6.

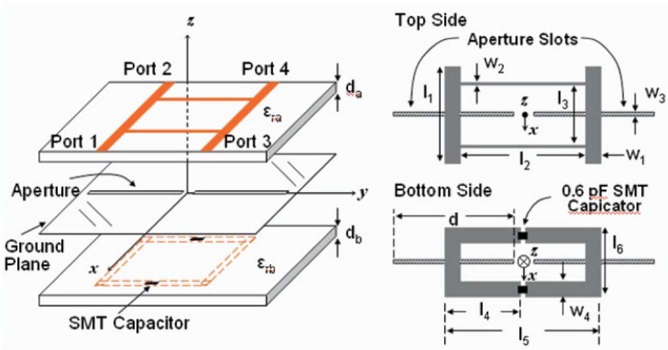


**Fig. 6** Layout schematic for the proposed dual-mode coupler circuit. From [9]: ©2007 IEEE. Reprinted with permission.

Numerical simulation indicates that, in the range of 1.80–1.95 GHz, the unit cell supports a LH wave with an odd excitation and a RH wave with an even excitation. The measured results shown in Fig. 7 indicate this range shifted somewhat to 1.86–2.00 GHz. The narrow band operation exists due to the use of a slot aperture for the transformer. The frequency shift can be attributed to the difficulty in alignment of the multiple slots in this multi-layered structure.

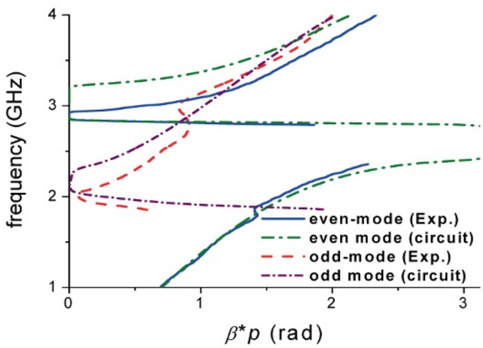


**Fig. 7** Experimental dispersion diagram. From [9]: ©2007 IEEE. Reprinted with permission.

This demonstration of mode selectivity introduces the possibility of developing unique metamaterial components capable of selective wave steering for signal routing and multiplexing applications. A preliminary simulated result utilizing this mode selective structure in a 2D arrangement was carried out in [9] to demonstrate the effectiveness of this concept. Increasing the isolation between two signals and improving the bandwidth of dual-mode operation are two of the key factors for future consideration.

### *3.3 Dual-mode compact antenna*

In the previous two sections, the even and odd modes of a coupled CRLH structure were used to provide unique device characteristics. In a resonant type of structure, there exist the dominant and higher order modes. In many compact resonant antennas, these modes can be used for dual-mode operation at different frequencies. The issue with these conventional resonant antennas is that these higher order modes generally resonate at integer multiples of the dominant mode frequency. This effect is typically unwanted because harmonic energy that is generated by components that interface with the antenna will also be radiated, leading to potential interference and additional wasted energy.

The dual-mode concept can be extended to the operation of CRLH based resonant antennas. The CRLH structure provides a very unique property for antenna applications. Specifically, the CRLH-based antenna can be engineered to provide a monopolar pattern at one resonant frequency while providing a patch-like pattern at another frequency. This is caused by the unique nature of the resonator that is developed from a CRLH structure. For example, an ordinary segment of CRLH TL consisting of *N* unit-cells with its ends either open- or short-circuited will produce a dispersion diagram as shown in Fig. 8. It will consist of a number of periodic resonant points based on the amount of cells (*N*) and are indicated by the black dots. The frequencies at which these points resonate are dictated by the design of the unit-cell's parameters, and in other words the slope of the dispersion curve.

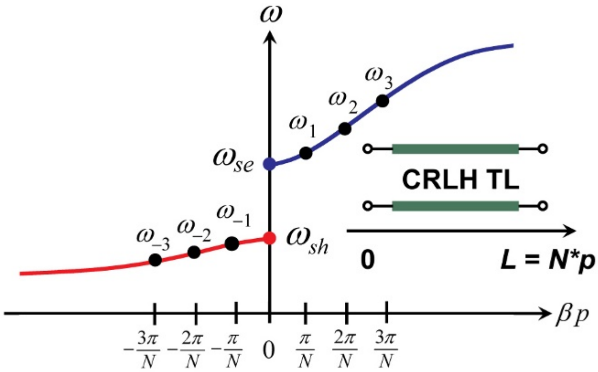


**Fig. 8** Dispersion curve with resonant points for a CRLH made of *N* unit cells. From [10]: ©2005 IEEE. Reprinted with permission.

Two important features can be noted from this generalized diagram. First, in addition to resonances in the RH and LH sections, there are two 0th (zeroth) order resonances, $\omega_{se}$ and $\omega_{sh}$, where the propagation constant is zero. Depending on the boundary condition being applied, either one of them can be excited. Also, under the zeroth order resonance, the field along the CRLH resonator is constant both in phase and amplitude. The second feature is that the resonant spacing is not linear and is basically determined by the unit-cell design. This means that the resonant frequencies of the modes are not necessarily harmonically related, and instead the dispersion can be engineered by the choice of the unit-cell parameters.

A two unit-cell CRLH antenna based on this principle is shown in Fig. 9. This prototype was fabricated on Duroid 5880, $\varepsilon_r = 2.2$, $h = 1.57$ mm, substrate. The antenna structure is made of the so-called "mushroom" structure with its stem providing the shunt inductance and the gap capacitance between the patches generating the series capacitance for the LH operation. When this mushroom structure is utilized as an antenna, it resembles that of an inductor loaded patch. However, the difference in this structure is in the addition of the LH behavior due to the series gap capacitance between unit-cells which does not exist in the conventional inductor loaded case. This also leads to the possibility of multiple resonances, rather than a single one. Lastly and most importantly for this design, whereas conventional planar resonant antennas are vulnerable to radiation of harmonics, this proposed CRLH-based antenna can operate at its $n = 0$ or $n = -1$ mode while avoiding radiation at harmonically related frequencies at both modes. This can also be seen in the input return loss characteristics shown in Fig. 9. This is achieved because its resonant frequency is primarily determined by the design of the unit cell parameters. This intrinsic harmonic suppression radiation can help to benefit overall system efficiency as well as to reduce interference in high-traffic environments. Also due to this same principle, the physical size of the $n = 0$ structure is not dependent on a resonant length and it is seen that the fabricated prototype covers a $\lambda_o/6$ x $\lambda_o/6$ footprint, offering a significant size reduction compared with a conventional resonant type microstrip patch antenna operating at the same frequency.

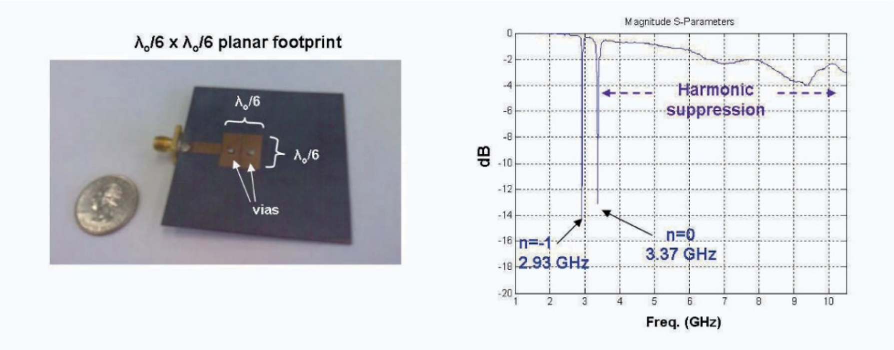


**Fig. 9** Dual-mode antenna operated at two resonant modes. From [10]: ©2005 IEEE. Reproduced with permission.

For this particular design, the zeroth order resonance is at 3.37 GHz and the $n = -1$ frequency is at 2.93 GHz. At the $n = 0$ mode, the antenna operates under the infinite wavelength phenomenon (where $\beta = 0$), and produces a monopolar radiation pattern because the field is constant all around the structure. In contrast, the $n = -1$ mode generates a patch like pattern similar to the dominant mode radiation pattern of the conventional RH microstrip patch. The field profile for each mode that leads to this pattern diversity is shown in Fig. 10. The radiation patterns are plotted in Fig. 11.

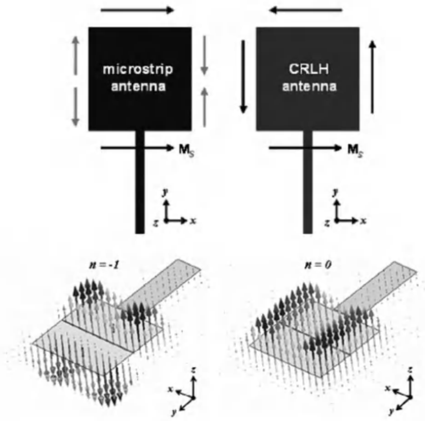


**Fig. 10** Operation and field profiles at both $n = -1$ (*left*) and $n = 0$ (*right*) modes. From [10]: ©2005 IEEE. Reprinted with permission.

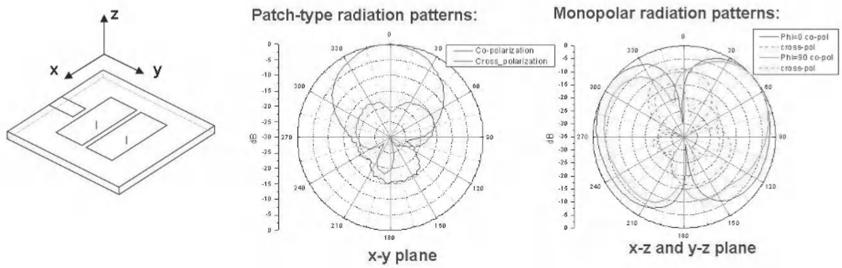


**Fig. 11** Measured radiation patterns. $n = 0$ mode (*left*) and $n = -1$ mode (*right*). From [10]: ©2005 IEEE. Reprinted with permission.

## *3.4 Integrated CRLH leaky-wave antenna front end*

Up to this point, various dual-mode components have been presented in this chapter that take advantage of some of the unique properties of the CRLH TL structure. In this section, a CRLH-based leaky-wave antenna (LWA) is demonstrated in an integrated mixer front-end, offering benefits in terms of a system application point of view [11].

The CRLH-based LWA has been well documented in previous literature [12, 13]. Under a balanced design, the series resonance ($\omega_{se}$) and shunt resonance ($\omega_{sh}$) are equal at $\beta = 0$, no stop-band exists between the LH and RH regions, and a constant characteristic impedance can be expected. Therefore this structure is able to radiate a continuously scanned beam from backfire to endfire through broadside. The slope of the dispersion curve and the zero propagation constant frequency can be engineered by controlling the four circuit parameters. A common and straightforward planar implementation of such an antenna is realized by utilizing interdigital capacitors for the LH capacitance and shunt shorted stubs for the LH inductance.

Whereas many CRLH structures require via connections for shunt inductance implementation, including this common CRLH LWA architecture, the structure proposed in this section uses a symmetric approach that essentially eliminates this requirement [14, 15]. Its symmetry allows for the elimination of via connections when utilized under its odd mode excitation. It is this symmetric architecture that also allows the exploitation of the structure's even and odd mode properties. The equivalent circuit model of the unit-cell structure indicating the symmetry plane is shown in Fig. 12 along with its microstrip implementation. Also shown is the dispersion diagram for the structure, depicting the contrasting operation between the differential and common modes.

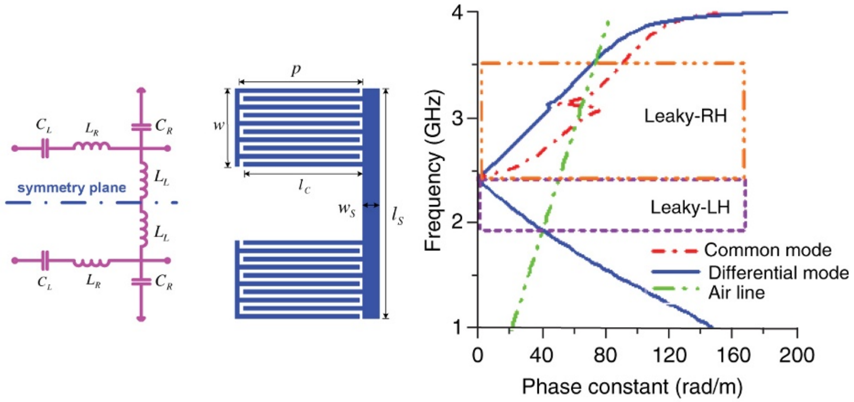


**Fig. 12** Equivalent circuit of symmetric unit-cell structure with microstrip implementation. From [11]: ©2008 IEEE. Reprinted with permission.

Based on this unit cell design, under a differential or odd-mode excitation, the metamaterial unit-cell behaves simply like a balanced CRLH unit-cell, where a fundamental backward wave is supported below the unit-cell's series resonance ($f_{se}$). On the other hand, when this structure is excited by a common mode (or even mode), the metamaterial unit-cell is under cut-off below $f_{se}$. Put into another perspective, a virtual ground is obtained under differential mode and the structure operates as a CRLH structure. Conversely, no LH behavior can be seen under its common mode excitation because the shunt inductance no longer exists (from a virtual open condition). This structure therefore offers an even mode filtering capability and is therefore employed for two reasons; to offer even/odd mode diversity, and to simplify the overall physical structure.

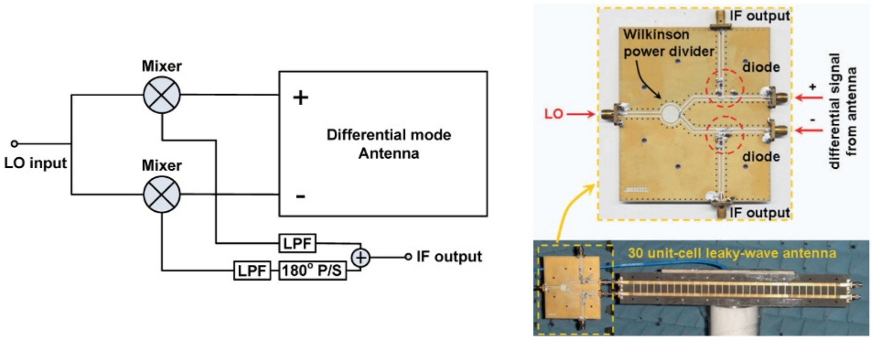


**Fig. 13** Schematic of proposed system application (*left*) and fabricated and assembled integrated mixer/CRLH LWA (*right*). From [11]: ©2008 IEEE. Reprinted with permission.

The beneficial application of this structure becomes evident when it is integrated into a system application. The block diagram schematic of this system and the fabricated prototype operating from 1.96–2.40 GHz is shown in Fig. 13. The fabricated symmetric, completely planar and single-layered CRLH LWA structure consisted of 30 unit-cells. The opposing ports of the differential structure are connected to the two ports of a balanced mixer design. The LO signal to the balanced mixer is fed in phase to two mixing diodes (common-mode). Due to the common-mode filtering effect previously discussed, any LO leakage that reaches the antenna interface is intrinsically suppressed while the antenna provides an odd mode excitation to the mixer diodes. This feature therefore eliminates the need for separate RF filters for common-mode LO leakage. In addition, since the LWA is based on differential-mode excitation, the filter on the LO side is also eliminated. In other words, this architecture also has a built-in protection for the LO source since a received RF signal (only differential signals are excited) will add out of phase at the LO port. The measured IF antenna patterns and LO leakage patterns are shown in Fig. 14. The measured radiation patterns demonstrate consistent beam scanning with the predicted LH region operation. The LO leakage is suppressed between 20–40 dB, and greater than 20 dB of RF-LO isolation is achieved through this integrated approach.

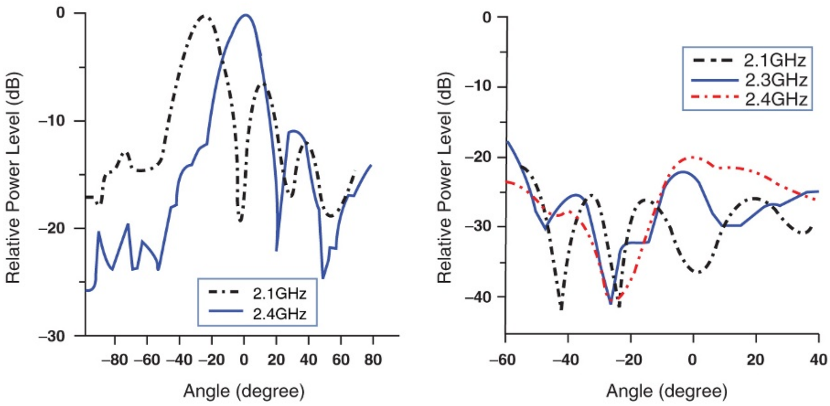


**Fig. 14** Measured IF received patterns at 30 MHz (*left*) and measured LO leakage patterns (*right*). From [11]: ©2008 IEEE. Reprinted with permission.

In this section, a system application of a CRLH-based metamaterial structure with intrinsic even mode suppression is presented. This integrated system approach offered several benefits including space and component savings through the reduction or elimination of additional filtering between the component interfaces. This feature also becomes attractive from a security point of view as the EMI problem is reduced through leakage suppression.

## 4 Summary

The unique properties of the CRLH TL structure have been exploited in numerous recent efforts that introduce enhanced features to a variety of microwave components. In this chapter it was demonstrated how dual-mode behavior can be realized by utilizing the even and odd mode, polarization, and varying field profile characteristics of the CRLH structure. The continuing study of this type of application of the CRLH structure's unique properties can lead to the development of novel metamaterial components and systems.

## References

1. C. Caloz and T. Itoh, Electromagnetic Metamaterials: Transmission Line Theory and Microwave Applications. New York: Wiley (2005)
2. Lai, T. Itoh, and C. Caloz, "Composite right/left-handed transmission line metamaterials", IEEE Microwave Magazine, Volume 5, Issue 3, Page(s):34–50 (2004)

3. C. Caloz and T. Itoh, "Positive/negative refractive index anisotropic 2-D metamaterials", IEEE Microwave and Wireless Components Letters, Volume 13, Issue 12, Page(s):547–549 (2003)
4. C. Caloz and T. Itoh, "Transmission line approach of left-handed (LH) materials and microstrip implementation of an artificial LH transmission line", IEEE Transactions on Antennas and Propagation, Volume 52, Issue 5, Page(s):1159–1166 (2004)
5. A. Lai and T. Itoh, "Microwave composite right/left-handed metamaterials and devices", APMC Microwave Conference Proceedings, Volume 1, Page(s):4, 4–7 (2005)
6. C.-J. Lee, K.M.K.H. Leong, and T. Itoh, "Metamaterial transmission line based bandstop and bandpass filter designs using broadband phase cancellation", IEEE MTT-S International Microwave Symposium Digest, Page(s):935–938 (2006)
7. S. Lim, C. Caloz and T. Itoh, "Metamaterial-based electronically controlled transmission-line structure as a novel leaky-wave antenna with tunable radiation angle and beamwidth", IEEE Transactions on Microwave Theory and Techniques, Volume 52, Issue 12, Page(s):2678–2690 (2004)
8. C. Caloz, A. Sanada and T. Itoh, "A novel composite right/left-handed coupled line directional coupler with arbitrary coupling level and broad bandwidth", IEEE Transactions on Microwave Theory and Techniques, Volume 52, Issue 3, Page(s):980–992 (2004)
9. A. Lai, K. M.K.H. Leong and T. Itoh, "Dual-mode metamaterial with backward and forward wave selectivity", IEEE International Microwave Symposium, Honolulu, HI, pp. 1423–1426, June 3–8 (2007)
10. A. Lai, K. M.K.H. Leong and T. Itoh, "Infinite wavelength resonant antennas with monopolar radiation pattern based on periodic structures", Transactions on Antennas and Propagation, Volume 55, Issue 3, Part 2, Page(s):868–876 (2007)
11. Y. Kim, E-K Kim, A. Lai, D. S. Goshi and T. Itoh, "Integrated mixer based on composite right/left-handed leaky-wave antenna", IEEE International Microwave Symposium Digest, Atlanta, GA (2008)
12. L. Liu; C. Caloz and T. Itoh, "Dominant mode leaky-wave antenna with backfire-to-endfire scanning capability", Electronics Letters, Volume 38, Issue 23, Page(s):1414–1416, 7 (2002)
13. C. Caloz and T. Itoh, "Array factor approach of leaky-wave antennas and application to 1-D/2-D composite right/left-handed (CRLH) structures", IEEE Microwave and Wireless Components Letters, Volume 14, Issue 6, Page(s):274–276 (2004)
14. K. Sato, S.H. Yonak, T. Nomura, S. Matsuzawa, and H. Iizuka, "Metamaterials for automotive applications", IEEE Antennas and Propagation International Symposium, Page(s):1144–1147, 9–15 (2007)
15. K. Sato, S. Matsuzawa, Y. Inoue and T. Nomura, "Electronically scanned left-handed leaky wave antenna for millimeter-wave automotive applications", IEEE International Workshop on Antenna Technology on Small Antennas and Novel Metamaterials, Page(s):420–423, March 6–8 (2006)

# Chiral Swiss Rolls

**Michael Wiltshire** [1,2]

[1]Imaging Sciences Department, Clinical Sciences Centre, Imperial College London, Hammersmith Hospital Campus, Ducane Road, London W12 0NN, UK
[2]The Blackett Laboratory, Department of Physics, Imperial College London, South Kensington, London SW7 2AZ, UK
michael.wiltshire@imperial.ac.uk

**Abstract** Chiral Swiss Rolls, consisting of a metal/dielectric laminate tape helically wound on an insulating mandrel, have been developed to form the basis of a highly chiral metamaterial. We report here on the fabrication of these elements using a custom-built machine, and on their characterization. The metamaterial obeys constitutive equations of the form $\mathbf{D} = \varepsilon\varepsilon_0\mathbf{E} + i\sqrt{\varepsilon_0\mu_0}\,\kappa\mathbf{H}$ and $\mathbf{B} = -i\sqrt{\varepsilon_0\mu_0}\,\kappa\mathbf{E} + \mu\mu_0\mathbf{H}$ and has a resonant permeability, $\mu$, permittivity, $\varepsilon$, and chirality, $\kappa$, in the region of 80 MHz. Moreover, the chirality is large enough to be directly measurable from observing the magnetic response to an applied electric field. Examination of the resonant frequency of chiral and enantiomeric pairs shows that the chirality is larger than the permeability, and so these elements can form a super-chiral medium.

## 1 Introduction

The engineered response of artificially constructed metamaterials has had a dramatic impact on the physics, optics, and engineering communities, because these metamaterials can offer electromagnetic properties that are difficult or impossible to achieve with conventional, naturally occurring materials. For example, metamaterials based on the "Swiss Roll" [1–3] element have proved to be extremely effective in the radiofrequency (RF) regime. Their low resonance frequency and intense magnetic activity have been exploited to demonstrate RF flux guiding [4, 5] at the resonant frequency. Moreover, their strong response allied with dense packing gives rise to a large negative permeability bandwidth [6], and sub-wavelength imaging [7, 8] has been demonstrated when the permeability $\mu = -1$.

The majority of work on metamaterials has concentrated on the control of their permittivity, $\varepsilon$, and permeability, $\mu$, across a frequency range from the RF through

S. Zouhdi et al. (eds.), *Metamaterials and Plasmonics: Fundamentals, Modelling, Applications*,

the microwave regime to the optical. When material is made that has both $\varepsilon$ and $\mu$ negative, the refractive index, *n*, becomes negative [9], and such materials are sometimes known as left-handed. However, it is important to note that these materials are not chiral; the name [10] refers to the sense of the $\mathbf{E}\times\mathbf{H}$ product with respect to the wavevector ***k***. It is of course possible to make metamaterials that do have a genuine handedness or chirality, and these have in fact been studied for some years. For example, materials based on the incorporation of small wire helices in a non-chiral matrix [11] exhibit chirality in the microwave regime, as do the so-called omega particles [12]. A further development has been the introduction of planar chiral materials [13]. However in all of these cases, the chirality is still quite weak (albeit significantly stronger than anything available in nature). Nevertheless, they have interesting properties, particularly when the medium is constructed so that $\varepsilon$ and $\mu$ are approximately zero, and so less than the chirality, $\kappa$, a condition known as chiral nihility [14]. It has also been shown that strongly chiral metamaterials could offer an alternative route [15] to negative refraction and sub-wavelength imaging, and the chiral Swiss Roll was proposed as a possible metamaterial element to achieve this. In this case, we achieve the desired phenomena not by making $\varepsilon$ and $\mu$ small, but by making the chirality large. Here, we report on an initial investigation of such a medium.

The definitive signature of a chiral material is the coupling of the electric and magnetic response through the chirality, as shown in the constitutive relations [16]

$$\begin{aligned}\mathbf{D} &= \varepsilon\varepsilon_0\mathbf{E} + i\sqrt{\varepsilon_0\mu_0}\,\kappa\mathbf{H},\\ \mathbf{B} &= -i\sqrt{\varepsilon_0\mu_0}\,\kappa\mathbf{E} + \mu\mu_0\mathbf{H}\end{aligned} \tag{1}$$

For an isotropic chiral medium, $\varepsilon$, $\mu$, and $\kappa$ are all scalars; for a uniaxial medium having the z-axis unique, $\varepsilon$, $\mu$, and $\kappa$ become diagonal tensors with $\varepsilon_{xx} = \varepsilon_{yy} \neq \varepsilon_{zz}$ and similar relations for $\mu$ and $\kappa$. Thus the key characteristic is that an exciting magnetic field **H** should induce responses in both **D** and **B** which should be parallel to the exciting field – there are no off-diagonal terms.

In our previous work [3–6, 8] the Swiss Rolls were wound and tuned by hand. This is not feasible for the chiral elements: their performance depends critically on the pitch and it is impossible to keep this uniform in a manual process. Therefore a machine was commissioned to wind the rolls, and the capability of this is described, along with a survey of the resulting rolls. We also report on the direct observation of an electric response to a magnetic field, as predicted by Eq. (1). We have then measured the permittivity, permeability and chirality (or more strictly the appropriate polarisabilities) of the rolls. The machine can wind either left handed or right handed chiral material (in addition to the conventional non-chiral, square-wound rolls), and we have exploited the existence of enantiomeric pairs (i.e. pairs of opposite handedness) to investigate the relative magnitudes of the magnetic and chiral coupling, and to show that the chirality is indeed strong in this material.

## 2 Fabrication

Chiral Swiss rolls are made by winding a strip of metal – dielectric laminate around a suitable mandrel in a helical fashion, so that each successive turn extends beyond the underlying layer. In this way, a spiral structure can be built up. The mandrel radius, $r$, the winding angle, $\theta$, and the strip width, $w = N.2\pi r \sin\theta$, define the geometry of the element as shown in Fig. 1a; here N is the local number of overlapping turns in a cross-section of the element. The pitch of the winding is given by $P = w/N\cos\theta$.

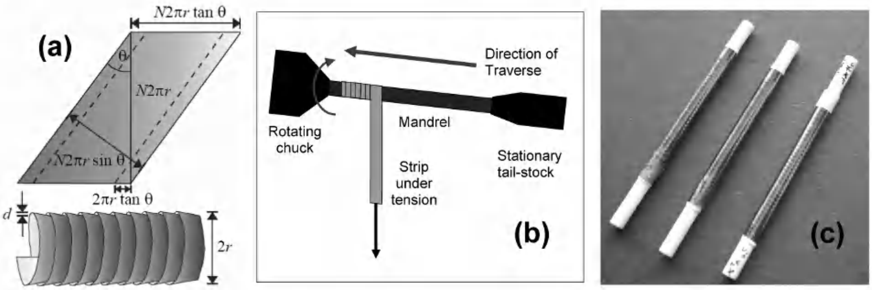


**Fig. 1** The construction of chiral Swiss Rolls. (**a**) Showing the relations between the mandrel radius, $r$, the pitch angle, $\theta$, and the number of turns, $N$, and the strip width; (**b**) schematic of the winding process, showing the strip held under tension being wound on an inclined, translating mandrel. (**c**) a photograph of completed rolls (with the outer wrap removed), showing the helical structure of the elements.

The essential concept of the machine [17] that can achieve this winding is shown in Fig. 1b. A tape of copper – dielectric laminate, under tension from a hanging weight, is wound onto an oblique, rotating mandrel. The strip used here was NovaClad material (Sheldahl G2202), slit to a 5 mm width. The mandrel traverses at a rate commensurate with the winding angle and the pitch, so that the structure indicated in Fig. 1a is generated. Once the winding is complete, when the roll is ~50 mm long, an adhesive label is wrapped around the structure. The winding angle can be selected in the range ±5°, and the traverse can be either left-to-right or right-to-left as appropriate, so that we can make either left-handed or right-handed material. The mandrels were glass fibre rods, with diameters of 3, 4 or 5 mm. The process was monitored by measuring the transmission between two loops (not shown); the transmitter loop was placed around the chuck and the receiver loop around the tail-stock. Once the winding had started, a resonant transmission peak was observed, whose frequency fell, initially rapidly and then more slowly, towards the final, stable frequency of the element. A photograph of some completed rolls (without their adhesive labels) is shown in Fig. 1c.

A critical parameter in the fabrication is the tension in the strip. It is clear from Fig. 1a that one edge of the tape lies on the mandrel, whereas the other lies over the previous windings, so there is a difference in the diameters experienced by the two edges of the tape. To accommodate this, the tape has to stretch differentially, and this is assisted by increasing the tension on the tape itself. However, this introduces a limitation on the range of geometries that can be achieved: it has not been possible to make rolls with a pitch below 2° on a 5 mm diameter mandrel because the tape kinks rather than stretching, and this angle is larger for smaller diameter cores. This, in turn, limits the frequency range that can be accessed for any particular mandrel size, and the range of frequencies achieved is shown in Fig. 2, where we plot the resonant frequency as a function of winding angle for the range of mandrel sizes that we have used.

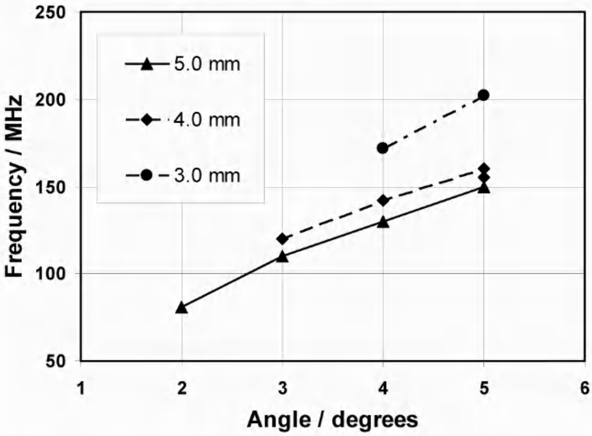


**Fig. 2** The fundamental frequency of the chiral rolls as a function of winding angle and mandrel diameter, showing the range of material that can be fabricated.

It will be noted that smaller mandrels lead to higher frequency and a more limited range of angles. Moreover, for maximum chirality, the winding angle needs to be small [15], so that we concentrate here on the elements wound at 2° on a 5 mm mandrel, that have a resonant frequency of about 80 MHz.

## 3 Characterisation

As was pointed out above, the defining characteristic of a chiral medium is the generation of an electric response to an applied magnetic field. Moreover, the chirality predicted for the Swiss Roll medium is sufficiently large that this field should be readily detectable: we emphasize that this has not been the case for previous materials (either natural or artificial), whose chirality could only be detected from optical rotation measurements. Accordingly, a preliminary investigation was performed using the arrangement shown in Fig. 3a, based on the monitor in the winding machine described earlier. A magnetic signal is generated by a loop placed at one end of the sample. The transmitted magnetic signal is detected by a second loop at the other end, whereas the electric field signal is measured with a dipole antenna placed parallel to the length of the roll.

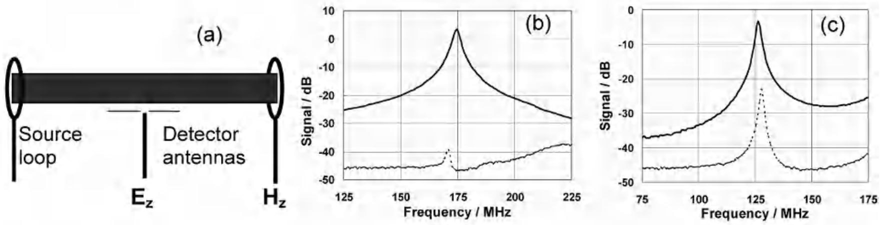


**Fig. 3** (**a**) Schematic of the preliminary measurements of magnetic and electric response, showing a source loop to generate a magnetic field, and magnetic and electric field detectors to measure the respective responses. (**b**) the magnetic response (full line) and electric response +20 dB (dotted line) responses for a non-chiral, conventional Swiss Roll; (**c**) the responses for a chiral roll.

Measurements were made of both a non-chiral conventional roll and a chiral roll, and these are shown in Fig. 3b, c respectively. In both cases, the magnetic signal was normalized to the case were the two loops were very close together (without the sample); the electric field measurements were not normalized, but are plotted with a 20 dB offset in the figure, i.e. the baseline of the electric measurements was about −65 dB. It is clear from these data that the electrical response for the non-chiral roll is negligible, whereas there is a strong response at the resonant frequency for the chiral roll. Thus the chiral rolls do indeed generate an electric response to a magnetic field, as required by Eq. (1).

In a second set of experiments, we measured the permeability, permittivity and chirality of single rolls and pairs of rolls as a function of frequency. First it should be noted that it is not strictly accurate to refer to these properties of a single element: they apply to the bulk. The single element characteristic is the polarisability, which, when averaged over a suitable volume of material leads to the effective bulk parameters. Nevertheless, it is convenient to refer to the data and its measurement using the bulk nomenclature.

The three parameters were measured as follows. The permeability was deduced from the increase in mutual inductance of a pair of coaxial loops when the sample was inserted along their common axis. This method works well for the conventional non-chiral rolls, but may be open to criticism for the chiral material because the magnetic field is not uniform along the length of the sample. The permittivity was measured by inserting the sample between two parallel conducting plates, and measuring the change of capacitance. Because the samples are long rods (typically 50 mm long and 6 mm diameter), there are significant corrections due to stray fields and parasitic impedances that have to be compensated in these measurements, and further work is necessary to obtain a consistent set of measurements across a range of sample shapes and sizes. We therefore label the permittivity data as having arbitrary units. Finally, the chirality was measured by placing a detector loop at the mid-plane of the capacitance measuring equipment, thus measuring the magnetic response to an electrical excitation. Again, no absolute values have yet been deduced for these data (although this work is in progress), so they are given in arbitrary units. However, for the purpose of this paper, the qualitative data, along with the frequencies of the various features, are sufficient.

Figure 4 shows the results of these measurements. First, we measured a non-chiral roll that shows a resonant response at about 145 MHz only in its permeability; the permittivity is approximately constant across the frequency band of interest, and the chirality is zero. The second sample was a chiral roll constructed with a winding angle of 2° on a 5 mm diameter mandrel: this is the lowest frequency element that has been made and has the lowest winding angle and hence the largest chirality. There is a resonant response at about 80 MHz in all three parameters, but the chirality is 90° out of phase with the permeability and permittivity. This is consistent with Eq. (1) where we see the chirality enters as $\pm i\kappa$, whereas the permeability and permittivity enter as $\mu$ and $\varepsilon$ respectively. The third sample was a roll of the same design as the previous element, but wound with the opposite handedness. Here, the permeability and permittivity are unaffected, but the chirality has been inverted. Finally, we show the results for two pairs of rolls. A chiral pair (i.e. two rolls of the same handedness) shows enhanced response for all three parameters, whereas an enantiomeric pair (i.e. two rolls of opposite handedness) shows no chiral response: the two opposing chiralities cancel.

A further notable feature of the data in Fig. 4 is the change in the peak frequency of the permeability resonance between the chiral and enantiomeric pairs: whereas the frequency of the chiral pair is slightly higher than that of the single rolls, the frequency of the enantiomeric pair is significantly lower. This indicates that the electric dipole induced by the chirality is larger than the magnetic dipole arising from the permeability. We see from Eq. (1) that an applied magnetic field induces both an electric and a magnetic response. We can write

$$\begin{aligned} \mathbf{D} &= \varepsilon_0 \boldsymbol{\varepsilon}\mathbf{E} + i\sqrt{\varepsilon_0\mu_0}\,\boldsymbol{\kappa}\mathbf{H} \quad so \quad \mathbf{P} = \varepsilon_0(\boldsymbol{\varepsilon}-1)\mathbf{E} + i\sqrt{\varepsilon_0\mu_0}\,\boldsymbol{\kappa}\mathbf{H} \\ \mathbf{B} &= -i\sqrt{\varepsilon_0\mu_0}\,\kappa\mathbf{E} + \mu_0\boldsymbol{\mu}\mathbf{H} \quad so \quad \mathbf{M} = (\boldsymbol{\mu}-1)\mathbf{H} - i\sqrt{\varepsilon_0/\mu_0}\,\boldsymbol{\kappa}\mathbf{E} \end{aligned} \tag{2}$$

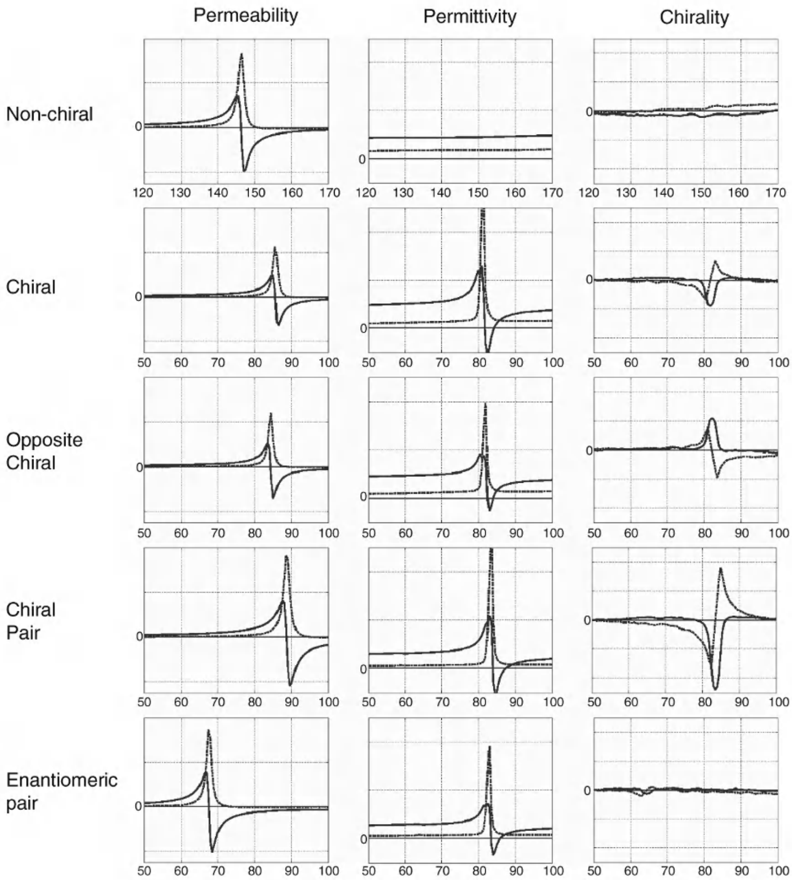


**Fig. 4** Measured permeability (*left column*), permittivity (*centre column*) and chirality (*right column*) as a function of frequency for Swiss Rolls, showing results for (*from top to bottom*) a non-chiral roll, a chiral roll, a chiral roll of opposite handedness, a pair of chiral rolls (same handed) and an enantiomeric pair (opposite handed). The full lines are the real part, the dotted lines the imaginary part, and the ordinates are arbitrary (see text), but are the same within each column.

thus defining the induced electric and magnetic polarizations, **P** and **M** respectively. In a uniform applied magnetic field with no electric field, these become

$$\mathbf{P} = i\sqrt{\varepsilon_0 \mu_0}\,\boldsymbol{\kappa}\mathbf{H} \quad \text{and} \quad \mathbf{M} = (\boldsymbol{\mu} - 1)\mathbf{H} \tag{3}$$

We treat these polarizations as extended induced dipoles of length $L$ and separation $d$, and consider their interaction energy. This is

$$U = A\left(\frac{1}{\sqrt{L^2+d^2}} - \frac{1}{d}\right) \tag{4}$$

where $A = P^2/4\pi\varepsilon_0$ for electric dipoles and $A = \mu_0 M^2/4\pi$ for magnetic dipoles. The ratio of the interaction energies is then

$$\frac{U_E}{U_M} = \frac{P^2}{\varepsilon_0 \mu_0 M^2} = -\left(\frac{\kappa}{\mu - 1}\right)^2 \tag{5}$$

Now, in the chiral pair both elements have the magnetic and the electric dipoles in the same sense, so $U_C = U_M + U_E$, whereas the enantiomeric pair has the electric dipole reversed, so $U_R = U_M - U_E$. Assigning the shifts in peak frequency to these energies, we find $U_C$ = 3.7 MHz and $U_R$ = –17.3 MHz, so $U_M$ = –6.8 MHz and $U_E$ = 10.5 MHz, and hence

$$\frac{\chi}{\mu - 1} = 1.24 \tag{6}$$

Thus the electrical interaction energy is larger than the magnetic energy, and the chirality is larger than the permeability.

## 4 Discussion and Conclusions

In this paper, we have described the construction and characterization of a novel chiral metamaterial based on the Swiss Roll structure. It consists of a narrow strip of material wound in a helical fashion along a mandrel, and the performance depends on the pitch of the winding: shallower angles imply more turns of material and so a lower resonance frequency along with a stronger chirality. To obtain a uniform winding, a suitable machine has been developed for producing the Swiss Roll elements.

According to the constitutive relations (Eq. (1)) for a chiral material, an applied magnetic field induces not only a magnetic but also an electric response: in this case, it is large enough to be observed directly. We have also conformed that non-chiral material does not produce an electric response.

The material elements have been characterized by measuring their permeability, permittivity and chirality. Although the absolute values of the measured parameters are not reliable, because of fringing fields and parasitic effects, the overall nature of the response (i.e. resonant or non-resonant) is correctly determined: the non-chiral material has a resonant response only in the permeability, whereas chiral material shows resonances in all three parameters. Moreover, the chirality is correctly shown to be out of phase with the permeability and permittivity (it appears in the constitutive equations as $i\kappa$ ) and its sign depends on the handedness of the material: changing handedness changes the sign of $\kappa$ . To the author's knowledge, this is the first reported material whose chirality is so large that it can be measured directly, rather than having to be deduced from optical rotation data.

Pairs of similar elements show an enhanced response, whereas an enantiomeric pair (consisting of two elements of opposite handedness) shows no chiral response: the electric dipoles induced by the magnetic field are of opposite sign and cancel each out. Moreover, the frequency of the resonance in the magnetic response of such pairs is significantly lower that that of the single element, whereas the resonance of the chiral pair is only slightly higher than the single element frequency, showing that the induced electric dipole is larger than the magnetic dipole. This has been quantified by measuring the frequencies of the permeability resonance in the different combinations, and using their differences to deduce that the chirality is actually larger than the permeability: $\kappa = 1.24(\mu - 1)$.

In conclusion, we have fabricated and demonstrated a super-chiral medium based on the Swiss Roll structure. The chirality is sufficiently large that it can be measured directly. Accordingly, there is every prospect that a bulk medium constructed from these elements will obey the condition for strong chirality, i.e. $\kappa > \sqrt{\mu\varepsilon}$ , and so we will be able to demonstrate novel phenomena such as negative refraction [15] in chiral media.

**Acknowledgments** This work is funded by the UK EPSRC. I am grateful to Sir John Pendry for many helpful discussions, and to Dave Woodman for expert assistance with the material fabrication.

## References

1. Pendry, J. B., Holden, A. J., Robbins, D. J., and Stewart, W. J., Magnetism from conductors and enhanced nonlinear phenomena, *IEEE Transactions on Microwave Theory and Techniques* **47** (11), 2075–2084 (1999).
2. Smith, D. R., Pendry, J. B., and Wiltshire, M. C. K., Metamaterials and negative refractive index, *Science* **305** (5685), 788–792 (2004).
3. Wiltshire, M. C. K., Radio frequency (RF) metamaterials, *Physica Status Solidi B-Basic Solid State Physics* **244** (4), 1227–1236 (2007).
4. Wiltshire, M. C. K., Pendry, J. B., Young, I. R., Larkman, D. J., Gilderdale, D. J., and Hajnal, J. V., Microstructured magnetic materials for RF flux guides in magnetic resonance imaging, *Science* **291** (5505), 849–851 (2001).
5. Wiltshire, M. C. K., Hajnal, J. V., Pendry, J. B., Edwards, D. J., and Stevens, C. J., Metamaterial endoscope for magnetic field transfer: near field imaging with magnetic wires, *Optics Express* **11** (7), 709–715 (2003).
6. Wiltshire, M. C. K., Pendry, J. B., Williams, W., and Hajnal, J. V., An effective medium description of 'Swiss Rolls', a magnetic metamaterial, *Journal of Physics-Condensed Matter* **19**, 456216 (2007).

7. Pendry, J. B., Negative refraction makes a perfect lens, *Physical Review Letters* **85** (18), 3966–3969 (2000).
8. Wiltshire, M. C. K., Pendry, J. B., and Hajnal, J. V., Sub-wavelength imaging at radio frequency, *Journal of Physics-Condensed Matter* **18** (22), L315–L321 (2006).
9. Shelby, R. A., Smith, D. R., and Schultz, S., Experimental verification of a negative index of refraction, *Science* **292** (5514), 77–79 (2001).
10. Veselago, V. G., The Electrodynamics of Substances with simultaneously negative values of mu and epsilon, *Soviet Physics Uspekhi* **10** (4), 509–514 (1968).
11. Varadan, V. V., Ro, R., and Varadan, V. K., Measurement of the electromagnetic properties of Chiral composite-materials in the 8-40 GHz range, *Radio Science* **29** (1), 9–22 (1994).
12. Kharina, T. G., Tretyakov, S. A., Sochava, A. A., Simovski, C. R., and Bolioli, S., Experimental studies of artificial omega media, *Electromagnetics* **18** (4), 423–437 (1998).
13. Fedotov, V. A., Mladyonov, P. L., Prosvirnin, S. L., Rogacheva, A. V., Chen, Y., and Zheludev, N. I., Asymmetric propagation of electromagnetic waves through a planar chiral structure, *Physical Review Letters* **97** (16), 167401 (2006).
14. Tretyakov, S., Nefedov, I., Sihvola, A., Maslovski, S., and Simovski, C., Waves and energy in chiral nihility, *Journal of Electromagnetic Waves and Applications* **17** (5), 695–706 (2003).
15. Pendry, J. B., A chiral route to negative refraction, *Science* **306** (5700), 1353–1355 (2004).
16. Sihvola, A. H. and Lindell, I. V., Chiral Maxwell-Garnett Mixing Formula, *Electronics Letters* **26** (2), 118–119 (1990).
17. Constructed by 3Pinnovation Ltd., Budbrooke Industrial Estate, Warwick, CV34 5WP, UK.

# Trapped-Mode Resonances in Planar Metamaterials with High Structural Symmetry

**Sergey Prosvirnin**[1], **Nikitas Papasimakis**[2], **Vassili Fedotov**[2], **Said Zouhdi**[3] **and Nikolay Zheludev**[2]

[1] Institute of Radio Astronomy, Kharkov, 61002, Ukraine
prosvirn@rian.kharkov.ua
[2] Optoelectronics Research Centre, University of Southampton, SO17 1BJ, UK
[3] University Paris Sud, France

**Abstract** We report a type of planar metamaterials that can support a high-quality factor resonance mode, namely trapped-mode, excitation of which is polarization insensitive. The strong energy density of electromagnetic field between metallic patterns of the metamaterial structures shows the potential for development of spaser (surface plasmon amplification by stimulated emission of radiation) and related novel photonics.

## 1 Introduction

Controlling the reflection and/or the transmission frequency properties of surfaces is an important problem of applied electromagnetics. For various microwave applications, there is a need to use controlling material layers with thicknesses extremely small in comparison to the wavelength. These frequency selective surfaces (FSS) are boundary surfaces consisting of some metal or dielectric bodies.

There are well known periodic arrays of different shapes metal patches and the self-resonant grids such as grids of Jerusalem conducting crosses which are used as FSS. Practically, the first low frequency resonance of such structures appears for a wavelength a bit greater than the array period. The quality factor of such structures resonances is not high. However, achieving resonances with high-Q factors is essential for various applications of planar metamaterials.

Generally speaking, the high quality factor and the layer small thickness are contradictory requirements. Actually, a thin open structure cannot have inner resonating volumes and on the other hand, resonating inclusions usually are strongly coupled with free space. Consequently, their resonance quality factor is low. Nevertheless, there are ways to produce very thin structures showing high quality factor frequency resonances (see [1]). This has been achieved by a resonance regime of so-called *trapped modes*.

S. Zouhdi et al. (eds.), *Metamaterials and Plasmonics: Fundamentals, Modelling, Applications*,

If we want to design very thin structures having resonant band characteristics of reflection or transmission with a high quality factor, the consistent step is to focus on the way of structure complexity. Certain of the *multi-element* arrays have this desired property.

Due to radiation losses, resonance frequencies of open systems composed of nondissipative elements are generally complex valued. The quality factor of the system depends from ratio of power of stored energy to power of radiation losses. However, exceptionally strong and narrow resonances are possible in planar metamaterials build upon multi-element arrays via engaging *trapped modes*. The trapped modes correspond to real eigenvalues of the relevant boundary value problem that is *real* resonance frequency of an open system.

Consequently, the trapped modes are of considerable importance in applications because the system can be excited more efficiently due to low radiation losses.

Few years ago extremely high-quality factor double-periodic two-element arrays of split C-shaped particles (double-split rings with certain small asymmetries) were proposed and theoretically studied in [1]. The evidence of high-Q trapped mode resonances of arrays of asymmetrically split C-shaped elements was argued by our experimental study [2]. These designs were shown to be promise for various applications. They were studied theoretically as high-Q metafilms for improved spectral and spatial filtering in WLAN bands in [3, 4]. Numerical simulation of the structures was performed as frequency selective surfaces for high sensitivity terahertz sensing in [5]. Recently we showed [6] by simulation that combining of this type of planar metamaterials and surface plasmon amplification by stimulated emission of radiation (spaser) ideas [7] one can create a narrow-diversion coherent source of electromagnetic radiation that is fueled by plasmonic oscillations.

Characteristic feature of all designs involved the using of excitation of the current trapped modes and considered before was that they led to polarization sensitive planar metamaterials. The main purpose of this work is an introducing of four-fold symmetry polarization insensitive planar periodic two-element structures and the study of resonance properties of these arrays which can possess frequency characteristics with high quality factors due to excitation of trapped mode kind of field.

## 2 Results and Discussions

In this paper, we identify a new class of four-fold symmetry planar metamaterials that can support a trapped mode. The sharp high quality-factors resonances are demonstrated theoretically and experimentally. Remarkably, achieving the sharp high quality-factors resonances in such metamaterial requires no symmetry breaking, and therefore excitation of the trapped modes is polarization insensitive.

We study two fashions of our metamaterial. They both are double-element planar arrays of a metal strip pattern, which are arranged in a regular square periodic grid and placed on a thin dielectric substrate. The first one consists of pairs of concentric metal rings, as shown in Fig. 1a. Computation of transmission of this kind array

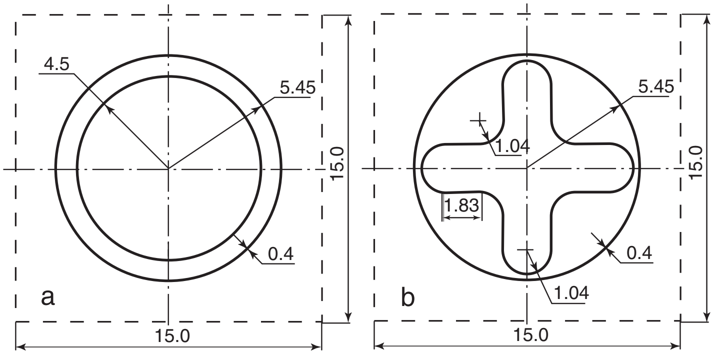


**Fig. 1** Translational cell of the planar array of concentric metal rings (**a**) and metal complex elements consisted of the cross placed inside of the ring (**b**). The sizes are pointed in millimeters. The arc radii are pointed to middle lines of curvilinear strip elements of the arrays. All metal strip elements of both arrays are 0.4 mm width. The metal elements of arrays are placed on a dielectric 1.6 mm thickness substrate.

was fulfilled in [8]. The second fashion of our metamaterial is composed from more complex double elements consisted of crosses placed inside of rings, see Fig. 1b. Diameter of the ring is the same as a diameter of the outer ring of the array of concentric rings. The shape and sizes of the cross were chosen so that its perimeter along middle line of strip would be exactly the same as the length of the ring.

The double-element pattern of each sample was etched from 35 μm copper cladding covering FR4 PCB substrate of 1.6 mm thickness. Relative permittivity of substrate is approximately $\varepsilon = 4.5 - i0.1$. The unit translational cell of the patterns is a square with the size of $15 \times 15$ mm (see Fig. 1). Such arrays do not diffract for any angle of plane wave incidence at frequencies below 10 GHz and they do not diffract normally incident electromagnetic wave for frequencies lower than 20 GHz.

The overall size of the samples used in our experiments was approximately $220 \times 220$ mm. All our measurements were performed in a microwave anechoic chamber in 2–12 GHz frequency range using linearly polarized broadband horn antennas (Schwarzbeck BBHA 9120D) equipped with dielectric lens concentrators and a vector network analyzer (Agilent E8364B).

Reflected and transmitted electromagnetic fields and surface currents induced on the arrays strip elements were calculated with the well established method described in [9]. The method is based on the method of moments to solve a vectorial integral equation for the surface current induced by the electromagnetic field on the thin narrow metal elements of array followed by calculation of scattered fields. The equation is derived with boundary conditions that assume a zero value for the tangential component of the electric field on the metal strips.

Figure 2 shows the results of transmission and reflection measurements and numerical simulations conducted at normal incidence on the array of double concentric rings (DR-metamaterial). Here and below, we present the values $20\ \lg|R|$ (dB) and $20\ \lg|T|$ (dB) to characterize the reflection and the transmission of arrays where

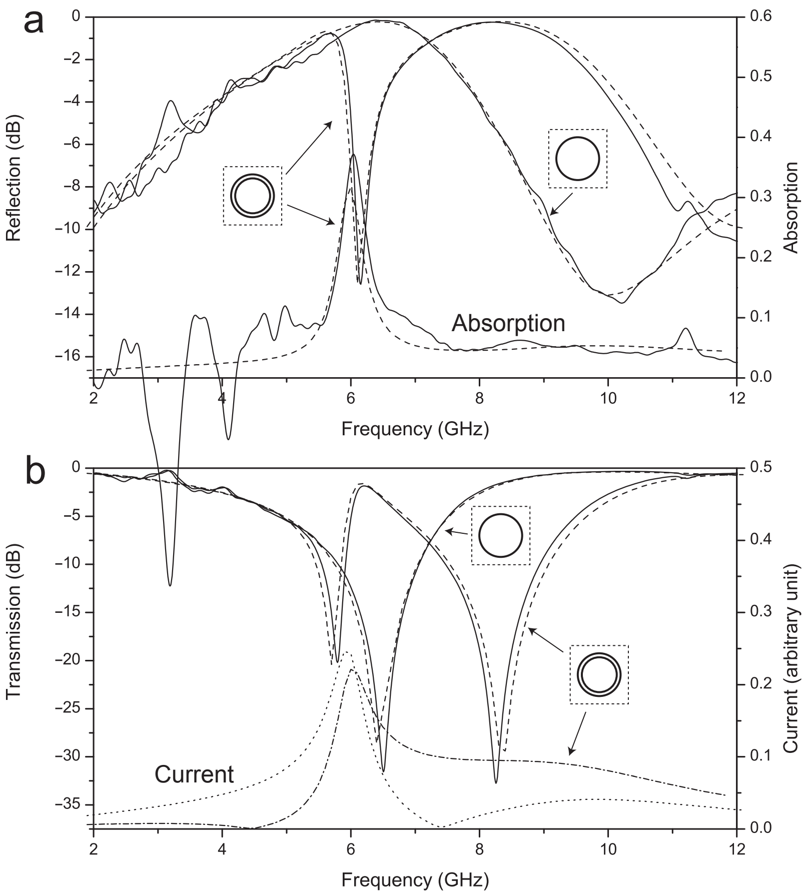


**Fig. 2** Normal incidence reflection (**a**) and transmission (**b**) spectra of the planar DR-metamaterial and the reference one-element periodic structure composed of the larger rings. Solid lines represent experimental data, dashed lines correspond to the theory (the method of moments). Calculated current values (**b**) are shown by dotted line for the outer ring and dash-doted line for the inner ring at the point of corresponded ring with maximal amplitude of the current.

$R$ and $T$ are the classical reflection and transmission coefficients determined via electric field strength. For both transmission and reflection, the theoretical calculations showed exceptionally good agreement with the experimental results assuming $\varepsilon = 4.5 - i0.1$. It should be noted that the spectral response of the planar metamaterial showed no polarization dependence, which is consistent with the high degree of symmetry of its unit cell.

The measured spectra reveals a very broad stop-band split by a sharp resonant feature at around 6.2 GHz . In reflection it is seen as a narrow dip, where the reflectivity level drops below 5%, that separates two broad reflection resonances centered at correspondingly 5.8 and 8.3 GHz. In transmission it corresponds to a narrow pass-band with the maximum transmission level exceeding 65% and the spectral width of about 0.7 GHz measured as a full width at half maximum (the quality factor is approximately $Q \approx 9$).

Importantly, the response of a reference metamaterial composed of the single rings of the larger radius revealed a very broad stop-band (reflection resonance with $Q \approx 1$) (see Fig. 2).

The origin of the narrow resonant band of transparency can be traced to the excitation of so-called trapped mode, which are anti-symmetric current mode that is weakly coupled to free space. These modes are normally inaccessible, but can be excited if, for example, the metamaterials particles have certain structural asymmetry [1, 2]. The trapped-mode nature of the metamaterial's response was confirmed by our numerical simulations of current distributions.

We have calculated the current distribution along the inner and outer rings of array. The currents have maximal amplitudes at the points with tangent to the ring parallel to the polarization direction of a normally incident wave. In Fig. 2b we present the modeled frequency dependencies of the current amplitudes at these neighboring points of the inner and outer rings. It can be seen that both rings appear to be equally strong excited in the frequency of the narrow pass-band. The analysis of currents phases reveals that the induced currents in the inner and outer rings oscillate in opposite directions. An electromagnetic field of two close strips of the rings is similar to the nonradiating field of a double-wire line of resonance length. Thus, the opposite directed but being equal currents of the inner and outer rings of array yield an electromagnetically trapped mode. Indeed, the scattered fields produced by such current configuration is very weak since the electrical dipole moment is almost compensated, while higher multipole moments such as, for example, magnetic dipole and electric quadrupole are absent due to symmetry of the DR-structure. As a consequence, the coupling of the metamaterial array to free space and therefore its radiation losses are reduced dramatically, which ensures much stronger induced currents and higher $Q$-factors of the response than in the case of the dipole excitation of the one-directional currents in the frequencies of the stop-bands.

It is important to note that in the DR-structure excitation and control of the trapped mode requires no symmetry breaking, which makes it markedly different from the trapped modes demonstrated recently in asymmetrically-split ring metamaterials [1, 2]. In the present case the free-space coupling of DR-structure (and consequently the width of the pass-band exhibited by the metamaterial) is exclusively controlled by the difference in circumferences of the inner and outer rings. Indeed, the pass-band is squeezed between two stop-bands related to the resonance frequencies of inner and outer rings.

Since the resonance frequency of narrow metal strip element is controlled mainly its stretched length, we designed a four-fold structure with equal circumferences of inner and outer elements of double-element array composed from crosses and rings (CR-array) (see Fig. 1b).

The measured and simulated frequency dependencies of reflection and transmission of CR-array are presented in Fig. 3. One can see a typical trapped mode resonance confirmed by frequency dependencies of the calculated current amplitudes

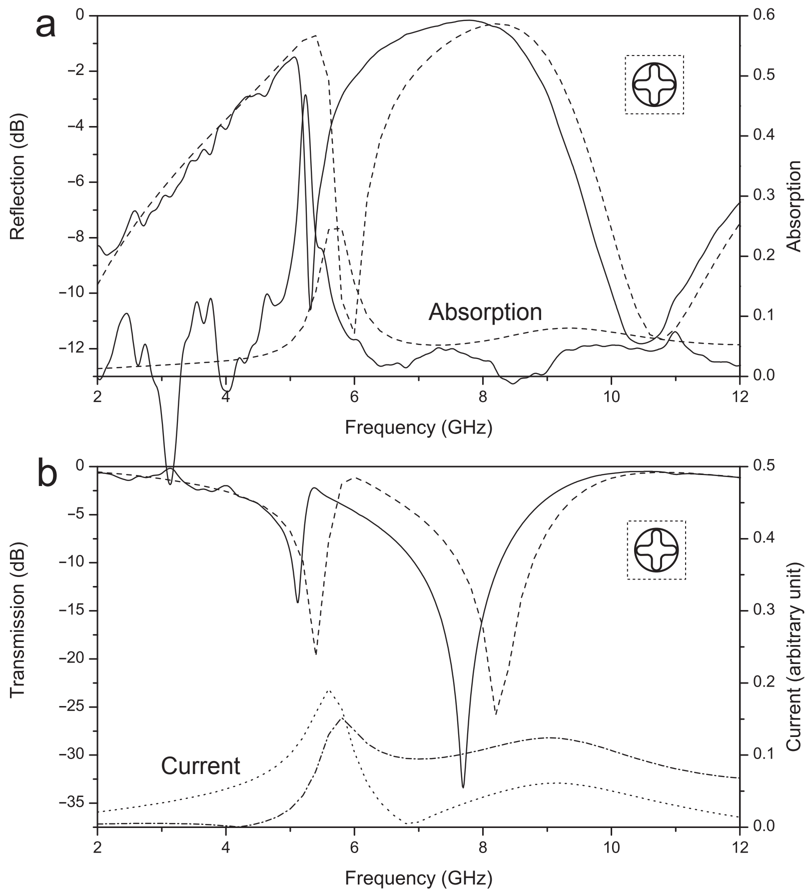


**Fig. 3** Normal incidence reflection (**a**) and transmission (**b**) spectra of the planar cross-ring pattern metamaterial. Solid lines represent experimental data, dashed lines correspond to the theory (the method of moments). Calculated current values (**b**) are shown by dotted line for the ring and dash-doted line for the cross at the points of ring and cross with maximal amplitude of the current.

for crosses and rings of the array. The resonance frequency of pass-band is lower than has been mentioned for the DR-array design. However, we do not observe an enlarged quality factor. This CR-array of being equal-circumferential but complex-shaped elements reveals approximately the same radiation losses as the DR-array. Nevertheless, we suppose that double complex-shaped elements may be optimized to high-Q resonance of four-fold symmetry array by using any algorithm of multi-variate optimization.

The great feature of trapped mode resonances is a high density of electromagnetic field energy concentrated inside and close to array. The electric field strength reaches great values in the resonance frequency. Indeed, we observe an enlarged absorption $(1-|T|^2-|R|^2)$ because of the power dissipation inside the substrate of both arrays (see Fig. 2a and Fig. 3a). Thus, the reflection and transmission of trapped mode arrays are extensively dependent from dissipation. Therefore, these arrays may serve to indicate a weak absorption of media located close to their surface. On the other hand, the remarkably strong energy density of high-Q trapped mode resonance clears the way to achieve orders of magnitude enhancement of single-pass amplification [6] of thin active medium layer with trapped mode array.

## 3 Conclusions

We demonstrate both numerically and experimentally that a trapped mode may be excited in planar four-fold symmetry structures. Thus, high-Q very thin layers may be designed with polarization insensitive features.

The type of polarization insensitive planar metamaterials is proposed that reveal high quality-factor resonance transmission in a wide stop-band range. The trapped mode nature of this transmission resulting from excitation of anti-symmetric weak radiative resonance currents is clearly recognized both theoretically and experimentally.

The results also indicate that strong electric field strength concentrated by this type of periodic structures is potential for development of metamaterial combining with spaser (surface plasmon amplification by stimulated emission of radiation) and related novel photonics.

**Acknowledgements** The authors would like to acknowledge the financial support of the EPSRC (UK), National Academy of Sciences of Ukraine (grant no. 1-02-a) and Metamorphose NoE.

## References

1. Prosvirnin, S., Zouhdi, S.: Resonances of closed modes in thin arrays of complex particles. In: Zouhdi, S., et. al. (eds) Advances in Electromagnetics of Complex Media and Metamaterials, pp. 281–290. Kluwer, Dordrecht, Printed in the Netherlands (2003)
2. Fedotov, V.A., Rose, M., Prosvirnin, S.L., Papasimakis, N., Zheludev, N.I.: Sharp trapped-mode resonances in planar metamaterials with a broken structural symmetry. Phys. Rev. Lett. **99**(14), 147401 (2007)
3. Blackburn, J.F., Arnaut, L.R.: High performance split ring FSS for WLAN bands. In: Proc. 27th ESA Antenna Technology Workshop on Innovative Periodic Antennas: Electromagnetic Bandgap, Left-handed Material, Fractal and Frequency Selective Surfaces, European Space Agency, pp. 329–336. Santiago de Compostela, Spain (2004)
4. Arnaut, L.R.: High-Q planar chiral metafilms for improved spectral and spatial filtering. In: Olyslager, F., Franchois, A., Sihvola, A. (eds) Proceedings of the 10th Conference on Complex Media and Meta-Materials, pp. 185–187. Het Pand, Ghent, Belgium (2004)
5. Debus, C., Bolivar, P.H.: Frequency selective surfaces for high sensitivity terahertz sensing. Appl. Phys. Lett. **91**(18), 184102 (2007) doi: 10.1063/1.2805016
6. Zheludev, N.I., Prosvirnin, S.L., Papasimakis, N., Fedotov, V.A.: Lasing spacer. Nature Photon. **2**(6), 351–354 (2008) doi: 10.1038/nphoton.2008.82

7. Bergman, D.J., Stockman, M.I.: Surface plasmon amplification by stimulated emission of radiation: Quantum generation of coherent surface plasmons in nanosystems. Phys. Rev. Lett. **90**(2), 027402 (2003) doi: 10.1103/PhysRevLett.90.027402
8. Misran, N., Cahill, R., Fusco, V.F.: Design optimization of ring elements for broadband reflectarray antenna. IEE Proc.-Microw. Antenn. Propag. **150**(6), 440–444 (2003)
9. Prosvirnin, S.L.: Transformation of polarization when waves are reflected by a microstrip array made of complex-shaped elements. J. Commun. Technol. Electron. **44**(6), 635–640 (1999)

# Fabricating Plasmonic Components for Nano- and Meta-Photonics

**Alexandra Boltasseva[1], Rasmus B. Nielsen[1], Claus Jeppesen[1], Anders Kristensen[1], Reuben Bakker[2], Zhengtong Liu[2], Hsiao-Kuan Yuan[2], Alexander V. Kildishev[2], and Vladimir M. Shalaev[2]**

[1]Technical University of Denmark
DTU Building 343, DK-2800 Kongens Lyngby, Denmark
aeb@com.dtu.dk
[2]Birck Nanotechnology Center, Purdue University
West Lafayette, IN 47907, USA

**Abstract** Different fabrication approaches for realization of metal-dielectric structures supporting propagating and localized surface plasmons are described including fabrication of nanophotonic waveguides and plasmonic nanoantennae.

## 1 Introduction

One of the main research goals in modern photonics is to find optimal configurations that can efficiently guide and strongly focus optical fields. Developing structures offering efficient propagation and strong localization of light opens up new application possibilities in sensing, nanoscale manipulation and optical characterization. One of the avenues in the field of compact photonic devices and nanophotonics that has recently attracted considerable interest is optics based on the controlled excitation of *surface plasmons* (SPs) [1–3]. SPs on metal-dielectric interfaces and metal nanoparticles are characterized by strong confinement of the electromagnetic field in the direction perpendicular to the metallic surface. This feature makes plasmonic structures very attractive candidates for developing new photonic components. Recently, resonant interactions in metal nanostructures involving both localized and propagating surface plasmons have been broadly investigated both theoretically and experimentally using nanostructures of different shapes and configurations. A variety of promising geometries for SP directional propagation, bending, focusing and localization have been reported [1–3].

Examples of metal-dielectric structures investigated for guiding and manipulation of SPs range from special configurations of nanoscatterers on metal surfaces

S. Zouhdi et al. (eds.), *Metamaterials and Plasmonics: Fundamentals, Modelling, Applications*,

[4, 5], chains of metal nanoparticles [6], metal strips with nm-scale thickness [7–11] and subwavelength metal nanowires [12, 13] to profiled metal surfaces [14–22]. Different geometries used to control the SP propagation are investigated with respect to the trade-off between confinement and loss [1], and the structure choice is further governed by the length scale over which energy is to be transferred and routed. One of the most promising directions in the area of plasmonic waveguides is investigation of profiled metal surfaces, namely grooves and wedges, as waveguides supporting strongly localized plasmon modes [14–23]. The requisite for the further development of such plasmonic components for real-life applications is availability of robust large scale manufacturing processes for making profiled and nanostructured metal-dielectric surfaces.

Equally advancing are studies of localized surface plasmons. Highly efficient, localized surface plasmon resonance of paired gold nanoparticles (optical nanoantennae) gives rise to significantly enhanced and highly confined electromagnetic fields that have a great importance for sensing and tagging applications, nanoscale lithography, and as the basis for nanolasers [24–29]. While very high intensity enhancements ($\geq 10^3$) have been reported (for example, for the experiments on surface enhanced Raman scattering (SERS) [29]) large variations in the resonant effects were observed for nominally identical structures due to the fact that SP resonance is strongly dependent on structural parameters, especially on the distance between the two interacting particles and their sizes. Thus, fabrication procedures that combine high reproducibility, robustness and ability of creating small interparticle gaps in a controlled way are required.

Over the last decades, modern nanofabrication techniques have opened new possibilities for controlling and preparing profiled and patterned metal surfaces in order to tailor the properties of excited surface plasmons. Fabrication of plasmonic structures requires development of robust processes that offer high reproducibility, low loss, and flexibility, and can be adaptable for different designs and applications. So far, one of the most frequently used techniques is *electron beam lithography* (EBL) that is widely used for manufacturing of different plasmonic components, see for example in [2, 4–6, 11, 13, 27]. However, if a large area has to be patterned (up to millimeters or centimeters in size) EBL-based fabrication becomes quite time-consuming, and therefore, expensive, which makes this technique not suitable for real device applications. Thus, there is a constant search for alternative high-throughput nanofabrication techniques that can be compatible with large-scale fabrication. For example, for plasmonic components based on nanostructured sub-wavelength thin metal strips where efficient gratings were first introduced via EBL [10, 11] a simple and cheap fabrication process compatible with *nanoimprint lithography* (NIL) was recently developed [30]. For creating various infinite and finite-area arrays of plasmonic nanoparticles, a high-throughput nanofabrication technique based on soft interference lithography that combines the ability of interference lithography [31] to produce wafer-scale nanopatterns with the versatility of soft lithography [32] was recently proposed for producing plasmonic nanostructures over tens of square centimetres [33].

In addition to the high-throughput requirement, the choice of the optimal nanofabrication technique is also governed by the loss issue in plasmonic structures. It was reported that the surface roughness of fabricated metal-dielectric structures has an effect on the increased losses at the plasmon resonances [34]. Comparison of existing planar fabrication methods and chemical approaches also deserved a great deal of attention yielding important results on the issue of surface roughness that contributes to the SP loss [12].

Here, we focus on fabrication of metal-dielectric configurations supporting propagating and localized SP modes that requires development of nanoscale patterning tools and production-compatible techniques for structures with real-device applications potential.

## 2 Profiled Metal Surfaces as Plasmonic Waveguides

Coupling of SPs on opposite sidewalls of either a channel or wedge made in metal leads to formation of highly localized plasmonic modes that can be used for making compact optical components (Fig. 1).

(a) (b)

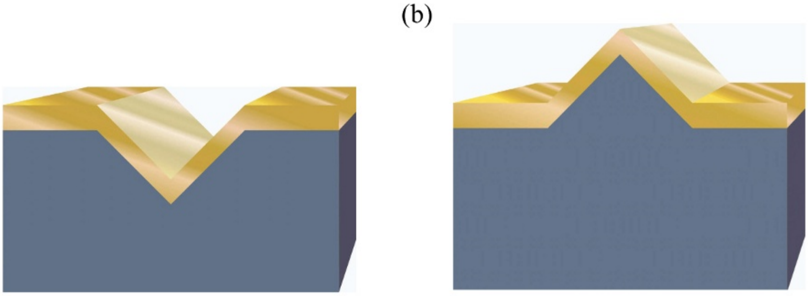

**Fig. 1** Schematic of (**a**) a V-groove and (**b**) wedge made in metal. Both structures support plasmonic modes localized at and propagating along the groove bottom/wedge apex [14–20].

A V-shaped metal groove supporting a strongly localized plasmon-polariton mode (called *channel plasmon-polariton*, CPP) is of particular interest due to high degree of the CPP mode confinement, relatively low propagation and bending losses, and single mode operation achievable for the CPP [14–18]. The inverse geometry, namely, a triangular metal wedge supports a plasmon-polariton mode (*wedge plasmon-polariton*, WPP) that is, in a way, complementary to the CPP mode. Edge modes were shown to support strongly localized plasmons both theoretically and experimentally [19–22] and it was recently shown that WPPs, while showing significantly smaller modal size than CPPs, exhibit similar propagation length as CPPs [21]. At telecom wavelengths (wavelength bands around 1.31 and 1.55 μm), WPP guiding properties were found to be superior to the ones offered by CPPs, where low losses for CPPs are achievable for relatively large mode sizes [23].

First experimentally investigated structures were fabricated using the *focused ion beam* (FIB) technique. In the perspective of future applications, the FIB-based approach has certain limitations due to high cost, complexity and low throughput. In addition, FIB-fabricated components are hard to interface with optical fibers to achieve efficient end-fire excitation. Thus, experimental realization of components that are robust, simple to fabricate and easy to interface with outside world is of great interest for future investigations of subwavelength plasmon guiding as well as for development of functional plasmonic devices.

Large-scale fabrication of profiled metal surfaces remains a challenging task. While sharp grooves and wedges can easily be made in silicon using standard lithographic and etching techniques, profiling metal surfaces often requires complex fabrication techniques like FIB [17, 18, 20]. Here, we describe wafer-scale fabrication methods that allows replicating a profiled silicon surface in metal. The fabrication approach is based on standard planar cleanroom processes and allows integration of plasmonic structures with lab-on-a-chip devices.

## *2.1 Making metal V-grooves*

A large-scale method for the fabrication of V-groove plasmonic waveguides is based on the nanoimprint lithography process [35]. A schematic of the fabrication method is presented in Fig. 2. The developed process where V-grooves are first

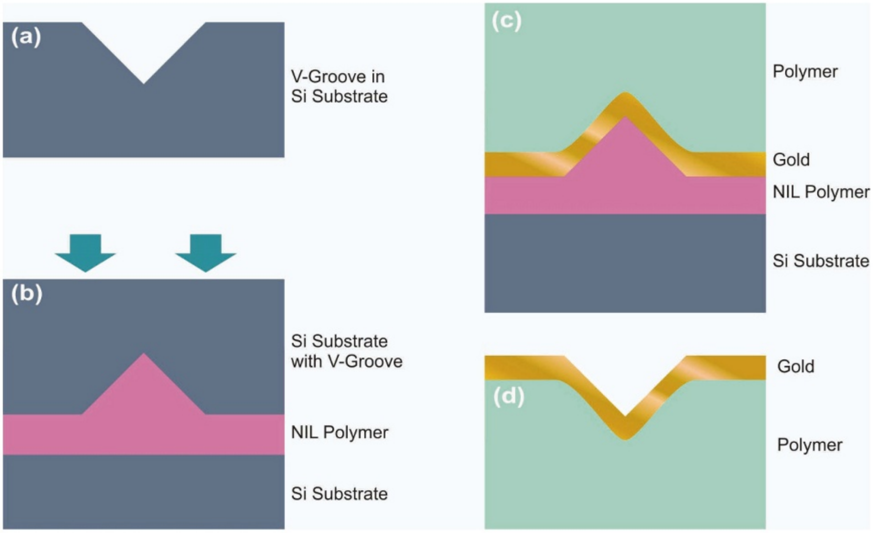


**Fig. 2** Schematic of the fabrication steps: (**a**) V-grooves are made in a silicon stamp, (**b**) the silicon stamp is imprinted into a nanoimprint polymer layer (PMMA) on a silicon carrier wafer, (**c**) a negative copy of the stamp is covered with a layer of gold and then UV curable polymer (Ormocomp), (**d**) PMMA layer is dissolved releasing the V-groove structure.

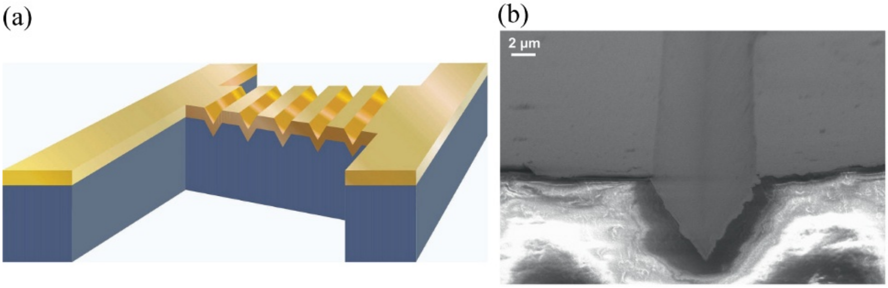


**Fig. 3** (**a**) Schematic of the fabricated sample with V-grooved waveguides (gold on polymer substrate) having easy fiber-access configuration (not in scale) together with (**b**) the scanning electron microscope (SEM) image of the fabricated V-groove, 200-nm-gold layer on top of a transparent polymer (the polymer is charging during SEM investigation). The gold edge is ragged due to breaks from ultrasound agitation.

made in a silicon substrate and then replicated in metal using nanoimprint process allows reducing the roughness of the metal film on the sidewalls of the groove. This is achieved by using the backside of the deposited film, similar to the process of template-stripping [36]. The main idea of the method is to make a metal replica of a profiled silicon structure where any desired geometry can be obtained via standard patterning and etching techniques. This approach is used to transfer structures from a silicon stamp to a PMMA (polymethyl methacrylate polymer) layer. After the imprint process, gold is deposited on the PMMA, followed by deposition and selective UV exposure of a hybrid polymer (Ormocomp). Once the Ormocomp layer has been post exposure baked, the PMMA layer can be dissolved, leaving a gold-on-polymer replica of the initial silicon stamp (Fig. 3). In this approach, the quality of the gold surface is expected to be better than that achieved with standard deposition techniques [35, 37].

The method described here should be viewed as a general template for replicating silicon structures in gold on polymer, and can be readily changed to different geometries. Profiling of silicon stamps can be achieved by using a variety of established techniques including reactive ion etching (RIE) (both isotropic and anisotropic) and wet etching using KOH. For example, samples fabricated via wet etch of silicon have limitations of an apex angle fixed to 70° and easy patterning of only straight waveguides [35]. In this case, thermal oxidization of silicon structures can be used to alter the groove geometry, providing different apex angles, for example, decreasing the angle from 70° to 50° [35]. In order to make waveguides of different geometries (bends, couplers) wet etch of silicon can be replaced by RIE where nearly any desired channel geometry is achievable. Since RIE is a complex process, better reproducibility and homogeneity across the wafer can be achieved via combination of RIE with oxidization process that helps to change the geometry and smoothen out the surface (Fig. 4).

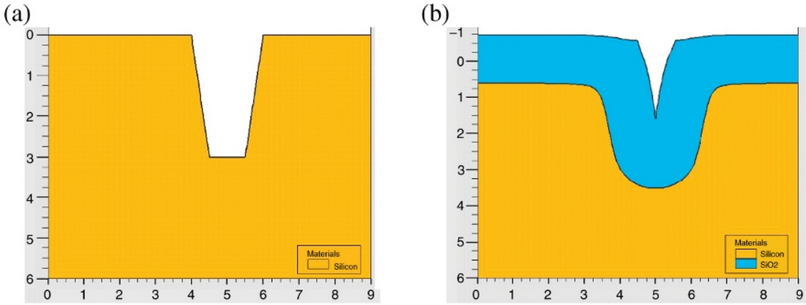


**Fig. 4** Simulation of thermal oxidization on (**a**) a reactive ion etched channel with sloped sidewalls and flat bottom: an oxidization step can transform this geometry into (**b**) smooth high angle V-grooves (2D process simulator from Silvaco, SSupprem4). Scales are in micrometers.

The results of optical characterization of the fabricated V-groove waveguides using scanning near field microscopy (SNOM), showing broadband transmission with subwavelength confinement and propagation lengths exceeding one hundred microns are reported elsewhere [37].

## *2.2 Making metal wedges*

For fabricating triangular metal wedge waveguides a wafer-scale, parallel method based on standard UV lithography is developed. The developed fabrication procedure provides waveguides that are compatible with fiber optics giving the possibility of easy in- and out coupling. Such geometry can not be achieved by standard deposition techniques since depositing a metal layer on a sharp tip (for example, in silicon) would result in smoothening of the edge. A standard fabrication sequence of lithographic and etching steps to achieve a wedge in a substrate combined with standard metal deposition can therefore only be used for making rounded-top or trapezium-shaped wedges [38]. The fabrication steps of the developed procedure are shown schematically in Fig. 5. First, V-grooves are etched in silicon via standard KOH-etch process, and 500 nm of gold is e-beam evaporated on the silicon wafer with etched V-grooves.

The described procedure provides straight wedges with the fixed apex angle of 70.5° (due to wet etch of silicon). The apex angle of the V-groove made in a substrate can be changed via an oxidation process [35]. Experimental observations of plasmon-polariton low-loss guiding at telecom wavelengths (propagation length ~120 μm) by triangular metal wedges made by the described technique are reported in [22].

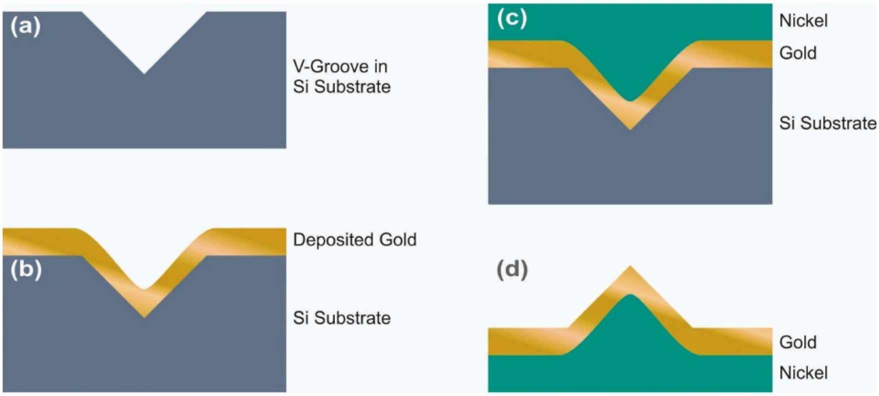


**Fig. 5** Schematic of the fabrication steps: (**a**) V-grooves are etched in a silicon substrate using wet etch, (**b**) gold is deposited (note smoothening of the V-groove bottom after the deposition), (**c**) nickel is deposited, (**d**) silicon substrate is dissolved leaving the wedges in gold.

Using electroplating deposition, 53-μm-thick layer of nickel is then deposited on top of the gold-covered wafer. Removal of silicon substrate completes the fabrication sequence yielding straight wedges of gold (Fig. 6).

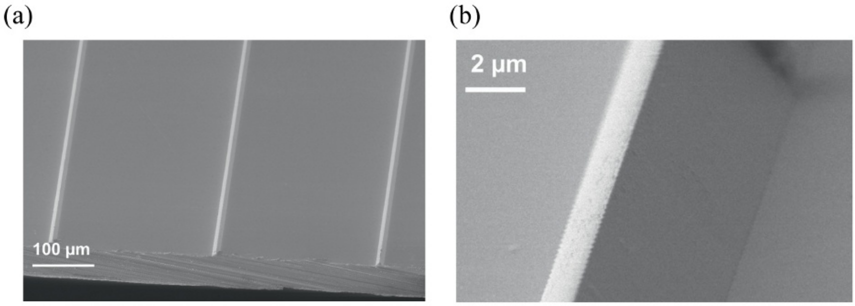


**Fig. 6** (**a**) SEM image of the fabricated wedge gold waveguides together with (**b**) a close-up of the fabricated wedge (wavy edge at the lower end is due to charging effects). Marks and facet defects are due to rough sawing of the metal.

Metal wedges can also be produced via a nanoimprint lithography process similar to the fabrication technique used for making V-grooves (Fig. 2). In this case, sharp wedges are first made in silicon and then replicated in metal. By successive reactive ion etching and oxidation processing steps, different-shape silicon wedges can be fabricated [39, 40]. Figure 7 shows an example of a silicon wedge made via RIE, oxidization and the oxide etch processes.

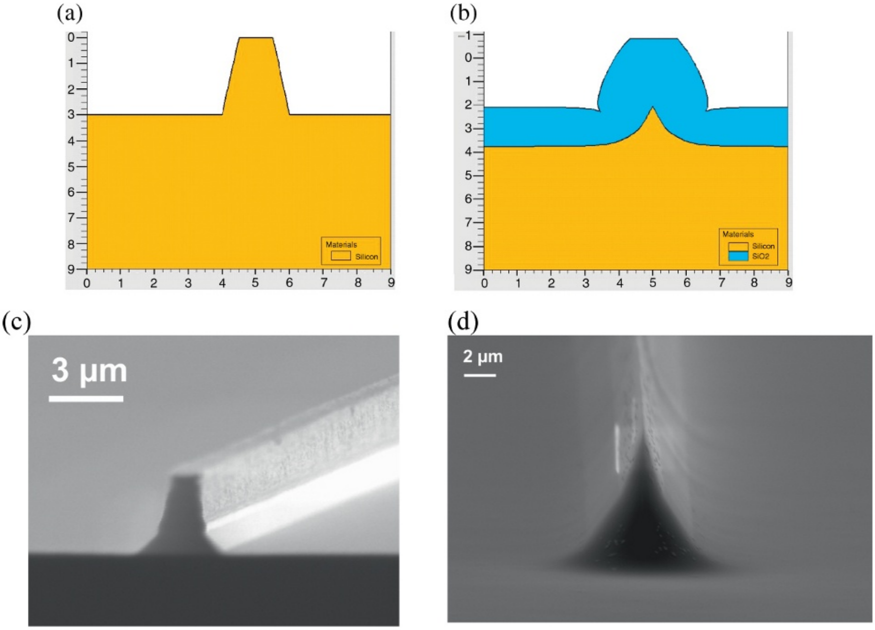


**Fig. 7** Simulation of thermal oxidization on (**a**) a reactive ion etched silicon wedge where (**b**) oxide (blue) can be removed subsequently in a highly selective etch (buffer hydrofluoric), leaving sharp wedge (scales are in micrometers) together with SEM images of the fabricated silicon wedge (**c**) after RIE and (**d**) after oxidation and subsequent oxide removal.

## 3 Fabricating Plasmonic Nanoantennae

Nanoantenna fabrication requires a procedure that combines high reproducibility, robustness and ability of creating small interparticle gaps. Here, we report on nanoantennae fabrication method based on electron beam lithography that offers controllable way of manufacturing high density plasmonic substrates for example, for surface enhanced Raman scattering. Using EBL nanoantenna arrays made of paired elliptical gold particles for particle sizes down to several tens of nm and gaps between particles down to 15 nm can be fabricated (Fig. 8).

In this approach, the arrays are first patterned on an EBL resist and then created either on a substrate or inside the etched holes via metal deposition and lift-off

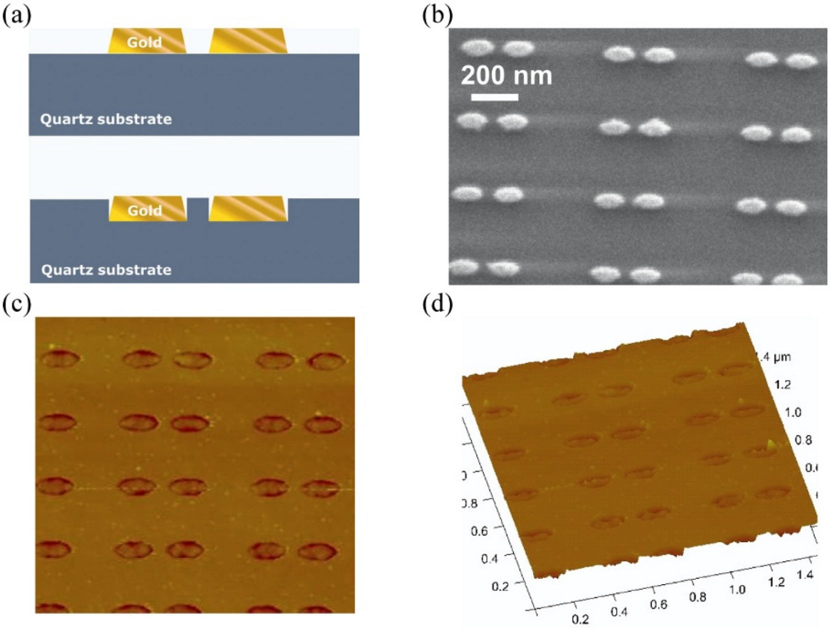


**Fig. 8** (**a**) Schematic of the paired gold particles on top of or embedded into a quartz substrate together with (**b**) SEM image of the antenna array on top of a quartz substrate and (**c, d**) atomic force microscope (AFM) images of the embedded antenna array (AFM scale is in micrometers).

process. Detailed samples' description together with the transmittance and reflectance spectra in the visible range exhibiting strong resonances for the polarization, where the electric field is parallel to the major axis of the elliptical particle, are reported in [41].

For optical nanoantennae, two fabrication issues are of great importance, namely, reproducibility of particle sizes and especially interparticle gaps and surface roughness. For gold particles on quartz, the surface roughness is quite low (around 1 nm RMS) [41]. However, structures with gold particles created inside the etched holes have increased roughness due to an additional step of RIE. Moreover, creating a flat surface with embedded metal particles is a challenging task requiring careful optimization of both etching and deposition processes. A possible way of making flat nanoantennae structures is based on a 'flip' process. In this approach, the gold structures are first fabricated on a smooth substrate surface (quartz) and then covered with a curable polymer (like Ormocomp) followed by the substrate removal (Fig. 9).

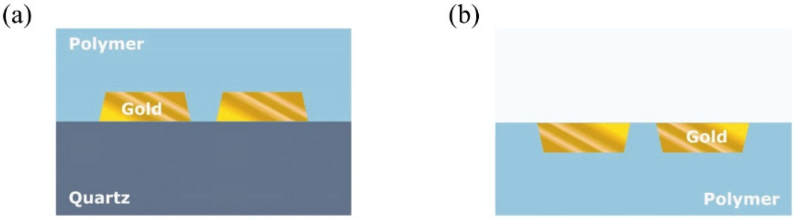


**Fig. 9** Schematic for making low-roughness flat nanoantennae array: (**a**) gold particles are patterned on a quartz substrate via electron beam lithography, metal deposition and lift-off and covered with a curable polymer followed by (**b**) substrate removal.

In contrast to chemical methods that always have a dispersion of particle sizes, EBL offer a highly controllable way of producing nanoparticles of the same size and interparticle gaps. However, making interparticle gaps below 10 nm becomes increasingly difficult. This calls for new methods that could combine controllable planar methods as lithography and chemical approaches of creating reproducible interparticle gaps [42]. Thus, a large-scale technique for creating nanoantennae requires novel assembly methods, for example, where chemically created dimers are assembled on a prepatterned or functionalized surface.

## 4 Conclusion

Development of robust large-scale fabrication techniques based on standard parallel processes is a requisite for further progress in application-oriented or ‘practical’ plasmonics. In the area of subwavelength plasmon-polariton guiding along metal grooves or wedges, nanoimprint-based technique of producing plasmonic waveguides that are compatible with fiber optics opens up the possibility of developing components for ‘real-life’ applications ranging from integrated optics to biosensors. The method based on combined nanoimprint and standard photolithography is highly adaptable to different designs and is compatible with lab-on-chip technology that is important for future bio-technology applications. Along with the development of large-scale nanofabrication techniques, improving and perfecting the structural quality of plasmonic structures is the key step towards plasmonic applications. Besides conventional methods of decreasing surface roughness of deposited metal films like optimization of the electron beam deposition process [43], employing new fabrication techniques based on replica or ‘flip’ processes offers simultaneous substrate planarization that allow reducing the surface roughness of the metal structures and thus creating plasmonic components with improved performance.

**Acknowledgments** Support from the NABIIT project (contract No. 2106-05-033) and FTP project (274-07-0057) from the Danish Research Agency is gratefully acknowledged.

## References

1. Maier, S. A., Plasmonics: Fundamentals and Applications, Springer, New York, 2007.
2. Barnes, W.L., Dereux, A., and Ebbesen, T.W., "Surface plasmon subwavelength optics," Nature 424, 824–830 (2003).
3. Lal, S., Link, S., and Halas, N.J., "Nano-optics from sensing to waveguiding," Nature Photonic. 1, 641–648 (2008).
4. Bozhevolnyi, S.I., Erland, J., Leosson, K., Skovgaard, P.M.W., and Hvam, J.M., "Waveguiding in surface plasmon polariton band gap structures," Phys. Rev. Lett. 86, 3008–3011 (2001).
5. Bozhevolnyi, S.I., Volkov, V.S., and Leosson, K., "Localization and waveguiding of surface plas-mon polaritons in random nanostructures," Phys. Rev. Lett. 89, 186801 (2002).
6. Maier, S.A., Kik, P.G., Atwater, H.A., Meltzer, S., Harel, E., Koel, B.E., and Requicha, A.A.G., "Lo-cal detection of electromagnetic energy transport below the diffraction limit in metal nanoparticle plasmon waveguides," Nature Mat. 2, 229–232 (2003).
7. Charbonneau, R., Lahoud, N., Mattiussi, G., and Berini, P., "Demonstration of integrated optics elements based on long-ranging surface plasmon polaritons," Opt. Exp. 13, 977–984 (2005).
8. Boltasseva, A., Nikolajsen, T., Leosson, K., Kjaer, K., Larsen, M.S., and Bozhevolnyi, S.I., "Inte-grated optical components utilizing long-range surface plasmon polaritons," J. Lightw. Technol. 23, 413–422 (2005).
9. Berini, P., "Plasmon-polariton waves guided by thin lossy metal films of finite width: Bound modes of symmetric structures," Phys. Rev. B 61, 10484–10503 (2000).
10. Bozhevolnyi, S.I., Boltasseva, A., Søndergaard, T., Nikolajsen, T., and Leosson, K., "Photonic band gap structures for long-range surface plasmon polaritons," Optics Commun. 250, 328–333 (2005).
11. Boltasseva, A., Bozhevolnyi, S.I., Nikolajsen, T., and Leosson, K., "Compact Bragg gratings for long-range surface plasmon polaritons," J. Lightw. Technol. 24, 912–918 (2006).
12. Ditlbacher, H., Hohenau, A., Wagner, D., Kreibig, U., Rogers, M., Hofer, F., Aussenegg, F.R., and Krenn, J.R., "Silver nanowires as surface plasmon resonators," Phys. Rev. Lett. 95, 257403 (2005).
13. Leosson, K., Nikolajsen, T., Boltasseva, A., and Bozhevolnyi, S.I., "Long-range surface plasmon polariton nanowire waveguides for device applications," Opt. Exp. 14, 314–319 (2006).
14. Novikov, I.V. and Maradudin, A.A., "Channel polaritons," Phys. Rev. B 66, 035403 (2002).
15. Gramotnev, D.K. and Pile, D.F.P., "Single-mode subwavelength waveguide with channel plas-mon-polaritons in triangular grooves on a metal surface," Appl. Phys. Lett. 86, 6323–6325 (2004).
16. Pile, D.F.P. and Gramotnev, D.K., "Plasmonic subwavelength waveguides: next to zero losses at sharp bends," Opt. Lett. 30, 1186–1188 (2005).
17. Bozhevolnyi, S.I., Volkov, V.S., Devaux, E., and Ebbesen, T.W., "Channel plasmon subwavelength waveguide components including interferometers and ring resonators," Nature 440, 508–511 (2006).

18. Bozhevolnyi, S.I., Volkov, V.S., Devaux, E., and Ebbesen, T.W., "Channel plasmon-polariton guid-ing by subwavelength metal grooves," Phys. Rev. Lett. 95, 046802-1-4 (2005).
19. Dobrzynski, L. and Maradudin, A.A., "Electrostatic edge modes in a dielectric wedge," Phys. Rev. B 6, 3810–3815 (1972).
20. Pile, D.F.P., Ogawa, T., Gramotnev, D.K., Okamoto, T., Haraguchi, M., Fukui, M., and Matsuo, S., "Theoretical and experimental investigation of strongly localized plasmons on triangular metal wedges for subwavelength waveguiding," Appl. Phys. Lett. 87, 061106-1-3 (2005).
21. Moreno, E., Rodrigo, S.G., Bozhevolnyi, S.I., Martin-Moreno, L., and Garcia-Vidal, F.J., "Guiding and focusing of electromagnetic fields with wedge plasmon-polaritons," Phys. Rev. Lett. 100, 023901-1-4 (2008).
22. Boltasseva, A., Volkov, V.S., Nielsen, R.B., Moreno, E., Rodrigo, S.G., and Bozhevolnyi, S.I., "Tri-angular metal wedges for subwavelength plasmon-polariton guiding at telecom wavelengths," Opt. Exp. 16, 5252–5260 (2008).
23. Moreno, E., Garcia-Vidal, F.J., Rodrigo, S.G., Martin-Moreno, L., and Bozhevolnyi, S.I., "Channel plasmon-polaritons: modal shape, dispersion, and losses," Opt. Lett. 31, 3447–3449 (2006).
24. Fromm, D.P., Sundaramurthy, A., Schuck, P.J., Kino, G., and Moerner, W.E., "Gap-dependent opti-cal coupling of single "bowtie" nanoantennas resonant in the visible," Nano Lett. 4, 957–961 (2004).
25. Muhlschlegel, P., Eisler, H.J., Martin, O.J.F., Hecht, B., and Pohl, D.W., "Resonant optical anten-nas," Science 308, 1609 (2005).
26. Cubukcu, E., Kort, E.A., Crozier, K.B., and Capasso, F., "Plasmonic laser antenna," Appl. Phys. Lett. 89 093120 (2006).
27. Rechberger, W., Hohenau, A., Leitner, A., Krenn, J.R., Lamprecht, B., and Aussenegg, F.R., "Optical properties of two interacting gold nanoparticles," Optics Commun. 220, 137 (2003).
28. Farahani, J.N., Eisler, H.-J., Pohl, D.W., Pavius, M., Fluckiger, P., Gasser, P., and Hecht, B., "Bow-tie optical antenna probes for singleemitter scanning near-field optical microscopy," Nanotechnology 18, 125506 (2007).
29. Moskovits, M., "Surface-enhanced Raman spectroscopy: a brief retrospective," J. Raman Spectrosc. 36, 485–496 (2005).
30. Pedersen, R.H., Boltasseva, A., Johansen, D.M., Nielsen, T., Jørgensen, K.B., Leosson, K., Erland, J., and Kristensen, A., "Nanoimprinted reflecting gratings for long-range surface plasmon polari-tons," Microelectr. Eng. 84, 895–898 (2007).
31. Smith, H.I., Hector, S.D., Schattenburg, M.L., and Anderson, E.H., "A new approach to high fidelity e-beam lithography based on an in-situ, global fiducial grid," J. Vac. Sci. Technol. B 9, 2992–2995 (1991).
32. Xia,Y. and Whitesides,G.M., "Soft lithography," Angew. Chemie Intern. Ed. 37, 550–575 (1998).
33. Henzie, J., Lee, M.H., and Odom, T.W., "Multiscale patterning of plasmonic metamaterials," Nature Nanotechn. 2, 549–554 (2007).
34. Drachev, V.P., Chettiar, U.K., Kildishev, A.V., Yuan, H.K., Cai, W., and Shalaev, V.M., "The Ag dielectric function in plasmonic metamaterials," Opt. Exp. 16, 1186–1195 (2007).
35. Fernandez-Cuesta, I., Nielsen, R.B., Boltasseva, A., Borrisé, X., Pérez-Murano, F., and Kristensen, A., "V-groove plasmonic waveguides fabricated by nanoimprint lithography," J. Vac. Sci. Technol. B 25, 2649–2653 (2007).
36. Chai, L. and Klein, J., "Large area, molecularly smooth (0.2 nm rms) gold films for surface forces and other studies," Langmuir 23, 7777–7783 (2007).
37. Nielsen, R.B., Fernandez-Cuesta, I., Boltasseva, A., Volkov, V.S., Bozhevolnyi, S.I., Klukowska, A., and Kristensen, A., "Channel plasmon polariton propagation in nano-imprinted V-groove waveguides," in submission (2008).

38. Yatsuia, T., Kourogi, M., and Ohtsu, M., "Plasmon waveguide for optical far/near-field conversion," Appl. Phys. Lett. 79, 4583–4585 (2001).
39. Boisen, A., Hansen, O., and Bouwstra, S., "AFM probes with directly fabricated tips," J. Micromech. Microeng. 6, 58–62 (1996).
40. Bilenberg, B., Jacobsen, S., Pastore, C., Nielsen, T., Enghoff, S.R., Jeppesen, C., Larsen, A.V., and Kristensen, A., "Technology for fabrication of nanostructures by standard cleanroom processing and nanoimprint lithography," Jpn. J. Appl. Phys. 44, 5606-1-8 (2005).
41. Fang, N., Lee, H., and Zhang, X., "Sub-diffraction-limited optical imaging with a silver superlens," Science 308, 534–537 (2005).
42. Liu, Z., Boltasseva, A., Pedersen, R.H., Bakker, R., Kildishev, A.V., Drachev, V.P., and Shalaev, V.M., "Plasmonic nanoantenna arrays for the visible," Metamaterials 2, 45–51 (2008).
43. DeVries, G.A., Brunnbauer, M., Hu, Y., Jackson, A.M., Long, B., Neltner, B.T., Uzun, O., Wunsch, B.H., and Stellacci, F., "Divalent Metal Nanoparticles," Science 315, 358–361 (2008).
44. Yuan, H.K., Chettiar, U.K., Cai, W., Kildishev, A.V., Boltasseva, A., Drachev, V.P., and Shalaev, V.M., "A negative permeability material at red light," Opt. Exp. 15, 1076–1083 (2007).

# Line Source Excitation of an Array of Circular Metamaterial Cylinders: Boundary Value Solution and Applications

**Bassem H. Henin[1], Atef Z. Elsherbeni[1], Mohamed H. Al Sharkawy[2], and Fan Yang[1]**

[1]The Center of Applied Electromagnetic Systems Research (CASER), Department of Electrical Engineering, The University of Mississippi, University, MS 38677, USA
[2]Arab Academy for Science and Technology and Maritime Transport, College of Engineering and Technology, Alexandria, Egypt

**Abstract** A rigorous semi-analytical solution for electromagnetic scattering from an array of parallel circular cylinders of arbitrary radii and positions due to a line source excitation is developed. The cylinders can be any of three materials: metamaterial, dielectric, perfect electric conductor or a combination. Two different applications are presented here; the use of the characteristics of metamaterial to enhance the performance of corner reflector antennas, and the creation of a plane wave in the near field from an array of conducting cylinders excited by a line source.

## 1 Introduction

The analyses of plane wave scattering from an array of parallel circular cross-section cylinders can be used to study the radar cross-section of two-dimensional scattering object that can be constructed from an array of parallel circular cylinders [1–4]. The scattering of an obliquely incident plane wave on an array of parallel-coated circular cylinders is considered for TMz polarization in [5]. The scattering from an array of cylinders due to an electric line source excitation is important to study the radiation characteristics of an antenna. This paper will present a brief summary of this technique first, followed by a set of numerical validations of the results based on results reported in [6, 7].

Two practical applications are to be presented using the developed formulation. The first is the enhancement of a two dimensional reflector antenna. Metamaterial cylinders are placed in strategic positions adjacent to the reflector surface to increase the strength of the field at the feed/receiver element in the receiving antenna mode, and to enhance the scattered far field in the transmitting antenna mode.

S. Zouhdi et al. (eds.), *Metamaterials and Plasmonics: Fundamentals, Modelling, Applications*,

The second application is related to the creation of a plane wave region over a prescribed area for antenna measurement applications using an array of conducting cylinders. The size and position of the cylinders are to be optimized for controlling the amplitude and phase variation across the antennae under test [8]. The genetic algorithm (GA) [9–12] is used here to optimize the array configuration.

## 2 Formulation

The formulation is based on the scattering from an array of $M$ cylinders parallel to each other and to the $z$-axis of a global coordinate system ($\rho$, $\phi$, $z$) due to electric line source excitation. The incident electric and magnetic fields from an electric line source are expressed in the global cylindrical coordinate system ($\rho$, $\phi$, $z$), for $e^{j\omega t}$ time dependence as

$$E_z^{inc}(\rho,\phi) = \frac{-\omega\mu I_0}{4}\sum_{n=-\infty}^{\infty} e^{jn(\phi-\phi_0)}\begin{Bmatrix} J_n(k\rho)H_n^{(2)}(k\rho_0) & \rho<\rho_0 \\ J_n(k\rho_0)H_n^{(2)}(k\rho) & \rho>\rho_0 \end{Bmatrix} \tag{1}$$

$$H_z^{inc}(\rho,\phi) = 0. \tag{2}$$

In terms of the cylindrical coordinates of the $i$th cylinder, whose center is located at $(\rho_i', \phi_i')$ as shown in Fig. 1, the incident electric field can be expressed as:

$$E_z^{inc}(\rho_i,\phi_i) = \frac{-\omega\mu I_0}{4}\sum_{n=-\infty}^{\infty} e^{jn(\phi_i-\phi_{0i})}\begin{Bmatrix} J_n(k\rho_i)H_n^{(2)}(k\rho_{0i}) & \rho<\rho_{0i} \\ J_n(k\rho_{0i})H_n^{(2)}(k\rho_i) & \rho>\rho_{0i} \end{Bmatrix} \tag{3}$$

Where the parameter $k$ is the free space wave number, ($\rho_{0i}$, $\phi_{0i}$) is the position of the line source relative to the coordinate system of cylinder "$i$", $J_n(\xi)$ is the Bessel function of order $n$ and argument $\xi$, and the $H_n^{(2)}(\xi)$ is the Hankel function of the second type of order $n$ and argument $\xi$.

The resulting $z$ component of the scattered electric field from the $i$th cylinder and the transmitted $z$ component of the field inside the cylinder material can be expressed, respectively, as

$$E_z^s(\rho_i,\phi_i) = \frac{-\omega\mu I_0}{4}\sum_{n=-\infty}^{\infty} A_{in} H_n^{(2)}(k\rho_i)e^{jn\phi_i} \tag{4}$$

$$E_z^d\left(\rho_i,\phi_i\right)=\frac{-\omega\mu I_0}{4}\sum_{n=-\infty}^{\infty}B_{in}J_n\left(k_d\rho_i\right)e^{jn\phi_i}. \tag{5}$$

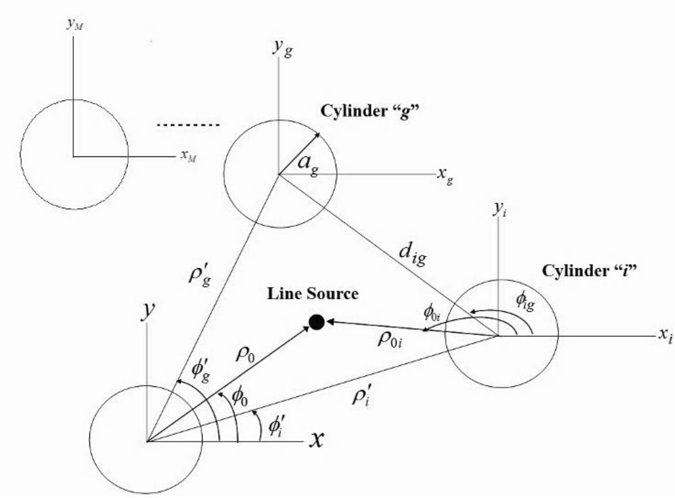


Fig. 1 The problem configuration.

The $\phi$ components of incident, scattered, and inside the cylinder magnetic field can be expressed based on Maxwell's equations as:

$$H_\phi^{inc}(\rho_i,\phi_i)=\frac{jI_0k}{4}\sum_{n=-\infty}^{\infty}e^{jn(\phi_i-\phi_{0i})}\begin{Bmatrix}J'_n\left(k\rho_i\right)H_n^{(2)}\left(k\rho_{0i}\right) & \rho<\rho_{0i}\\ J_n\left(k\rho_{0i}\right)H_n^{(2)'}\left(k\rho_i\right) & \rho>\rho_{0i}\end{Bmatrix} \tag{6}$$

$$H_\phi^s(\rho_i,\phi_i)=\frac{jI_0k}{4}\sum_{n=-\infty}^{\infty}A_{in}H_n^{(2)'}\left(k\rho_i\right)e^{jn\phi_i} \tag{7}$$

$$H_\phi^d\left(\rho_i,\phi_i\right)=\frac{jI_0k_d}{4}\sum_{n=-\infty}^{\infty}B_{in}J'_n\left(k_d\rho_i\right)e^{jn\phi_i}. \tag{8}$$

The expressions in Eqs. (4) and (7) indicate that both the electric and magnetic field components are based on the local coordinates ($\rho_i$ , $\phi_i$ , $z$) of cylinder "$i$". However, the interaction between the $M$ cylinders in terms of multiple scattered fields requires a representation of the scattered field from one cylinder in terms of the local coordinates of another as shown in [13]. Therefore, the additional theorem of Bessel and Hankel functions are used to transfer the scattered field components from one set of coordinates to another. As an example the scattered fields from the $g$th cylinder in terms of the $i$th cylinder coordinates are

$$E^{s}_{z_g}\left(\rho_i,\phi_i\right) = -\frac{\omega\mu I_0}{4}\sum_{n=-\infty}^{\infty} A_{gn} H^{(2)}_{n}\left(k\rho_g\right) e^{jn\phi_g} = -\frac{\omega\mu I_0}{4}\sum_{n=-\infty}^{\infty} A_{gn}\sum_{m=-\infty}^{\infty} J_m\left(k\rho_i\right) H^{(2)}_{m-n}\left(kd_{ig}\right) e^{jm\phi_i} e^{-j(m-n)\phi_{ig}} \tag{9}$$

$$H^{s}_{\phi_g}(\rho_i,\phi_i) = \frac{1}{j\omega\mu}\frac{\partial E^{s}_{z_g}}{\partial\rho_i} = \frac{jI_0 k}{4}\sum_{n=-\infty}^{\infty} A_{gn}\sum_{m=-\infty}^{\infty} J'_m\left(k\rho_i\right) H^{(2)}_{m-n}\left(kd_{ig}\right) e^{jm\phi_i} e^{-j(m-n)\phi_{ig}} \tag{10}$$

The solution of the unknown coefficients $A_{in}$ and $B_{in}$ can be obtained by applying the appropriate boundary conditions on the surface of all cylinders. For example the boundary conditions on the surface of the $i$th cylinder are given by:

$$E^{inc}_{z_i} + \sum_{g=1}^{M} E^{s}_{z_g} = E^{d}_{z_i},\ H^{inc}_{\phi_i} + \sum_{g=1}^{M} H^{s}_{\phi_g} = H^{d}_{\phi_i}. \tag{11}$$

After some mathematical manipulations and the application of the boundary conditions on the surfaces of all $M$ cylinders one obtains

$$V^{l}_{i} = \sum_{g=1}^{M}\sum_{n=-\infty}^{\infty} A_{gn} S^{ln}_{ig} \tag{12}$$

Where

$$V^{l}_{i} = e^{-jl\phi_{0i}} H^{(2)}_{l}\left(k\rho_{0i}\right), \tag{13}$$

$$S^{ln}_{ig} = \begin{cases} 0 & i = g\ ,\ l \neq n \\ \dfrac{\dfrac{k}{k_d} H^{(2)\prime}_{l}\left(ka_i\right) J_l\left(k_d a_i\right) - H^{(2)}_{l}\left(ka_i\right) J'_l\left(k_d a_i\right)}{J_l\left(ka_i\right) J'_l\left(k_d a_i\right) - \dfrac{k}{k_d} J'_l\left(ka_i\right) J_l\left(k_d a_i\right)} & i = g\ ,\ l = n \\ -H^{(2)}_{l-n}\left(kd_{ig}\right) e^{-j(l-n)\phi_{ig}} & i \neq g \end{cases} \tag{14}$$

while the integers $n$, $l$ = 0, ±1, ±2,… …, $\pm N_i$ and $i$, $g$ = 0, 1, 2, ……, $M$. Theoretically, $N_i$ is an integer which is equal to infinity; however, it is related to the radius "$a_i$" of cylinder "$i$", and type of the $i$th cylinder by the relation $N_i \approx (1 + 2k_i a_i)$. Equation (12) then can be represented in a matrix form such that:

$$[V]=[S][A]. \tag{15}$$

The solution of the above truncated matrix equation yields the unknown scattering coefficients $A_{in}$.

For the case of normal incident $TM_z$ plane wave, one can easily express the field components be applying the same procedure used to derive the fields from a line source illumination, where the z component of the scattered field and the transmitted z component of the field inside the cylinder material have the same form as in Eqs. (4) and (5). The difference is in Eq. (13), such that

$$V_i^l = e^{-jl\phi_0} j^l e^{jk_0\rho_i' \cos(\phi_i'-\phi_0)} \tag{16}$$

where $\phi_0$ is the plane wave incident angle with respect to the negative $x$ axis. Therefore the numerical simulation of normal incident $TM_z$ plane wave can be easily obtained from the line source simulation.

The scattering of an obliquely incident plane wave on an array of parallel circular cylinders is considered for both $TM_z$ and $TE_z$ polarization in [4]. The case of coated cylinders was discussed in [5]. In this work, we consider only double negative (DNG) metamaterial with negative permittivity and permeability [14]. To show the effect of metamaterial, the wave number and the intrinsic impedance for the cylinder "$i$" can be expressed as

$$k_i = k_0 n_{ri} \qquad \text{and} \qquad \eta_i = \eta_0\sqrt{\mu_{ri}/\varepsilon_{ri}};$$
$$n_{ri} = \sqrt{\mu_{ri}\varepsilon_{ri}} \quad \text{dielectric,} \quad n_{ri} = -\sqrt{\mu_{ri}\varepsilon_{ri}} \quad \text{metematerial.} \tag{17}$$

## 3 Validation of the Numerical Results

In order to prove the validity of the presented formulation, the total far electric field of a conducting cylinder is calculated at 300 MHz using a single and multiple cylinders simulations. The radius of the cylinder is a = 5λ and the position of the line source is $\rho_0$ = 5.25λ and $\phi_0$ = 0. The results generated using the developed formulation as shown in Fig. 2, show a complete agreement with those given in Figs. 11–18 of [6]. In the multiple cylinders simulations, the scattered field from one conducting cylinder is expected to be the same as that of an array of cylinders having the same outer shape. In Fig. 3, 28 non-intersected conducting cylinders of radius 0.02λ are used to simulate a conducting cylinder of radius 0.2λ.

In order to prove the accuracy of the technique in the case of metamaterial cylinders, Fig. 4 shows the near field distribution of a cylinder of radius 2λ excited by an electric line source located at $\rho_0$ = 3λ and $\phi_0$ = 0. Figure 4a shows the case of a dielectric cylinder with $\varepsilon_r = 2$, and Fig. 4b shows the case of a metamaterial cylinder with $\varepsilon_r = -2$, and $\mu_r = -1$. The results show a complete agreement with the corresponding results presented in [7].

## 4 Enhancement of Corner Reflector Performance

In this section a 90° corner reflector antenna of arm length 1.2λ is simulated by 11 conducting cylinders each having radius 0.1λ. To show the effect of metamaterial loading in capturing the incident electric field by the antenna receiving element, two metamaterial cylinders of $\varepsilon_r = -5$ and $\mu_r = -1$ are added in front of the reflector at the middle of each arm as shown in Fig. 5. Figures 6–7 show the enhancement in the magnitude of the $E_z$ component in front of the reflector due to the presence of the metamaterial cylinders in comparison with the unloaded corner reflector. For normal incidence, Fig. 6 represents the case of $\phi_I = 0$, while Fig. 7 represents the case of $\phi_I = 30$.

To further illustrate the radiation characteristics enhancement of corner reflectors, an electric line source is used to excite the antenna. The electric line source is added in front of the reflector at a distance S (the focal point) as shown in Fig. 8. The value of S was chosen to match the position of the focal point predicted from the results shown in Fig. 6. Figure 9a shows the near field distribution for a corner reflector excited by a line source at a distance S = 0.6λ, while Fig. 9b shows the case of corner reflector loaded with metamaterial cylinders excited by a line source at a distance S = 0.4λ. Figure 10 shows the scattered far field for both cases where a large enhancement of about 10 dB in the forward direction is observed.

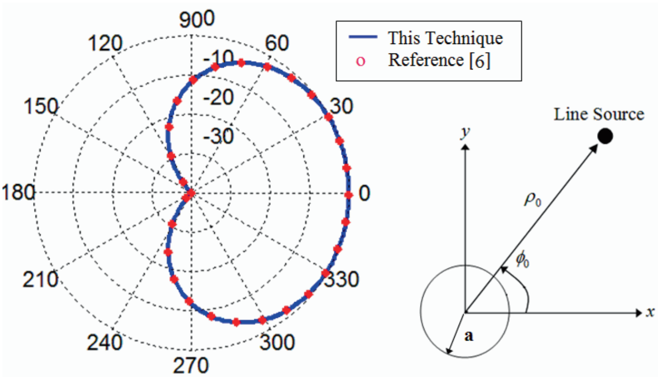


**Fig. 2** Total $E_z$ far field of a conducting cylinder of a radius a = 5λ excited by a line source at $\rho_0$ = 5.25λ and $\phi_0 = 0$.

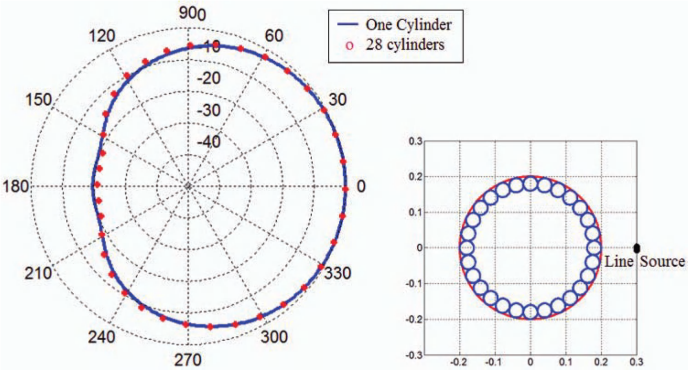


**Fig. 3** Total $E_z$ far field of a conducting cylinder of a radius a = 0.2λ simulated by 28 conducting cylinders each of a radius a = 0.02λ excited by a line source at $\rho_0$ = 0.3λ and $\phi_0$ = 0.

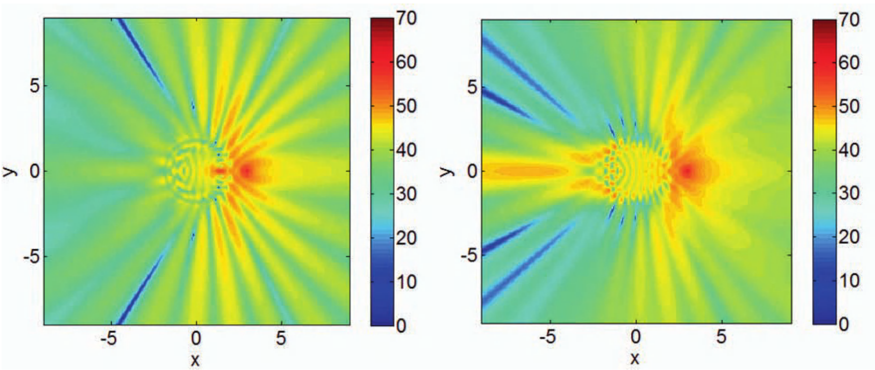

(a) (b)

**Fig. 4** Total $E_z$ far field of a cylinder of a radius a = 2λ excited by a line source at $\rho_0$ = 3λ and $\phi_0$ = 0. (**a**) Dielectric cylinder of $\varepsilon_r$ = 2, (**b**) Metamaterial cylinder of $\varepsilon_r$ = −2 and $\mu_r$ = −1.

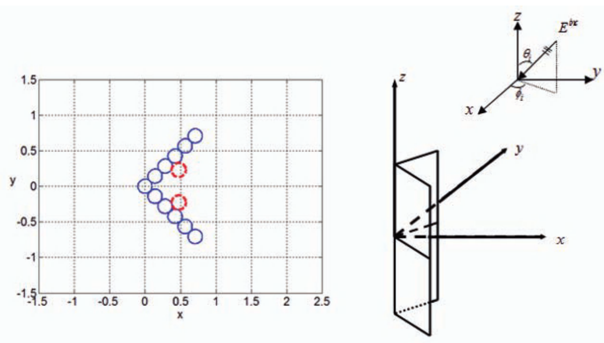

**Fig. 5** The configuration of a 90° corner reflector antenna excited by a plane wave.

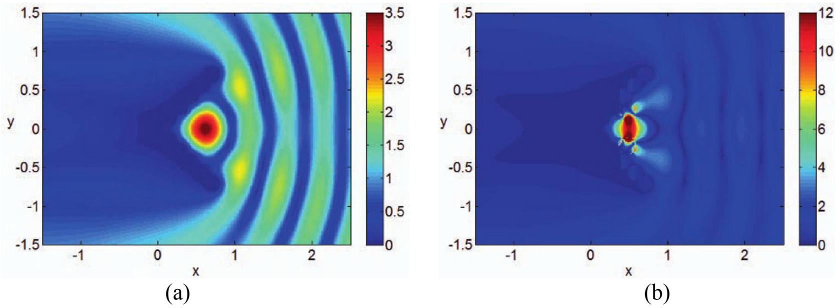

Fig. 6 The $E_z$ near field distribution of a corner reflector excited by a plane wave incident at $\theta_I = 90$ and $\phi_I = 0$. (**a**) Conducting reflector, (**b**) Conducting reflector loaded with two metamaterial cylinders.

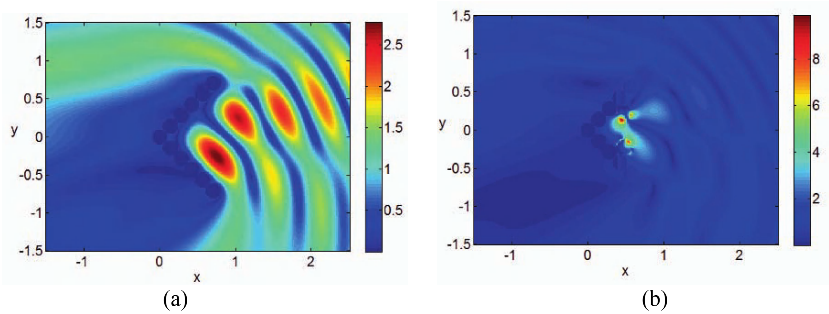

Fig. 7 The $E_z$ near field distribution of a corner reflector excited by a plane wave incident at $\theta_I = 90$ and $\phi_I = 30$. (**a**) Conducting reflector, (**b**) Conducting reflector loaded with two metamaterial cylinders.

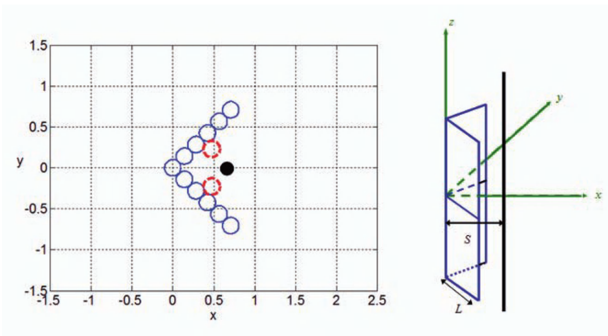

**Fig. 8** The configuration of a 90° corner reflector antenna excited by a line source.

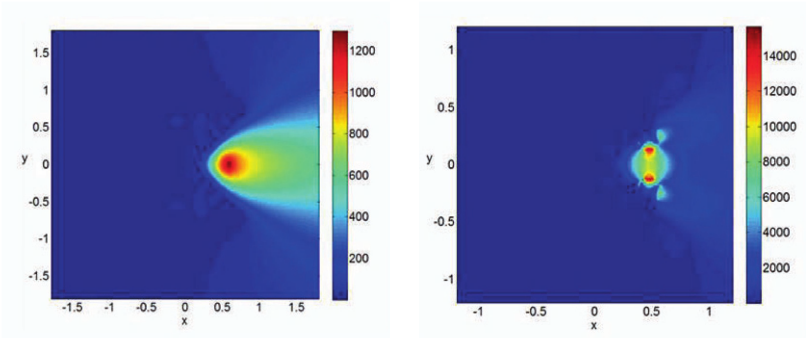


(a) (b)

**Fig. 9** The $E_z$ near field distribution of a corner reflector excited by an electric line source (**a**) Conducting reflector with S = 0.6λ, (**b**) Conducting reflector loaded with two metamaterial cylinders with S = 0.4λ.

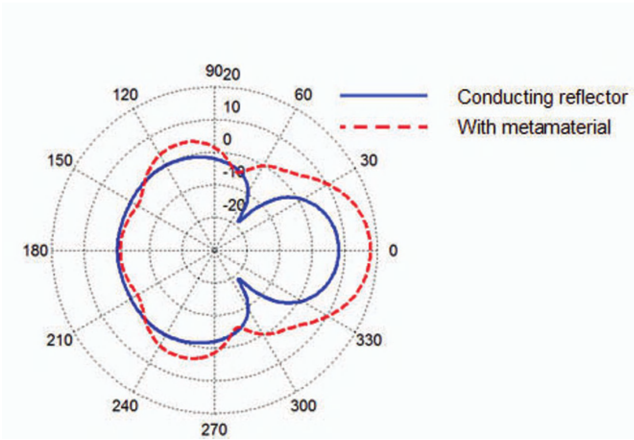


**Fig. 10** The scattered far field of a corner reflector excited by an electric line source.

## 5 Generation of a Plane Wave in the Near Field of a Line Source

Creating a plane wave around an antenna is very important for accurate antenna measurements. The phase and amplitude variations through the antenna under test (AUT) must be within specified tolerances. The IEEE standard for non-low sidelobe antennas requires the separation distance R between the transmitting antenna and the AUT to be [8]

$$R_{ff} = \frac{2D^2}{\lambda} \tag{18}$$

for a maximum phase error of $\pi/8$, where $\lambda$ is the wavelength and D is the maximum dimension of the antenna. An antenna of maximum dimension of $10\lambda$ requires the separation of the transmit antenna to be $R_{ff} = 200\lambda$. Since it is impractical to go far away from the transmit antenna to satisfy that, therefore other methods are needed to approximate a plane wave in the near field of the AUT. One possibility is to build an array of radiating elements that can project a plane wave at a prescribed distance [11–12]. Another method is to design an array of line sources that creates an approximate plane wave over a prescribed area. A new method to generate a plane wave in the near field using only one line source is to place an array of cylinders in front of the line source. The positions, spacing, and diameters of these cylinders are to be optimized to minimize the amplitude and phase variation at a certain prescribed plane wave area.

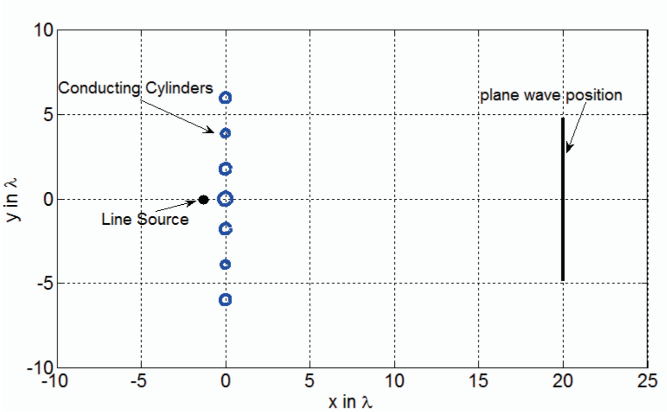


**Fig. 11** The size and position of the optimized array of seven conducting cylinders.

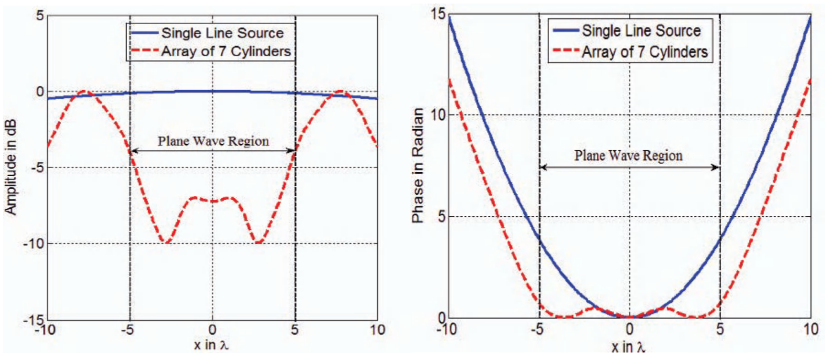


**Fig. 12** (**a**) Field amplitude, (**b**) Field phase of an optimized seven element array of conducting cylinders at a distance of $20\lambda$.

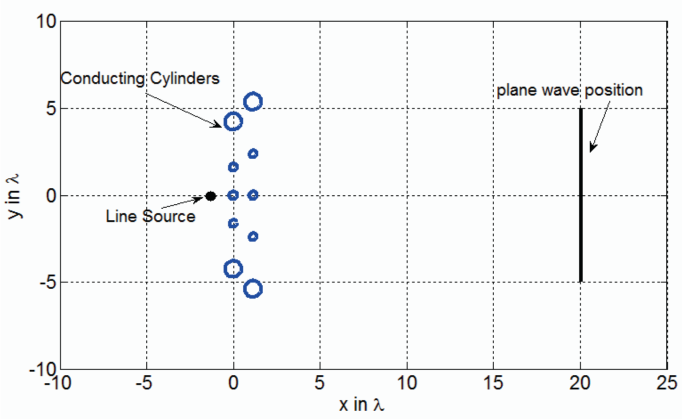


**Fig. 13** The size and position of the optimized array of ten conducting cylinders.

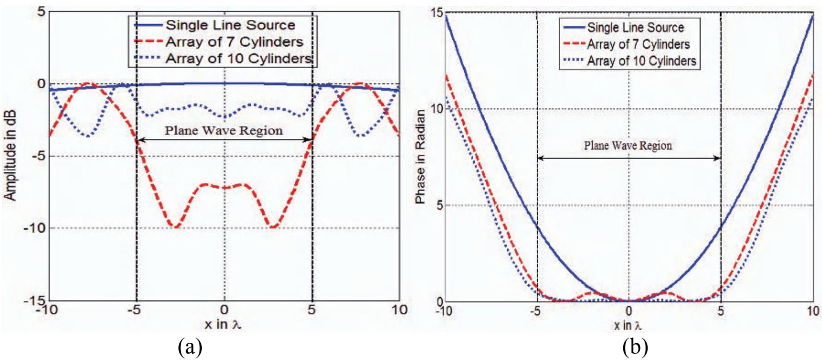


**Fig. 14** (**a**) Field amplitude, (**b**) Field phase of an optimized ten element array of conducting cylinders at a distance of 20λ.

Figure 11 shows an array of seven conducting cylinders. The cylinders are parallel to the $z$ axis, and the centers of all the cylinders are on the $y$ axis. The line source is placed on the negative $x$ axis at a distance λ from the cylinders. Genetic algorithm optimization is used to find the optimum diameter and position of the cylinders to construct a plane wave of width 10λ at a distance 20λ from the cylinders. The goal of the optimization is to get minimum variation in the amplitude and phase of the electric field in the specified positions. The optimized diameter and position for each cylinder relative to the line source position are shown in Fig. 11. Figure 12 shows the optimized amplitude and phase of the electric field relative to the amplitude and phase of a single line source. It is clear that the single line source field has less amplitude variation at the AUT than that of the array of cylinders, while the uniform array has less phase variation than the single line source.

To get a better plane wave representation, more degrees of freedom are needed for the optimization. Figure 13 shows an array of ten conducting cylinders. The cylinders are parallel to the *z* axis, and the centers of the cylinders are on the *y* axis and another line parallel to the *y* axis. The line source is placed on the negative *x* axis at a distance λ from the *y* axis. The optimized diameter and position of the cylinders relative to line source are shown also in Fig. 13. Figure 14 shows the optimized amplitude and phase of the electric field. The amplitude variation in this case is less than 1 dB, and the phase variation is smaller than π/8.

## 6 Conclusions

The analysis of the scattering from an array of parallel circular cross-section cylinders due to an electric line source is summarized. This solution is verified for metamaterial cylinders, and can be used to study electromagnetic interaction with two-dimensional scattering object that can be constructed from an array of parallel dielectric, conducting or metamaterial circular cylinders. The effect of metamaterial in enhancing the performance of a corner reflector antenna was studied. Significant enhancement of focused field in front of corner reflector antennas, and enchantment in the scattered far field are achieved. An array of conducting cylinders was used to generate a plane wave in the near field of a line source. A good approximation of a plane wave was achieved with less than 1 dB magnitude variation and less than π/8 phase variation.

## References

1. Elsherbeni, A.Z., Hamid, M.: Scattering by parallel conducting circular cylinders. IEEE Trans. Antenn. Propag. **35**, 355–358 (1987)
2. Elsherbeni, A.Z., Kishk, A.: Modeling of cylindrical objects by circular cylinders. IEEE Trans. Antenn. Propag. **40**, 96–99 (1992)
3. Li, C., Shen, Z.: Electromagnetic scattering by a conducting cylinder coated with metamaterials. PIER **42**, 91–105 (2003)
4. Henin, B.H., Elsherbeni, A.Z., Al Sharkawy, M.H.: Oblique incidence plane wave scattering from an array of circular dielectric cylinders. PIER **68**, 261–279 (2007)
5. Henin, B.H., Al Sharkawy, M.H., Elsherbeni, A.Z.: Scattering of obliquely incident plane wave by an array of parallel concentric metamaterial cylinders. PIER **77**, 285–307 (2007)
6. Balanis, C.A.: Advanced Engineering Electromagnetics. Wiley, New York (1989)
7. Arslanagic, S., Breinbjerg, O.: Electric-line-source illumination of a circular cylinder of lossless double-negative material: an investigation of near field, directivity, and radiation resistance. IEEE Antenn. Propag. Mag. **48**, 38–54 (2006)
8. IEEE Standard Definitions of Terms for Antennas. IEEE, New York (1993)
9. Haupt, R.L., Haupt, S.E.: Practical Genetic Algorithms. Wiley, New York (1998)
10. Haupt, R.L.: An introduction to genetic algorithms for electromagnetics. IEEE Antenn. Propag. Mag. **37**, 7–15 (1995)

11. Hackson, N.N., Excell, P.S.: Genetic-algorithm optimization of an array for near-field plane wave generation. Appl. Comput. Electromag. Soc. **35**, 61–74 (2000)
12. Haupt, R.L.: Generating a plane wave with a linear array of line sources. IEEE Antenn. Propag. Mag. **51**, 273–278 (2003)
13. Elsherbeni, A.Z.: A comparative study of two-dimensional multiple scattering techniques. Radio Sci. **29**, 1023–1033 (1994)
14 Ziolkowski, R.W., Heyman, E.: Wave propagation in media having negative permittivity and permeability. Phys. Rev. E. **64**, 056625 (2001)

# Analytical Modeling of Surface Waves on High Impedance Surfaces

**Alexander B. Yakovlev**[1], **Olli Luukkonen**[2], **Constantin R. Simovski**[2,3], **Sergei A. Tretyakov**[2], **Simone Paulotto**[4], **Paolo Baccarelli**[4], **and George W. Hanson**[5]

[1]Department of Electrical Engineering, University of Mississippi, University, MS 38677-1848, USA
yakovlev@olemiss.edu
[2]Department of Radio Science and Engineering/SMARAD, TKK Helsinki University of Technology, P.O. Box 3000, FI-02015 TKK, Finland
[3]Physics Department, State University of Information Technologies, Mechanics and Optics, Sablinskaya 14, 197101 St. Petersburg, Russia
[4]Electronic Engineering Department, "SAPIENZA" University of Rome, via Eudossiana 18, 00184, Rome, Italy
[5]Department of Electrical Engineering and Computer Science, University of Wisconsin Milwaukee, Milwaukee, WI 53211, USA

**Abstract** In this paper, analytical modeling of natural modes is proposed for the rapid and accurate analysis of various high impedance surfaces (HIS) composed of dense grids of frequency selective surface (FSS) elements printed on an electrically thin grounded dielectric slab, and on a wire media slab. The dynamic model of the grid is based on the homogenized surface impedance, which is obtained from the full-wave solution in a spectral domain. The homogenization model of mushroom-like HIS structures consists of local model of the wire media slab (based on the epsilon-negative (ENG) approximation) and dynamic model of the grid. This enables one to accurately capture the physics of surface-wave propagation in the resonance band of HIS structures within the limits of homogenization.

## 1 Introduction

In recent years, there has being a growing interest in the area of artificial magnetic conductors (AMC) realized by FSS elements on a thin dielectric slab for their use as high-impedance surface (HIS) substrates for low-profile antennas and hard walls in the TEM waveguides. HIS structures composed of various FSS elements on a grounded dielectric slab have been proposed, including patches with vias

S. Zouhdi et al. (eds.), *Metamaterials and Plasmonics: Fundamentals, Modelling, Applications*,

[1, 2] or without vias [3, 4] in the grounded dielectric slab, printed dipole/slot arrays [5, 6], dipole/slot arrays of different resonant length in order to achieve a multiband response of AMC surfaces [7, 8], and more complicated configurations of unit cells [9]. Also, electromagnetic band-gap (EBG) properties of periodic structures implemented by various FSS elements have been studied. This includes the analysis of surface waves on mushroom-like structures [1, 2], characterization of the modal spectrum on planar periodic patches [10], study of dispersion diagrams of printed dipole/slot arrays [5], transmission line analysis of periodic structures with negative refraction [11], analysis of surface waves on HIS structures based on effective medium models [12], and study of dispersion diagram of modes supported by two-dimensional (2D) periodic printed structures [13, 14], among others.

An alternative approach for the accurate and rapid analysis of resonance characteristics of dense HIS structures (with the grid period much smaller than effective wavelength) has been proposed in [15–19] and summarized in [20]. This dynamic model is based on the full-wave solution of a scattering problem with the averaged impedance boundary condition, and enables one to accurately capture the physics of plane-wave interaction with HIS structures by modeling a single unit cell of a periodic grid. It is based on the homogenization of grid impedance in terms of effective inductance and capacitance.

In this chapter, we present surface-wave analytical models for the analysis of natural modes of various HIS structures composed of dense FSS grids printed on a thin grounded dielectric slab, and on a wire media slab. Dispersion characteristics of natural modes of HIS structures are studied either by considering an impedance surface composed of grid and dielectric slab surface impedances [20] (grid and wire media slab surface impedances for mushroom-like structures [19]), or by implementing a two-sided impedance boundary condition for the grid in the boundary-value problem for the grounded dielectric slab. The discrete spectrum of natural modes of HIS structures without vias consists of proper real (bound) and improper real and complex (leaky) wave solutions. In addition, in mushroom-like HIS structures proper complex (leaky) solutions occur, which are associated with backward radiation [21]. Numerical results are presented for HIS structures with and without vias and compared with those obtained with HFSS [22] and a full-wave numerical approach proposed in [14] for a complete dispersion analysis of natural modes, showing good agreement in the resonance band. In dense HIS structures without vias (with the grid period much smaller than the effective wavelength) no stopband between TM and TE surface-wave modes occurs at low frequencies (in the resonant frequency band where the structure experiences AMC properties). This is in contrast to conventional FSS structures (with the grid period comparable to the effective wavelength), wherein stopbands occur due to Bragg diffraction at resonance frequency. However, in mushroom-like dense HIS structures, a bandgap between proper real (bound) TM and TE surface-wave modes occurs due to the presence of a wire media slab implemented with a capacitive grid. Also, it is observed that within the bandgap a proper complex mode occurs, which can result in backward radiation from mushroom-like HIS structures at low frequencies.

Wire medium is known to exhibit strong spatial dispersion [23]. Even in the cases of electrically thin grounded wire medium slabs the charges accumulate to the tips of the vias, and the spatial dispersion should be taken into account [24–27]. Having said this, it is also possible to suppress the spatial dispersion in the wire medium. One way to do this is to pack the metallic vias densely so that the lattice spacing is extremely small [24]. Depending on the operational frequency regime this might turn out to be close to impossible from the practical point of view, especially for the higher frequency bands. However, there is yet another way to suppress the spatial dispersion in the wire medium, which is intrinsic to most of the high-impedance surface structures. For instance, in the case of the electrically thin mushroom-like HIS the vias are connected on one side to the metallic patches and on the other side to the ground plane. When the metallic patches are considerably larger than the diameter of the metallic pins, the charges will no longer accumulate on the tips of the vias but spread over the metallic patch (see also [20]). In addition, because of the constraints on the thickness of the HIS set by the manufacturing processes and the applications, the HIS are commonly electrically thin. Therefore the phase variation along the vias is minimum. Together these two features of a common HIS (metallic patches and electrically thin slabs) cause the spatial dispersion to be negligible in the HIS structures. In the analytical models that follow, we have neglected the spatial dispersion in the wire medium slabs of HIS and therefore limited the validity of the analytical model to the aforementioned conditions.

## 2 Surface-Wave Analytical Model

In this section, two analytical models for the analysis of natural modes of HIS structures are described. In the first model, the surface waves are studied for propagation along the impedance surface obtained as a parallel connection of grid surface impedance and surface impedance of the grounded dielectric slab or surface impedance of wire media slab in the case of mushroom-like HIS structures. The second model is based on the implementation of a two-sided impedance boundary condition in the boundary-value problem for a grounded dielectric slab. It should be noted that both models result in the same dispersion equations for surface waves on HIS structures without vias. The surface waves on mushroom-like structures are studied based on the dispersion equation of the impedance surface model.

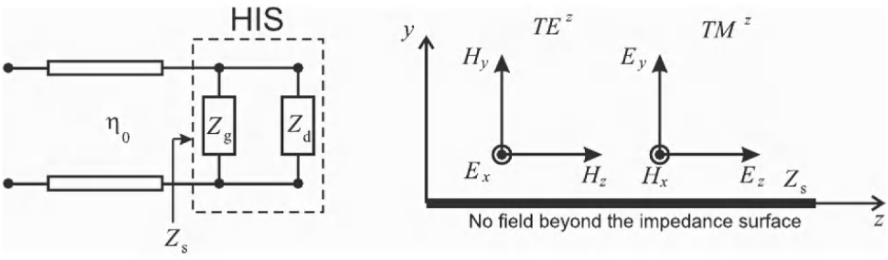


(a) (b)

**Fig. 1** (**a**) Transmission line network analysis of HIS structure characterized by surface impedance $Z_s$ obtained as a parallel connection of grid impedance $Z_g$ and grounded dielectric slab or wire media slab impedance $Z_d$. (**b**) Surface waves propagating along the impedance surface characterized by the surface impedance $Z_s$.

## 2.1 Model 1

A transmission-line network of an HIS structure is shown in Fig. 1a, wherein the surface impedance $Z_s$ is obtained as a parallel connection of the grid impedance $Z_g$ and the grounded dielectric slab or wire media slab impedance $Z_d$. Then, the surface waves associated with an HIS structure can be modeled as waves propagating along the impedance surface with the surface impedance $Z_s$, as shown in Fig. 1b, [20]. $Z_s$ is obtained as follows:

$$Z_s = \frac{Z_g Z_d}{Z_g + Z_d}. \tag{1}$$

The solution of Helmholtz's equations for $H_x$ (TM$^z$-modes) and $E_x$ (TE$^z$-modes) components subject to the impedance boundary condition,

$$\vec{E} = Z_s \hat{y} \times \vec{H} \text{ at } y=0, \tag{2}$$

where for TM$^z$-even surface-wave modes, $E_z = -Z_s^{TM} H_x$, and for TE$^z$-odd surface-wave modes, $E_x = Z_s^{TE} H_z$, results in the following dispersion equations for the propagation constant $k_z$ of TM$^z$ and TE$^z$ modes, respectively:

$$k_z^{TM} = k_0\sqrt{1-\left(\frac{Z_s^{TM}}{\eta_0}\right)^2}, \; k_z^{TE} = k_0\sqrt{1-\left(\frac{\eta_0}{Z_s^{TE}}\right)^2}. \tag{3}$$

Here, $\eta_0$ and $k_0$ are the characteristic impedance and the wave number of free space, respectively.

In the absence of vias, the surface impedance of a thin grounded dielectric slab $Z_d$ in (1) "seen" by the $TM^z$ surface-wave modes is obtained from the surface impedance boundary conditions for thin layers [20]

$$Z_d^{TM}\left(\omega,k_z^{TM}\right)=j\omega\mu_0\frac{\tan\left(k_{yd}^{TM}h\right)}{k_{yd}^{TM}}\left(1-\frac{\left(k_z^{TM}\right)^2}{k_0^2\varepsilon_r}\right),\tag{4}$$

and for $TE^z$ surface-wave modes

$$Z_d^{TE}\left(\omega,k_z^{TE}\right)=j\omega\mu_0\frac{\tan\left(k_{yd}^{TE}h\right)}{k_{yd}^{TE}},\tag{5}$$

where $k_{yd}^{TM(TE)}=\sqrt{k^2-\left(k_z^{TM(TE)}\right)^2}$ is the wave number in the dielectric slab in the normal direction, $k=k_0\sqrt{\varepsilon_r}$, $\omega$ is the angular frequency, $\varepsilon_r$ is the dielectric permittivity of the grounded slab, and $h$ is the slab thickness.

If vias are present, these are taken into account by treating the material slab as a uniaxial wire medium composed of infinitely long wires [19]. The ground plane acts as one of the image planes and the capacitive grid is considered approximately to act as the other image plane. As the period of wires is directly proportional to the period of the HIS, the length of the wires is small compared to the wavelength, and the propagation of surface waves is mainly perpendicular to the wires, a quasi-static model (ENG approximation as a local model) of the wire media connected to metal plates can be used. It should be noted that the physical assumption behind this approximation is that the currents in the wires are nearly uniform over the slab thickness. This assumption is justified for electrically thin slabs because both ends of the wires are connected to metal plates. Therefore, charge cannot accumulate at the wire ends, although, since the wire is electrically short, charge density is approximately zero along the whole wire. Based on the quasi-static approximation the surface impedance of a wire media slab comprising thin perfectly conducting wires is obtained for the $TM^z$ surface-wave modes [20]:

$$Z_d^{TM}\left(\omega,k_z^{TM}\right)=j\omega\mu_0\frac{\tan\left(k_{y,wm}^{TM}h\right)}{k_{y,wm}^{TM}}\frac{k^2-\left(k_z^{TM}\right)^2-k_p^2}{k^2-k_p^2},\tag{6}$$

where $k_{y,wm}^{TM}$ is the wave number in the uniaxial wire medium in the normal direction ($y$-direction),

$$k_{y,wm}^{TM} = \sqrt{\omega^2 \varepsilon_0 \varepsilon_t \mu_0 - \frac{\varepsilon_t}{\varepsilon_n} \left(k_z^{TM}\right)^2}\,, \tag{7}$$

$k_p$ is the plasma wave number (the quasi-static approximation), which depends only on the geometrical parameters of the wire lattice,

$$k_p = \frac{1}{D\sqrt{\dfrac{1}{2\pi} \ln \dfrac{D^2}{4r_0(D-r_0)}}}\,, \tag{8}$$

$k = k_0\sqrt{\varepsilon_r}$ is the wave number in the host medium, $D$ is the period of the wire lattice, $r_0$ is the radius of wires, $\varepsilon_t$ is the relative permittivity of the uniaxial wire medium along the transverse plane ($z$-direction), and $\varepsilon_n$ is the relative permittivity of the uniaxial wire medium normal to the slab ($y$-direction):

$$\varepsilon_n = \varepsilon_t \left(1 - \frac{k_p^2}{k_0^2 \varepsilon_t}\right). \tag{9}$$

In the case when the vias are thin and vertically oriented, the relative permittivity $\varepsilon_t$ equals approximately to the relative permittivity of the host medium, $\varepsilon_r$. In this case the transversal electric field components do not interact with the vias and for the $TE^z$ surface-wave modes expression (5) for the surface impedance of the grounded dielectric slab is still valid.

The expressions for the grid impedance $Z_g$ in (1) will be presented later in the paper for several structures of interest.

## 2.2 Model II

Consider the geometry of a grounded dielectric slab with a periodic planar grid structure positioned at the air-dielectric interface and characterized by the surface impedance $Z_g$ (Fig. 2).

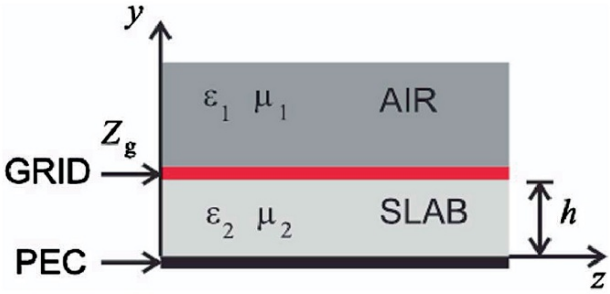


**Fig. 2** Geometry of a grounded dielectric slab with FSS grid on the air-dielectric interface.

By solving Helmholtz's equations in the air and in the dielectric regions for $H_x$ ($TM^z$-modes) and $E_x$ ($TE^z$-modes) components subject to appropriate boundary conditions on the ground plane (at $y = 0$) and infinity, and by implementing a two-sided impedance boundary condition for the grid at the air-dielectric interface,

$$\vec{E}_1 = \vec{E}_2 = Z_g \hat{y} \times \left( \vec{H}_1 - \vec{H}_2 \right) \text{ at } y = h, \tag{10}$$

where for $TM^z$-even surface-wave modes

$$E_{z1} = E_{z2} = -Z_g^{TM} \left( H_{x1} - H_{x2} \right) \text{ at } y = h, \tag{11}$$

and for $TE^z$-odd surface-wave modes

$$E_{x1} = E_{x2} = Z_g^{TE} \left( H_{z1} - H_{z2} \right) \text{ at } y = h, \tag{12}$$

the dispersion equations for $TM^z$-even and $TE^z$-odd modes of the structure depicted in Fig. 2 are obtained:

$$k_{y2} \tanh\left(k_{y2} h\right) = -Z_g^{TM} \frac{j\omega\varepsilon_2 k_{y1}}{j\omega\varepsilon_1 Z_g^{TM} + k_{y1}}, \tag{13}$$

$$\frac{\mu_2}{\mu_1} k_{y1} + k_{y2} \coth\left(k_{y2} h\right) = -\frac{j\omega\mu_2}{Z_g^{TE}}. \tag{14}$$

Here, $k_{yi} = \sqrt{k_z^2 - k_i^2}$, $k_i = \omega\sqrt{\varepsilon_i \mu_i}$, $i = 1, 2$. For HIS structures with the grid positioned on the air-dielectric interface, $\varepsilon_1 = \varepsilon_0$, $\varepsilon_2 = \varepsilon_r \varepsilon_0$, and $\mu_1 = \mu_2 = \mu_0$. The wave number $k_{y1}$ induces branch points in the complex $k_z$- plane at

$k_z = \pm k_1$. Proper modes (above cutoff) reside on the proper Riemann sheet, where $\operatorname{Re}(k_{y1}) > 0$ (the wave dependence is of the form $e^{-k_{y1}y}$), and improper modes (below cutoff) reside on the improper Riemann sheet, where $\operatorname{Re}(k_{y1}) < 0$. Hyperbolic branch cuts separate proper and improper Riemann sheets, defined by

$$\operatorname{Im}(k_z) = \frac{\operatorname{Im}(k_1)\operatorname{Re}(k_1)}{\operatorname{Re}(k_z)}, \quad |\operatorname{Re}(k_z)| < |\operatorname{Re}(k_1)|. \tag{15}$$

It should be noted that the dispersion Eqs. (13) and (14) of Model II can be derived from the Eq. (3) of Model I, by substituting the expressions of dielectric impedance (4) and (5), respectively. Both models can be used for more complicated substrates: for example, wire media metamaterials, or a slab composed of spherical dielectric inclusions (as an example of an isotropic metamaterial). However, Model II gives better physical insight for proper and improper surface-wave solutions, and can be used for the calculation of fields in the slab region to some level of approximation.

Below we present a summary of expressions for the grid impedance $Z_g$ of an array of printed patches and Jerusalem crosses, which are obtained from full-wave solutions via the averaged impedance boundary condition.

### 2.2.1 Array of printed patches

The geometry of an HIS structure composed by the 2D array of printed patches on a grounded dielectric slab is shown in Fig. 3. The expressions of homogenized grid impedance of the patch array on the air-dielectric interface "seen" by the surface waves are obtained by first considering the strip mesh with square holes and then applying the approximate Babinet principle [20], resulting in the capacitive grid impedance of the complimentary structure (i.e. array of patches) [18]:

$$Z_g^{TM}(\omega) = -j\frac{\eta_{eff}}{2\alpha}, \tag{16}$$

$$Z_g^{TE}(\omega, k_z^{TE}) = -j\frac{\eta_{eff}}{2\alpha\left(1 - \frac{1}{2}\left(\frac{k_z^{TE}}{k_{eff}}\right)^2\right)}, \tag{17}$$

where $\eta_{eff} = \eta_0 / \sqrt{\varepsilon_{eff}}$, $\varepsilon_{eff} = (\varepsilon_r + 1)/2$, $k_{eff} = k_0\sqrt{\varepsilon_{eff}}$, and $\alpha$ is the grid parameter of an electrically dense array of ideally conducting strips (with the period much smaller than the effective wavelength),

$$\alpha = \frac{k_{eff} D}{\pi} \ln\left(\csc\left(\frac{\pi w}{2D}\right)\right). \tag{18}$$

Here, $D$ is the period of patch array and $w$ is the gap width, such that $w << D$ [20].

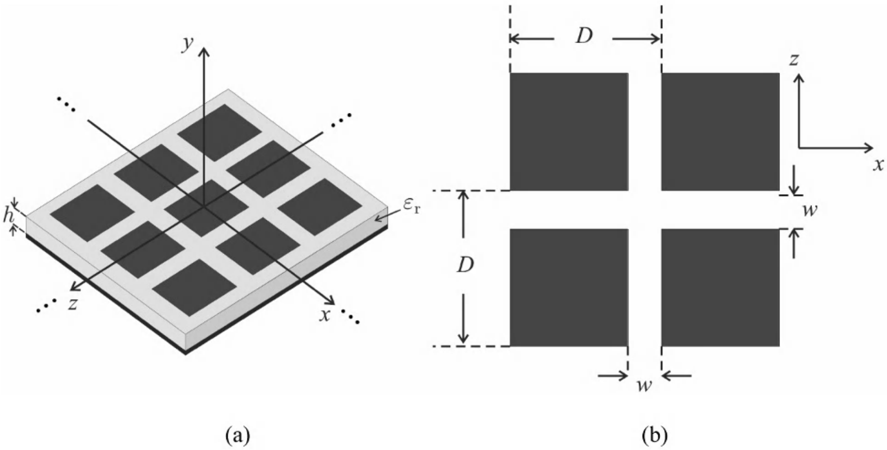


**Fig. 3** HIS structure composed of patch array on a grounded dielectric slab: $D$ = 2 mm, $w$ = 0.2 mm, and $h$ = 1 mm. The relative permittivity of substrate is 10.2.

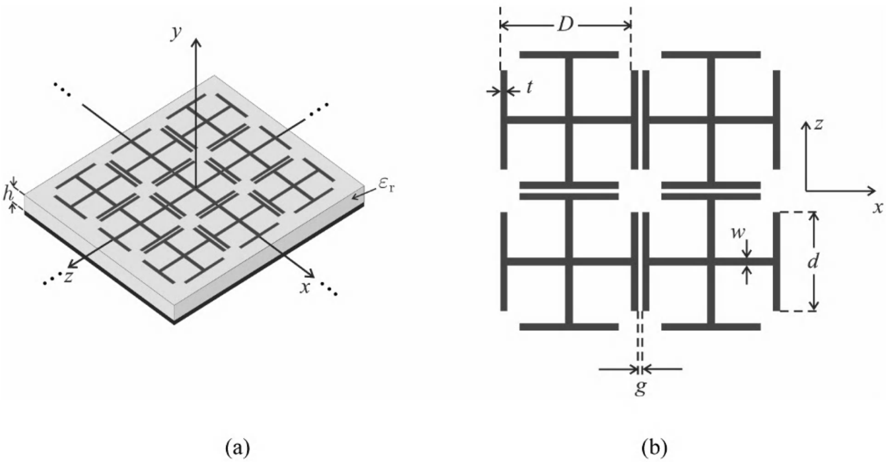


**Fig. 4** Geometry of 2D periodic Jerusalem cross FSS printed on a grounded dielectric slab: $g$ = 0.1 mm, $d$ = 2.8 mm, $t$ = $w$ = 0.2 mm, $D$ = 4 mm, and $h$ = 6 mm. The relative permittivity of substrate is 2.7.

### 2.2.2 Array of printed Jerusalem crosses

The geometry of an HIS structure realized by the 2D periodic printed Jerusalem cross FSS is shown in Fig. 4. The grid impedance of the series resonance grid is obtained in terms of an effective inductance $L_g$ and effective capacitance $C_g$, and for TM$^z$ and TE$^z$ surface-wave propagation is given by

$$Z_g^{TM}\left(\omega, k_z^{TM}\right) = j\omega L_g \left(1 - \left(\frac{k_z^{TM}}{k_{eff}}\right)^2\right) + \frac{1}{j\omega C_g}, \tag{19}$$

$$Z_g^{TE}\left(\omega\right) = j\omega L_g + \frac{1}{j\omega C_g}, \tag{20}$$

where the inductance is that of the strip grid of period $D$ and the strip width $w$ ($w << D$) [20],

$$L_g = \frac{\eta_{eff}\alpha}{2\omega}. \tag{21}$$

Here, $\alpha$ is the grid parameter given by (18), and $\eta_{eff}$, $\varepsilon_{eff}$, $k_{eff}$ are the parameters of the effective medium described above.

The effective capacitance between Jerusalem crosses was derived in [28] in the solution of scattering from a thin capacitive diaphragm in rectangular waveguide,

$$C_g = \frac{\varepsilon_0 \varepsilon_r d}{\pi}\left(\ln \csc\left(\frac{\pi g}{2D}\right) + F\right), \tag{22}$$

where $F = Qu^2 / \left[1 + Q\left(1-u\right)^2\right] + \left[du\left(3u-2\right)/4\lambda\right]^2$, $Q = \left[1 - \left(d/\lambda\right)^2\right]^{1/2}$, $\lambda = 2\pi / k$, $u = \cos^2\left(\pi g / 2d\right)$.

## 3 Numerical Results and Discussions

The analysis of surface waves has been performed for several HIS structures. Below we present the numerical results for arrays of patches and Jerusalem crosses printed on a grounded dielectric slab and the results for mushroom-like HIS structures composed of these grids (patches and Jerusalem crosses) and a wire media slab.

In the first example of HIS composed of a patch array on a grounded slab (with the geometry and dimensions shown in Fig. 3), the dispersion behavior of TM$_0$ and TE$_1$ surface-wave modes, including proper real and improper real and complex solutions, is shown in Fig. 5, and compared with the full-wave solution obtained both by the integral equation method as in [14] and by HFSS [22]. A good agreement between the analytical and full-wave results is obtained at low frequencies within the limits of homogenization of HIS structures. Some disagreement is noticed for improper (real and complex) solutions and for proper solutions at higher frequencies. It can be also observed that in dense HIS structures composed of printed patches (with grid period much smaller than effective wave-ength) no stopband occurs between TM and TE surface-wave modes at low freuencies, wherein the structure experiences AMC properties.

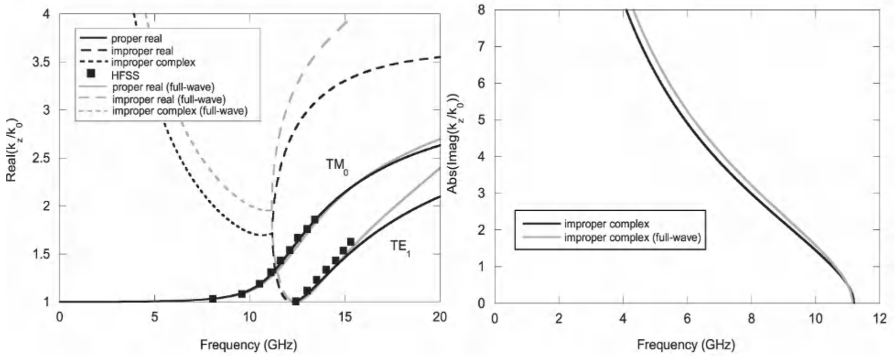


(a) (b)

**Fig. 5** Dispersion behavior of proper real (bound) and improper real and complex solutions of patch HIS structure; (**a**) real part of the normalized propagation constant and (**b**) absolute value of the imaginary part of the normalized propagation constant. The analytical results are compared with the full-wave results of [14] and HFSS [22].

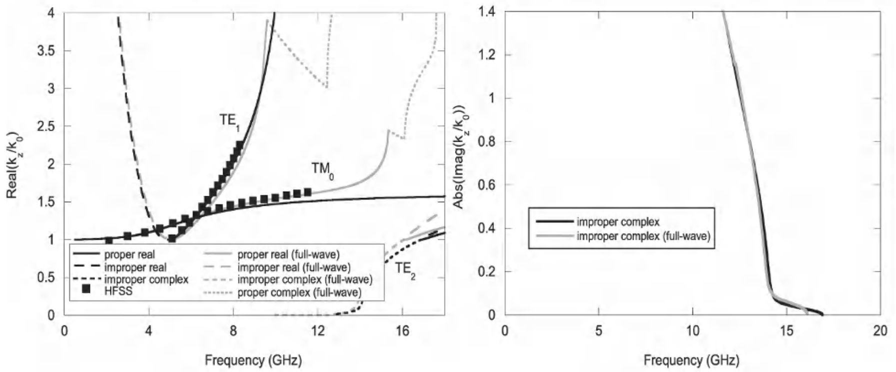


(a) (b)

**Fig. 6** Dispersion behavior of proper real (bound) and improper real and complex solutions of Jerusalem cross HIS structure; (**a**) real part of the normalized propagation constant and (**b**) absolute value of the imaginary part of the normalized propagation constant. The analytical results are compared with the full-wave results of [14] and HFSS [22].

In the second example of a HIS structure realized by the array of Jerusalem crosses printed on a grounded dielectric slab (with the geometry and dimensions shown in Fig. 4), the results of analytical modeling are demonstrated in Fig. 6 for the dispersion behavior of $TM_0$, $TE_1$, and $TE_3$ surface-wave modes (proper and improper real and complex solutions), showing a good agreement with the full-wave results of [14] and HFSS [22].

It can be seen that the physics of modal behavior of proper and improper solutions is well captured by the analytical model. Furthermore, good agreement is also observed for the improper complex (leaky) solution of the $TE_3$ mode, associated with forward radiation when excited by finite sources. However, the analytical model does not predict correctly the bandstop behavior at higher frequencies associated with Bragg diffraction in the first Brillouin zone (stopbands of $TM_0$ and $TE_1$ modes, indicated as proper complex solutions in Fig. 6a, [14]).

In the third example, the surface-wave behavior is studied in the mushroom structure composed of patch array and wire media slab as shown in Fig. 7. The dispersion behavior of surface waves obtained by the homogenization model (ENG approximation for the wire media slab and dynamic model for the patch array grid) are compared with those generated by HFSS for proper real. Good agreement is found, as shown in Fig. 8. A bandgap between proper real (bound) TM and TE surface-wave modes occurs due to the interaction of the wire media and the capacitive grid of patches, resulting in backward propagation of $TM_0$ mode. In addition, a proper complex (leaky) wave propagates within the bandgap up to the plasma frequency of 12.27 GHz. This kind of proper leaky wave can be associated with backward radiation, when excited by finite sources, if low values of the imaginary part of the propagation constant are obtained. It should be noted that close to the plasma frequency the ENG approximation fails, resulting in fictitious higher-order modes, which have to be discarded from the solution (not shown here).

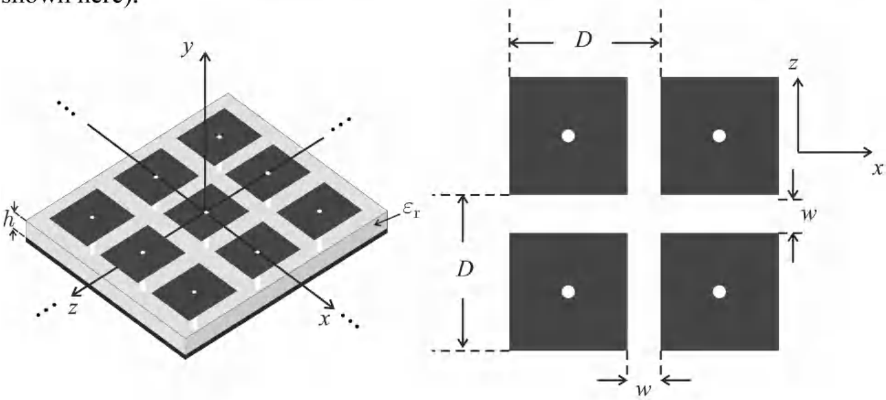


(a) (b)

**Fig. 7** Mushroom-like HIS structure composed of patch array on a wire media slab: $D$ = 2 mm, $w$ = 0.2 mm, $h$ = 1 mm, and $r$ = 0.05 mm. The relative permittivity of substrate is 10.2.

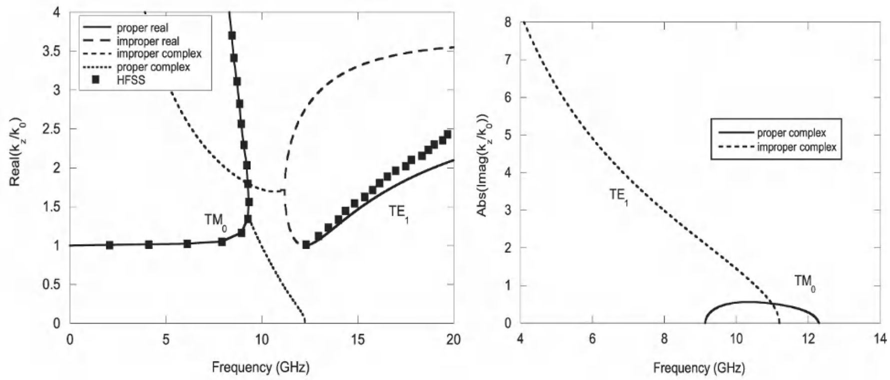


(a) (b)

**Fig. 8** Dispersion behavior of proper real (bound), proper complex (leaky), improper real, and improper complex (leaky) solutions of mushroom-like HIS structure composed of patch array and wire media slab; (**a**) real part of the normalized propagation constant and (**b**) absolute value of the imaginary part of the normalized propagation constant. The analytical results are compared with HFSS [22].

An example of mushroom-like HIS structure realized by a 2D periodic Jerusalem cross FSS grid printed on a wire media slab (with the geometry shown in Fig. 9) has been considered for the analysis of surface-wave propagation. The physics of surface-wave behavior on this structure is similar to that of the mushroom-like patch HIS. The dispersion behavior of proper real TM and TE surface-wave

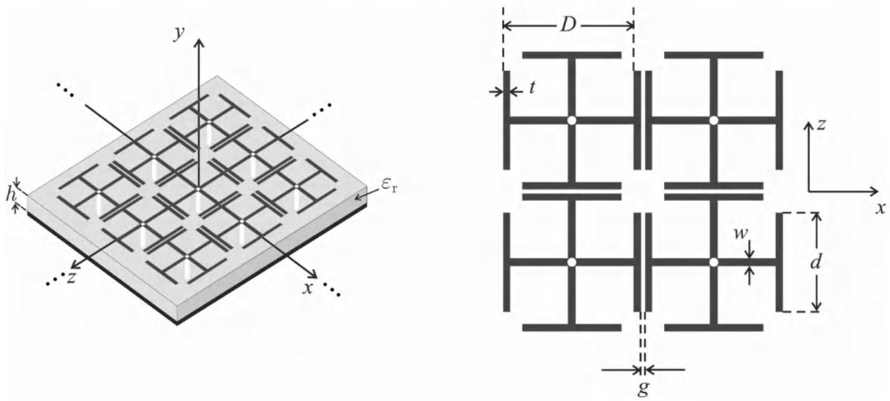


(a) (b)

**Fig. 9** Geometry of mushroom-like HIS structure composed of 2D periodic Jerusalem cross FSS printed on a wire media slab: $g = 0.1$ mm, $d = 2.8$ mm, $t = w = 0.2$ mm, $D = 4$ mm, $h = 6$ mm, and $r_0 = 0.05$ mm. The relative permittivity of substrate is 2.7.

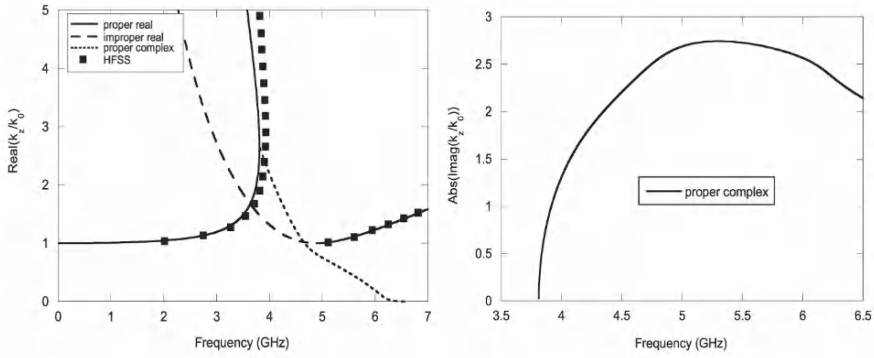


(a) (b)

**Fig. 10** Dispersion behavior of proper real (bound), proper complex (leaky), improper real, and improper complex (leaky) solutions of mushroom-like HIS structure composed of patch array and wire media slab; (**a**) real part of the normalized propagation constant and (**b**) absolute value of the imaginary part of the normalized propagation constant. The analytical results are compared with HFSS [22].

modes and proper complex TM mode are shown in Fig. 10. It can be seen that the bandgap between proper real TM and TE surface-wave modes occurs due to the backward nature of the TM mode interacting with the wire medium in the presence of the capacitive grid of the Jerusalem cross array. Moreover, for the specific geometrical parameters used, the value of the imaginary part of the propagation constant of proper complex TM mode (shown in Fig. 10b) is very large (in the fast-wave region), which results in rapid attenuation and poor radiation and, hence, in an effective bandgap at low frequencies for this kind of structure.

## 4 Conclusions

Analytical models for the accurate and rapid analysis of surface waves on dense HIS structures with and without vias have been presented. These models utilize the expressions of surface grid impedance obtained from the full-wave scattering problem via the averaged impedance boundary condition in terms of effective circuit parameters. The homogenization model of mushroom-like HIS structures is based on the ENG approximation (as a local model) of wire media slab in conjunction with the dynamic model for the grid. Dispersion behavior of surface-wave modes, including proper real (bound), proper complex (leaky-wave solution associated with backward radiation), improper real, and improper complex (leaky-wave solution associated with forward radiation) solutions, has been studied for several printed FSS grids on a grounded dielectric slab and wire media slab. The analytical results have been compared with the full-wave results obtained by the integral equation method of [14] and with HFSS [22], showing a good agreement at low frequencies within the limits of homogenization.

**Acknowledgments** The authors are thankful to Mário G. Silveirinha and Igor S. Nefedov for fruitful discussions of homogenization models of wire media and mushroom-like structures.

## References

1. Sievenpiper, D., L. Zhang, R. F. J. Broas, N. G. Alexopolous, and E. Yablonovitch: High-impedance electromagnetic surfaces with a forbidden frequency band. IEEE Trans. Microw. Theory Tech., **47**, 2059–2074 (1999).
2. Sievenpiper, D., High-impedance electromagnetic surfaces, Ph.D. dissertation, University of California, Los Angeles, CA (1999).
3. Zhang, Y., J. von Hagen, M. Younis, C. Fischer, and W. Weisbeck: Planar artificial magnetic conductors and patch antennas. IEEE Trans. Antenn. Propag., **51**, 2704–2712 (2003).
4. Goussetis, G., A. P. Feresidis, and J. C. Vardaxoglou: Tailoring the AMC and EBG characteristics of periodic metallic arrays printed on grounded dielectric substrate. IEEE Trans. Antenn. Propag., **54**, 82–89 (2006).
5. Maci, S. and P.-S. Kildal: Hard and soft Gangbuster surfaces. Proceedings of URSI International Symposium on Electromagnetic Theory, Pisa, Italy, 290–292 (2004).
6. Maci, S., M. Caiazzo, A. Cucini, and M. Casaletti: A pole-zero matching method for EBG surfaces composed of a dipole FSS printed on a grounded dielectric slab. IEEE Trans. Antenn. Propag., **53**, 70–81 (2005).
7. Goussetis, G., Y. Guo, A. P. Feresidis, and J. C. Vardaxoglou: Miniaturized and multi-band artificial magnetic conductors and electromagnetic band gap surfaces. Proceedings of IEEE Antennas Propagation Society International Symposium, **1**, 293–296 (2004).
8. Hiranandani, M., A. B. Yakovlev, and A. A. Kishk,: Artificial magnetic conductors realized by frequency selective surfaces on a grounded dielectric slab for antenna applications. IEE Proc.-Microw. Antenn. Propag. (Part H), **153**, 487–493 (2006).
9. Kern, D. J., D. H. Werner, A. Monorchio, L. Lanuzza, and M. J. Wilhelm: The design synthesis of multiband artificial magnetic conductors using high impedance frequency selective surfaces. IEEE Trans. Antenn. Propag., **53**, 8–17 (2005).
10. Yang, H.-Y. D., R. Kim, and D. R. Jackson: Design consideration for modeless integrated circuit substrates using planar periodic patches. IEEE Trans. Microw. Theory Tech., **48**, 2233–2239 (2000).
11. Grbic, A. and G. V. Eleftheriades: Dispersion analysis of a microstrip-based negative refractive index periodic structures. IEEE Microw. Wireless Comp. Lett., **13**, 155–157 (2003).
12. Clavijo, S., R. E. Diaz, and W. E. Mckinzie, III: High-impedance surfaces: An artificial magnetic conductor for a positive gain electrically small antennas. IEEE Trans. Antenn. Propag., **51**, 2678–2690 (2003).
13. Bozzi, M., S. Germani, L. Minelli, L. Perregrini, and P. de Maagt: Efficient calculation of the dispersion diagram of planar electromagnetic band-gap structures by the MoM/BI-RME method. IEEE Trans. Antenn. Propag., **53**, 29–35 (2005).
14. Baccarelli, P., S. Paulotto, and C. Di Nallo: Full-wave analysis of bound and leaky modes propagating along 2D periodic printed structures with arbitrary metallisation in the unit cell. IET Microw. Antenn. Propag., **1**, 217–225 (2007).

15. Tretyakov, S. A. and C. R. Simovski: Dynamic model of artificial impedance surfaces. JEMWA, **17**, 131–145 (2003).
16. Simovski, C. R., P. de Maagt, S. A. Tretyakov, M. Paquay, and A. A. Sochava: Angular stabilization of resonant frequency of artificial magnetic conductors for TE-incidence. Electron. Lett., **40**, 92–93 (2004).
17. Simovski, C. R., P. de Maagt, and I. V. Melchakova: High-impedance surfaces having stable resonance with respect to polarization and incidence angle. IEEE Trans. Antenn. Propag., **53**, 908–914 (2005).
18. Luukkonen, O., C. Simovski, G. Granet, G. Goussetis, D. Lioubtchenko, A. Räisänen, and S. Tretyakov: Simple and accurate analytical model of planar grids and high-impedance surfaces comprising metal strips or patches. IEEE Trans. Antenn. Propagat., **56**, 1624–1632 (2008).
19. Luukkonen, O., C. Simovski, A. Räisänen, and S. Tretyakov: An efficient and simple analytical model for the analysis of propagation properties in impedance waveguides. IEEE Trans. Microw. Theory Tech., **56**, 1624–1632 (2008).
20. Tretyakov, S. A., Analytical Modeling in Applied Electromagnetics, Artech House, Boston, MA (2003).
21. Hessel, A., General characteristics of traveling-wave antennas, ch. 19, in R. E. Collin and F. J. Zucker, Antenna Theory, McGraw-Hill, New York (1969).
22. HFSS: High Frequency Structure Simulator based on the Finite Element Method, v. 9.2.1, Ansoft Corporation (2004).
23. Belov, P., R. Marqués, S. I. Maslovski, I. S. Nefedov, M. Silveirinha, C. R. Simovski, and S. A. Tretyakov: Strong spatial dispersion in wire media in the very large wavelength limit, Phys. Rev. B, **67**, 113103 (2003).
24. Silveirinha. M. G., C. A. Fernandes, and J. R. Costa: Electromagnetic characterization of textured surfaces formed by metallic pins, IEEE Trans. Antenn. Propag., **56**, 405–415 (2008).
25. Silveirinha, M.: Nonlocal homogenization model for a periodic array of epsilon-negative rods, Phys. Rev. E, **73**, 046612(1-10) (2006).
26. Silveirinha, M. and C. A. Fernandes: Homogenization of 3D-connected and non-connected wire metamaterials, IEEE Trans. Microw. Theory Tech., **53**, 1418–1430 (2005).
27. Silveirinha, M.: Additional boundary condition for the wire medium, IEEE Trans. Antenn. Propag., **54**, 1766 (2006).
28. Marcuvitz, N., Waveguide Handbook, Peter Peregrinus, London, UK (1986).

# Migration and Collision of Magnetoplasmon Modes in Magnetised Planar Semiconductor-Dielectric Layered Structures

**Alexander G. Schuchinsky and Xiyu Yan**

Queen's University Belfast, ECIT, Belfast, BT3 9DT, UK
a.schuchinsky@qub.ac.uk

**Abstract** The eigenmodes in the planar layered structures containing magnetically biased semiconductor films exhibit the unusual features of migrating between the frequency bands and layer interfaces. It is shown that at certain combinations of the structure parameters, the magnetoplasmons localised at opposite interfaces of the guiding layer can interchange their locations while preserving the parity of their field distributions. The intriguing properties of the nonreciprocal magnetoplasmons are illustrated by their field and power flow distributions.

## 1 Introduction

Magnetically biased semiconductor-dielectric layered structures have been studied as an alternative to ferrite devices for mm-wave applications, see e.g. [1–4]. Magnetoplasmons guided by the semiconductor layers in Voigt configuration (magnetic bias in the layer plane perpendicular to the direction of wave propagation) are of particular interest owing to nonreciprocity of their propagation [4, 5]. Various approximations and direct numerical methods have been usually used for analysis of magnetoplasmons at the semiconductor-dielectric interfaces but the obtained results frequently suffered from uncertainty in identification of the physical solutions and interpretation of the numerical data [4, p. 260]. The difficulties were further compounded by the multiscale nature of the investigated structures and strong effect of the layer parameters on the characteristics of propagating waves.

In order to address these problems, the spectra of magnetoplasmon modes and dynamic waves (leaky and ordinary surface waves) in a parallel-plate waveguide loaded with a tangentially magnetised semiconductor film are analysed in this paper using the rigorous dispersion equation (DE) for TM waves. The asymptotic solutions for the magnetoplasmonic resonances are obtained and applied to numerical evaluation of dispersion characteristics, and field and power flux

S. Zouhdi et al. (eds.), *Metamaterials and Plasmonics: Fundamentals, Modelling, Applications*,

distributions of eigenmodes. The results of the analytical and numerical analyses presented in the paper demonstrate the novel properties of magnetoplasmons in thin semiconductor films surrounded by dissimilar dielectric layers. The features of nonreciprocal magnetoplasmon migration between the frequency bands are discussed in detail, and the effect of dielectric layers adjacent to the semiconductor film on the properties of magnetoplasmons is illustrated by the examples of the dispersion characteristics and field and Poynting vector distributions of eigenmodes in the canonical structure of the layered waveguide.

## 2 Dispersion Equation of Tangentially Magnetised Semiconductor Film

To investigate the properties of magnetoplasmons guided by the tangentially magnetised semiconductor film, let us consider a canonical layered structure shown in Fig. 1. It is composed of a semiconductor film of thickness $a_0$, magnetised by external biasing field $\mathbf{H_0}$ and sandwiched between two dielectric layers with permittivities $\varepsilon_{1,2}$ and thicknesses $a_{1,2}$, all enclosed into a parallel-plate waveguide with perfectly conducting walls [1]. For time harmonic fields of frequency $\omega$ with the time dependence $exp\{i\omega t\}$, the semiconductor film is described by the permittivity tensor $\boldsymbol{\varepsilon}_s$ of the following form [4]

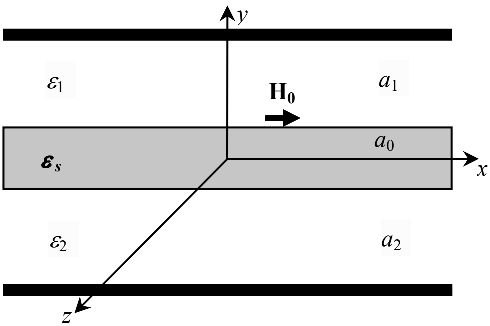


**Fig. 1** Cross-section of the parallel plate waveguide with a semiconductor film sandwiched between two dissimilar dielectric layers and magnetised by external biasing field $\mathbf{H_0}$.

[1] The waveguide enclosure is used here with a sole purpose of formulating the boundary value problem for the bounded structure. In this case, the dispersion equation is expressed by an analytical function without branch cuts, cf. (5). The latter property is essential for the rigorous analysis of the complete spectrum of eigenwaves including complex modes [6].

$$\boldsymbol{\varepsilon}_s = \varepsilon_L \begin{bmatrix} \varepsilon_x & 0 & 0 \\ 0 & \varepsilon_p & -i\varepsilon_a \\ 0 & i\varepsilon_a & \varepsilon_p \end{bmatrix} \tag{1}$$

where

$$\varepsilon_x = 1 - \frac{\omega_p^2}{\omega(\omega - i\nu)}; \quad \varepsilon_p = 1 - \frac{\omega_p^2(\omega - i\nu)}{\omega\left[(\omega - i\nu)^2 - \omega_c^2\right]}; \quad \varepsilon_a = \frac{\omega_p^2\omega_c}{\omega\left[(\omega - i\nu)^2 - \omega_c^2\right]} \tag{2}$$

$\omega_p$, $\omega_c$ and $\nu$ are the plasma, cyclotron and collision frequencies, respectively, and $\varepsilon_L$ is the background relative permittivity. An effective transverse permittivity $\varepsilon_T$ is additionally introduced to characterise the magnetically biased semiconductor medium in the plane perpendicular to the direction of magnetisation $\mathbf{H_0}$. It is defined as follows

$$\varepsilon_T = \varepsilon_L\left(\varepsilon_p - \frac{\varepsilon_a^{\,2}}{\varepsilon_p}\right) = \varepsilon_L\left(1 + \frac{\omega_{pn}^2\left(\omega_n\Omega_n - \omega_{pn}^{\,2}\right)}{\omega_n\left[\Omega_n\left(\omega_n\Omega_n - \omega_{pn}^{\,2}\right) - \omega_n\right]}\right); \quad \Omega_n = \omega_n - i\nu_n \tag{3}$$

where all frequencies are normalised to $\omega_c$ and are labelled by subscript $n$, i.e. $\omega_n = \omega/\omega_c$, $\nu_n = \nu/\omega_c$, $\omega_{pn} = \omega_p/\omega_c$.

The function $\varepsilon_T(\omega_n)$ has two nulls $\omega_{nL}$ and $\omega_{nH}$, and two poles $\omega_{nT}$ and $\omega_{n0} = 0$ in the half-plane Re $(\omega_n) \geq 0$ of complex plane $\omega_n$.

$$\begin{aligned} \omega_{nL} &= \frac{1}{2}\left(\sqrt{(1 - i\nu_n)^2 + 4\omega_{pn}^2} - 1 - i\nu_n\right); \\ \omega_{nH} &= \frac{1}{2}\left(\sqrt{(1 + i\nu_n)^2 + 4\omega_{pn}^2} + 1 - i\nu_n\right); \\ \omega_{nT} &\approx \sqrt{1 + \omega_{pn}^2} - i\nu_n\frac{1 + \omega_{pn}^2/2}{1 + \omega_{pn}^2}. \end{aligned} \tag{4}$$

The frequencies $\omega_{nLr} = \mathrm{Re}\,\omega_{nL}$, $\omega_{nHr} = \mathrm{Re}\,\omega_{nH}$ and $\omega_{nTr} = \mathrm{Re}\,\omega_{nT}$ play a pivotal role in formation of the eigenwave spectrum because they determine transverse resonances of the medium and separate the frequency bands corresponding to the negative $\mathrm{Re}\,\varepsilon_T$ (bands I and III) and positive $\mathrm{Re}\,\varepsilon_T$ (bands II and IV) as illustrated in Fig. 2.

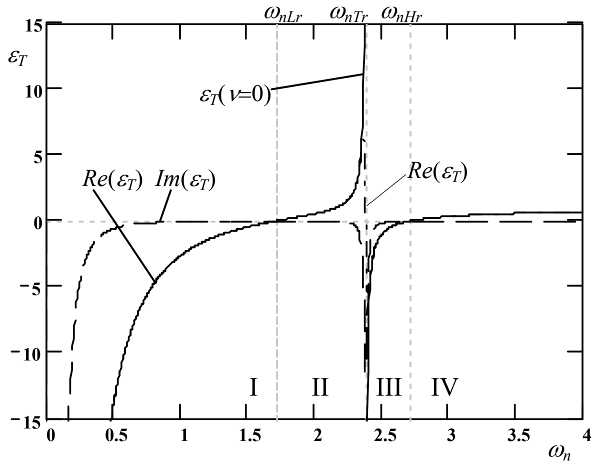


**Fig. 2** Frequency dependence of $\varepsilon_T$ for magnetised semiconductor.

TM (extraordinary) waves propagating towards $z$-axis without field variations along the magnetisation direction ($x$-axis) in the structure of Fig. 1 represent an important special case often referred to as Voigt configuration [4, 5]. TM waves including magnetoplasmons with the field components $H_x$, $E_y$, $E_z$ constitute the complete set of eigenmodes, which strongly interact with the gyrotropic semiconductor film and exhibit nonreciprocal behaviour. The latter feature of magnetoplasmons is of particular interest for the applications in nonreciprocal devices and will be discussed in detail in Section 3.

The dispersion equation (DE) for TM waves with the time $t$ and coordinate $z$ dependences in the form $exp\{i(\omega t\text{-}k_0\gamma_n z)\}$ can be expressed in the form [6]

$$\coth(\beta_{0n}k_0a_0)\beta_{0n}(A_1+A_2)\varepsilon_L\varepsilon_p+\gamma_n^{\ 2}-\varepsilon_L\varepsilon_p+A_1A_2\varepsilon_T\varepsilon_L\varepsilon_p-\gamma_n(A_1-A_2)\varepsilon_L\varepsilon_a=0 \qquad (5)$$

where $k_0$ is the free space wavenumber and $\gamma_n$ is the normalised longitudinal wavenumber;

$$\beta_{0n}=\sqrt{\gamma_n^{\ 2}-\varepsilon_T};\quad \beta_{mn}=\sqrt{\gamma_n^{\ 2}-\varepsilon_m};\quad A_m=\frac{\beta_{mn}\tanh(\beta_{mn}k_0a_m)}{\varepsilon_m};\quad m=1,2.$$

Examination of the DE (5) shows that the fundamental properties of the magnetoplasmons can be directly inferred from (5). Namely, nonreciprocity of eigenwave propagation is determined by the last term in (5), i.e. in asymmetric structures with $A_1 \neq A_2$, the waves travelling in opposite directions of $z$-axis have different wave numbers $\gamma_n$. However, it is necessary to note that even at $A_1 = A_2$, the cross-sectional field distributions of TM modes are asymmetric due to the effect of nonreciprocal field displacement to one of the semiconductor film interfaces (see Section 3). On the other hand, symmetry of the structure is not a prerequisite for fulfilling the condition $A_1 = A_2$, which can also be satisfied in the asymmetric structures with the special combinations of the dielectric layer parameters.

The resonance frequencies of the magnetoplasmons at the semiconductor-dielectric interfaces are obtained from the asymptotic solutions of (5) at $\mathrm{Re}\gamma_n \to +\infty$ and have the following form

$$\omega_{nas}^{-+} = \frac{1}{2}\left(\sqrt{4\omega_{pn}^{\ 2}\frac{\varepsilon_L}{\varepsilon_L+\varepsilon_1}+1}+1\right); \quad \omega_{nas}^{++} = \frac{1}{2}\left(\sqrt{4\omega_{pn}^{\ 2}\frac{\varepsilon_L}{\varepsilon_L+\varepsilon_2}+1}-1\right). \tag{6}$$

where the 1st superscript denotes the magnetoplasmon type and the 2nd superscript represents the direction of wave propagation, corresponding to the sign of $\mathrm{Re}\gamma_n$. For $\mathrm{Re}\gamma_n < 0$, $\omega_{nas}^{\pm -}$ has the same form of (6) with $\varepsilon_1$ and $\varepsilon_2$ interchanged. It immediately follows from (6) that at $\varepsilon_1 > \varepsilon_2$, $\omega_{nas}^{-+} < \omega_{nas}^{--}$ and $\omega_{nas}^{++} > \omega_{nas}^{+-}$, i.e. both the magnetoplasmonic resonance frequencies for $\mathrm{Re}\gamma_n > 0$ are contained between the respective resonances for $\mathrm{Re}\gamma_n < 0$. The latter relationship between the pairs of the magnetoplasmonic resonances is inverted at $\varepsilon_1 < \varepsilon_2$.

It is necessary to stress that the magnetoplasmonic resonance frequencies have been obtained in (6) without any constraints on $\varepsilon_T(\omega_n)$, assuming only that $|\gamma_n| \to \infty$. Therefore it is essential to examine the locations of $\omega_{nas}^{\pm\pm}$ in the frequency bands I-IV separated by the poles and zeros of $\varepsilon_T(\omega_n)$. The results of such an analysis for $\mathrm{Re}\gamma_n > 0$ are summarised in Table 1 and show that $\omega_{nas}^{+\pm}$ are always confined to the frequency band I where $\mathrm{Re}\varepsilon_T < 0$, whereas $\omega_{nas}^{-\pm}$ can be located in any frequency band I, II or III with $\omega_{nas}^{-\pm} < \omega_{nHr}$. Hence, in contrast to the case of demagnetised semiconductor films, the requirement of $\mathrm{Re}\varepsilon_T < 0$ (which is held in bands I and III)

**Table 1.** Frequency bands of magnetoplasmon resonances at $\mathrm{Re}\gamma_n \gtrless 0$.

| Frequency band | | | Modes | | Conditions for $\omega_{nas}^{-+}$ location |
|---|---|---|---|---|---|
| I | $0 < \omega_n < \omega_{nLr}$ | $\varepsilon_T < 0$ | $\omega_{nas}^{++}$ | $\omega_{nas}^{-+}$ | $\varepsilon_L/\varepsilon_1 < \omega_{nTL} \wedge \omega_{pn} > \sqrt{2}$ |
| II | $\omega_{nLr} < \omega_n < \omega_{nTr}$ | $\varepsilon_T > 0$ | – | $\omega_{nas}^{-+}$ | $\omega_{nTL} < \varepsilon_L/\varepsilon_1 < \omega_{nTr}$ |
| III | $\omega_{nTr} < \omega_n < \omega_{nHr}$ | $\varepsilon_T < 0$ | – | $\omega_{nas}^{-+}$ | $\varepsilon_L/\varepsilon_1 > \omega_{nTr}$ |
| IV | $\omega_n > \omega_{nHr}$ | $\varepsilon_T > 0$ | – | | |

where $\omega_{nTL} = \left(\sqrt{1+4\omega_{pn}^{\ 2}}-3\right)/4$

is no more mandatory for existence of the plasmonic resonances at $\omega_{nas}^{-\pm}$. These resonances are also permitted in the frequency band II where Re$\varepsilon_T > 0$, cf. Fig. 2. Furthermore, the pairs of plasmonic resonances, $\omega_{nas}^{+\pm}$ and $\omega_{nas}^{-\pm}$, can occur either in the same or different frequency bands depending on the characteristic frequencies $\omega_{nLr}$, $\omega_{nTr}$, $\omega_{nHr}$ and the dielectric layer permittivities $\varepsilon_{1,2}$. This implies that the resonance frequencies $\omega_{nas}^{-\pm}$ may migrate between the bands I–III. The conditions for $\omega_{nas}^{-\pm}$ location in a particular frequency band have been obtained from (4) and (6), and are provided in Table 1.

Inspection of Table 1 shows that whenever $\omega_{nas}^{-+}$ is located in bands II or III, it always satisfies the inequality $\omega_{nas}^{-+} > \omega_{nas}^{++}$. However this may not be the case in band I, where the frequency $\omega_{nas}^{-+}$ can be either above or below $\omega_{nas}^{++}$. Analysis of (6) demonstrates that the latter case is possible indeed, i.e. $\omega_{nas}^{-+} < \omega_{nas}^{++}$, if the following conditions are satisfied simultaneously:

$$\varepsilon_1 > \varepsilon_2 \quad \text{and} \quad \frac{\varepsilon_1 + \varepsilon_L}{\varepsilon_2 + \varepsilon_L}\left(\frac{\omega_{pn}^2 \varepsilon_L}{\varepsilon_2 + \varepsilon_L} - 2\right) > 6. \tag{7}$$

It is necessary to emphasise that the interchange of $\omega_{nas}^{-+}$ and $\omega_{nas}^{++}$ positions has been obtained asymptotically and, therefore, it is applicable to the magneto-plasmonic resonances only. The respective dispersion curves may “collide” but do not intersect each other. It is also evident from (7) that the interchange of the resonance frequencies is essentially nonreciprocal phenomenon which can occur for the modes of one propagation direction only due to the first condition in (7) which cannot be fulfilled simultaneously for the magnetoplasmons propagating in both directions. These features and other properties of nonreciprocal magneto-plasmons are further elaborated in the next Section with the aid of the results of the numerical solution of the rigorous DE (5).

## 3 Migrating Magnetoplasmon Modes: Numerical Results and Discussion

As demonstrated in the preceding sections, gyrotropy of the magnetised semi-conductor film enables the unique features of the nonreciprocal magnetoplasmons propagating in asymmetric layered structures. So far the discussion has been limited to the qualitative analysis of the DE and its asymptotic solutions, which indicated that variations of the layers’ parameters may cause qualitative changes of the magnetoplasmon properties. To gain insight into the exact effect of the structure parameters on the characteristics of the magnetoplasmons guided by the magnetised semiconductor films, the DE (5) has been analysed numerically in the cases of dissimilar thicknesses and permittivities of dielectric layers. The characteristics of the magnetoplasmons presented in this Section have been obtained for the lossless[2] ($\nu_n$=0) $n$-GaAs films with the following parameters: $\varepsilon_L$ = 13.1, $\omega_{pn}$ = 2.17, $f_c$ = 62.21 GHz, $\omega_c = 2\pi f_c$.

Fig. 3 displays the dispersion characteristics of the fundamental magnetoplasmon modes C', $O^{++}$ and $O^{-+}$ (labels of the modes $O^{\pm+}$ correspond to the convention for the respective resonance frequencies $\omega_{nas}^{\pm+}$ defined in (6)) in the symmetric structure at several values of the dielectric layer permittivities. Since the DE (5) for the symmetric structure is an even function of $\gamma_n$, the dispersion characteristics are presented for Re$\gamma_n$ > 0 only. It is noteworthy that the higher order forward and backward type complex modes of magnetoplasmons with nearly the same values of Re($\gamma_n$) also exist in the film, cf. [6].

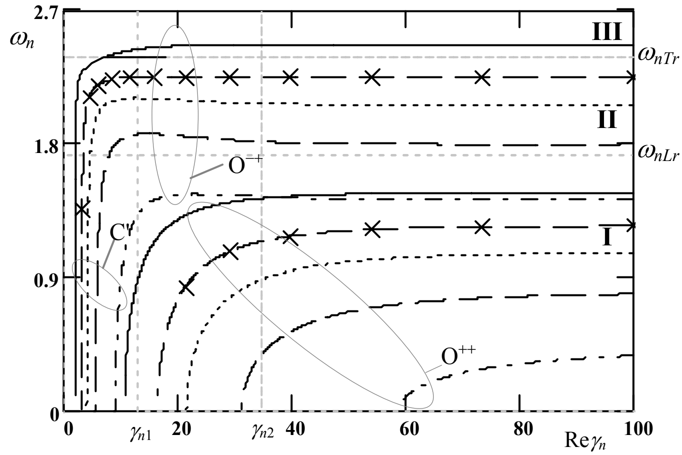


**Fig. 3** Dispersion characteristics of the magnetoplasmon modes in the symmetric structure with different permittivities of dielectric layers: $\varepsilon_1 = \varepsilon_2$ = 3.9 (solid line), 9 (dash line with crosses), 15 (dotted line), 30 (dash line) and 90 (dash-dot line). The structure parameters: $\varepsilon_L$ = 13.1, $f_c$ = 62.21 GHz, $\omega_c = 2\pi f_c$, $\omega_p = 2.17\omega_c$, $a_0$ = 20 μm, and $a_1 = a_2$ = 40 μm; $\gamma_{n1}$ = 13 and $\gamma_{n2}$ = 35 are the sampling points for the field and Poynting vector distributions displayed in Fig. 4.

At low permittivity of dielectric layers, $\varepsilon_1 = \varepsilon_2$ = 3.9, the magnetoplasmon mode $O^{-+}$ exists only in the frequency band III ($\omega_n > \omega_{nTr}$), whilst the mode C' is confined to the bands I and II ($0 < \omega_n < \omega_{nTr}$). In the frequency band I ($\omega_n < \omega_{nLr}$) where Re$\varepsilon_T$ < 0, the mode C' is a surface wave, and it also remains a surface wave with $\mathrm{Re}\,\gamma_n > \sqrt{\mathrm{Re}\,\varepsilon_T(\omega_n)} > \sqrt{\varepsilon_1}$ in the frequency band II ($\omega_n > \omega_{nLr}$) despite Re$\varepsilon_T$>0 here. At frequencies approaching the transverse resonance $\omega_{nTr}$ where

[2] Effect of loss in the semiconductor films on the properties of magnetoplasmon modes has been discussed in [6, 7].

Re$\varepsilon_T \rightarrow +\infty$, the mode C' turns into a bound dynamic (bulk) wave guided by the semiconductor film with $\mathrm{Re}\,\gamma_n < \sqrt{\mathrm{Re}\,\varepsilon_T(\omega_n)}$.

When permittivities $\varepsilon_1 = \varepsilon_2$ of both dielectric layers increase, the magnetoplasmon mode $O^{-+}$ migrates (Fig. 3) from the frequency band III ($\omega_{nTr} < \omega_n < \omega_{nHr}$) into the band II ($\omega_{nLr} < \omega_n < \omega_{nTr}$) where it exhibits a negative slope of the dispersion curve at Re$\varepsilon_T > 0$. It can be directly verified that the respective permittivity values obey the conditions specified in Table 1 ($\omega_{nTL} = 0.363$) for the magnetoplasmonic resonance $\omega_{nas}^{-+}$ to occur in the corresponding bands. The mode C' experiences a high frequency cut-off at $\omega_{nc}$ ($\omega_{nc} < \omega_{nTr}$) simultaneously with the mode $O^{-+}$ as shown in Fig. 3. It is necessary to note that both modes $O^{-+}$ and C' remain the surface waves in the frequency band II ($\omega_{nLr} < \omega_n < \omega_{nTr}$) despite Re$\varepsilon_T > 0$, and this effect is solely related to gyrotropy of the magnetised semiconductor film.

The qualitative changes of the magnetoplasmon modes $O^{-+}$ and C', migrating between the frequency bands, are associated with the competing mechanisms of nonreciprocal field displacement due to the semiconductor film gyrotropy and reciprocal effect of the surrounding dielectric layers. These features are illustrated in Fig. 4 by the field and Poynting vector distributions of the magnetoplasmon $O^{-+}$. Indeed, at low permittivities $\varepsilon_1 = \varepsilon_2 = 3.9$, when the mode $O^{-+}$ is confined to the frequency band III ($\omega_n > \omega_{nTr}$), the fields and power flow (Poynting vector $P_z$) are localised at the interface $y = a_0/2$ at both values of $\gamma_{n1}$ and $\gamma_{n2}$ as shown in Fig. 4.

When permittivity of the dielectric layers increases to $\varepsilon_1 = \varepsilon_2 = 9$, the mode $O^{-+}$ migrates into the frequency band II ($\omega_{nLr} < \omega_n < \omega_{nTr}$) with Re$\varepsilon_T > 0$, and its field and power distributions are barely affected especially at larger values of $\gamma_n = \gamma_{n2}$. Moreover the mode $O^{-+}$ still remains a forward type wave as long as $\varepsilon_1 = \varepsilon_2 < \varepsilon_L$. This implies that gyrotropy of the semiconductor film primarily determines the magnetoplasmon properties. This conclusion is consistent with the distribution of E-field polarisation ($E_z/E_y$) in Fig. 4, which shows nearly equal magnitudes of both electric field components. Further increase of $\varepsilon_1 = \varepsilon_2$ causes migration of the mode $O^{-+}$ towards lower frequencies and into the band I ($\omega_n < \omega_{nL}$). At higher permittivities $\varepsilon_1 = \varepsilon_2 = 15$, 30 and 90, the field and power flow localisation at a single interface decreases because the nonreciprocal field displacement is counteracted by the reciprocal effect of the dielectric layers. This effect is readily observable in Fig. 4, which illustrates that permittivity of dielectric layers has much stronger impact on the field distributions at $\gamma_{n1}$ than at $\gamma_{n2}$ ($\gamma_{n2} > \gamma_{n1}$), while the film gyrotropy remains the dominant mechanism of the magnetoplasmon propagation in the band II with Re$\varepsilon_T > 0$. At $\varepsilon_1 = \varepsilon_2 = 90$ the mode $O^{-+}$ migrates into the frequency band I where Re$\varepsilon_T < 0$ and the negative diagonal components of the tensor $\varepsilon_s$ become dominant. Then the magnetoplasmons $O^{-+}$ and $O^{++}$ resemble the perturbed plasmonic modes of the demagnetised semiconductor film.

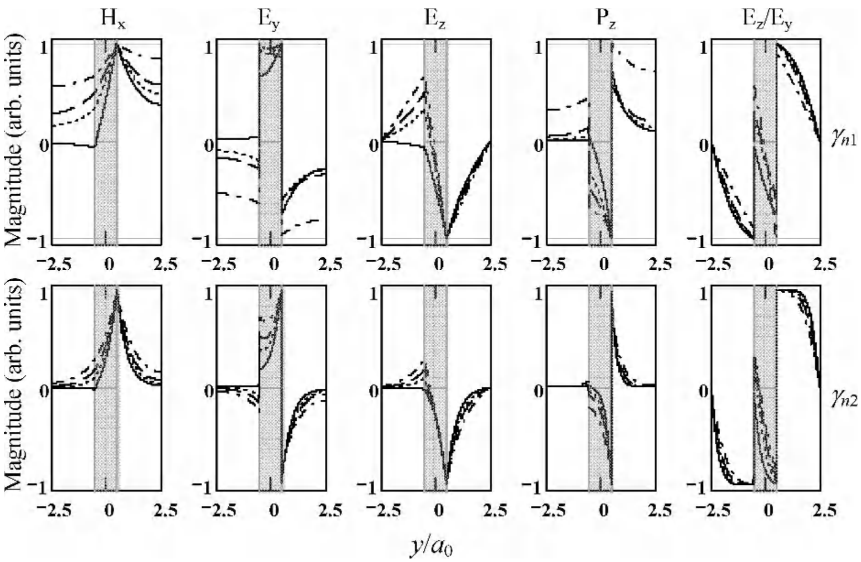


**Fig. 4** Normalized cross-sectional distributions of fields $H_x$, $E_y$, $E_z$, Poynting vector ($P_z$) and ratio ($E_z/E_y$) of the mode $O^{-+}$ in the cross-section of the symmetric structure sampled at $\gamma_{n1} = 13$ and $\gamma_{n2} = 35$ (see Fig. 3) and different permittivities of dielectric layers: $\varepsilon_1 = \varepsilon_2 = 3.9$ (solid line), 15 (dotted line), 30 (dash line) and 90 (dash-dot line). Shaded areas at $|y/a_0| < 1/2$ correspond to the semiconductor film of thickness $a_0 = 20$ μm sandwiched between dielectric layers of thicknesses $a_1 = a_2 = 40$ μm. The structure parameters: $\varepsilon_L = 13.1$, $f_c = 62.21$ GHz, $\omega_c = 2\pi f_c$, $\omega_p = 2.17\omega_c$.

In the case of asymmetric structure with $\varepsilon_1 \neq \varepsilon_2$, the combined effect of reciprocal and nonreciprocal field displacements to the layer interfaces leads to the intricate behaviour of magnetoplasmonic modes as they migrate between the frequency bands. The dispersion characteristics of magnetoplasmons in Fig. 5 show that only the mode $O^{-+}$ moves across the frequency bands when $\varepsilon_1$ increases from 3.9 to 90. Moreover at $\varepsilon_1 = 90$, the conditions (7) are satisfied so that $\omega_{nas}^{-+} < \omega_{nas}^{++}$, i.e. the modes $O^{-+}$ and $O^{++}$ should "collide" and interchange their field patterns at a certain finite value of $\gamma_n$. Indeed, the surface mode $O^{++}$ exists only in the frequency band I ($\omega_n < \omega_{nLr}$), and due to nonreciprocal field displacement, its fields should be primarily localised at the interface with dielectric layer of permittivity $\varepsilon_2$ at $y = -a_0/2$. However, when $\varepsilon_1$ increases, the nonreciprocal field displacement of the mode $O^{++}$ is distorted, and a considerable part of the power flow is transported inside the film and at the opposite interface, $y = +a_0/2$, as illustrated in Fig. 6.

Conversely, the mode $O^{-+}$ experiences both nonreciprocal and reciprocal field displacements to the same interface with the dielectric layer of higher permittivity $\varepsilon_1$ at $y = +a_0/2$. Therefore as $\varepsilon_1$ increases, the mode $O^{-+}$ migrates from the frequency band III to the band II ($\omega_{nL} < \omega_n < \omega_{nTp}$), where $\varepsilon_T > 0$. Then it becomes connected with the mode $C'^{+}$. Further increase of $\varepsilon_1$ causes conversion of the mode $O^{-+}$ from the forward type to backward wave with negative dispersion ($d\omega_n/d\gamma_n < 0$) at $\varepsilon_1 > 9$. At higher $\varepsilon_1$ ($\varepsilon_1 = 90$ in Fig. 5), the mode $O^{-+}$ expands to the lower frequency band I ($\omega_n < \omega_{nL}$). When the corresponding magnetoplasmonic resonance occurs at $\omega_{nas}^{-+} < \omega_{nas}^{++}$, the modes $O^{-+}$ and $O^{++}$ "collide" at a finite value of $\mathrm{Re}\gamma_n$ and are influenced by both resonances $\omega_{nas}^{++}$ and $\omega_{nas}^{-+}$ simultaneously. This causes the qualitative changes of the field and power distributions of both modes in the layers. At the "collision" frequency, the modes $O^{-+}$ and $O^{++}$ interchange their patterns of the power flow distribution and the asymptotic limits of the magnetoplasmonic resonance frequencies $\omega_{nas}^{++}$ and $\omega_{nas}^{-+}$ but preserve the parity of their field distributions, i.e. the type[3] of the field symmetry in the film, which is inherited from the respective original modes $O^{-+}$ and $O^{++}$ before the collision.

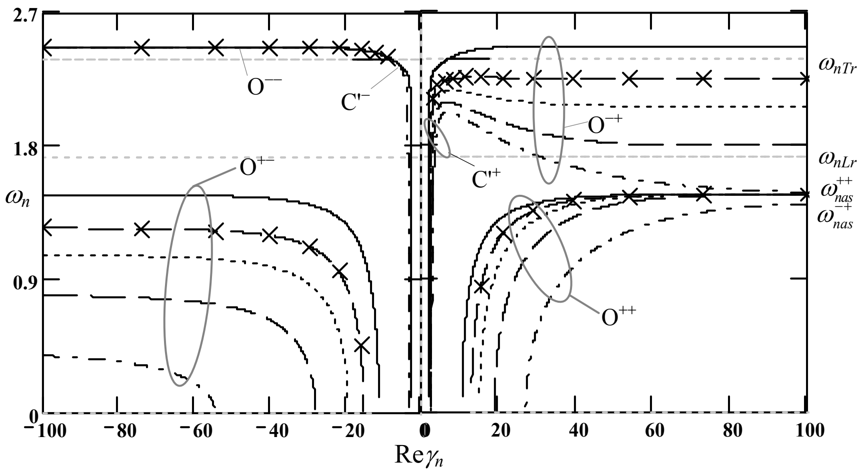


**Fig. 5** Dispersion characteristics of magnetoplasmons in the asymmetric structure at different permittivities of the dielectric layer 1: $\varepsilon_1 = 3.9$ (solid line), 9 (dash line with crosses), 15 (dot line), 30 (dash line) and 90 (dash-dot line). The structure parameters: $\varepsilon_2 = 3.9$, $\varepsilon_L = 13.1$, $f_c = 62.21$ GHz, $\omega_c = 2\pi f_c$, $\omega_p = 2.17\omega_c$, $a_0 = 20$ μm, and $a_1 = a_2 = 40$ μm; $\omega_{nas}^{\pm +}$ correspond to the magnetoplasmonic resonance frequencies at $\varepsilon_1 = 90$.

[3] The type of field distribution identifies, for example, the $H_x$ symmetry in the semiconductor film, viz. the modes $O^{-+}$ and $O^{++}$ are distinguished by the in-phase and anti-phase $H_x$, respectively, at the opposite interfaces of the semiconductor film, cf. Fig. 6.

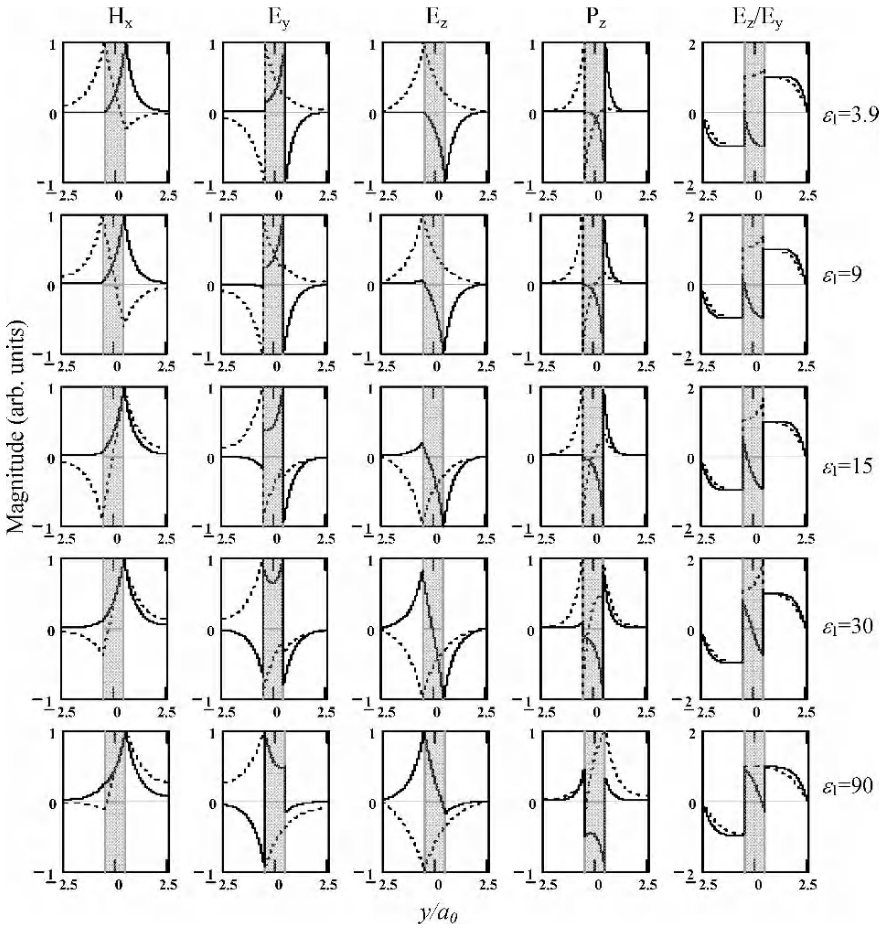


**Fig. 6** Normalized cross-sectional distribution of fields $H_x$, $E_y$, $E_z$, Poynting vector ($P_z$) and ratio ($E_z/E_y$) of the surface modes $O^{-+}$ (solid line) and $O^{++}$ (dotted line) in Fig. 5 sampled at $\gamma_n = 40$ and variable $\varepsilon_1$. Shaded areas at $|y/a_0| < 1/2$ correspond to the semiconductor film of thickness $a_0 = 20$ μm sandwiched between dielectric layers of thicknesses $a_1 = a_2 = 40$ μm. The structure parameters: $\varepsilon_2 = 3.9$, $\varepsilon_L = 13.1$, $f_c = 62.21$ GHz, $\omega_c = 2\pi f_c$, $\omega_p = 2.17\omega_c$.

## 3 Conclusions

The properties of nonreciprocal magnetoplasmons in the canonical structure of parallel-plate waveguide with a thin magnetised semiconductor film in Voigt configuration have been analysed using the rigorous dispersion equation for TM waves. The asymptotic solutions have been obtained for the magnetoplasmonic resonances, and the dispersion characteristics and field and power flux distributions of the corresponding magnetoplasmon modes have been evaluated numerically. The results of the analytical and numerical studies have revealed the novel properties of the guided nonreciprocal magnetoplasmonic waves:

– Migration of the magnetoplasmonic modes between the frequency bands, separated by the characteristic frequencies (poles and zeros) of the effective transverse permittivity $\varepsilon_T$ of the magnetised semiconductor film
– "Collision" of the magnetoplasmons in the low frequency band where the modes $O^{-+}$ and $O^{++}$ interchange their locations but preserve the parity of their field distributions inherited from the original modes.

The presented comprehensive analysis of the dispersion characteristics and the field and power flow distributions of magnetoplasmons provide the self-consistent interpretation of the complex phenomena of nonreciprocal wave propagation and mode transformations in the asymmetric layered structures containing tangentially magnetised semiconductor films.

**Acknowledgments** This work was supported by the International Centre for System-on-Chip and Advanced Microwireless Integration (SoCaM), Queen's University Belfast, UK.

## References

1. Bolle, D. M., Talisha, S. H.: Fundamental considerations in millimeter and near-millimeter component design employing magnetoplasmons. IEEE Trans. Microw. Theory Tech., **MTT-29**, 916–923 (1981)
2. Mok, V. H., Davis, L. E.: Nonreciprocal GaAs phase-shifters and isolators for millimetric and sub-millimetric wavelengths. In: Proceedings of the IEEE MTT-S International Microwave Symposium, **3**, 2249–2252 (2003)
3. Mok, V. H., Davis, L. E.: Nonreciprocal wave propagation in multilayer semiconductor films at frequencies up to 200 GHz. IEEE Trans. Microw. Theory Tech., **MTT-51**, 2453–2460 (2003)
4. Kushwaha, M. S.: Plasmons and magnetoplasmons in semiconductor heterostructures, Surf. Sci. Rep., **41**, 1–416 (2001)
5. Kushwaha, M. S., Halevi, P.: Magnetoplasmons in thin films in the Voigt configuration. Phys. Rev. B, **36**, 5960–5967 (1987)
6. Schuchinsky A. G., Yan X.: Nonreciprocal magnetoplasmons in imperfect layered structures. In Proceedings of the SPIE, **6987**, 69870W (2008)
7. Schuchinsky, A. G., Yan, X.: Effect of loss on spectra and properties of eigenwaves in imperfect metal films and magnetised semiconductor-dielectric structures. In: Proceedings of the Metamaterials 2007, 1st International Congress on Advanced Electromagnetic Materials in Microwaves and Optics, Rome, Italy, 908–910 (2007)

# Dispersion Engineering in Resonant Type Metamaterial Transmission Lines and Applications

**Jordi Bonache, Gerard Sisó, Marta Gil, and Ferran Martín**

CIMITEC, Departament d'Enginyeria Electrònica, Universitat Autònoma de Barcelona
08193 BELLATERRA (Barcelona), Spain
Ferran.Martin@uab.es

**Abstract** In this chapter, it is demonstrated that metamaterial transmission lines based on complementary split ring resonators (CSRRs) are useful for applications requiring dispersion engineering, such us broadband or multi-band components. These artificial lines, consisting on a host line and loading elements (CSRRs and series gaps), exhibit a major number of degrees of freedom as compared to conventional lines, this being the relevant characteristic for tailoring their dispersion diagram. The theoretical foundations, as well as prototype device examples, illustrative of the achievable results, are provided.

## 1 Introduction

Enhanced bandwidth components and multi-band devices are a demand in modern wireless communication systems. In planar technology, such components can be designed by replacing transmission lines and stubs with metamaterial transmission lines [1, 2]. Such lines are artificial propagating media consisting on a host line loaded with reactive elements. Thanks to the presence of additional elements, as compared to conventional lines, metamaterial transmission lines exhibit further degrees of freedom that make possible to tailor their dispersion diagram to some extent. This is the basis for the design of both enhanced bandwidth components and multiband components. There are two main approaches for the implementation of metamaterial transmission lines: (i) the CL-loaded approach, where a host line is loaded with series capacitances and shunt inductances [3–5], and (ii) the resonant type approach, where the host line is either loaded with split ring resonators (SRRs) and shunt connected inductors [6], or with complementary split ring resonators (CSRRs) combined with series capacitances [7]. Such artificial transmission lines (CL-loaded and resonant-type) exhibit a composite right/left handed

S. Zouhdi et al. (eds.), *Metamaterials and Plasmonics: Fundamentals, Modelling, Applications*,

(CRLH) behavior [1, 2]. That is, wave propagation in those lines is backward in that frequency region where the series reactance and shunt susceptance are negative (low frequency band), and it is forward at higher frequencies, where these signs are positive. Although by metamaterial transmission lines we normally refer to those artificial lines at least exhibiting left handed wave propagation, and the occurrence of backward waves is very useful for many applications, the key aspect of metamaterial transmission lines is the controllability of their electrical characteristics, namely the phase constant and the characteristic impedance, rather than the sign of the effective permeability and permittivity (and hence of the phase constant). Thus, it is also possible to implement artificial lines with forward wave behavior [8]. As long as these lines consist on a host line loaded with reactive elements and its dispersion and characteristic impedance can be engineered, such lines must be also considered to belong to the category of metamaterial transmission lines. Finally, we would like to mention that contrarily to effective media metamaterials (i.e. those media exhibiting a controllable effective permittivity and/or permeability), in metamaterial transmission lines the control of the phase constant and characteristic impedance does not necessarily require a periodic repetition of a basic unit cell. Indeed, to reduce line (and hence circuit) dimensions, it is necessary to reduce the number of cells as much as possible. For this reason, in many of our metamaterial-based circuits, only one single stage is considered for either line or stub [9]. Figure 1 depicts the typical unit cell of a CRLH line and an artificial right handed line, as well as their corresponding lumped element equivalent circuits. The interpretation of the elements of those circuit models has been given before in [10], and has been revised in the recent work [11].

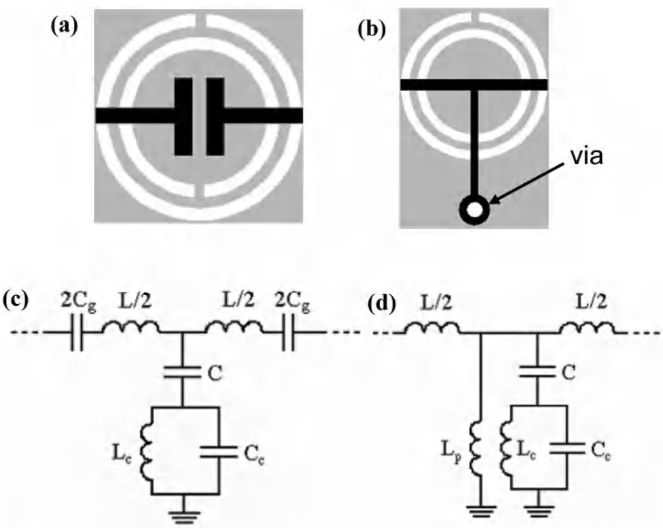


**Fig. 1** Typical unit cell of a left handed (actually composite right/left handed, CRLH) transmission line (**a**) and right handed artificial transmission line (**b**) based on CSRRs. In (**c**) and (**d**) are depicted the corresponding circuit models. Ground plane is depicted in grey.

## 2 Dispersion Engineering in Metamaterial Transmission Lines

Dispersion engineering makes reference to the possibility of controlling (to some extent) the dispersion diagram of metamaterial transmission lines. Such control is not possible by means of conventional lines. That is, the dispersion diagram (under ideal conditions) is simply a straight line with the slope given by the phase velocity of the line. Obviously, in open lines such as the coplanar waveguide (CPW) or the microstrip transmission lines, the phase velocity depends on the geometry of the line (lateral dimensions and substrate thickness), but it does not provide the necessary flexibility that many applications demand. For instance, in conventional lines, bandwidth is intimately related to line length. Such bandwidth is given by that frequency interval where the required phase is satisfied within certain limits. In a conventional transmission line of length $l$, the phase of the line at a certain angular frequency $\omega_o$ is given by:

$$\phi_o = \beta l = \frac{l}{v_p}\omega_o \tag{1}$$

where $v_p$ is the phase velocity of the line. Thus, bandwidth is intimately related to the derivative of $\phi$ with frequency, also known as group delay. From this, it follows that the shorter the line is, the broader the bandwidth becomes. In other words, bandwidth is inversely proportional to the required phase of the line, which is dictated by the design. This means that the operative bandwidth is not an easily controllable parameter in conventional transmission line based circuits.

Another important aspect of dispersion engineering is the possibility to force certain characteristics (phase) at different arbitrary frequencies. This is the key point to implement multiband components by means of metamaterial transmission lines. In conventional lines, the phase is a periodic function of frequency, and hence such lines exhibit multiband behavior, but not necessarily at the required frequencies, but at the odd harmonics of the fundamental. Let us consider in the following sections the applications of metamaterial transmission lines to both broadband and multiband components.

## 3 Application of Resonant-Type Metamaterial Transmission Lines to Bandwidth Enhancement

First of all we will discuss the possibilities and limits to bandwidth enhancement, and after that, several examples will be provided. This discussion is valid for metamaterial transmission lines that can be described by means of lumped element models (unit cell) expressible as T or $\pi$-circuits. Let us explicitly consider a

T-circuit model for the unit cell. The electrical length of the unit cell, $\phi$, and the characteristic impedance, $Z_B$, are given by the following expressions [12]:

$$\cos\phi = 1 + \frac{Z_s(\omega)}{Z_p(\omega)} \tag{2}$$

$$Z_B = \sqrt{Z_s(\omega)[Z_s(\omega) + 2Z_p(\omega)]} \tag{3}$$

where $Z_s$ and $Z_p$ are the series and shunt impedance, respectively, of such circuit. Assuming that, for a certain transmission line, the required phase and characteristic impedance at the operating frequency are $\phi_o$ and $Z_o$, the previous equations can be inverted and the series and shunt impedances must take the following values at the design frequency:

$$Z_s = Z_o\sqrt{\frac{\cos\phi_o - 1}{\cos\phi_o + 1}} \tag{4}$$

$$Z_p = \frac{Z_o}{\sqrt{\cos^2\phi_o - 1}} \tag{5}$$

On the other hand, the relevant parameter for our purposes, the derivative of the phase shift with frequency at $\omega_o$, can be inferred from (2):

$$\left.\frac{d\phi}{d\omega}\right|_{\omega_o} = -\frac{1}{\sin\phi_o}\frac{1}{Z_p^2}\left(Z_p\left.\frac{dZ_s}{d\omega}\right|_{\omega_o} - Z_s\left.\frac{dZ_p}{d\omega}\right|_{\omega_o}\right) \tag{6}$$

By introducing (4) and (5) in (6), and after some simple calculation, we finally obtain:

$$\left.\frac{d\phi}{d\omega}\right|_{\omega_o} = -\frac{j}{Z_o}\left(\left.\frac{dZ_s}{d\omega}\right|_{\omega_o} - (\cos\phi_o - 1)\left.\frac{dZ_p}{d\omega}\right|_{\omega_o}\right) \tag{7}$$

Significant for our discussion, the two right hand side terms in (7) are effectively positive since according to the Foster reactance theorem [13], the derivative of any purely reactive reactance or susceptance with frequency is always positive, and

$\cos\phi_o \leq 1$. To enhance bandwidth, we must force the derivative of $\phi$ with frequency to be as small as possible. Thus, according to (7), the frequency derivatives of the series and shunt reactances must be both as small as possible. From the Foster theorem, it follows that the optimum metamaterial transmission line model to minimize expression (7) is the canonical dual transmission line [1, 2]. Hence, it is convenient to calculate expression (7) for this particular case. By introducing

$$Z_s = \frac{1}{2jC\omega} \tag{8}$$

$$Z_p = jL\omega \tag{9}$$

in (7), we obtain, after some straightforward calculation:

$$\left.\frac{d\phi}{d\omega}\right|_{\omega_o} = \frac{2}{\omega_o}\sqrt{\frac{1-\cos\phi_o}{1+\cos\phi_o}} = \frac{2}{\omega_o}\tan\frac{|\phi_o|}{2} \tag{10}$$

Thus, for the optimum transmission line model (in terms of the operative bandwidth) the derivative of phase with frequency does not depend on the required characteristic impedance. It is simply determined by the operating frequency and phase. This is indeed a consequence of the fact that the phase and frequency determine unequivocally the dispersion relation of the structure.

It is important to take into account that expression (10) is the derivative of the phase with frequency corresponding to a single unit cell. If a number $N$ of cells is used to obtain the nominal phase shift, $\phi_o$, then the phase shift of either cell is $\phi_o/N$, and expression (10) rewrites as:

$$\left.\frac{d\phi}{d\omega}\right|_{\omega_o} = \frac{2}{\omega_o}N\tan\frac{|\phi_o|}{2N} \tag{11}$$

A simple analysis of expression (11) reveals that $d\phi/d\omega$ decreases as $N$ increases, namely,

$$\frac{2}{\omega_o}N\tan\frac{|\phi_o|}{2N} > \frac{2}{\omega_o}(N+1)\tan\frac{|\phi_o|}{2(N+1)} \tag{12}$$

for $N = 1, 2\ldots, \infty$. Therefore, in terms of bandwidth, the optimum solution is an $N$-stage artificial line with $N \to \infty$. In this case, (11) can be expressed as:

$$\left.\frac{d\phi}{d\omega}\right|_{\omega_o} = \frac{|\phi_o|}{\omega_o} \tag{13}$$

According to (13), the derivative of phase with frequency for a dual transmission line in the considered limiting case ($N \to \infty$) is identical to that of a conventional line with identical phase (but different sign) at the same frequency. Therefore, from this result we may conclude that, in those applications where the sign of the phase shift is irrelevant (for instance in 90$^o$ impedance inverters and many microwave components based on them), it is not possible to enhance bandwidth by using artificial lines. If the number of cells is limited to a finite number, the derivative of phase with frequency increases, and the operative bandwidth is degraded, as compared to that of a conventional transmission line. Bandwidth improvement can be obtained if the sign of the phase is relevant. In this case we have to compare the dual transmission line with phase $\phi_o$ ($\phi_o$ being negative) with a conventional transmission line with equivalent phase shift, that is $2\pi + \phi_o$. From this comparison, it is obvious (from 13) that, as long as the required phase shift is higher than $\pi$ rad (or lower than $-\pi$ rad), the dual transmission line exhibits smaller phase dependence with frequency and, hence, it exhibits a better solution in terms of bandwidth. If the number of stages is limited to a finite number, then the limiting phase value above which the artificial lines exhibit a better phase response, (lower derivative) is no longer $\pi$ rad. For a single stage dual transmission line, such limiting phase can be inferred by simply forcing (10) to be $(2\pi + \phi_o)/\omega_o$. It gives $\phi_o = -0.7\pi$ rad, or a positive phase (conventional line of $1.3\pi$ rad). It means that, in applications where the sign of the phase shift is fundamental, by using a single-stage dual transmission line, bandwidth can be improved if the required (positive) phase shift is higher than $1.3\pi$ rad.

As it has been highlighted above, the optimum metamaterial transmission line for bandwidth enhancement is the dual transmission line. Thus, the phase shifts ($\pi$ for the infinite stage structure and $1.3\pi$ rad for the one-stage transmission line) below which the dual transmission line is not able to provide an improved bandwidth are fundamental limits. If instead of the dual transmission line, other circuit models are considered, bandwidth is further limited. Nevertheless, it has been shown that transmission line bandwidth can be improved under certain conditions.

On the other hand, there are many devices whose behaviour is based on phase differences. In that case, the key idea to enhance bandwidth is to design the artificial lines with dispersion diagrams as much parallel as possible in the vicinity of the operating frequency. This strategy has been followed in the example provided below, a rat race hybrid coupler. The rat race has been implemented by replacing the conventional lines with metamaterial transmission lines based on CSRRs [14]. Specifically, the +90° lines have been replaced with +90° artificial right handed lines, whereas the +270° conventional line has been replaced with a −90° left handed line (a similar implementation was done before by replacing only the +270° with an artificial CL loaded line [15]). In the design process, we have pursued the parallelism between the dispersion characteristics of such lines, as has been mentioned. The layout of the structure is shown in Fig. 2, whereas its characterization is shown in Fig. 3. The phase balance bandwidth is superior to that of the conventional rat race, whereas the transmission characteristics exhibit comparable bandwidth (see Table 1). Other examples illustrative of the possibility of bandwidth enhancement by using metamaterial transmission lines are given in Refs. [16, 17].

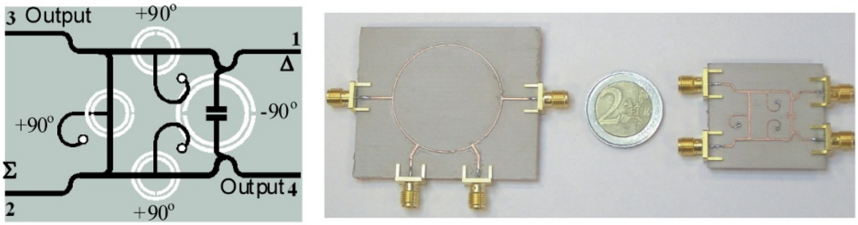


**Fig. 2** Layout of the metamaterial based rat race hybrid coupler and comparison with a conventional rat race with similar characteristics. The fabricated device has been implemented on the *Rogers RO3010* substrate with dielectric constant $\varepsilon_r = 10.2$ and thickness $h_2 = 635$ µm. The active area (excluding access lines) of the CSRR-based hybrid coupler is 3.62 cm , whereas the conventional one occupies an area of 10.33 cm². The device has been designed to operate at 1.6 GHz.

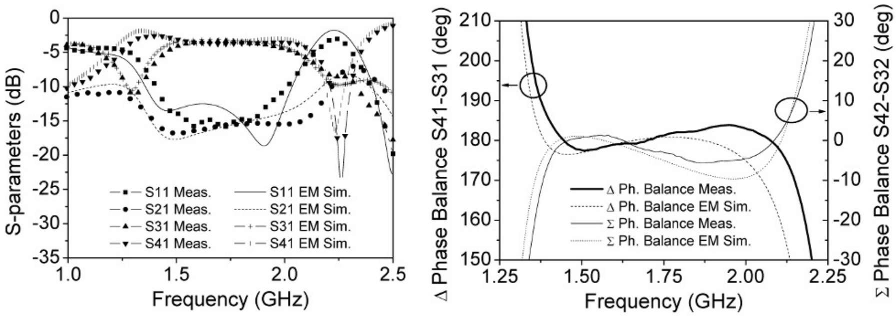


**(a)** **(b)**

**Fig. 3** Impedance matching ($S_{11}$), coupling ($S_{31}$, $S_{41}$) and isolation ($S_{21}$) for the CSRR-based hybrid coupler (**a**) and phase balance for the Δ and Σ ports (**b**). Figure 3a has been reproduced with permission from [14]. (Copyright 2007 IEEE.)

**Table 1.** Comparison of the measured bandwidth characteristics in the conventional and metamaterial-based (fully artificial) rat-race hybrid couplers.

| | *Conventional* | | *Fully artificial* | |
|---|---|---|---|---|
| | Σ Input | Δ Input | Σ Input | Δ Input |
| **Output (dB)** | **3.10 ± 0.25** | **3.10 ± 0.25** | **3.5 ± 0.25** | **3.38 ± 0.25** |
| Range (GHz) | 1.38–1.70 | 1.40–1.72 | 1.55–1.89 | 1.54–1.89 |
| Bandwidth (%) | 20 | 20 | 20 | 20 |
| **Phase balance (degrees)** | **0 ± 5** | **180 ± 5** | **0 ± 5** | **180 ± 5** |
| Range (GHz) | 1.40–1.65 | 1.40–1.65 | 1.40–2.10 | 1.40–2.10 |
| Bandwidth (%) | 16 | 16 | 40 | 40 |
| **Isolation (dB))** | **<–15** | | **<–15** | |
| Range (GHz) | 1.20–1.90 | | 1.35–2.10 | |
| Bandwidth (%) | 45 | | 44 | |
| **Return loss (dB)** | **<–10** | | **<–10** | |
| Range (GHz) | 1.13–1.99 | 0.59–2.50 | 1.41–2.26 | 1.40–2.01 |
| Bandwidth (%) | 55 | 123 | 46 | 36 |

## 4 Application of Resonant-Type Metamaterial Transmission Lines to Multiband Components

Multiband components are devices able to exhibit certain functionality at different arbitrary frequencies. Owing to the possibility to control the dispersion diagram of metamaterial transmission lines, it is possible to implement at least dual band components [18], as will be shown in this section. Specifically, we will discuss in this work the possibility of implementing dual band impedance inverters, since such components are exhaustively used in many microwave circuits. The idea is to implement these dual band inverters by considering a single unit cell CRLH transmission line, with the lower frequency allocated in the lower (left handed) band, and the upper operating frequency allocated in the right handed transmission band. To implement these dual band inverters, we force the phase to −90° and +90°, respectively at the lower and upper operating frequencies, and the characteristic impedance to the required value. Thus, we have four conditions, whereas the CRLH line based on CSRR depends on five elements. Thus, analytical solution exists. To demonstrate the possibilities of this approach, we have designed a dual band 35.35 Ω impedance inverter that has been used for the implementation of a dual band Y-junction power divider functional at 0.9 and 1.8 GHz [19]. The layout of the fabricated device is depicted in Fig. 4a, and the simulated/measured frequency responses are depicted in Fig. 4b. The measured characteristics of this dual-band component are good and it exhibits a larger bandwidth in the second band. Other dual band components based on CSRR-loaded CRLH transmission lines, such as branch-line couplers have been recently reported [20].

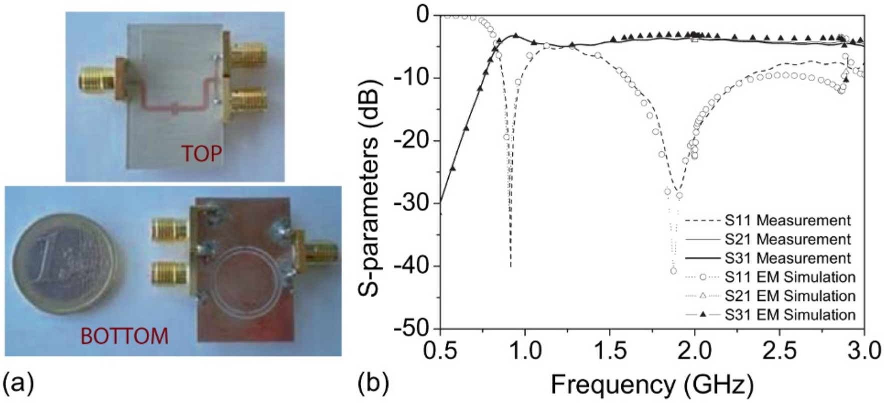


**Fig. 4** Topology of the designed dual-band power divider and simulated and measured power splitting ($S_{21}$, $S_{31}$) and matching ($S_{11}$). CSRR dimensions are: external radius $r$ = 7.90 mm, ring width $c$ = 0.50 mm and separation between rings $d$ = 0.57 mm. The width of the host line is $W$ = 1.00 mm and gap dimensions are: separation $s$ = 0.27 mm and width $W_g$ = 2.77 mm. (From [19]. Copyright 2008 IEEE. Reprinted with permission.)

## 5 Conclusion

In conclusion, it has been shown in this paper that resonant type metamaterial transmission lines are useful for the design of enhanced bandwidth and dual band components. This owes to the possibility of tailoring the dispersion diagram of such lines. Both theory and prototype devices have been presented to illustrate the possibilities of the approach.

**Acknowledgments** This work has been supported by Spain MEC (project TEC2007-68013-C02-02) and EU through the NoE METAMORPHOSE. Thanks are also given to the Catalan Government for funding CIMITEC and for the project 2005SGR-00624. Marta Gil has been awarded with an FPU Grant (ref. AP2005-4523).

## References


1. C. Caloz and T. Itoh, Electromagnetic Metamaterials: Transmission Line Theory and Microwave Applications, Wiley, New York (2006).
2. R. Marqués, F. Martín and M. Sorolla, Metamaterials with Negative Parameters: Theory, Design and Microwave Applications, Wiley, New York (2007).
3. A.K. Iyer and G.V. Eleftheriades, Negative refractive index metamaterials supporting 2-D waves, in IEEE-MTT International Symposium, vol. 2, Seattle, WA, pp. 412–415, June 2002.
4. A.A. Oliner, A periodic-structure negative-refractive-index medium without resonant elements, in URSI Digest, IEEE-AP-S USNC/URSI National Radio Science Meeting, San Antonio, TX, p. 41, June 2002.
5. C. Caloz and T. Itoh, Application of the transmission line theory of left-handed (LH) materials to the realization of a microstrip LH transmission line, in Proceedings of the IEEE-AP-S USNC/URSI National Radio Science Meeting, vol. 2, San Antonio, TX, pp. 412–415, June 2002.
6. F. Martín, F. Falcone, J. Bonache, R. Marqués and M. Sorolla, A new split ring resonator based left handed coplanar waveguide, Appl. Phys. Lett., **83**, 4652–4654 (2003).
7. F. Falcone, T. Lopetegi, M.A.G. Laso, J.D. Baena, J. Bonache, R. Marqués, F. Martín, M. Sorolla, Babinet principle applied to the design of metasurfaces and metamaterials, Phys. Rev. Lett., **93**, 197401 (2004).
8. G. Sisó, J. Bonache, M. Gil and F. Martín, Application of resonant-type metamaterial transmission lines to the design of enhanced bandwidth components with compact dimensions, Microw. Opt. Technol. Lett., **50**, 127–134 (2008).
9. M. Gil, J, Bonache, I. Gil, J. García-García and F. Martín, Miniaturization of planar microwave circuits by using resonant-type left handed transmission lines, IET Microw. Antenn. Prop., **1**, 73–79 (2007).
10. J.D. Baena, J. Bonache, F. Martín, R. Marqués, F. Falcone, T. Lopetegi, M.A.G. Laso, J. García, I Gil and M. Sorolla, Equivalent circuit models for split ring resonators and complementary split rings resonators coupled to planar transmission lines, IEEE Trans. Microw. Theory Tech., **53**, 1451–1461 (2005).
11. F. Aznar, M. Gil, J. Bonache and F. Martín, Revising the equivalent circuit models of resonant-type metamaterial transmission lines, IEEE MTT-S Inter. Microw. Symp., 323–326, Atlanta, GA, June 2008.
12. D.M. Pozar, Microwave Engineering, Addison-Wesley, New York (1993).
13. R.A. Foster, Bell Syst. Tech. J., **3**, 259 (1924).
14 G. Sisó, J. Bonache, M. Gil, J. García-García and F. Martín, Compact rat-race hybrid coupler implemented through artificial left handed and right handed lines, IEEE MTT-S Inter. Microw. Symp., 25–28 Honolulu (Hawaii), June 2007.
15. H. Okabe, C. Caloz and T. Itoh, A compact enhanced bandwidth hybrid ring using an artificial lumped element left handed transmission line section, IEEE Trans. Microw. Theory Tech., **52**, 798–804 (2004).
16. M.A. Antoniades and G.V. Eleftheriades, A broadband series power divider using zero-degree metamaterial phase shifting lines, IEEE Microw. Wireless Comp. Lett., **15**, 808–810 (2005).
17. I.B. Vendik, O.G. Vendik, D. V. Kholodnyak, E.V. Serebryakova and P.V. Kapitanova, Digital phase shifters based on right- and left-handed transmission lines, Proc. Euro. Microw. Assoc., **2**, 30–37 (2006).
18. Lin, I.H., De Vincentis, M, Caloz, C. and Itoh, T, Arbitrary dual-band components using composite rigth/left handed transmission lines, IEEE Trans. Microw. Theory Tech., **52**, 1142–1149 (2004).

19. G. Sisó, J. Bonache and F. Martín, Dual-band Y-junction power dividers implemented through artificial lines based on complementary resonators, IEEE MTT-S Inter. Microw. Symp., 663–666, Atlanta, GA, June 2008.
20. J. Bonache, G. Sisó, M. Gil, A. Iniesta, J. García-Rincón and F. Martín, Application of composite right/left handed (CRLH) transmission lines based on complementary split ring resonators (CSRRs) to the design of dual band microwave components, IEEE Microw. Wireless Comp. Lett., **18**, 524–527 (2008).

# Compact Dual-Band Rat-Race Coupler Based on a Composite Right/Left Handed Transmission Line

**Xin Hu[1,2] and Sailing He[1,2,*]**

[1]Division of Electromagnetic Engineering, School of Electrical Engineering, Royal Institute of Technology, S-100 44 Stockholm, Sweden
[2]Centre for Optical & Electromagnetic Research, Zhejiang University, Hangzhou 310058, China
[*]sailing@kth.se

**Abstract** A general model for dual band rat-race couplers is presented through an odd-even mode analysis approach. The requirements for the impedances and electrical lengths of the branches are derived. To verify this model, a dual-band rat-race coupler is designed utilizing the balanced composite right/left handed transmission line. The whole structure is much more compact than the existing dual-band rat-race couplers and easy to fabricate. The simulated results are given. Return loss and port isolation of better than −30 dB are achieved at the central frequencies of both operating bands. Furthermore, the requirements of equal amplitude and balanced phase conditions are well fulfilled (within 0.5 dB and 5°) over a frequency range of almost 50 and 90 MHz at the two central frequencies.

## 1 Introduction

The rat-race coupler is one of the most basic microwave components in a wide range of circuit and system applications [1]. It is commonly used in balanced amplifiers and mixers for achieving minimal return loss, as well as spurious signal rejection. It consists of four branches forming a loop with appropriate impedances determined by specific requirements. However, due to the inherent nature of the conventional design, it is hard to be used in a multiband device, which is required in many of the modern RF systems. Recently, some dual band rat-race coupler schemes have been reported using additional stubs [1, 2], or composite right/left

S. Zouhdi et al. (eds.), *Metamaterials and Plasmonics: Fundamentals, Modelling, Applications*,

handed (CRLH) transmission lines (TL) [3]. However, their circuits exhibit the following drawbacks:

1. Complicated structure: more than one branches are non-microstrip lines [3] or
2. Occupying a substrate area much larger than the conventional design (some branch-lines are at least half-wavelength long) [1, 2]

In this work we first give a generalized formulation of dual-band rat-race couplers with an analysis of odd and even modes. From this formulation, the requirements of impedances and electrical length of the branches are derived.

In [4], a more general configuration of the planar negative refractive index (NRI) transmission line (TL) [5] – CRLH TL, which includes both right-handed (RH) and LH effects, was proposed and discussed. As an example for the verification of our model derived in this work, a novel compact dual-band rat-race coupler is designed utilizing the balanced CRLH TL (CRLH TL can provide opposite phase shifts at two different frequencies). In our proposed design, all branch lines are only around a quarter-wavelength long evaluated at the mid-frequencies of the two operating bands, and no stub is used so that the whole structure is much more compact than the existing dual-band rat-race couplers. The simulated results are given in the end.

## 2 Generalized Formulation and Circuit Realization

The schematic diagram of the dual-band rat-race coupler structure is shown in Fig. 1. The conventional single band rat-race coupler consists of three identical branches with a length of $\lambda/4$ (at the central frequency) and one branch with a length of $3\lambda/4$ (at the central frequency), and all the branches have a fixed impedance of $\sqrt{2}\,Z_0$ (i.e., 70.7 Ω for a 50 Ω system). However, our proposed structure consists of branches whose electrical lengths and impedances are decided by $f_1$ and $f_2$ (the central frequencies of the lower and upper bands).

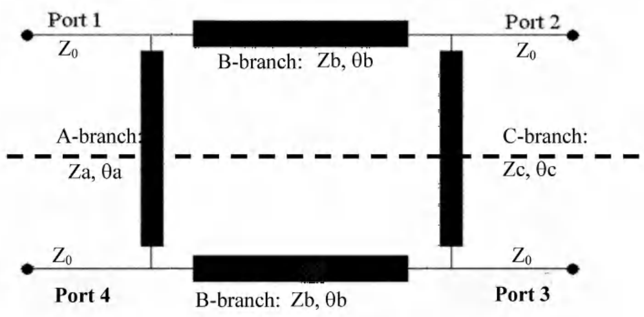


**Fig. 1** Schematic diagram for a rat-race coupler structure.

The four-port scattering matrix elements of the rat-race coupler should satisfy $S_{13} = 0$, $S_{11} = 0$ and $|S_{12}| = |S_{14}|$ [their phases could be of in-phase ($\angle S_{12} - \angle S_{14} = 0°$) or anti-phase ($\angle S_{12} - \angle S_{14} = 180°$)] at two different frequencies $f_1$ and $f_2$. To derive the impedance values and electrical lengths of the branch-lines, we use an odd-even mode analysis (in Fig. 2). The rat-race coupler structure shown in Fig. 1 is equivalent to topologies of Fig. 2a (for the even-mode case) and Fig. 2b (for the odd-mode case), where

$$B_1 = Y_a \tan\frac{\theta_a}{2}; B_2 = Y_c \tan\frac{\theta_c}{2}; B_3 = -Y_a \cot\frac{\theta_a}{2}; B_4 = -Y_c \cot\frac{\theta_c}{2} \quad (1)$$

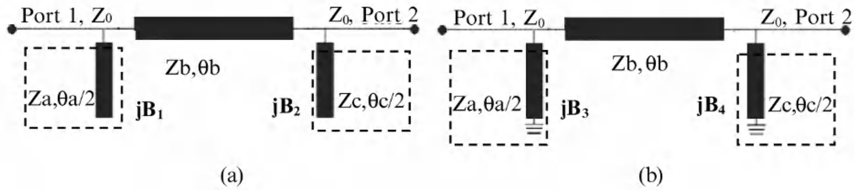


**Fig. 2** (**a**) Even- and (**b**) odd-mode topologies of Fig. 1.

For the even-mode case, the two-port scattering-matrix elements can be written as [6],

$$\begin{aligned} S_{11}^{even} &= \left[Y_0^2 - Y_b^2 + B_1B_2 - (B_1+B_2)Y_b\cot\theta_b + jY_0(B_2 - B_1)\right]/\Delta_{even} \\ S_{22}^{even} &= \left[Y_0^2 - Y_b^2 + B_1B_2 - (B_1+B_2)Y_b\cot\theta_b + jY_0(B_1 - B_2)\right]/\Delta_{even} \\ S_{12}^{even} &= S_{21}^{even} = -j2Y_0Y_b\csc\theta_b/\Delta_{even} \end{aligned} \quad (2)$$

where $\Delta_{even} = Y_0^2 + Y_b^2 - B_1B_2 + (B_1+B_2)\,Y_b\cot\theta_b + jY_0(B_2 + B_1 - 2Y_b\cot\theta_b)$. By replacing $B_1$ with $B_3$, and $B_2$ with $B_4$, we can obtain the scattering matrix parameters for the odd-mode case. Due to the inherent symmetry of the structure, the four-port scattering matrix elements of the rat-race coupler can be determined from the two-port scattering-matrix elements as follows,

$$\begin{aligned} S_{11} &= (S_{11}^{even} + S_{11}^{odd})/2, S_{22} = (S_{22}^{even} + S_{22}^{odd})/2 \\ S_{12} &= (S_{12}^{even} + S_{12}^{odd})/2, S_{13} = (S_{12}^{even} - S_{12}^{odd})/2 \\ S_{14} &= (S_{11}^{even} - S_{11}^{odd})/2, S_{32} = (S_{22}^{even} - S_{22}^{odd})/2 \end{aligned} \quad (3)$$

The requirement of isolation between port1 and port3 (i.e., $S_{13} = 0$) can only be satisfied if $\Delta_{even} = \Delta_{odd}$, which gives

$$B_1 + B_2 = B_3 + B_4\,;\, B_1 B_2 = B_3 B_4 \tag{4}$$

Under condition $\Delta_{even} = \Delta_{odd}$, the requirement of minimal return loss (i.e., $S_{11} = 0$) gives

$$B_1 + B_3 = B_4 + B_2 \tag{5}$$

$$2(Y_0^2 - Y_b^2) + B_1 B_2 + B_1 B_2 = (B_1 + B_2 + B_3 + B_4) Y_b \cot\theta_b \tag{6}$$

From Eqs. (4) and (5), we can obtain $B_1 = B_4$ and $B_2 = B_3$. It thus follows from Eq. (1) that $Y_a / Y_c = -\sin\theta_a / \sin\theta_c$. Assuming $B_1 = B_4 = P$, $B_2 = B_3 = R$, Eq. (6) can be simplified to

$$(Y_0^2 - Y_b^2) + PR = (P + R) Y_b \cot\theta_b \tag{7}$$

The requirement of $|S_{12}| = |S_{14}|$ gives

$$|P - R| = |2Y_b \csc\theta_b| \tag{8}$$

The solution to the system of Eqs. (7) and (8) gives the impedances and electrical lengths of the branches. The solution varies with *K*, defined as the ratio of the impedances of the B-branch and the input port (i.e., $K = Z_b/Z_0$). In Table 1, we list different possible in-phase ( $\angle S_{12} - \angle S_{14} = 0°$ ) or anti-phase ( $\angle S_{12} - \angle S_{14} = 180°$ ) solutions according to two different choices of *K*.

**Table 1.** Solutions to the system of Eqs. (7) and (8).

| Case 1: in-phase outputs | | Case 2: anti-phase outputs | |
|---|---|---|---|
| $P - R = 2Y_b \csc\theta_b$, $\angle S_{12} - \angle S_{14} = 0°$ <br> $\begin{cases} P = Y_b\left(\cot(\theta_b/2) \pm \sqrt{2/\sin^2\theta_b - K^2}\right) \\ R = Y_b\left(-\tan(\theta_b/2) \pm \sqrt{2/\sin^2\theta_b - K^2}\right) \end{cases}$ | | $P - R = -2Y_b \csc\theta_b$, $\angle S_{12} - \angle S_{14} = 180°$ <br> $\begin{cases} P = Y_b\left(-\tan(\theta_b/2) \pm \sqrt{2/\sin^2\theta_b - K^2}\right) \\ R = Y_b\left(\cot(\theta_b/2) \pm \sqrt{2/\sin^2\theta_b - K^2}\right) \end{cases}$ | |
| $K^2 = 2/\sin\theta_b^2$ | $K^2 = -2\cos(2\theta_b)/\sin\theta_b^2$ | $K^2 = 2/\sin\theta_b^2$ | $K^2 = -2\cos(2\theta_b)/\sin\theta_b^2$ |
| (1) $\begin{cases} P = Y_b \cot(\theta_b/2) \\ R = -Y_b \tan(\theta_b/2) \end{cases}$ | (2) $\begin{cases} P = Y_b \tan(\theta_b/2) \\ R = -Y_b \cot(\theta_b/2) \end{cases}$ | (3) $\begin{cases} P = -Y_b \tan(\theta_b/2) \\ R = Y_b \cot(\theta_b/2) \end{cases}$ | (4) $\begin{cases} P = -Y_b \cot(\theta_b/2) \\ R = Y_b \tan(\theta_b/2) \end{cases}$ |

As an example for circuit realization and verification, we design and simulate a dual-band microstrip branch-line coupler (as shown in Fig. 3) operating at 900/2,000 MHz.

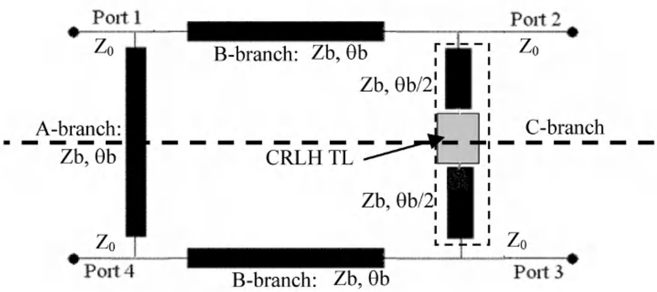


**Fig. 3** Proposed dual-band rat-race coupler structure.

We select a simpler solution, namely, solution (2) in Table 1 with in-phase outputs. Then the ratio $K$ of the impedances of the B-branch and the input port satisfies

$$K^2 = -2\cos(2\theta_b)/\sin\theta_b^2 \text{ when frequency } f = f_1 \text{ or } f_2 \tag{9}$$

With the following relation between the electrical lengths of B-branch (i.e., $\theta_b$) at two different frequencies $f_1$ and $f_2$

$$\theta_{b1}/\theta_{b2} = f_1/f_2 \tag{10}$$

we can obtain that $\theta_b$ is equal to 90° at 1.45 GHz (the center of $f_1$ and $f_2$), and $Z_b$ = 52 Ω when the impedance of the input port is 50 Ω. For the requirements of A-branch and C-branch, we choose the following simple one of different possible results from solution (2) of $P$ and $R$,

$$\begin{aligned} &Z_a = Z_b;\ \theta_a = \theta_b \text{ when } f = f_1 \text{ or } f_2 \\ &Z_c = Z_b;\ \theta_c = \begin{cases} \theta_b + 180° \text{ when } f = f_1 \\ \theta_b - 180° \text{ when } f = f_2 \end{cases} \end{aligned} \tag{11}$$

This means that A-branch is identical to B-branch, while C-branch has the same impedance as B-branch but a phase shift difference of +180° and −180° at $f_1$ and $f_2$, respectively. In our proposed coupler, four unit cells (Fig. 4 shows one unit cell) of balanced CRLH transmission line [4] are utilized in the C-branch to provide the necessary +180° and −180° phase shift at $f_1$ and $f_2$, respectively.

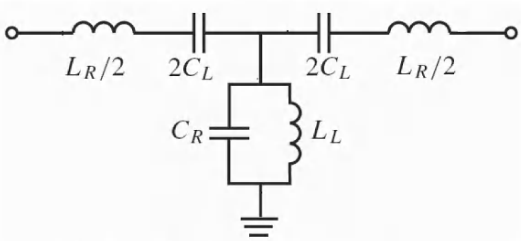


**Fig. 4** Unit cell of CRLH transmission line.

The values of the inductances and capacitors in the unit cell can be derived from

$$\begin{aligned} &\sqrt{\frac{L_R}{C_R}} = \sqrt{\frac{L_L}{C_L}} = Z_c = Z_b; \\ &\Delta\phi = -N\left(\omega\sqrt{L_R C_R} - \frac{1}{\omega\sqrt{L_L C_L}}\right) = \begin{cases} +180^\circ @ f_1 \\ -180^\circ @ f_2 \end{cases} \end{aligned} \tag{12}$$

where the number of the unit cell N = 4 in the proposed structure, and $C_R$ = 2.1pF, $L_R$ = 5.9nH, $C_L$ = 2.5pF, and $L_L$ = 6.5nH. To keep the symmetry of the structure, we insert the CRLH TL in the middle of two halves of B-branch, as shown in Fig. 3. Figure 5 gives the overall performance of the proposed coupler simulated at the two central frequencies. Return loss and port isolation of better than −30 dB are achieved at the central frequencies of both operating bands. Furthermore, both requirements of equal amplitudes and balanced phases are well fulfilled (within 0.5 dB and 5°) over a wide frequency range of almost 50 and 90 MHz at the two central frequencies.

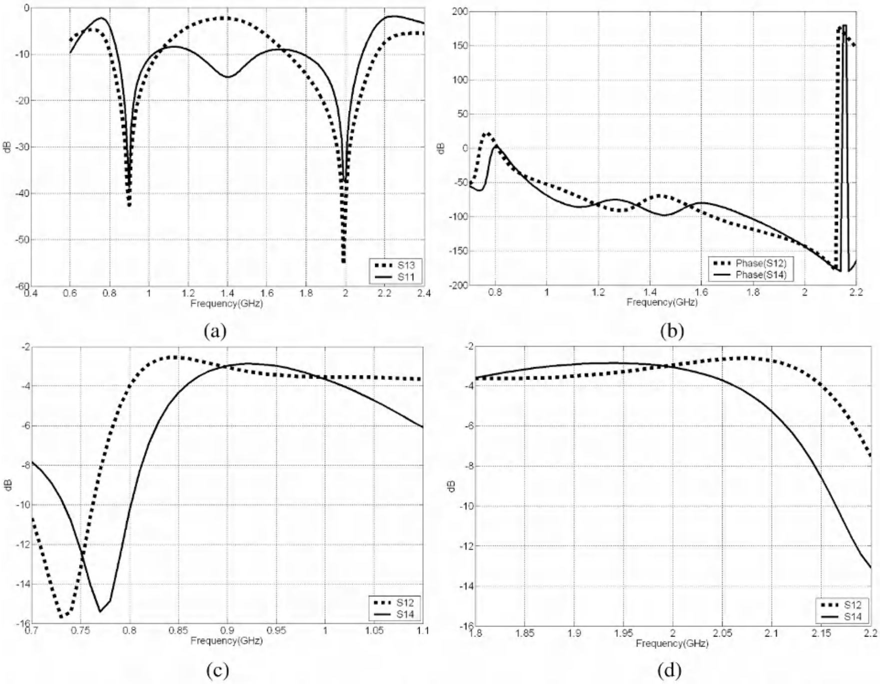


**Fig. 5** Simulated performance of the proposed structure. (**a**) return loss and port isolation; (**b**) phase response; (**c**) insertion loss (*lower band*); (**d**) insertion loss (*upper band*).

## 3 Conclusions

In the present work, a general model for dual band rat-race couplers has been given through an odd-even mode analysis approach. The requirements for the impedances and electrical lengths of the branches have been given. To verify the model, a compact dual-band rat-race coupler has been designed by utilizing a balanced CRLH TL since the opposite phase shifts at two different central frequencies can be provided by a CRLH TL. Choosing an appropriate ratio of the impedances for a branch and the input port according to two different central frequencies, we can obtain an arbitrary dual-band rat-race coupler. The whole structure is much more compact than the existing dual-band rat-race couplers since the branches in the coupler are all around one quarter wavelength at the center of the two frequencies, and no stubs are involved. The structure is also easy to fabricate. Return loss and port isolation of better than −30 dB have been achieved at the central frequencies of both operating bands. Furthermore, the conditions of equal amplitudes and balanced phases are well satisfied (within 0.5 dB and 5°) over a wide frequency range of almost 50 and 90 MHz for the two desired lower and upper frequency bands.

**Acknowledgments** This work was supported by the National Basic Research Program (973) of China (NO.2004CB719802) and the Swedish Research Council (VR) under Project No. 2006-4048.

## References

1. K. K. M. Cheng and F. L. Wong: A novel rat race coupler design for dual-band applications, IEEE Microwave and Wireless Components Letters, 15(8):521–523 (2005)
2. K. K. M. Cheng and F. L. Wong: Dual-band rat-race coupler design using tri-section branch-line, Electronics Letters, 43(6):41–42 (2007)
3. I. H. Lin, M. De Vincentis, C. Caloz and T. Itoh: Arbitrary dual-band components using composite right/left-handed transmission lines, IEEE Microwave Theory and Techniques, 52(4):1242–1249 (2004)
4. A. Lai, C. Caloz, T. Itoh: Composite right/left-handed transmission line metamaterials, IEEE Microwave Magazine, 5(3):34–50 (2004)
5. A. K. Iyer, G. V. Eleftheriades: Negative refractive index metamaterials supporting 2-D waves, Proceedings of the IEEE International Symposium on Microwave Theory and Techniques, 2:1067–1070 (2002)
6. R. E. Collin: Foundations for Microwave Engineering, Chapter 6, Second Edition, McGraw-Hill, New York (1992)

# Dispersion and Losses in Metamaterial DNG H-Guides

**António L. Topa, Carlos R. Paiva, and Afonso M. Barbosa**

Instituto de Telecomunicações and Department of Electrical and Computer Engineering, Instituto Superior Técnico, Av. Rovisco Pais 1, 1049-001 Lisboa, Portugal
antonio.topa@lx.it.pt

**Abstract** This article addresses the influence of the metamaterial losses and dispersion on the performance of double negative H-guides. The lossy dispersive Lorentz model is adopted for both the electric permittivity and the magnetic permeability. The dispersion properties of the longitudinal section magnetic modes and their root dynamics in the complex plane of the longitudinal wavenumber are analyzed. To emphasize that the modal characteristics must be analyzed taking losses into consideration, results for the lossless approximation are also presented. Finally, it is shown that the effect of metamaterial losses may suggest some potential applications.

## 1 Introduction

The propagation characteristics of waveguiding structures containing metamaterials have been subject to intense investigation in the last years, having always in mind their potential application in microwave and millimeter-wave guiding and radiating devices [1–11]. This article presents a systematic analysis of the effects of losses on the dispersion characteristics of the modes supported by a double negative (DNG) H-guide [1].

In a DNG H-guide, a metamaterial slab with simultaneously negative permittivity and negative permeability is sandwiched between two metal plates. H-guides involving metamaterials have been already addressed in the literature [1, 5], but the analysis has been mostly limited to single frequency operation.

The electromagnetic coupling between two parallel double-positive (DPS) and DNG H-guides [1], their field distribution, mode bifurcation and super-slow modes [5], have been already reported. Single-negative (SNG) metamaterials have also been considered, either to reduce the radiation at bends and discontinuities [10], or to achieve unimodal propagation [11]. Although a frequency dispersive

S. Zouhdi et al. (eds.), *Metamaterials and Plasmonics: Fundamentals, Modelling, Applications*,

DNG metamaterial was considered in [9], the metamaterial losses have been disregarded.

The main goal of this article is to show that unphysical results arise when simple dispersion models, disregarding losses, are adopted, therefore violating causality. In fact, according to the Kramers-Kronig relations, a causal dispersive metamaterial model must necessarily include the losses. In this article, a lossy dispersive DNG metamaterial is considered, exhibiting a permeability and permittivity modeled according to the Lorentz model. The propagation of lossy surface and leaky modes in this type of waveguide is analyzed and its performance is investigated.

This article is organized as follows. In Section 2, the electromagnetic problem is formulated and the modal equations for the modes of the DNG H-guide are presented. Moreover, the dispersion Lorentz homogenization model, accounting for both dispersion and losses, is described. In Section 3, the numerical results of the simulation are presented, namely the dispersion characteristics of the LSM modes are analyzed and the effects of the metamaterial losses are discussed. Finally, in Section 4, some concluding remarks are outlined.

## 2 Modal Analysis and Dispersive Model

In this section, the electromagnetic problem under analysis is defined, namely the waveguiding structure and respective modal equations are presented and the constitutive parameters of the metamaterial medium are characterized.

The DNG H-guide [1] consists of a metamaterial slab of width $2l$, with simultaneously negative relative electric permittivity $\varepsilon$ and negative relative magnetic permeability $\mu$, sandwiched between two metal plates spaced a distance $b$ apart (Fig. 1).

When the spacing $b$ is less than half a free-space wavelength, undesired radiation from the structure is prevented, since higher-order parallel-plate waveguide modes are below cutoff, and the TEM parallel-plate waveguide mode is not excited provided that symmetry with respect to the $y$ axis is maintained. In this case, the H-guide is working in the closed waveguide regime and is usually termed DNG NRD waveguide [11]. In the frequency range and for the numerical dimensions considered in this article the H-guide is always working in this regime, therefore behaving as a closed waveguide.

The full discrete spectrum of a NRD waveguide filled with isotropic DNG metamaterials comprises both longitudinal section magnetic (LSM) and longitudinal section electric (LSE) modes whilst, due to spatial symmetry of the structure, these modes can be divided into even and odd modes.

The modal equations for the even and odd $\mathrm{LSM}_{mn}$ modes can be written, respectively, as [1]

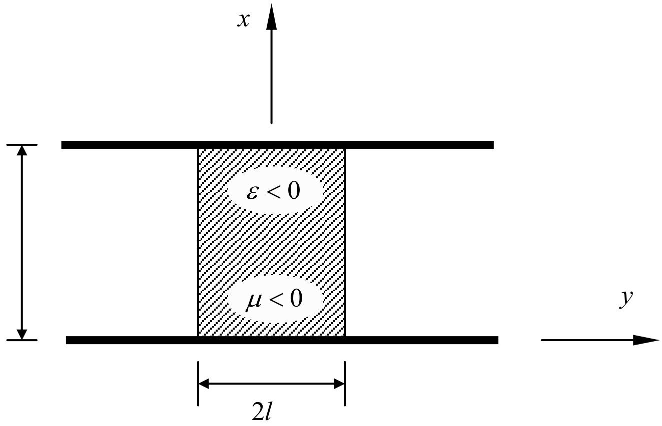


**Fig. 1** The DNG H-guide.

$$|\varepsilon|\rho + h\tan(hl) = 0 \tag{1}$$

and

$$|\varepsilon|\rho - h\cot(hl) = 0 \tag{2}$$

where $\rho^2 = k^2 + k_y^2 - k_0^2$ and $h^2 = \varepsilon\mu k_0^2 - k^2 - k_y^2$ are the transverse wavenumbers inside and outside the metamaterial slab, respectively, and where $k_0 = \omega\sqrt{\varepsilon_0\mu_0}$ and $k_y = n\pi / b$, with $n$ being an integer.

The modal equations for the LSE modes can be easily derived by duality directly from (1) and (2). However, the most interesting mode in this waveguide is the $\mathrm{LSM}_{01}$ mode which, when the slab is made of a conventional dielectric ($\varepsilon > 0$, $\mu = 1$) exhibits a low attenuation loss which decreases with frequency. Therefore, without loss of generality, this article is restricted to the modal analysis of the LSM modes.

To avoid unphysical effects and results, the analysis of electromagnetic waves in waveguides containing DNG metamaterials cannot be based on a simple parameter model that disregards dispersion effects and losses. To ensure causality, the model for the constitutive parameters of a DNG metamaterial must take both dispersion and losses into account. In fact, losses and dispersion are just two aspects of the same physical phenomenon: material interaction and microscopic resonance.

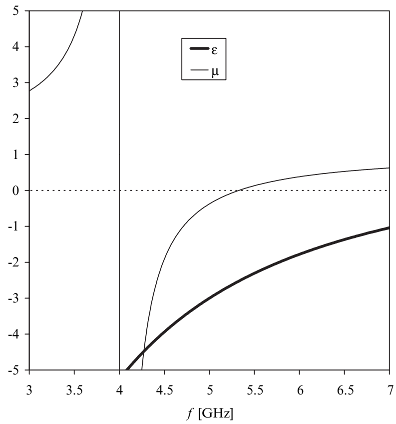


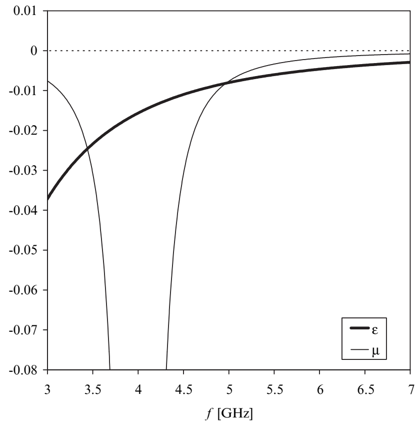


**Fig. 2** Relative permeability and relative permittivity of the DNG metamaterial as a function of the frequency, as given by the Lorentz dispersion model in the presence of losses: (**a**) Real part; (**b**) Imaginary part.

A lossy dispersive DNG metamaterial is considered for analysis throughout this article. The idea of realizing a metamaterial using split ring resonators and thin wires [12], which is the most popular among the physics community, is known to be a particular case of the generalized Lorentz medium [13, 14]. Therefore, the medium used in the present DNG H-guide is assumed to exhibit an electric permittivity and a magnetic permeability modeled according to the following Lorentz model:

$$\varepsilon(\omega) = 1 + \frac{\omega_{p_e}^2}{\omega_{0_e}^2 - \omega^2 + j\Gamma_e\omega} \tag{3}$$

and

$$\mu(\omega) = 1 + \frac{\omega_{p_m}^2}{\omega_{0_m}^2 - \omega^2 + j\Gamma_m\omega} \tag{4}$$

where $\omega_0$ are the resonance frequencies, $\omega_p$ the plasma frequencies and $\Gamma$ the collision losses.

The following values for the model parameters have been used in the numerical simulations of the next section: $\omega_{0_e} = 2\pi \times 10^8 \,\text{rad s}^{-1}$, $\omega_{0_m} = 2\pi \times 4 \times 10^9 \,\text{rad s}^{-1}$,

$\omega_{p_e} = 2\pi \times 10^{10}\,\text{rad s}^{-1}$ and $\omega_{p_m} = 2\pi \times 3.52 \times 10^{9}\,\text{rad s}^{-1}$. These values are of the order of magnitude as the ones used in [15].

With this material parameters, the frequency band where the real part of $\varepsilon$ and $\mu$ are simultaneously negative (DNG), ranges from $f = 4.0\,\text{GHz}$ to $f = 5.32\,\text{GHz}$. Immediately below and above this range, the magnetic permeability becomes positive and, therefore, the medium turns into an epsilon negative (ENG) metamaterial. These cases will not be addressed herein. In particular, this study is focused on the frequency range immediately above to the permittivity resonance.

To analyze the effect of losses on the performance of the metamaterial DNG H-guide, two cases are considered: (i) $\Gamma_e = \Gamma_m = 0$ (lossless medium); (ii) $\Gamma_e = \Gamma_m = 4\pi \times 10^{6}\,\text{rad s}^{-1}$, $\Gamma_e = \Gamma_m = \pi \times 10^{7}\,\text{rad s}^{-1}$, $\Gamma_e = \Gamma_m = 2\pi \times 10^{7}\,\text{rad s}^{-1}$, $\Gamma_e = \Gamma_m = 4\pi \times 10^{7}\,\text{rad s}^{-1}$ (lossy media).

In Fig. 2 the relative permeability and relative permittivity of a lossy DNG metamaterial are shown as a function of frequency, in the $3\,\text{GHz} < f < 7\,\text{GHz}$ band, when $\Gamma_e = \Gamma_m = 2\pi \times 10^{7}\,\text{rad s}^{-1}$. The almost vertical line that appears in the real part of the relative magnetic permeability is due to the magnetic resonance at $\omega_{0_m} = 2\pi \times 4 \times 10^{9}\,\text{rad s}^{-1}$, which also corresponds to the point where its imaginary part exhibits a peak.

## 3 Numerical Results

In this section we analyze the dispersion behavior of the LSM modes propagating in the DNG H-guide and their root dynamics in the complex plane of the longitudinal wavenumber. Although some dispersion curves of this waveguide have already been presented in [11] in the absence of losses, the results presented here are helpful to understand the modal behavior in the presence of losses and envisage potential applications. To better realize the modal behavior in the presence of losses a systematic comparison between the lossless and the lossy case is always presented.

The dispersion diagrams for the first LSM modes propagating in a DNG H-guide, with $l = 1\,\text{cm}$ and $b = 3\,\text{cm}$, are depicted in Fig. 3a for the lossless case, and in Fig. 3b for the lossy case. In both these figures, the thick solid lines stand for the proper surface modes, the thin lines for the proper leaky modes and the dashed lines for the improper leaky modes.

In the lossless case, a resonant behavior for $\beta$ is observed in the dispersion diagrams of the surface modes, leading to an infinite value of the phase constant, even in the case of finite values for the constitutive parameters. When accounting for losses, these unphysical solutions disappear while turning into improper leaky modes, whilst the dispersion branches with physical meaning turn into proper leaky modes.

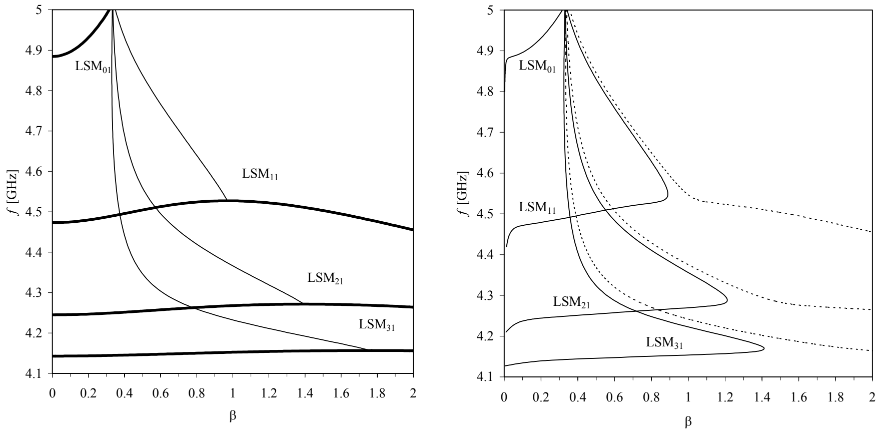


(a) (b)

**Fig. 3** Dispersion diagram for the first LSM modes propagating in the DNG H-guide, with constitutive parameters as in Fig. 2, $l = 1$ cm and $b = 3$ cm : (**a**) lossless case; (**b**) lossy case. The thick solid lines stand for the surface proper modes, the thin lines for the proper leaky modes and the dashed lines for the improper leaky modes.

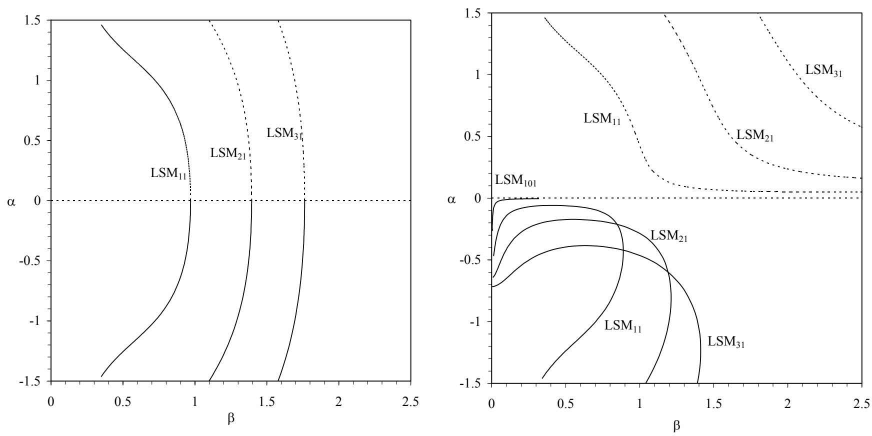


(a) (b)

**Fig. 4** Root loci in the complex plane of the longitudinal wavenumber for the leaky modes in Fig. 3: (**a**) Lossless case; (**b**) Lossy case. The solid lines stand for the proper leaky modes, while the dashed lines are for the improper leaky modes.

In Fig. 4, the modal equation root loci in the complex plane of the longitudinal wavenumber are presented for the first leaky modes propagating in the DNG

H-guide, for both the lossless and the lossy cases. As before, the solid lines stand for the proper leaky modes, while the dashed lines stand for the improper leaky modes.

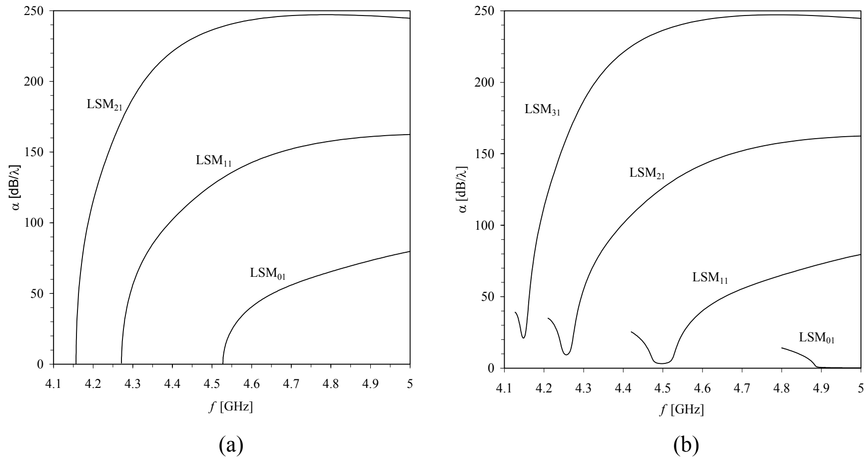


**Fig. 5** Leakage constant in dB/λ as a function of frequency for the proper leaky modes in Fig. 4: (**a**) Lossless case; (**b**) Lossy case.

One should stress that, the first and second quadrants of the complex plane of the longitudinal wavenumber $k$ correspond to the improper Riemann sheet in the complex plane of the transverse wavenumber $h$, while the third and fourth quadrants correspond to the proper Riemann sheet of the same plane.

Furthermore, one should note that, when considering a lossy dispersive metamaterial, all propagating modes become complex solutions of the modal equations and there is no distinction between surface and leaky modes propagating in the waveguide, although some of these modes may exhibit a larger leakage constant than the others.

The evolution of the leakage constant as a function of frequency is depicted in Fig. 5, again for both lossless and lossy cases. When losses are taken into account it is possible to see that there are very well defined narrow frequency bands where the attenuation constant can be considerably negligible, while it dramatically increases outside those bands.

This effect, reported here for the first time, opens the possibility of using these sharp frequency bands in the design of waveguiding filters having a very narrow passband with a high rejection band. This topic will be addressed in detail in a forthcoming publication.

The influence of introducing metamaterial losses in the modal dispersion and attenuation of the modes in the DNG H-guide is illustrated with more detail in Figs. 6 and 7. As an example, the dispersion diagram and the root loci of the $\mathrm{LSM}_{11}$ mode are depicted in Fig. 6, for different values of the loss parameter $\Gamma$. As a general conclusion, one may say that the smaller are the losses the stronger is the modal interaction between the proper and improper leaky modes, which causes a sharper frequency passband.

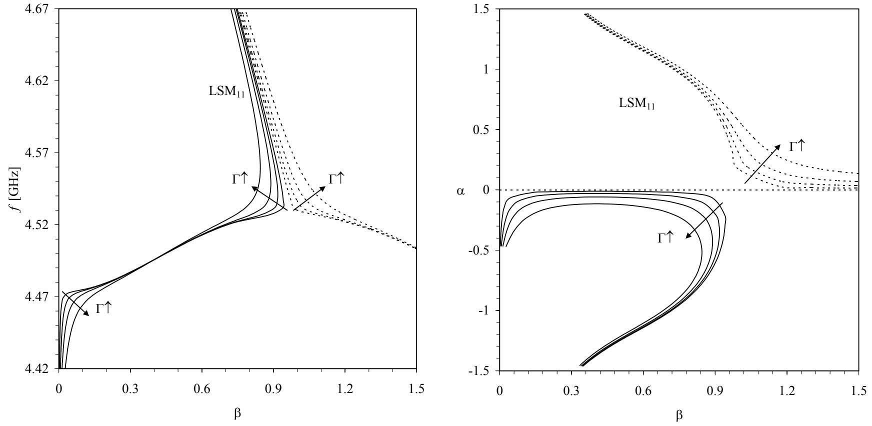


(a) (b)

**Fig. 6** Dispersion diagram (**a**) and root loci (**b**) for $\mathrm{LSM}_{11}$ mode: $\Gamma_e = \Gamma_m = 4\pi \times 10^6 \,\mathrm{rad\ s^{-1}}$, $\Gamma_e = \Gamma_m = \pi \times 10^7 \,\mathrm{rad\ s^{-1}}$, $\Gamma_e = \Gamma_m = 2\pi \times 10^7 \,\mathrm{rad\ s^{-1}}$ and $\Gamma_e = \Gamma_m = 4\pi \times 10^7 \,\mathrm{rad\ s^{-1}}$.

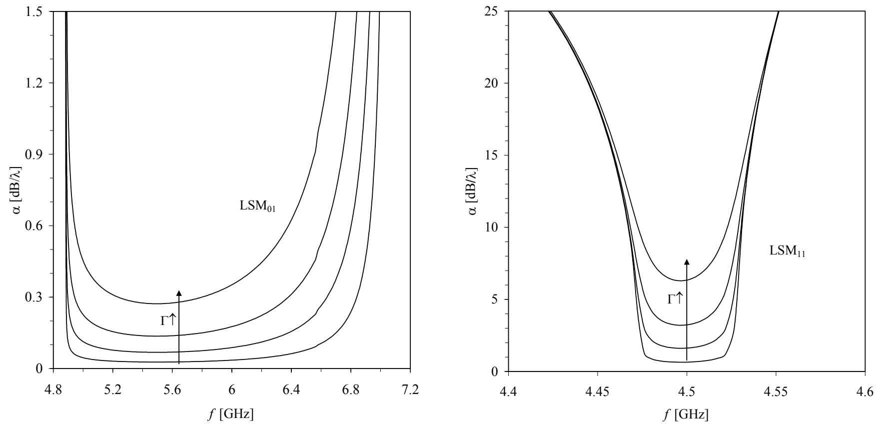


(a) (b)

**Fig. 7** Leakage constant as a function of frequency for $\mathrm{LSM}_{01}$ and $\mathrm{LSM}_{11}$ modes, when $\Gamma_e = \Gamma_m = 4\pi \times 10^6 \,\mathrm{rad\ s^{-1}}$, $\Gamma_e = \Gamma_m = \pi \times 10^7 \,\mathrm{rad\ s^{-1}}$, $\Gamma_e = \Gamma_m = 2\pi \times 10^7 \,\mathrm{rad\ s^{-1}}$ and $\Gamma_e = \Gamma_m = 4\pi \times 10^7 \,\mathrm{rad\ s^{-1}}$.

On the other hand, the variation of the leakage constant $\alpha$, in $\mathrm{dB}/\lambda$, as a function of the frequency is shown in Fig. 7 for the $\mathrm{LSM}_{01}$ and $\mathrm{LSM}_{11}$ modes, using the same set of values of $\Gamma$ as in Fig. 6. Again, it is shown that the smaller are the losses the sharper is the passband, therefore proving that losses play an important role in the dispersion characteristics of the waveguide.

# 4 Conclusion

Modal dispersion on DNG H-guides taking both metamaterial losses and dispersion into account has been studied here for the first time. In the absence of losses and for finite values of the constitutive parameters, unphysical resonances in the longitudinal wavenumber have been put in evidence. This unphysical modal behavior, disappears when losses are taken into account. It was shown that, when losses are introduced, these resonances turn into improper leaky modes not included in a spectral field representation. Moreover, it was shown that, in the presence of small losses, this waveguide exhibits sharp narrow passbands, hence suggesting its application in the design of waveguiding filters.

**Acknowledgment** This work was partially funded by FCT (Fundação para a Ciência e a Tecnologia), Portugal.

# References

1. Topa, A.L.: Contradirectional interaction in a NRD waveguide coupler with a metamaterial slab. Dig. XXVII URSI General Assembly, Maastricht, 1878 (2002).
2. Shadrivov, I.W., Sukhorukov, A.A., Kivshar, Y.S.: Guided modes in negative refractive-index waveguides. Phys Rev E **67**, 57602 (2003).
3. Wu, B.I., Grzegorczyk, T.M., Zhang, Y., Kong, J.A.: Guided modes with imaginary transverse wavenumber in a slab waveguide with negative permittivity and permeability. J Appl Phys **93**, 9386–9388 (2003).
4. Nefedov, I.S., Tretyakov, S.A.: Waveguide containing a backward-wave slab. Radio Sci **38**, 6, 1101–1110 (2003).
5. Lee, J.-G., Lee, J.-H.: Guided mode characteristics of NRD guide with left-handed materials (LHMs). Dig. 2003 ASAE, Seoul, 113–117 (2003).
6. Topa, A.L., Paiva C.R., Barbosa, A.M.: Guided wave propagation in H-guides using double negative materials. Dig. 2004 USNC/URSI National Radio Science Meeting Digest, Monterey, 156 (2004).
7. Alù, A., Engheta, N.: Guided modes in a waveguide filled with a pair of single negative (SNG), double-negative (DNG), and/or double-positive (DPS) layers. IEEE Trans Microw Theory Tech **52**, 199–210 (2004).
8. Topa, A.L., Paiva, C.R., Barbosa, A.M.: Novel propagation features of double negative H-guides and H-guide couplers. Microw Opt Technol Lett **47**, 2, 185–190 (2005).
9. Baccarelli, P., Burghignoli, P., Frezza, F., Galli, A., Lampariello, P., Lovat, G., Paulotto, S.: Effects of leaky-wave propagation in metamaterial grounded slabs excited by a dipole source. IEEE Trans Microw Theory Tech **53**, 32–44 (2005).

10. Yang, P., Lee, D., Wu, K.: Nonradiative dielectric waveguide embedded in metamaterial with negative permittivity or permeability. Microw Opt Technol Lett **45**, 3, 207–210 (2005).
11. Baccarelli, P., Burghignoli, P., Frezza, F., Galli, A., Lampariello, P., Paulotto, S.: Unimodal surface-wave propagation in metamaterial nonradiative dielectric waveguides. Microw Opt Technol Lett **48**, 12, 2557–2560 (2006).
12. Smith, D.R., Padilla, W.J., Vier, D.C., Nemat-Nasser, S.C., Schultz, S.: Composite medium with simultaneously negative permeability and permittivity. Phys Rev Lett **84**, 4184–4187, (2000).
13 Zedler, M., Caloz, C., Russer, P.: 3D Composite right-left Handed metamaterials with Lorentz-type dispersive elements. ISSSE – Int Symp Sign Syst Electron, 217–221 (2007).
14 Meyrath, T.P., Zentgraf, T., Giessen, H.: Lorentz model for metamaterials: Optical frequency resonance circuits: Phys Rev B **75**, 205102 (2007).
15 Mojahedi, M., Malloy, K.J., Eleftheriades, G.V., Woodley, J., Chiao, R.Y.: Abnormal wave propagation in passive media. IEEE J. Sel Top Quant Electron **9**, 30–39 (2003).

# Contributors

M. H. Al Sharkawy
Arab Academy for Science and Technology and Maritime Transport, College of Engineering and Technology, Alexandria, Egypt

A. Alù
University of Pennsylvania, Department of Electrical and Systems Engineering, 200 South 33rd St., Philadelphia, PA 19104, USA
University of Texas at Austin, Department of Electrical and Computer Engineering, 1 University Station C0803, Austin,TX 78712, USA

P. Baccarelli
Electronic Engineering Department, "SAPIENZA" University of Rome via Eudossiana 18, 00184, Rome, Italy

R. Bakker
Birck Nanotechnology Center, Purdue University, West Lafayette, IN 47907, USA

A. M. Barbosa
Instituto de Telecomunicações, Instituto Superior Técnico, Av. Rovisco Pais 1, 1049-001 Lisboa, Portugal

F. Bilotti
University "Roma Tre"– Department of Applied Electronics, Via della Vasca Navale, 84 – 00146 Rome, Italy

A. Boltasseva
Technical University of Denmark, DTU Building 343, DK-2800 Kongens Lyngby, Denmark

J. Bonache
CIMITEC, Departament d'Enginyeria Electrònica, Universitat Autònoma de Barcelona 08193 BELLATERRA (Barcelona), Spain

A. Bossavit
LGEP (CNRS, Univ. Paris Sud), 11 Rue Joliot-Curie, 91192 Gif-sur-Yvette, France

A. Z. Elsherbeni
The Center of Applied Electromagnetic Systems Research (CASER), Department of Electrical Engineering, The University of Mississippi, University, MS 38677, USA

N. Engheta
University of Pennsylvania, Department of Electrical and Systems Engineering, 200 South 33rd St., Philadelphia, PA 19104, USA

V. Fedotov
Optoelectronics Research Centre, University of Southampton, SO17 1BJ, UK

M. Gil
CIMITEC, Departament d'Enginyeria Electrònica, Universitat Autònoma de Barcelona, 08193 BELLATERRA (Barcelona), Spain

D. S. Goshi
Honeywell International Inc., Torrance, CA, USA

S. Guenneau
Department of Mathematical Sciences, University of Liverpool Peach Street, Liverpool L69 3BX, UK

M. Gustafsson
Department of Electrical and Information Technology, Lund University, P.O. Box 118, SE-221 00 Lund, Sweden

G. W. Hanson
Department of Electrical Engineering and Computer Science, University of Wisconsin-Milwaukee, Milwaukee, WI 53211, USA

S. He
Division of Electromagnetic Engineering, School of Electrical Engineering, Royal Institute of Technology, S-100 44 Stockholm, Sweden
Centre for Optical & Electromagnetic Research, Zhejiang University, Hangzhou 310058, China

B. H. Henin
The Center of Applied Electromagnetic Systems Research (CASER), Department of Electrical Engineering, The University of Mississippi, University, MS 38677, USA

S. Hrabar
Faculty of Electrical Engineering and Computing, University of Zagreb, Unska 3, Zagreb, HR 10 000, Croatia

X. Hu
Division of Electromagnetic Engineering, School of Electrical Engineering, Royal Institute of Technology S-100 44 Stockholm, Sweden
Centre for Optical & Electromagnetic Research, Zhejiang University, Hangzhou 310058, China

T. Itoh
Department of Electrical Engineering, University of California Los Angeles, 405 Hilgard Avenue, Los Angeles, CA 90095

C. Jeppesen
Technical University of Denmark, DTU Building 343, DK-2800 Kongens Lyngby, Denmark

H. Kettunen
Department of Radio Science and Engineering, Helsinki University of Technology (TKK), P.O. Box 3000, FI-02015 TKK, Finland

A. V. Kildishev
Birck Nanotechnology Center, Purdue University, West Lafayette, IN 47907, USA

A. Kristensen
Technical University of Denmark, DTU Building 343, DK-2800 Kongens Lyngby, Denmark

G. Kristensson
Department of Electrical and Information Technology, Lund University, P.O. Box 118, SE-221 00 Lund, Sweden

A. Lai
HRL Laboratories LLC, Malibu, CA, USA

T. Lam
The Boeing Company, M/C 3W-50, P.O. Box 3707, Seattle, Washington, USA

C. Larsson
Department of Electrical and Information Technology, Lund University, P.O. Box 118, SE-221 00 Lund, Sweden

N. Lassouaoui
University Paris X, Pôle Scientifique et Technique de Ville d'Avray, Groupe Electromagnétisme Appliqué, 50 rue de Sèvre 92410, Ville d'Avray, France

Z. Liu
Birck Nanotechnology Center, Purdue University, West Lafayette, IN 47907, USA

O. Luukkonen
Department of Radio Science and Engineering/SMARAD, TKK Helsinki University of Technology, P.O. Box 3000, FI-02015 TKK, Finland

F. Martín
CIMITEC, Departament d'Enginyeria Electrònica, Universitat Autònoma de Barcelona, 08193 BELLATERRA (Barcelona), Spain

A. Nicolet
Institut Fresnel – Aix-Marseille Université, Domaine Universitaire de Saint-Jérôme, F13397 Marseille cedex 20, France

R. B. Nielsen
Technical University of Denmark, DTU Building 343, DK-2800 Kongens Lyngby, Denmark

Y. Ould Agha
Institut Fresnel – Aix-Marseille Université, Domaine Universitaire de Saint-Jérôme, F13397 Marseille cedex 20, France

H. H. Ouslimani
University Paris X, Pôle Scientifique et Technique de Ville d'Avray, Groupe Electromagnétisme Appliqué,
50 rue de Sèvre 92410, Ville d'Avray, France

C. R. Paiva
Instituto de Telecomunicações, Instituto Superior Técnico, Av. Rovisco Pais 1, 1049-001 Lisboa, Portugal

N. Papasimakis
Optoelectronics Research Centre, University of Southampton, SO17 1BJ, UK

C. Parazzoli
The Boeing Company, M/C 3W-50, P.O. Box 3707, Seattle, Washington, USA

S. Paulotto
Electronic Engineering Department, "SAPIENZA" University of Rome via Eudossiana 18, 00184, Rome, Italy

A. Priou
University Paris X, Pôle Scientifique et Technique de Ville d'Avray, Groupe Electromagnétisme Appliqué, 50 rue de Sèvre 92410,Ville d'Avray, France

S. Prosvirnin
Institute of Radio Astronomy, Kharkov, 61002, Ukraine

Y. Rahmat-Samii
Department of Electrical Engineering, University of California at Los Angeles, Los Angeles, CA 90095, USA

M. A. Ribeiro
Instituto de Telecomunicações, and Department of Electrical and Computer Engineering, Instituto Superior Técnico, Av. Rovisco Pais 1, 1049-001 Lisboa, Portugal

A. G. Schuchinsky
Queen's University Belfast, ECIT, Belfast, BT3 9DT, UK

V. M. Shalaev
Birck Nanotechnology Center, Purdue University, West Lafayette, IN 47907, USA

A. Sihvola
Department of Radio Science and Engineering, Helsinki University of Technology, Box 3000, FI–02015 TKK, Finland

C. R. Simovski
Department of Radio Science and Engineering/SMARAD, TKK Helsinki University of Technology, P.O. Box 3000, FI-02015 TKK, Finland

G. Sisó
CIMITEC, Departament d'Enginyeria Electrònica, Universitat Autònoma de Barcelona, 08193 BELLATERRA (Barcelona), Spain

C. Sohl
Department of Electrical and Information Technology, Lund University, P.O. Box 118, SE-221 00 Lund, Sweden

M. Tanielian
The Boeing Company, M/C 3W-50, P.O. Box 3707, Seattle, Washington, USA

A. L. Topa
Instituto de Telecomunicações and Department of Electrical and Computer Engineering, Instituto Superior Técnico, Av. Rovisco Pais 1, 1049-001 Lisboa, Portugal

S. A. Tretyakov
Department of Radio Science and Engineering/SMARAD, TKK Helsinki University of Technology, P.O. Box 3000, FI-02015 TKK, Finland

L. Vegni
University “Roma Tre”, Department of Applied Electronics, Via della Vasca Navale, 84 – 00146 Rome, Italy

A. Vinogradov
Institute for Theoretical and Applied Electrodynamics, Russian Academy of Sciences, Ul. Izhorskaya, Moscow, 125412, Russia

H. Wallén
Department of Radio Science and Engineering, Helsinki University of Technology (TKK), P.O. Box 3000, FI-02015 TKK, Finland

M. C. K. Wiltshire
Imaging Sciences Department, Clinical Sciences Centre, Imperial College London, Hammersmith Hospital Campus, Ducane Road, London W12 0NN, UK

A. B. Yakovlev
Department of Electrical Engineering, University of Mississippi, University, MS 38677-1848, USA

X. Yan
Queen’s University Belfast, ECIT, Belfast, BT3 9DT, UK

F. Yang
Department of Electrical Engineering, The University of Mississippi, University, MS 38677, USA

H.-K. Yuan
Birck Nanotechnology Center, Purdue University, West Lafayette, IN 47907, USA

N. Zheludev
Optoelectronics Research Centre, University of Southampton, SO17 1BJ, UK

F. Zolla
Institut Fresnel – Aix-Marseille Université, Domaine Universitaire de Saint-Jérôme, F13397 Marseille cedex 20, France

S. Zouhdi
LGEP–SUPELEC, 11 Rue Joliot-Curie, 91192 Gif-sur-Yvette, France